Understanding the inhibition corrosion mechanisms for copper based alloys by a physico-chemical multi-scale approach

Erika Ferrari

université PARIS-SACLAY

Understanding the inhibition corrosion mechanisms for copper-based alloys by a physico-chemical multi-scale analytical approach

Compréhension des mécanismes d'inhibition de la corrosion du patrimoine métallique cuivreux par une approche physicochimique multi-échelle

Thèse de doctorat de l'université Paris-Saclay

École doctorale n°571 : sciences chimiques : molécules, matériaux, instrumentation et biosystèmes (2MIB)

Spécialité de doctorat : Chimie
Unité de recherche : Université Paris-Saclay, CEA, CNRS, NIMBE, 91191, Gif-sur-Yvette, France
Référent : Faculté des sciences d'Orsay

Thèse présentée et soutenue à Paris-Saclay, le 14/12/2021, par

Erika FERRARI

Composition du Jury

Ludovic BELLOT-GURLET Professeur, Sorbonne Université-MONARIS	Président
Emilio CANO Directeur de recherche, CENIM	Rapporteur & Examinateur
Tadeja KOSEC Directrice de recherche, ZAG	Rapporteur & Examinatrice
Philippe DILLMANN Directeur de recherche, CNRS	Examinateur

Direction de la thèse

Delphine NEFF Directrice de recherche, CEA	Directrice de thèse
Florence MERCIER Chargée de recherche, CNRS	Co-directrice de thèse
Philippe de VIVIES Conservateur, A-Corros	Invité

Thèse de doctorat

NNT : 2021UPASF053

Acknowledgments /Remerciments/ Ringraziamenti

Many people contributed to the development of this thesis work inside and outside chemical labs.

First, I would like to thank Philippe Dillmann for accepting me at the LAPA even though I did not speak a word of French in the beginning.

I thank my PhD director Delphine Neff who believed in this project and especially in the power of 5CBT from the beginning to the end.

I would like to thank the members of the jury who accepted to be part of this work and all the collaborators outside the laboratory that helped me realising a good part of the research. Nicolas Nuns for the Tof-SIMS analysis in real and in visio; “the TEM team” in Thiais with Eric Leroy, Julie Bourgon and Judith Monnier, thank you for the hours in the dark and for making me discover this incredible technique; Emmanuel Gardes for having tried plenty of things on the samples with the FIB in Caen.

I would like to acknowledge Aurelia Azema for taking the time to discuss the results and making the annual reports.

I also thank the team A-Corros and, in particular, Philippe de Vivies, Marine Bayle and Marine Crouzet for the discussions and the exchange and for having hosted me in Arles.

A special thanks goes to Mathias Clement who was so lucky to analyse the outdoor exposed samples..for me!

Je remercie vraiment beaucoup toutes et tous les membres du LAPA, permanents et non, d’hier et d’aujourd’hui ainsi que les collègues du LEEL et de la microsonde avec qui on a partagé des beaux moments dans la salle café !

Eddy Foy pour le soutien, les analyses DRX sur mes poudres qui ne terminais jamais (d’ailleurs j’ai un truc à analyser là) et les chansons.

Djibi Ba (ex LAPA), mon premier prof de français, compagnon de bureau et de café ! Merci aussi pour le café pimenté que difficilement j’oublierai !

Manon et Melissa pour avoir partagées des beaux moments pendant les années au labo et bien-sûr Dr Helene Lozt compagne de bureau, de discussions scientifiques, des aventures en conf et ailleurs !

Florian pour m’avoir fait participer à son intéressant projet sur le faux argent. Si dans quelques années je suis millionnaire vous savez pourquoi…

Jim, l’homme du « tout est possible » ! et oui je te dois quelque centaine des gâteaux pour ton travail.

Silvia, Thalie, Emilie, Charlie, Annabelle, Katya, Charlotte … pour tous les moments partagés ensemble. Nadia pour les recettes marocaines et pour ton sourire même dans les moments difficiles.

E infine un grazie a famiglia e amici, alcuni già citati, senza i quali niente sarebbe stato veramente possibile.

La mia mamma Carolina, il papà Walter e la mia sister Giulia, un pensiero ai miei nonni e al Turco.

Rouven, amico e compagno, per i viaggi fatti e quelli che faremo.

Isabella, per le centinaia di ore passate al telefono sempre con un ritardo pazzesco, grazie per le tue guide gastropornografiche.

Gaia per i pensieri positivi, per le riflessioni e per tutte le idee fantastiche che riesco ad avere quando parliamo insieme!

Les compagnons de la COLOC d'hier et d'aujourd'hui ! Emilie, Laurent, Maël, Timothée et Zoe : c'était un vrai plaisir de vivre ensable pendent ces années et ça va être super dur de quitter ce lieu aussi riche de relations humaines. Avec vous j'ai appris que on ne mange pas de la viandRe, j'étais dessOU mais bon je vais prendre un bOUs pour BOUres. Merci pour votre soutiens (et pour l'occupation du salon) pendant la rédaction.

Dr Ashish, a philosopher hidden behind a brilliant scientist! For his lovely food and all the discussions!

Caroline, ma pastèque du sud! pour avoir être été mon premier impact avec la France et Paris!!!

Sebastiano Berloffa, detto il bigolo, che ha stupito la Francia con il suo feticismo per i piedi.

Lorenzo, viaggiatore solitario e seriale, per la sua calma zen, i risotti e il buon vino.

Sabina ricercatrice e cultrice di insetti.

Jérôme, per aver aperto porte e spiriti !

Merci au gang des sud-américains : Andres, Consuelo, Ernesto, Dehni parce qu'avec vous c'est la fête!!!

List of contents

Introduction

Copper-based artefacts exposed outdoors represent part of our universal heritage. Atmospheric corrosion of metals can compromise the stability of such objects causing, over time, aesthetic damage and material loss. Therefore, the research for improving or finding new protection strategies represents an important challenge for scientists and conservators in a world characterized by evolving environmental conditions and limited availability of funding for regular maintenance.

The current conservation practice for copper-based exposed artefacts involves, after cleaning operations, the application of a coating (microcrystalline wax, acrylic resins) that is able to isolate the metal from the environment for a certain amount of time. Corrosion inhibitors might also be applied, usually as pre-treatments before the final coating application. Among the inhibitors, benzotriazole is the most commonly employed, despite no consensus exists on either its protection mechanism or its efficiency. In addition, considering the concern over its health and environments risks, the use of benzotriazole is discouraged and research is directed towards “green” and atoxic compounds.

Unlike coatings, for which an interaction with the surface of application is limited (silanes) or is not present (wax), corrosion inhibitors are generally small molecules that are chemically bonded to the substrate. In the case of corroded artefacts, the substrate is usually constituted by a complex system including layers composed by different mineral phases formed in the long-term (years, centuries). Most studies addressing inhibitors address industrial applications: the substrate considered is a bare metal or a metal covered by a thin oxide layer and the inhibitor is mixed to other aggressive species in solution.

In the present work, corrosion inhibitors for heritage applications are specifically addressed. The aim is to investigate the interactions between inhibitors and corroded surfaces and to understand how such interactions have an influence on the physico-chemical properties of the corrosion system most relevant for corrosion (permeability, passivity) without the application of a coating.

Considering the number of parameters that needs to be taken into account when dealing with ancient objects, a decision was made to work in specific conditions. The first choice concerns the inhibitors: three testing molecules have been selected including benzotriazole, decanoic acid and a benzotriazole derivative as some information on their inhibition mechanism already exists. The second concerns the substrate: experiments were realized on naturally corroded copper samples that represent a simpler

and more uniform substrate compared to other copper alloys. Despite this consideration, the ancient corrosion layer formed on copper can be considered as more representative of long outdoor exposure compared to freshly patinated coupons.

The objective is to improve the knowledge on existing treatments such as benzotriazole as well as introducing new elements for the future development of safer inhibitors for conservation.

A multi-analytical and multi-scale experimental protocol has been implemented during the work in order to address the study of two main complementary axes. In the first, the reaction mechanism has been studied by referring to the two main mineralogical components of the corrosion layers, cuprite and brochantite, investigated as distinct phases. This approach allowed to enlarge our observations by performing analysis at the nanometric scale, something otherwise difficult to realize on real samples. The second axis consists in the study of the change in the physico-chemical properties of naturally corroded old samples treated with an inhibitor's solution to determine the specific interaction on representative corrosion layers. Results have been discussed by integrating these two aspects.

The manuscript is divided in four main parts. In the first chapter, the context of the research is detailed and a bibliographic study with the actual knowledge concerning corrosion and inhibition mechanisms is included. The mechanism of copper corrosion in atmosphere and the evolution of the corrosion layer in urban environment are summarized. The definition and description of the most relevant families of corrosion inhibitors for copper in heritage follows; azole compounds and fatty acids are studied in more detail.

The second part, the methodology adopted to answer the research questions is described. As previously mentioned, the study is based on a multi-scale multi-analytical protocol, which was adapted for the investigation of synthetic mineral phases on one side and corroded samples on the other. The chapter on methodology includes the description of the protocols, analytical techniques employed and characterization of reference phases.

The third part concerns the results obtained. It is itself divided in two major blocks, one dedicated to the results on the mineral phases, the other to those on the corrosion layer of Metz before and after treatment. The results of the experiments carried out after outdoor exposure are also presented here.

Finally, the final part of the thesis consists in the discussion of the results obtained. The interpretation of the data concerning the treated mineral phases is relevant for the further interpretation of the results on the corrosion layer that follows. The reaction mechanism supposed for the mineral phases influences the reactivity and finally the protection mechanism on the corroded surfaces. The outdoor

exposure, despite its limited timeframe, allowed to suggest some tendencies of the different treatments.

Some reaction-protection mechanisms are exposed and relevant aspects for the protection of heritage corroded objects are considered. In addition, a simple testing procedure to evaluate inhibitors for heritage applications is proposed.

Literature review

Literature review

In order to address the subject of inhibitors for copper-based artefacts in the cultural heritage field, a general understanding of the corroded surface state is important. For this reason, a review of the corrosion mechanism of copper from the first stages to long-term atmospheric corrosion is presented. In the second part of this chapter, some of the most relevant organic molecules employed as corrosion inhibitors are described with particular emphasis on their applications for copper-based artifacts exposed outdoors. A final part is devoted to an overview on the approaches and methodologies used for studying protective systems in the field of cultural heritage.

1. Corrosion of copper

1.1 Definition of corrosion and general description of the reaction

Several official definitions of the term *corrosion* exist. According to the International Union of Pure and Applied Chemistry (IUPAC), "*corrosion is an irreversible interfacial reaction of a material (metal, ceramic, polymer) with its environment which results in consumption of the material [...]. Often, but not necessarily, corrosion results in effects detrimental to the usage of the material considered*". A similar description can be found in the international standard (ISO 8044-1986) specifically defining *corrosion of metals* as the "*physico-chemical interaction between a metal and its environment which results in changes in the properties of the metal*".

In terms of chemical reaction, wet corrosion[1] is an electrochemical process that involves the metal and the dissolved species present in a water solution (the electrolyte). Being a redox reaction, corrosion can be divided in two half reactions: the oxidation of the metal (Equation 1, anodic reaction) and the reduction of another specie (cathodic reaction). The most common cathodic reactions are reduction of oxygen in neutral to basic pH (Equation 2.1) and at acidic pH (Equation 2.2) as well as reduction of hydrogen ions in acidic solution (Equation 2.3).

$$M \rightarrow M^{2+} + 2e^{-} \qquad (1)$$

$$0.5\, O_2 + H_2O + 2e^{-} \rightarrow 2(OH)^{-} \qquad (2.1)$$

$$0.5\, O_2 + 2H^{+} + 2e^{-} \rightarrow H_2O \qquad (2.2)$$

[1] Other types of corrosion (dry corrosion in gases or corrosion in other liquids) are not considered here.

$$2H^+ + 2e^- \rightarrow H_2 \qquad (2.3)$$

In general, one or more cathodic processes can occur based on the characteristics of the environment surrounding the metal. The corrosion reaction for a general metallic substrate process is schematized in Figure 1.1.

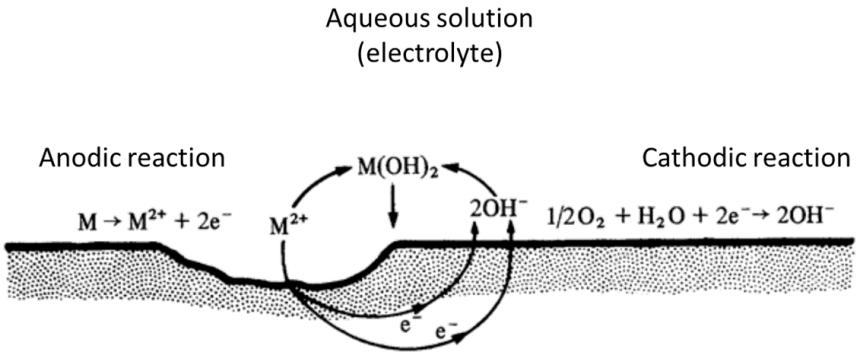

Figure 1. 1: Representation of corrosion system for a generic divalent metal (M) in an electrolyte containing oxygen [1].

Pourbaix diagrams are often used to represent the thermodynamically favoured processes for a certain metal in contact with a specific environment and show predictions about the state of the metal at different pH and potential conditions, although they do not provide information about the kinetics of the processes involved.

The Pourbaix diagram for copper in aqueous media at 25°C is presented in Figure 1.2.

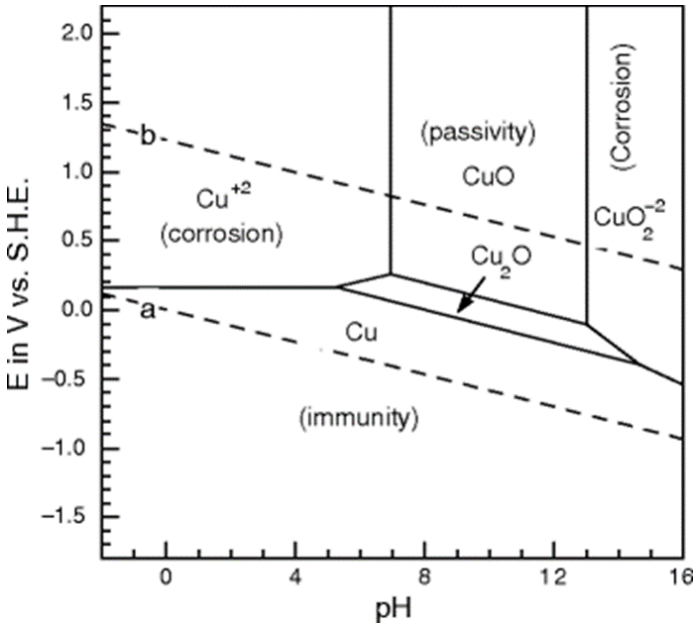

Figure 1. 2: Pourbaix diagram of copper in H_2O after [2].

Three regions corresponding to specific pH and potential values can be distinguished:

1. A stability region where copper does not dissolve under the line "a". The line represents the hydrogen equilibrium (Equation 2.3) (E°=0 V SHE) and, in these conditions, the reaction with copper (potential Cu/Cu^{2+} equal to + 0.33 V SHE) is not thermodynamically favoured. This means that copper is a relatively noble metal and does not corrode in acidic oxygen-free environments.
2. A corrosion region where copper is present in ionic form. Copper dissolution takes place in oxygen-containing environments at strongly acidic and alkaline pH.
3. A passivity region between pH 6 and 14. The passive state is related to the formation of cuprous oxides (Cu_2O) at the metal surface that separate the metal form the electrolyte and limit further corrosion.

The nanometric oxide layer covering the metal surface passivates the metal by acting as transport barrier layer for diffusion of water and dissolved species. It has been observed that the protective action of the oxide layer can be disrupted under certain conditions allowing further corrosion of the metal until a new oxide layer forms.

Local breakdown of passivity inducing re-corrosion of the metallic substrate can be induced by the presence of aggressive ions such as chlorides. Marcus and colleagues [3], [4] propose that passivity

breakdown in oxide films is related to the presence of grain boundaries where ionic conductivity is larger compared to the bulk oxide.

A model for passivity breakdown in presence of chlorides has been proposed [3] (Figure 1.3).

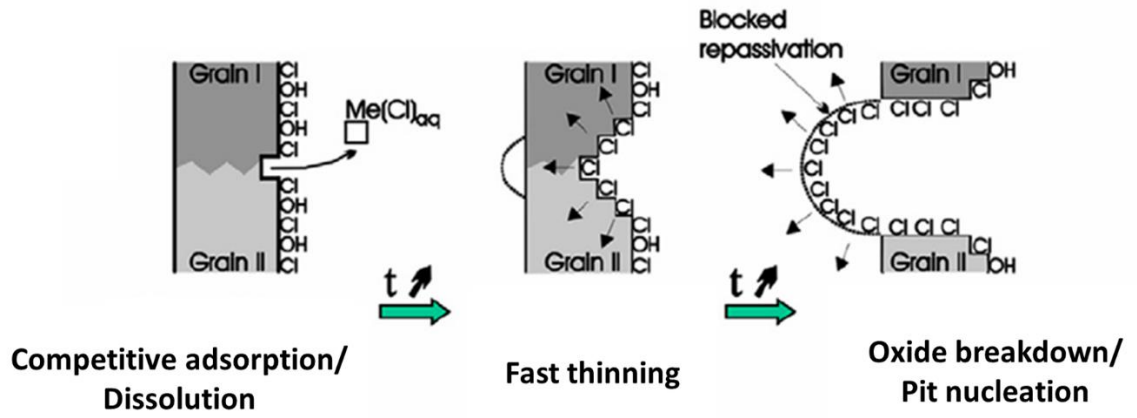

Figure 1. 3: Passivity breakdown of an oxide layer in presence of chloride ions, after [3].

The first step includes the competitive adsorption of hydroxides and chloride anions on the oxide surface, which promotes the dissolution of the oxide preferentially at grain boundaries and progressively causing local thinning. The last step consists in the breakdown of the oxide with formation of pits where corrosion can take place.

Re-passivation of the substrate, with formation of a new oxide layer is possible when the conditions related to depassivation change, in the case of chlorides, when a reduction of such specie occurs in the environment.

1.2 Copper corrosion in atmosphere

Atmospheric corrosion is as a particular kind of wet corrosion in which the metal taking part in the anodic reaction is covered by a thin water layer with the dissolved oxygen present in the water layer taking part in the cathodic reaction [5], [6]. Local environmental conditions are crucial for the corrosion layer evolution in time: relative humidity, wet/dry cycles, frequency of rainfalls, presence of pollution sources etc. (Figure 1.4).

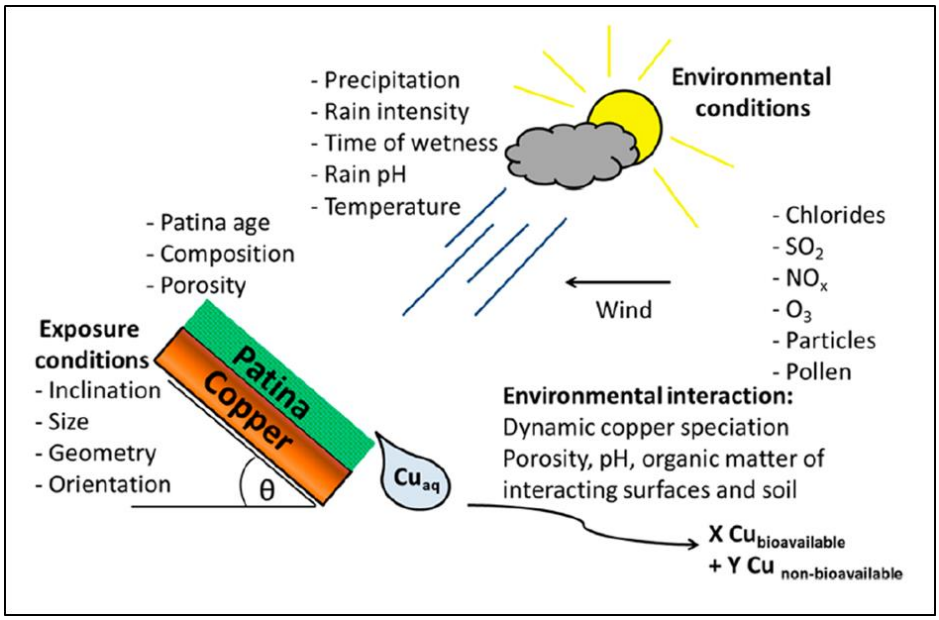

Figure 1. 4: Main environmental and exposure parameters affecting atmospheric corrosion of copper, after [7].

Main atmospheric pollutants present in urban environment that have an effect on corrosion of exposed metals are listed in Table 1.1.

Table 1. 1: Pollutants damaging metals, adapted after [5].

Compound	Effect on metals
SO_2	Corrodes metals and alloys especially in combination with oxidants.
NO_2, O_3, H_2O_2	Promotes SO_2-induced corrosion of metals and alloys.
H_2S	Tarnishes silver, copper and copper alloys.
NaCl	Corrodes metals and alloys
Organic acids	Corrodes metals and alloys

1.2.1 Morphological and structural evolution of a copper corrosion layer in atmosphere

In aerated moist environment, copper instantaneously undergoes oxidation by reacting with dissolved oxygen and a layer of cuprous oxide (Cu_2O) forms on the surface. The first step of copper oxidation is

the reduction and chemisorption of dissolved oxygen, which involve an electron transfer from metallic copper to molecular oxygen giving a layer of adsorbed O_2^- and OH^- [4], [5], [8]. At this point, copper ions and the hydroxyl/oxygen anions react and form the mineral cuprite, which, considering its poor solubility in water, deposits on the surface as separated nuclei. As corrosion reaction proceeds, coalescence of the oxide film is observed and the nuclei of cuprite grow to give a continuous, polycrystalline and adherent layer.

The surface cuprite layer rapidly grows up to approximately 1.6 to 2 nm [9], [10] and the excellent adherence to the underlying metal is ensured by the epitaxial growth of the first oxide layer as proposed by Ives and Rawson [9]. The cuprite crystallites continue growing and assume a characteristic cubo-octahedral shape (Figure 1.5).

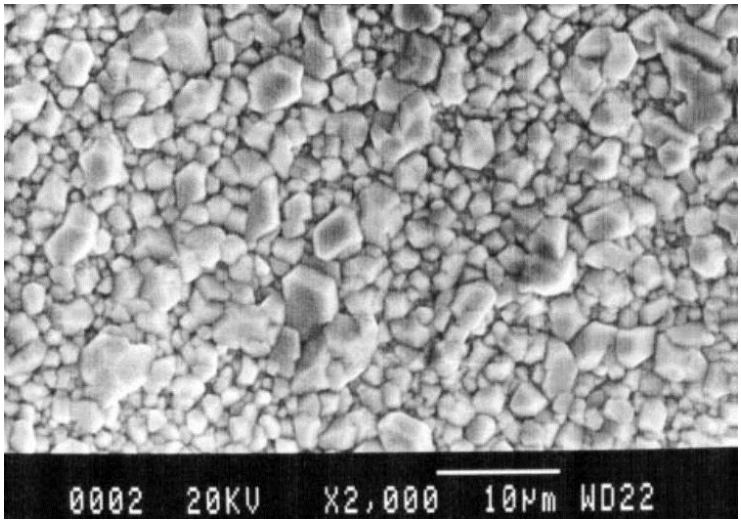

Figure 1. 5: Example of cubo-octahedral shaped crystals assumed on an artificially-corroded sample [11].

Ives and Rawson [9] studied the corrosion of copper in an oxygenated aqueous media. Based on their results, when the cuprite layer thickness exceeds 2 nm, the mechanical strains caused by crystal growth result in layer breakdown and determine the increase of porosity. According to the authors, this process originates a "duplex film" composed by an inner cuprite nanometric layer continuously regenerated and an outer, more porous and less adherent layer. The morphological characteristics of the external layer will prevent the circulation of electrons while allowing water penetration. In this conditions, oxidation of cuprite will take place and Cu^{2+} ions are formed [12]. The interaction of cupric ions with the chemical species that are present in the environment under specific conditions determine the further evolution in time of the corrosion layer components. In fact, it is observed how the cuprite is progressively covered by new mineral phases containing Cu(II) species and the stability of the new phases in the specific conditions will determine the composition of the outer layer. As corrosion and

oxidation reactions proceed, secondary minerals formed on top of cuprite might continue developing in thickness.

The "duplex film" proposed by Ives and Rawson was generalized by Merkel and co-authors [13] for corrosion in aqueous oxidized media containing carbonates as predominant anionic species. The duplex system consists of an inner thin cuprite layer and an outer thicker, porous layer dominated by Cu(II)-based minerals such as malachite. The reactions that take place within and on the surface of the duplex film are summarized in Figure 1.6: both redox reactions and non-redox processes are involved.

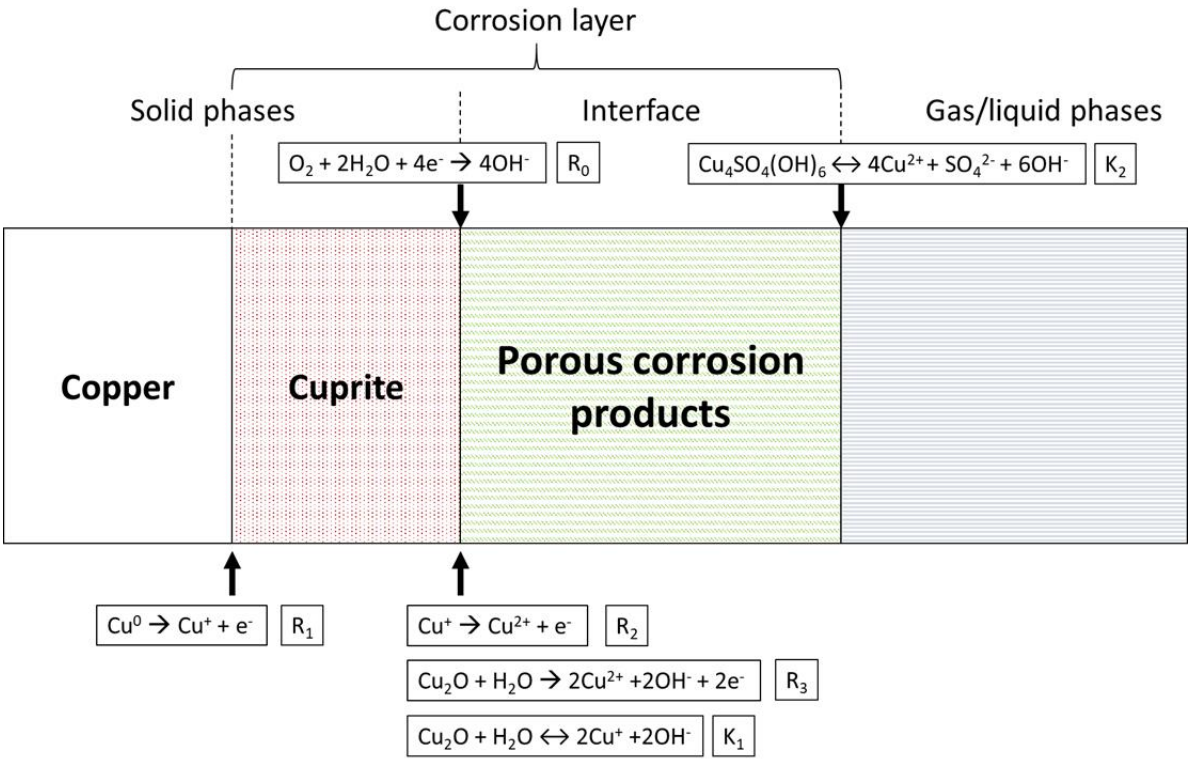

Figure 1. 6: Scheme of a general corrosion layer seen as a duplex film [13].

Reactions involving electron transfer (redox) are:

- Dissolved oxygen reduction (R_0): this reaction takes place at the cuprite/porous corrosion product interface. This represents the cathodic reaction in the electrochemical process. Other oxidants are chlorine and chlorine dioxide and cupric ions.
- Oxidation reactions. Several reactions are involved where metallic copper (R_1), dissolved Cu^+ ions (R_2) or solid cuprite (R_3) are oxidized. These processes constitute the anodic reactions.

Non-redox reactions are:

- Dissolution equilibrium of cuprite (K_1).
- Dissolution equilibrium of brochantite or other Cu(II)-minerals constituting the porous corrosion layer (K_2).

1.2.2 Transport in the duplex film

As the corrosion layer develops, transport properties become crucial to ensure or block access of water and dissolved species to the metal surface, thus controlling the corrosion reaction. In the outer corrosion layer, generally described as porous, diffusion phenomena can take place through pores and cracks. Therefore, this layer is generally considered as non-protective.

Different is the situation for the compact and less porous cuprite layer. Cuprite is described as a non-stoichiometric, p-type semiconductor [14]. This means that electronic and ionic transfer is ensured due to the intrinsic properties of the mineral and, as corrosion proceeds, electrons can move from the metal (anodic site) outwards through the cuprite layer until reaching the cuprite/porous layer interface where the reduction of oxygen (cathodic site) takes place. As electroneutrality must be maintained, to the electron transfer corresponds an outward displacement of positive charges (Cu^+) determined by the presence of cationic vacancies (defects points) within the cuprite. Electron transfer is the fast process compared to ionic mass transfer which means that the diffusion of Cu^+ through vacancies controls the reaction and therefore the dissolution of copper [15]. As previously reported, grain boundaries in an oxide layer can act as channels for preferential ion diffusion [3], [4].

According to Payer et al. [16], who studied the transport properties in a cuprite layer formed in atmosphere containing different molecular species (SO_2, Cl^-, CO_2), the presence of pollutants have an influence on the resulting oxide layer structure and on its transport properties, finally determining its protectiveness as passivating film. When the oxide is formed in moisture air without aggressive species, the oxide layer formed is thin (2-5 nm) and protective which means that the layer is characterized by a low ionic transport. On the contrary, the formation of the "duplex film" in SO_2-rich moist environments (in the order of the ppb) testifies that corrosion proceeds even after the formation of the oxide layer. Consequently, such layer is considered as non-protective and characterized by high ionic transport. Similarly to what was observed by Marcus and co-workers, Payer also relates the formation of "fast channels", involved in the transport of ionic species, to the presence of grain boundaries. Although in this case, the higher ionic transfer is justified by the incorporation at the grain

boundaries of copper sulphides[2], characterized by higher transport properties when compared to cuprite. The transport of species proposed by Payer is reported in Figure 1.7.

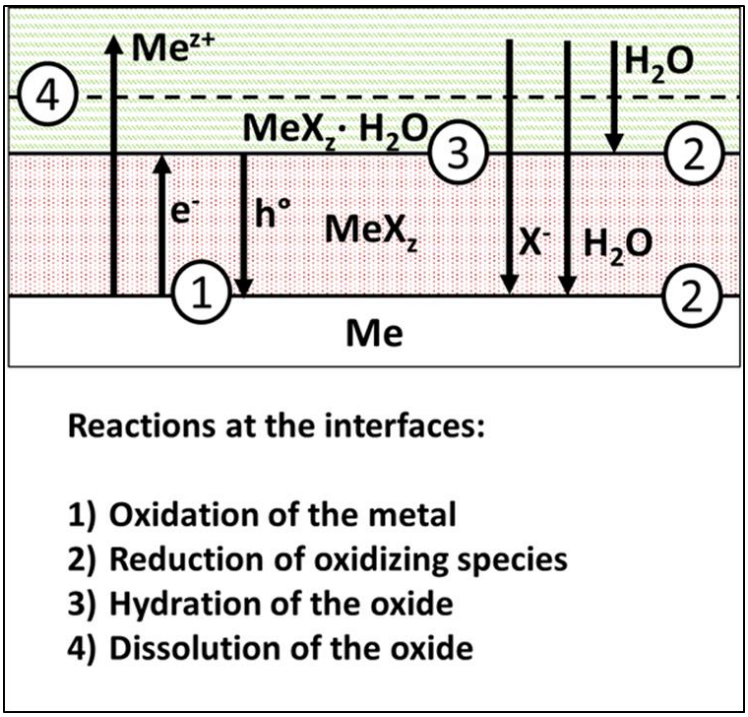

Figure 1. 7: Transport through the duplex film and reactions as proposed by Payer et al. [16].

1.2.3 Long-term corrosion layer in urban sites

1.2.3.1 General description

Corrosion layers on copper formed during long exposure times (several decades up to hundreds of years) have been described in several studies [17]–[19]. In general, the corrosion layer represents specific type of "duplex film" with cuprite at the metal/corrosion layer interface while the external porous layer is constituted by Cu(II) hydroxy sulphates, which formation is linked to the availability of atmospheric SO_2.

High SO_2 concentration deriving from the combustion of fossil fuels, characterize urban and industrial sites. Despite the decrease of SO_2 in the atmosphere observed in recent years in western countries [20], [21] (Figure 1.8), in other parts of the world, such as the Asiatic continent, the amount of SO_2 is progressively increasing.

[2] Graedel [17] reports the presence of copper sulfides in copper patinas from urban sites.

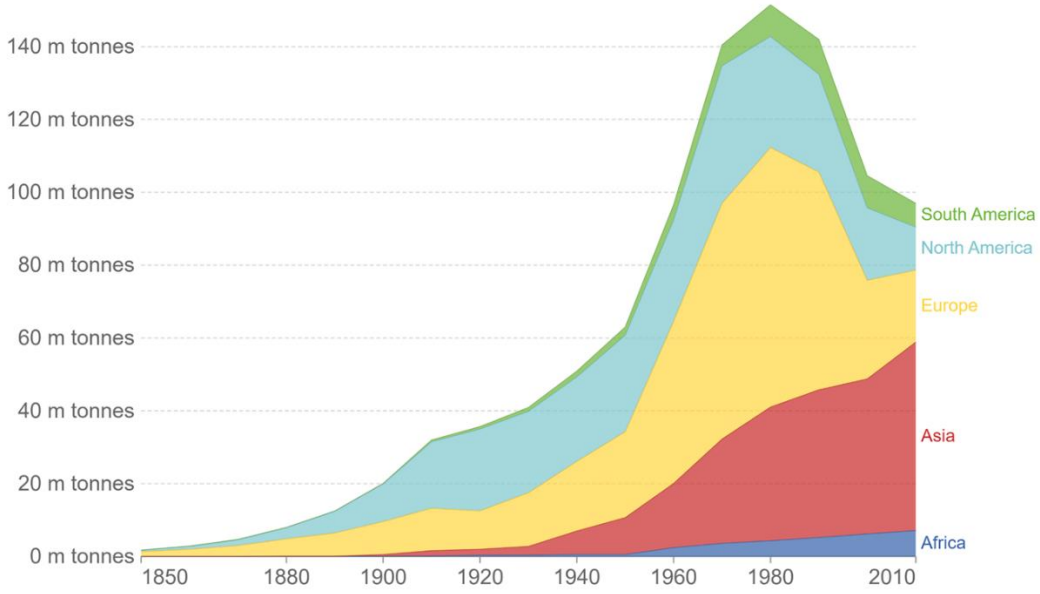

Figure 1. 8: Global SO_2 emissions. From OurWorldInData.org.

In urban environment, the presence of an outer layer constituted by copper hydroxy sulphate for long-time exposed samples is related to the availability of SO_4^{2-} derived from oxidation of SO_2 in the water film adsorbed on the cuprite layer (Equation 3). In parallel, Cu^{2+} ions are available in solution thanks to the oxidation of cuprite (Equation 4) giving the final reaction corresponding to brochantite precipitation (Equation 5). Strandberg [22] suggests that other pollutants (ozone, nitrates) by acting as oxidants, promote cuprite reactivity at 90% RH in presence of SO_2.

$$SO_2 + H_2O + 0.5\,O_2 \rightarrow H_2SO_4 \quad (3)$$

$$Cu_2O + 2H_2O + 0.5\,O_2 \rightarrow 2Cu^{2+} + 4OH^- \quad (4)$$

$$4Cu^{2+} + SO_4^{2-} + 6OH^- \rightarrow Cu_4SO_4(OH)_6 \quad (5)$$

According to Krätschmer et al. [23], brochantite layer formation is time related and the mineral does not immediately precipitate as such on top of the underlying cuprite layer. On the contrary, the outer layer formation involves a series of meta-stable intermediates including an amorphous copper sulphate formed within the first days of exposure (Figure 1.9).

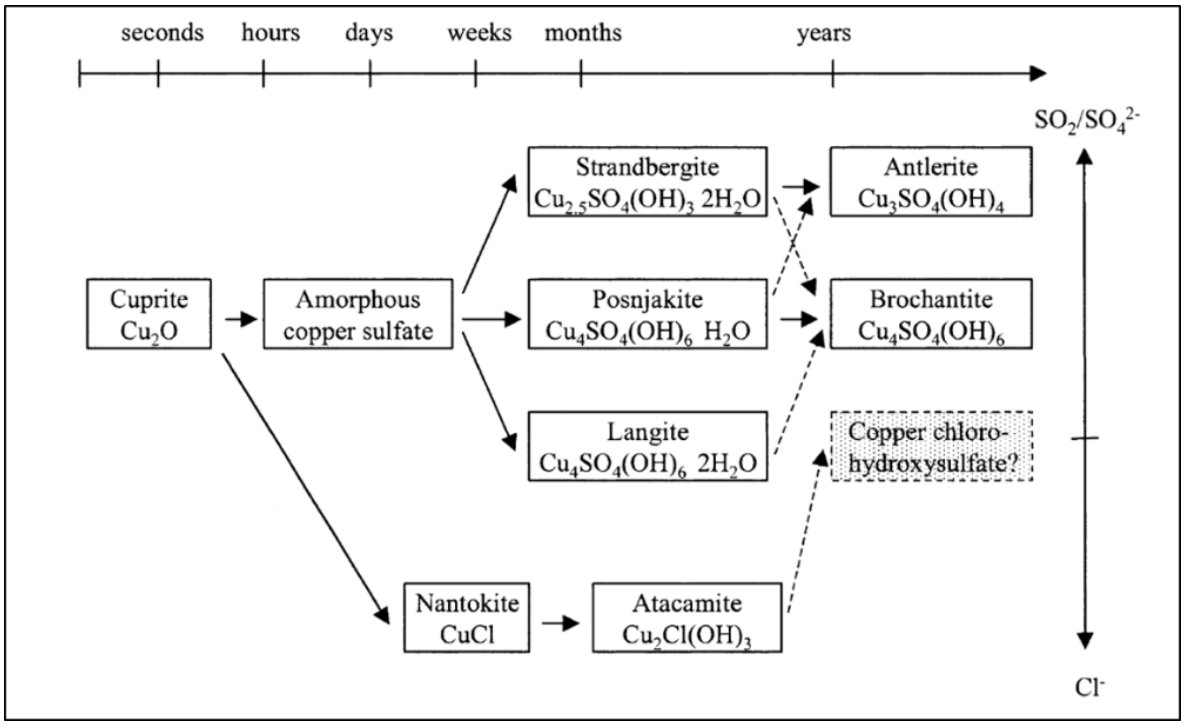

Figure 1. 9: Time evolution of mineral phases on copper based on sulphate and chloride concentration, after [23].

The two thermodynamically favoured phases, brochantite and antlerite, might form as confirmed by the Pourbaix diagram in SO_2 polluted atmosphere, with antlerite being more stable in acidic pH [24], [25] (Figure 1.10).

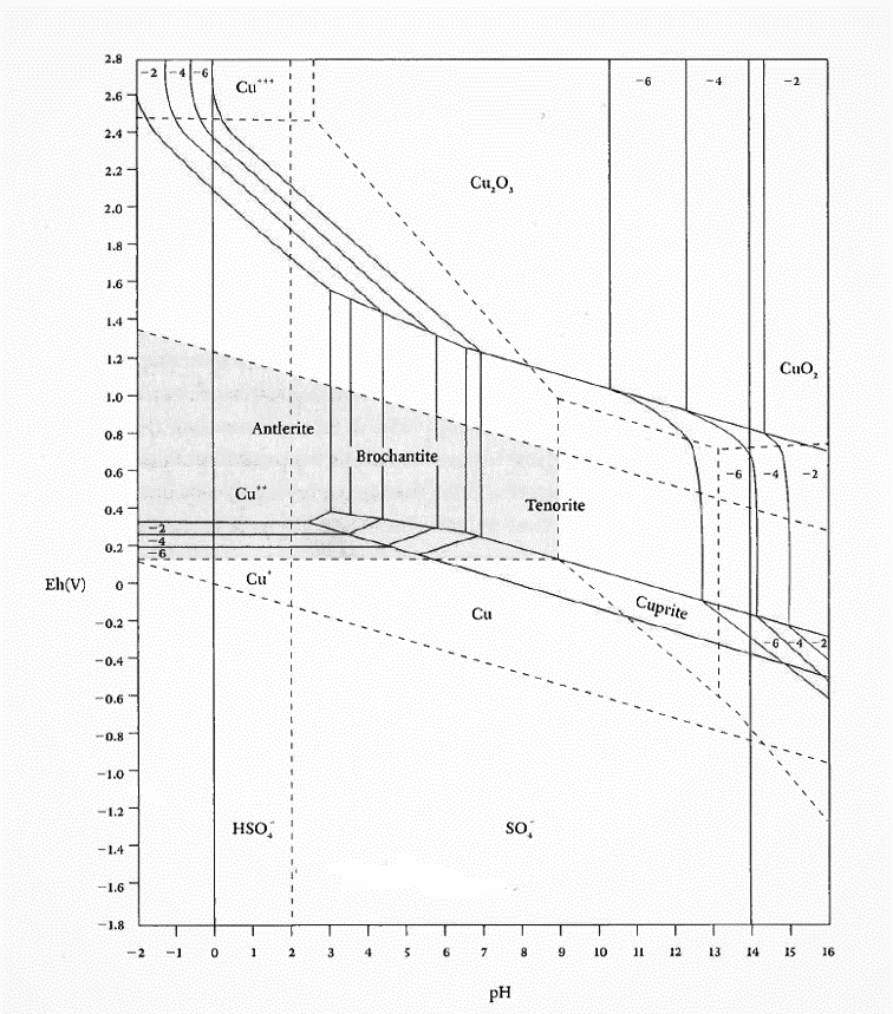

Figure 1. 10: Pourbaix diagram for the system Cu-SO_4^{2-} - H_2O after [24].

FitzGerald et al. [26] studied the evolution of ancient and newly formed (up to 2 years) copper corrosion layers upon exposure in Brisbane (Australia)[3]. By comparing copper roof tiles from different locations and ages, the authors observed that the thickness of the cuprite layer of objects dating between 15 and 142 years corresponds to a stable value of approximately 6 µm (Figure 1.11 red line). The authors suggested that a steady-state corrosion mechanism must exist where cuprite formation process proceeds at the same speed as cuprite oxidation. Corroded copper for up to 230 years, shows a cuprite layer between 4 and 10 µm, while in more ancient samples cuprite thickness is about 18-19 µm.

Unlike cuprite, brochantite thickness grows following a linear trend and increases of 0.2 µm/year in Brisbane atmosphere (Figure 1.11 green line).

[3] The city is located at 15km from the coast and the environment was classified as urban/light industrial with 35 µM SO_4^{2-} and 118 µM Cl^- measured in rainwater. Cumulative rain in one year is about 1000 mm.

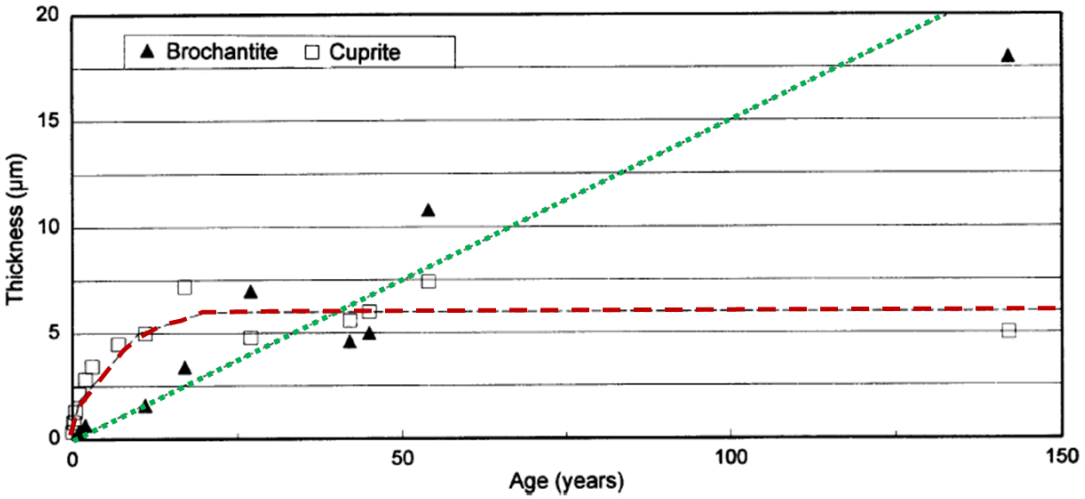

Figure 1. 11: Measured thickness of cuprite and brochantite layer upon outdoor exposure; data for long-exposed samples (more than 2 years) are from historical roof samples. After [26].

Presence of oxidized sulphur, low pH but also precipitations frequency and duration are among the factors responsible for the dissolution/oxidation of cuprite and the precipitation of copper hydroxy sulphates. The fate of the cupric ions from cuprite oxidation depends mostly upon environmental conditions such as rainfall and relative humidity. One part precipitates as insoluble brochantite within the porosity from an evaporating stagnant water film after a rainfall: this process is considered responsible for cementing the existing brochantite mineral. Another, important part of Cu^{2+} ions is lost by run-off. FitzGerald calculates that 70% of the oxidized cuprite is lost during rainfalls.

1.2.3.2 Role of brochantite layer

Different hypothesis exists on the role of the outer corrosion layer in the corrosion reaction.

In the long-term, outer corrosion layer is characterized by high porosity and by the presence of numerous cracks [10]. Graedel et al. [17] brings the fast adsorption of a water droplet as a proof of such porosity and consequently the high water intake ability of old sulphate patinas. Although, some authors hypothesize [26] that brochantite layers formed in the long-term might have a reduced porosity and limit ionic diffusion with a positive effect on the corrosion rate. Others authors observe that, despite the porosity, the brochantite outer exhibits a high adherence [17]. Muller and McCrory-Joy [27] by performing ion chromatography and gas chromatography-mass spectroscopy on the corrosion layer from the Statue of Liberty detected a series of organic compounds such as short and long chain fatty acid. The authors propose that the organic molecules might act as binder cementing the brochantite crystals, thus conferring compactness and adherence to the layer.

Other studies point out a possible negative role of brochantite. Lins and Power [28] studied the dissolution of corrosion products in different solutions such as at acidic pH and synthetic acid rain. They found that brochantite in acidic conditions (pH<3) does not transform into antlerite in more than 1 year (10000 hours), while $CuSO_4$ is produced by dissolution of the mineral. The authors consider the solution coming from dissolution of the sulphate-rich layer as aggressive[4] and is possibly involved in the evolution of the cuprite layer. Similarly, De la Fuente [10] reports that the presence of brochantite could accelerate the dissolution of cuprite since the porous layer would increase the time of wetness. This results in a longer interaction of the water film with cuprite when compared to brochantite-free surfaces and the effect is an increased ion transport through the cuprite.

Finally, higher run-off[5] rates are observed by He et al. [29] and Hedberg et al. [7] who studied one century-old samples compared to freshly corroded samples: the authors suppose that the reason could be a higher surface area due to the high porosity of the layer.

1.2.3.3 Colour evolution in atmospheric conditions

The evolution through time of the components of the corrosion layer leads to differences in the aesthetic appearance of the copper. Leygraf and colleagues [30] studied the colour of patina layers formed in marine and urban sites ranging from 1 day to 400 years of exposure. They conclude that the initial surface darkening is due to the formation of the surface cuprite layer (CuO is also suggested), while the typical blue-green patina observed on long-time exposed copper is related to Cu(II) species with colour homogeneity being reached as these minerals approach a thickness of 12 ± 2 µm (Figure 1.12). The formation of a "green patina" on copper is often considered positive from the aesthetic point of view.

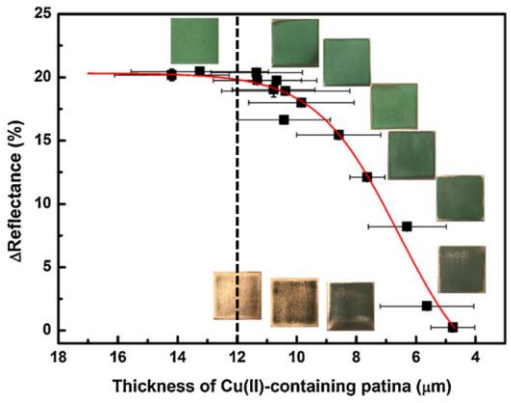

Figure 1. 12: Reflectance (ΔR%) change with outer layer thickness after [30].

[4] Cu^{2+} behaves as a Lewis acid in aqueous solution.
[5] The amount of copper released during a precipitation (rain) event.

2. Corrosion inhibitors for copper and copper alloys

In the following paragraphs, the main corrosion inhibitors mechanisms are briefly reviewed. The inhibitors families of azoles and fatty acids to which this research is addressed are described in more detail with reference to studies concerning industrial and heritage applications for the preservation of copper-based artefacts exposed outdoors.

2.1 Definition and categories of inhibitors

The standard ISO 8044-2015 defines a corrosion inhibitor as a "chemical substance that when present in the corrosion system at a suitable concentration decreases the corrosion rate, without significantly changing the concentration of any corrosive agent". Inhibitors are used and are effective at low concentrations while aggressive species causing corrosion are contemporary present in solution.

A key factor for the understanding of the role of inhibitors can be found in the definition proposed by Trabanelli and Carassiti [31]: a corrosion inhibitor is "any phase constituent whose presence is not essential to the occurrence of an electrochemical process, but leads to the retardation of this process by modifying the surface state of the metallic material". Here, the mechanism of action of inhibitors by modifying the surface state of the metal is introduced. In particular, adsorption phenomena lead to a competition between adsorption of aggressive species and inhibitor molecules. The bond with the inhibitors' molecules produce an interaction with the metallic surface and/or the formation of protective films by bonding with metal cations [4]. The protective films formed by inhibitors are classified in three types [32]:

- Passivating films: generally constituted by passivating oxides giving films with a thickness between 3 and 20 nm. They provide high corrosion protection but they are produced by oxidizing compounds such as chromates and nitrites which use is largely abandoned because of their toxicity;
- Precipitation films (insoluble) produced by the reaction between the inhibitor molecules and soluble species in the environment or metal ions from the substrate. Examples of this type of inhibitors are phosphonates and polyphosphonates that react with calcium and the benzotriazole reacting with copper ions to form an insoluble film.
- Adsorption films involve organic molecules having at least one atom that can share electrons with the metallic atoms. Two types of adsorption can occur: physisorption and chemisorption. Physisorption involves the formation of weak bond (van der Waals, electrostatic): these

interactions can form very fast but are also easy to break. Chemisorption on the contrary involves stronger bonds (charge sharing, charge transfer) require longer time and the interaction might not be reversible. Adsorption in some cases is considered the first step in the inhibition process with the formation of multi-molecular film on the surface. For example, surfactants can bond to the metallic substrate via the hydrophilic part of the molecule, while the hydrophobic part is directed towards the solution thus limiting both water and oxygen access to the surface.

Several classifications of corrosion inhibitors exist based on the nature of the compound (organic or inorganic), their physical state (liquid, gas), the type of environment in which they are effective (acid, alkaline, neutral). A largely used classification concerns the processes in the electrochemical reaction that the inhibitor is able to hinder: anodic, cathodic or mixed inhibitors can be distinguished based on this principle.

When considering organic inhibitors, a large number of organic molecules are employed in corrosion control. In general, the inhibition mechanism of organic inhibitors relies on their ability to be physically or chemically adsorbed on the metal surface. This implies the presence of specific polar atoms or functions (nitrogen, sulphur and oxygen atoms are some examples) with lone electron pairs that will act as electron donors while metal and metal ions will act as electron acceptors. The polar functions present within the inhibitor's molecule are often referred to as the adsorption centres.

The inhibition efficiency of organic molecules can be related to a certain number of parameters: the chemical and electronic structure of the compound [33], [34], the composition and pH of the corrosive environment and the characteristics of the metallic surface [35].

In the last years, a new class of so-called "green" and "eco/environmentally-friendly" organic inhibitors has received an increasing attention from the scientific community [36]. This is mainly caused by the raising awareness on environmental and health related issues with the purpose of finding new compounds to substitute toxic and hazardous ones. A simple search in Scopus, gives a rapid idea of the exponential increase of this kind of studies: the graph in Figure 1.13 presents the number of times the term "green inhibitor" was used in the title of a scientific publication in the last decades. In the studies, plant extracts composed by several organic molecules are considered as alternatives to traditional corrosion inhibitors.

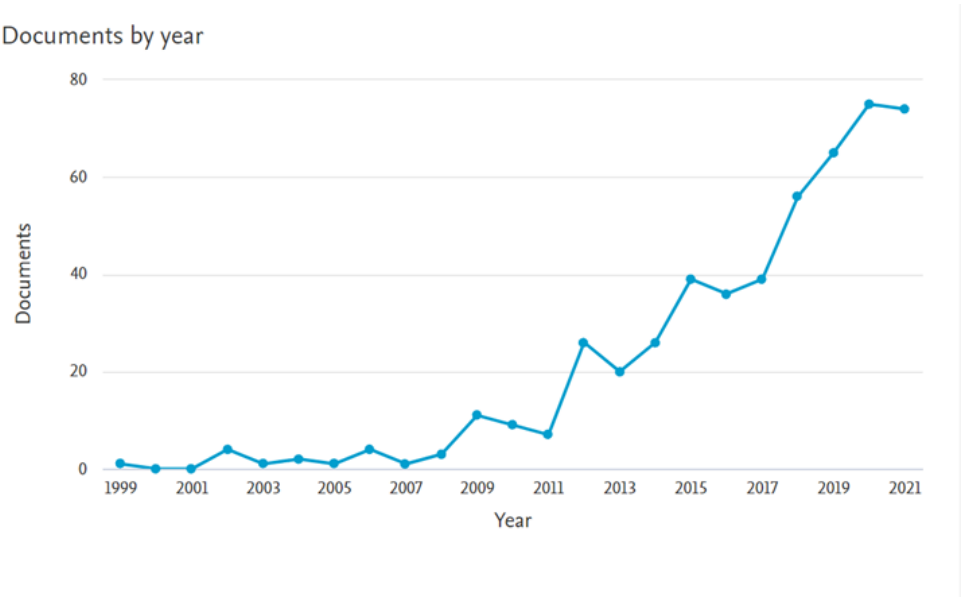

Figure 1. 13: Number of times the term "green inhibitor" appeared in the title of scientific publications (Scopus search).

In the next paragraphs, the main characteristics and properties of two classes of compounds (azoles and surfactants) are exposed with particular reference to the compounds selected for this study.

2.2 Azoles

Azoles are heterocyclic compounds having a 5-atoms cycle and containing at least one nitrogen as heteroatom. As at least one lone pair of electrons is present on the nitrogen atom, nitrogen can act as an adsorption centre and coordinates with metallic ions.

Among the azoles derivatives, benzotriazole is by far the most studied and employed corrosion inhibitor.

2.2.1. Benzotriazole

The introduction on the market of benzotriazole (BTAH) as an anticorrosion treatment for copper dates to 1947 when it was patented by Procter and Gamble Ltd. Since then, its importance for corrosion mitigation continued to grow. Nowadays BTAH is the most used corrosion inhibitor for copper and copper alloys and, in parallel to its use, a large amount of literature has been produced.

Considering the success of benzotriazole in the industrial field, it soon received the attention of conservators and conservation scientists with the first study dedicated to the use of BTAH for archaeological bronze dating back to the 1960s [37]. In a recent review [38], Letardi confirms the prominent role of benzotriazole in conservation up to now as it is “the more widely applied inhibitors for copper alloy heritage objects”.

Benzotriazole is a heterocyclic compound constituted by a benzene and a triazole ring. In the solid phase at room temperature, BTAH is a crystalline (monoclinic) compound in which molecules are linked together by hydrogen bonds [39], [40].

In solution, BTAH molecule exists as undissociated, deprotonated and protonated form stable at neutral, alkaline (pH>8.2) at acidic pH (pH<1) respectively (Figure 1.14) [41], [42].

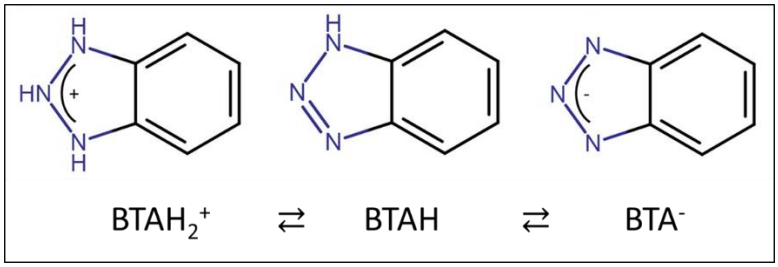

Figure 1. 14: Different forms of BTAH stable in solution.

The triazole moiety with three nitrogen atoms having π orbitals provides the electron donor properties to the molecule, which behaves as a weak base and offers different possibilities as ligand for metal ions (Figure 1.15) [43].

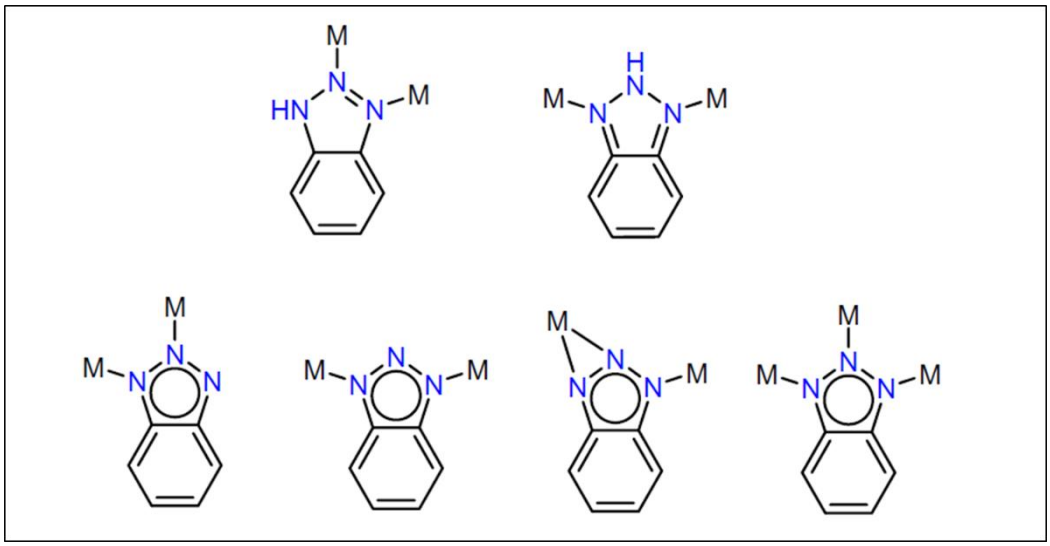

Figure 1. 15: Binding modes of BTAH with metal ions, after [43].

The formation of a polymeric film or layer of Cu(I)-BTA and/or Cu(II)-BTA on the metal and the metal oxide surface is generally accepted, although, despite the large number of studies, the exact inhibition mechanism, the steps involved in the film formation and the role of the surface protective complex are still debated [42].

Film formation and protectiveness is usually studied in solution when other aggressive species are present. The vast majority of research is conducted on bare copper samples while some studies also focus on the protective role of BTAH when copper is covered by an oxide layer [44]–[47]. In particular, studies based on DFT calculations are performed to investigate the interactions on complex surfaces covered by cuprite [4], [48], [49].

In the field of conservation for both archaeological artefacts and outdoor monuments, BTAH is rarely applied alone and it is most used as "pre-treatment" or it is added to a coating formulation. Madsen [37] suggests the use of an external coating (Paraloid B44) indicating the volatility and solubility of BTAH as responsible for its instability in exposed conditions. The concept is reiterated by Watkinson [50] and, more recently, by Albini [51]: the low stability of BTAH treatment for outdoor sculptures justifies the use of an additional coating system. It has to be pointed out that the authors base their considerations on the properties of unreacted BTAH, which is fairly soluble in water (25 g/L at 25°C) and has a low vapor pressure ($4 \cdot 10^{-2}$ mmHg at 25°C), without considering the properties of the complexed form[6]. In the majority of studies, BTAH is considered in combination with a coating and it is difficult to identify the effects of the inhibitor alone [52], [53].

[6] This aspect was already stated in a note from the Editor in Madsen's paper.

The following review takes into account both engineering related studies and studies for applications in cultural heritage. In the first case, BTAH is directly added to an aggressive solution, generally at low concentration, while for other studies and especially those related to heritage, BTAH is applied as a pre-treatment. In order to distinguish the two ways of application, the references concerning pre-treated surfaces (without a coating) are underlined in the text. Studies where no coating is applied are considered.

2.2.1.1 Protection efficiency

BTAH shows good to excellent inhibition efficiency (IE%)[7] on copper when it is present together with an aggressive solution [42]. For instance, copper immersed in a NaCl solution containing BTAH exhibits IE% ranging from 70.5 to 99.9% and the efficiency increases with increasing concentration as reported in Kosec et al. [54].

More problematic is the situation when BTAH is applied as pre-treatment and no reservoir is present in the testing solution.

Using Potentiodynamic Polarization, Žerjav and Milošev [55] report an inhibition efficiency of 98.6% for bare copper after immersion in synthetic urban rain for 1 hour. Copper was pre-treated with a 0.01 M BTAH/ethanol solution for 1 hour.

Dugdale and Cotton [56] have tested bare and BTAH-treated copper by salt spray and conclude that the pre-treatment is efficient in preventing corrosion; the authors conclude that the protection is long-lasting and a BTAH reservoir is not needed. In Brostoff [57], the application of "several brush coats" of 1.5% BTAH/ethanol solution prevented the formation of chlorinated phase after weathering (Table I-3) except for the bare bronze sample.

[7] Protection or inhibition efficiency is evaluated with different techniques and values are not always comparable.

Table 1. 2: Mineral phases detected by XRD on treated and untreated samples after weathering, [57].

Substrate	Without BTAH	With BTAH
Polished bronze	Cu_2O, CuO, copper hydroxy chlorides (atacamite/botallickite)	Same phases as untreated Samples appear less corroded (less black corrosion); Peak at d=3.22Å is attributed to tin oxide?
Patinated bronze (5.1 µm thick)	As for polished bronze (no CuO); original components of the artificial patina are not present	Copper nitrate hydroxide, unidentified peaks (d=12.59, 4.36); botallackite is absent
50-years naturally corroded copper (17.8 µm thick)	Cu_2O, $Cu_4SO_4(OH)_6$, copper chlorides (atacamite)	Cu_2O, $Cu_4SO_4(OH)_6$
50-years corroded copper walnutshell-blasted	Cu_2O, $Cu_4SO_4(OH)_6$, copper hydroxy chloride (paratacamite?)	Cu_2O, $Cu_4SO_4(OH)_6$

Despite these results, a relationship between the thickness of the Cu(I)BTA on bare bronze and the protectiveness leads the author to conclude that brush or spray applications only produce very thin films whose effect as physical barrier are negligible**.** Bierwagen et al. [58] also show the low efficiency of BTAH when it is applied as a pre-treatment on bronze after short immersion times. Better performances are obtained for longer immersion times (100 to 1000 minutes) and higher concentrations (10.5%).

The use of a much lower concentration (0.001M) is employed by Balbo et al. [59] for the pre-treatment of bare bronze: by Potentiodynamic Polarization in 3.5% NaCl solution, this procedure does not show any positive influence on the corrosion reaction.

Kosec et al. [60] have studied the efficiency of three protective methods, among which BTAH, on bare and artificially patinated bronze. Electrochemical tests (Potentiodynamic Polarization and EIS) showed that there is a protective effect of BTAH pre-treatment (3% in ethanol applied by brush) compared to the untreated samples although it seems to be dependent on the substrate as the efficiency is higher on bare bronze and bronze exhibiting a brown patina compared to the green patina. The Paraloid BTAH-doped coating shows the best protection.

In a second study, Kosec et al. [61] have evaluated the efficiency by Potentiodynamic Polarization of 3% BTAH solution applied by brushing and by immersion in a synthetic acid rain (pH=5) containing BTAH for 24 hours. BTAH applied by brushing does not show any beneficial effect, while for the 24 hours immersed sample, a lowering in current was registered.

As a reference inhibitor, Albini et al. [62] treated a modified-naturally corroded copper composed by cuprite covered by atacamite and residues of brochantite by immersion in a 3% BTAH/ethanol solution for 24 hours and 14 days. Results of the EIS experiments show that BTAH does not exhibit good corrosion protection and in general, a poor reproducibility is found.

2.2.1.2 Anodic or cathodic behaviour

According to the latest studies, when BTAH is present in the corrosive solution [42], the inhibitor exhibits a mixed-type behaviour with a more important action on the anodic reaction by preferentially blocking copper dissolution. Benzotriazole has been defined in the literature as both cathodic and anodic inhibitor also based on its concentration in solution. Frignani and co-workers [63] show that between 10^{-6} to 10^{-4} M solution (acidic 0.1 M Na_2SO_4) BTAH behaves as a cathodic inhibitor as it interferes with oxygen in the adsorption on the surface. At higher concentrations, it behaves as anodic inhibitor with the surface completely covered by a protective film.

Dugdale and Cotton [56] pre-treated copper shows cathodic behaviour in 3% NaCl solution. Such effect is explained by the presence of Cu-BTA complex acting as a physical barrier towards oxygen, a similar mechanism to the one proposed by Mansfeld [64]. According to Madsen [37], [65], the absence of re-corrosion when treated archaeological objects were exposed to humid chamber is explained by the action of BTAH in preventing water and dissolved oxygen from accessing to the reactive nantokite.

Brusic et al [66] describe a polymeric Cu(I)BTA formed in an aggressive solution containing 0.01 M BTAH. Based on Potentiodynamic polarization tests and the shift to higher potential values, BTAH is described here as a predominantly anodic inhibitor as oxygen is thought to be able to travel through the film and react with the underlying metal causing further oxidation at the film/metal interface.

2.2.1.3 Film formation: mechanism, kinetics and properties

The protectiveness of benzotriazole is often related to the formation of Cu-BTA complexes on the surface of the metal or metal oxide [67]. Such complexes are generally defined as amorphous organo-metallic insoluble compounds [4], [42] which exact composition is not given and for which several structures have been proposed (Figure 1.16).

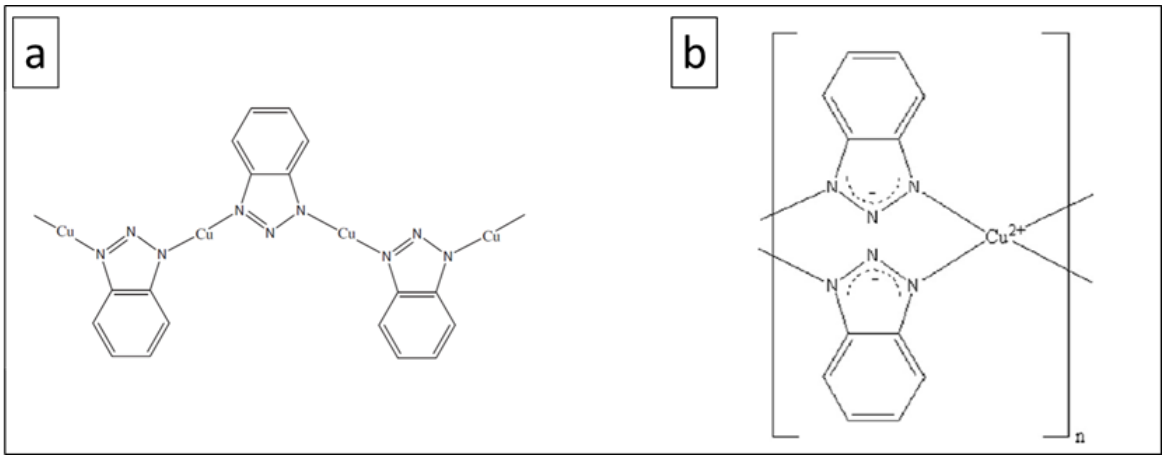

Figure 1. 16: (a) Cu(I)-BTA and (b) Cu(II)-BTA structures proposed in the literature in [68], [69] *respectively.*

The mechanism of formation of the complexes has been differently described and their physical-chemical properties depend on various factors among which solution pH and substrate oxidation. Cotton and Scholes [70] in their early work, proposed a two-dimensional coordination monolayer of chemically adsorbed BTAH having a thickness of approximately 50 Å. In contrast with this interpretation, Poling [71] suggests a multiple-layers film growth with an initial stage consisting in chemisorbed BTAH and successive reaction of copper ions with BTAH in solution leading to precipitation on the outer surface. The transport of copper ions through the Cu(I)-BTA layer controls the film formation reaction.

Fox [46] detected the formation Cu-BTA complexes by XPS on copper surfaces covered by cuprite or tenorite: the reaction mechanism proposed is reaction of copper ions and organic molecules in solution, followed by precipitation of the complex on the surface.

According to Brusic et al. [66], the film formed on copper and on copper covered with copper oxide has a different thickness depending on the solution pH (0.01 M BTAH) and time of immersion. At neutral pH, the layer growth is slow, which results in a thinner (for pH from 3 to 12 a thickness of 0.5 to 4 nm was measured) and highly polymerized layer. According to the author, these characteristics of the film determine a better protection after exposure to severe conditions even without a BTAH reservoir (2 weeks at 80°C and 80% RH). Differently, the film formed at pH 2 is thicker (25 nm), less polymerized and therefore less protective. Again, at neutral pH, based on the growth kinetics of the film, a difference between oxide-free and oxide-covered surface is observed. On the oxide-free surface, the curve corresponding to the layer growth is parabolic describing a process dominated by ion diffusion; the film thickness reaches 3.5 to 4 nm in 10 minutes. In the second case, the curve is

logarithmic which indicates that the major phenomenon is ion movement: the film thickness is 2 nm after 10 minutes and 2.3 nm after 30 minutes.

The first stage involved in the surface complex formation, according to Brusic, is not due to physical adsorption of BTAH since copper ions were found even after very short immersion time (less than 1 second). The author proposes a mechanism involving nuclei formation on the surface followed by successive layer growth.

In [72], Brostoff and co-authors discuss how the thickness of Cu-BTA film formed on bare bronze (Figure 1.17) depends on immersion time: a thickness of 10 to 15 nm is reached after 1 to 100 minutes immersion and reaches 35 nm after 16 hours in the 3% ethanol solution.

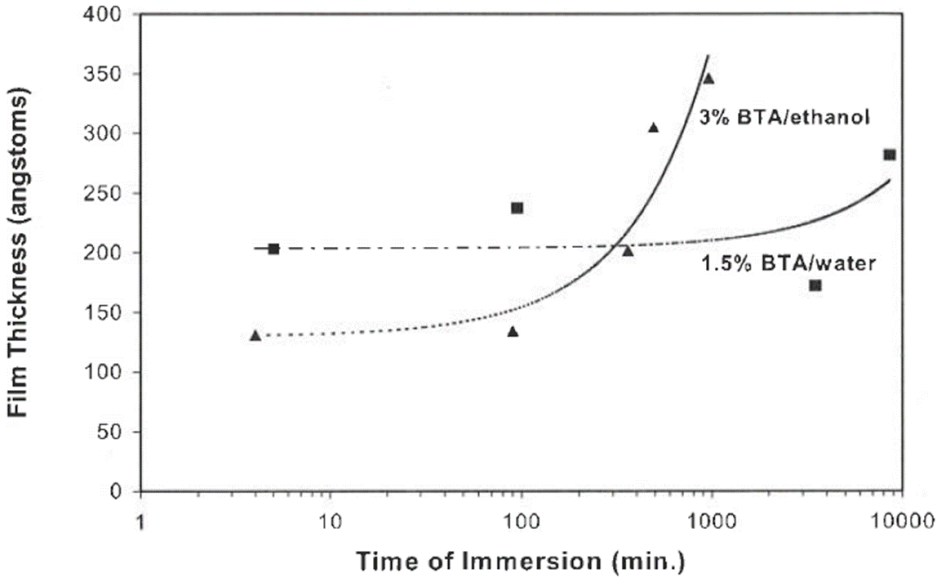

Figure 1. 17: Film growth on bare bronze, after [72].

Differently from the interpretation given by Brusic, a direct relationship between film thickness and protectiveness is proposed based on EIS measurements. The author proposes a kinetics of the surface film growth involving four steps:

1. Initial fast step with formation of a chemisorbed Cu-BTA layer (up to 1 minute).
2. Slow growth: nucleation and growth of Cu-BTA film by diffusion of copper ions through the CuBTA and reaction on the surface with physisorbed BTAH (at the solution/film interface).

3. Fast growth (at 17 hours immersion): formation of a second layer. This might be due to diffusion of copper ions in solution and further precipitation of Cu-BTA.
4. Slow growth to a maximum (40 days immersion): the slow diffusion of ions through the film could be due to the decrease in porosity.

Unlike the bare metal, when applied to patinated surfaces for long immersion time (several days), the authors observed the formation of inhomogeneous films with unevenly distributed thick and insoluble pustules of Cu(I)BTA/Cu(II)BTA. The film continued to grow through a "continuous precipitation mechanism" probably because of the availability of copper ions from copper corrosion due to uneven film formation.

In some studies, the oxidation state of copper in Cu-BTA is investigated usually by performing XPS analysis, and it has been related in opposite ways to the oxidation state of the substrate.

A thin Cu(I)-BTA film of 1.5 nm is detected on cuprite surfaces by Roberts [44] after 3 minutes of immersion in 0.017 M solution of BTAH at 60°C, while a Cu(II)-BTA thinner layer (0.7 nm) forms on a tenorite-composed substrate. The author observes oxidation of the Cu(I)-BTA to Cu(II)-BTA and concludes that the substrate determines the adsorption kinetics of the complex more than its oxidation state.

In [45], the Cu-BTA film on copper oxide is composed of copper in both Cu(I) and Cu(II) oxidation states and it is observed that the amount of Cu(II) increases after removal from the solution and based on the exposure time to air.

An opposite result is obtained by Fox and colleagues [46]. According to this study, the oxidation state of the final Cu-BTA complex investigated by XPS is related to the oxidation state of copper in the substrate (Cu(I) oxide or Cu(II) oxide); both complexes are considered protective.

Mezzi et al. [73] also investigated this aspect on the complex formed on different substrates by XPS analysis[8]. The results highlight that oxidation state of Cu-BTA depends on the substrate: on copper and copper covered with atacamite, Cu(I)-BTA is formed while on the cuprite on the copper substrate, Cu(II) is detected. Differently, on a bronze covered by cuprite, the authors suggest a physisorption more than a chemical interaction, while, when bronze is covered with atacamite (a Cu(II) hydroxy chloride), no change in oxidation state of copper is detected. The authors conclude that BTAH interacts with cuprite and atacamite by forming true chemical bonds and the insoluble complex Cu(I)-BTA and Cu(II)-BTA on

[8] Samples are cooled with liquid nitrogen to avoid reduction.

a copper substrate thus providing a “perfectly coating barrier layer that ensures a long-term chemical-physical stability to the ancient artefacts”.

2.2.1.4 Interaction with copper insoluble and soluble phases

As corrosion layers are composed by different mineral phases, the interaction with BTAH have been studied. In particular, Brostoff [57], [74], [75] investigated the reaction products of benzotriazole with various corrosion phases after 24 hours immersion. It is interesting to notice that no complex Cu-BTA is formed by the reaction with copper and cuprite in neutral BTAH-containing solution and Cu(I)-BTA is detected only when the reaction is carried out at low pH (pH 1). A summary of the results is presented in Table 1.3.

The conclusions of the author focus on the film-forming nature of BTAH with the compound being able to react “with a limited layer of copper minerals on corroded surfaces”. According to the study, pH (for example local acidity in bronzes showing bronze disease), mineral solubility, solvent and reaction time are factors that influence the formation, thickness and polymerization degree of the Cu-BTA film. In any case, the protective action of the surface Cu-BTA remains unclear.

Table 1. 3: Products of the reaction among common corrosion products of copper and benzotriazole solution. Data from XRD and IR-spectroscopy, after [57].

Reactant BTAH + (BTA:Cu molar ratio)	Conditions	Reaction product(s)
Cu powder (3:1)	Alcohol/insoluble	Cu
Cu powder (3:1)	Dil. HCl ; pH 1.0/insoluble	Cu_2O, Cu(I)BTA, Cu, $Cu_2(OH)_3Cl$, CuCl
Cu_2O (1.5:1) cuprite	Alcohol/insoluble	Cu_2O
Cu2O (1.5:1)	Diluted HCl ; pH 1.0/soluble	Cu_2O, Cu(I)BTA, $Cu_2(OH)_3Cl$
CuCl (1.5:1) nantokite	Alcohol/insoluble	CuCl, Cu(II)BTA
CuCl (1.5:1)	Dil. HCl ; pH 1.0/slightly soluble	$Cu_2(OH)_3Cl$, Cu_2O, Cu(II)BTA, Cu(I)BTA,
$CuCl_2$ (4:1-0.5:1) tolbachite	Alcohol/soluble	Cu(II)BTA
$CuCl_2$ (3:1-1:1)	Hot acetone 40°C/ slightly soluble	Cu(II)BTA+?
$CuCl_2$ (1:1)	CuCl2/alcohol/BTA/acetone	Cu(II)BTA
$CuCl_2$ (2:1)	Dil. HCl ; pH 1.0/soluble	Cu(II)BTA
$CuCl_2$ (1:1)	Dil. HCl ; pH 2.0/soluble	Cu(II)BTA
$CuCl_2$ (2:1)	Dil. HCl ; pH 4.5/soluble	Cu(II)BTA
$CuCl_2$ (2:1)	H2O, pH 7/soluble	Cu(II)BTA
$CuCl_2$ (2:1)	Dil. CaOH, pH 10/ soluble	Cu(II)BTA
$Cu_2(OH)_3Cl$ (3:1) atacamite	Alcohol/insoluble	Cu(OH)3Cl
$Cu_2(OH)_3Cl$ (3:1)	Dil. HCl ; pH<1.0/soluble	No precipitate
$Cu_2(OH)_3Cl$ (3:1)	Dil. HCl ; pH 1.0/soluble (pH->1.5)	Cu(II)BTA
$Cu_2(OH)_3Cl$ (3:1)	Dil. HCl ; pH 2.0/soluble (pH->4)	Cu(II)BTA
$Cu_2(OH)_3Cl$ (3:1)	Dil. HCl ; pH 3.5/soluble	Cu(II)BTA, $Cu_2(OH)_3Cl$, Cu2O
$Cu_2(OH)_3Cl$ (3:1)	H2O, pH 6/insoluble	$Cu_2(OH)_3Cl$, Cu(II)BTA
$Cu_2(OH)_3Cl$ (3:1)	Dil. CaOH, pH 9.5/ insoluble	$Cu_2(OH)_3Cl$, Cu(II)BTA
$Cu_2(OH)_2CO_3$ malachite	Alcohol/insoluble	$Cu_2(OH)_2CO_3$

Turgoose reports that the transformation of synthetic brochantite into a green hydrated copper-benzotriazolate salt ($Cu(BTA)_2 \cdot xH_2O$) occurs after three days of immersion [76] and proceeds through the reaction (Equation 5), while Watkinson [50] briefly mentions that complete transformation of brochantite into Cu-BTA occurs only after several weeks.

$$Cu_4SO_4(OH)_6 + 8BTAH \rightarrow 4Cu(BTA)_2 + SO_4^{2-} + 2H^+ + 6H_2O \qquad (5)$$

Li et al. [77] studied the formation of the complex when BTAH is added to a solution containing soluble Cu(II) from $Cu(NO_3)_2$ at different concentrations. According to the authors, nanoparticles of Cu-BTA complex form in solution. The nanoparticles size is related to both concentration of ions in solution and concentration of BTAH (Figure 1.18). The authors propose that the complex nanoparticles might re-precipitate onto the copper surface thus forming a protective film, in parallel or in competition with the mechanism of growth of the film directly on the metal surface.

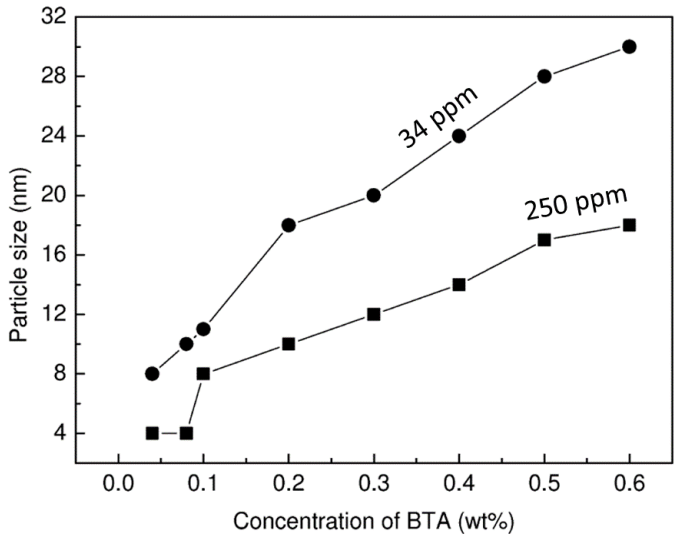

Figure 1. 18: Variation of nanoparticle size of samples containing varying amounts of BTA and cupric ions, after [77].

2.2.1.5 Influence of alloy composition

Artworks exposed outdoors are often ancient or modern copper-alloys that contain tin and other alloying elements. Several studies are devoted to understanding the influence on the efficiency of BTAH treatment on different alloys. BTAH reactivity with other components of the alloy and the resulting homogeneity of the film have been questioned [78].

Ammeloot and co-workers [79] investigate the oxide formation and properties on both pure copper and bronze (containing 13% wt. Sn) immersed in NaCl solution containing or not 0.1 M BTAH. A similar behaviour of the two substrates is observed for short immersion time, while at long immersion time (72 hours) differences in thickness of the oxide layer formed on the two substrates are noticed. For bronze, a thicker oxide layer forms in the solution without BTAH (compared to pure copper), while it is thinner in presence of BTAH. This behaviour is explained by the different conductivity of the oxide formed on bronze and on copper. Cuprite formed on bronze has higher cationic vacancies (because of Sn) and therefore higher mass transfer is permitted, resulting in a thicker oxide layer. If BTAH is present, the process of substitution of Cu(I) with Sn(IV) is hindered as dissolution of Cu(I) is limited by the presence of the inhibitor. The film is therefore thinner and BTAH has an indirect effect also on corrosion of tin.

Brunoro et al. [80] study the efficiency of octyl- BTAH (C8-BTA) on both copper and bronze containing different amount of alloying elements. The lower efficiency on the alloys compared to bare copper is attributed to the formation of weaker bonds between alloying elements and BTAH as well as to a heterogeneous distribution of the alloying elements.

An investigation on different substrates by XPS analysis has been performed by Galtayries and co-authors [81] to understand the adsorption of a mixture BTAH and hexyl-BTAH (C5-BTA)[9] on different substrates. Pure copper surface is covered by nanometric cuprite layer (0.5 ± 0.1 nm) and, after treatment, the strong N 1s peak reveals the presence of adsorbed inhibitor identified as Cu(I)-BTA. On the contrary, when applied on a pure tin surface, covered by a SnO_2 layer (5 nm in thickness), the signal corresponding to N 1s peak is absent indicating that no reaction occurred. In presence of Sn-containing alloys (CuSnPbZn and CuSnSi with Zn impurities), Cu(I)-BTA and Zn(II)-BTA are identified on the surface after treatment. The data are correlated with electrochemical tests (Potentiodynamic Polarization and EIS): the treatment improves corrosion resistance of the CuSnPbZn alloy while no effect is observed on the CuSnSi alloy. The best results are obtained on pure copper suggesting that a homogeneous Cu(I)-BTA film can form, while, when Sn is present, the Cu-BTA film is less homogeneous.

Similar conclusions can be found in [82]. Abu Baker and co-authors study the inhibitor efficiency of copper, 5% Sn-bronze and 12% Sn-bronze in a 0.1M NaCl solution containing 0.01M BTAH. Efficiency is high for the copper and low-Sn bronze (98.5% and 99.9% respectively), while it decreases (87.7%) for the 12% Sn sample. This shows that when Sn is present in relatively high concentration in the alloy,

[9] Treatment involved immersion of the samples for 1 hour at 75°C after which samples dry in air without rinsing.

the protectiveness by BTAH is lower. The authors suggest that Sn-BTA, unlike Cu-BTA complex, is not polymeric in nature thus limiting the protective effect.

In her PhD dissertation, Van der Stok-Nienhuis [83] studies the interaction between BTAH[10] and several reference substrates such as metallic tin, tin covered by a layer of SnO_2 and a bronze archaeological sample. Study by Surface Enhanced Raman Spectroscopy (SERS) reveals that a thin layer of Sn-BTA complex is formed on the tin substrate. Evidence of binding is also found where copper is present in the alloy (on bronzes), although, the author claims that further investigation is needed to evaluate the nature of the Sn-BTA complex.

Other components of the bronze alloy such as lead [84] and zinc [81] can also give complexes with BTAH, while silicon [81], does not react with the inhibitor.

2.2.1.6 Toxicity

One of the reasons that leads scientists to search for BTAH substitutes is its toxicity (and carcinogenicity) for humans and the environment. Similarly to other aspects related to this compound, the literature is not in agreement on this point. Concerns of the harmful effect of BTAH for conservators have been raised by Oddy [85], [86] at the very beginning of its use in conservation and the author suggests a specific protocol in order to minimize health-related risks.

In Finšgar and Milošev [42] the oral lethal dose (LD_{50}) for rats is reported as 560 mg/kg and the authors conclude that benzotriazole "does not constitute a major environmental hazard". Similar conclusions can be found on the website of the European Medical Agency where two studies are summarized and both conclude that BTAH has low toxicity and it is non-mutagenic[11].

According to [87], benzotriazole shows "moderate acute toxicity" with LD_{50} for BTAH and between 500 and 3400 mg/kg. In this study, it is stated that due to the lack of *in vivo* data, mutagenicity and genotoxicity of BTAH remain unclear.

BTAH raises concern considering its mutagenic effect suggested in [88] and also concerning its persistency in human tissues and urine [89]. Further investigation to understand the long-term exposure effect are still missing.

[10] A 3% BTAH solution was employed for treatment in vacuum. Pure ethanol was used as solvent for the artificially patinated coupons, while a mix of 70% ethanol and 30% water for the archaeological bronze sample.
[11] https://echa.europa.eu/registration-dossier/-/registered-dossier/14234/7/7/2

2.2.2 Benzotriazole derivatives

Molecules deriving from benzotriazole with different substituent groups on the benzene ring have been studied as corrosion inhibitors.

An example are alkyl derivatives, where a carbon chain is bond on the benzene at different ring positions. The preliminary study by Zucchi et al. [90] shows the good stability of copper electrodes pre-treated with 0.2 mM solution containing C_6-BTA and immersed in 0.1 M NaCl solution for 1000 hours.

Similar alkyl-derivatives of BTAH are investigated by Tommesani and co-workers [91] and their protectiveness on bare copper is evaluated in a solution containing the inhibitors and different corrosive species. The authors conclude that the protection efficiency increases with increasing the alkylic chain bond to the benzene ring: this behaviour is attributed to an improved hydrophobicity of the surface film formed as measurements of the contact angle have shown (Table 1.4).

Table 1. 4: Results of the sessile drop measurements on copper filmed with BTAH and BTAH-derivatives [91].

	Contact angle (°)
BTAH	80
C1-BTA	82
C4-BTA	85
C6-BTA	95

Similar hypothesis is reported in other studies on alkyl-BTAH derivatives of the same research group [63].The effect on inhibition efficiency due to the presence of a carboxylic group bonded to the benzene ring is also investigated. Otieno-Alego et al. [92] compare the inhibition efficiency of benzotriazole, benzotriazole-5-carboxylic acid (5-CBT) and benzotriazole-4-carboxylic acid (4-CBT) by weight loss measurement in acidic solution. The results indicate that inhibition efficiency varies from 20% for 4-CBT, 40% for BTAH and 70% for 5-CBT. Similarly to BTAH, SERS experiments show that coordination to the oxidized copper substrate is due to the interaction of the nitrogen atoms present in the azole ring, while differences between the two compounds is explained by the authors considering the electrophilic character of the carboxylic group making the protonated benzotriazole form more stable. As the –COOH group is more distant from the azole ring in the 5-CBT compound, the electrophilic effect is reduced and a better chemisorption is ensured.

2.3 Surfactants

Among organic compounds, linear carboxylic acids and their sodium salts have been studied as non-toxic [93] corrosion inhibitors. These molecules are characterized by a long hydrocarbon chain (hydrophobic) and a hydrophilic part, the carboxylic group that has electron-donor tendency. Through the carboxylic group, the molecules adsorb on the metallic surface while the hydrophobic tail remains in contact with the aggressive solution, which determines a change in surface tension properties (Figure 1.19) [94].

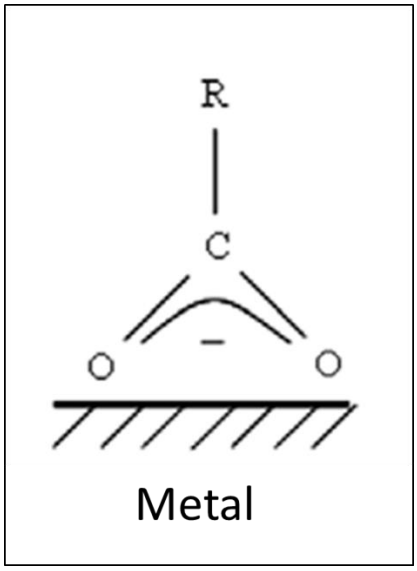

Figure 1. 19: Adsorption of carboxylic function on a metallic surface.

Moreover, carboxylic acids and their salts like other surfactants have the ability to form micelles when their concentration reaches a specific value (Critical Micellar Concentration). At this value, the surface coverage is higher thus giving better corrosion protection (Figure 1.20) [95].

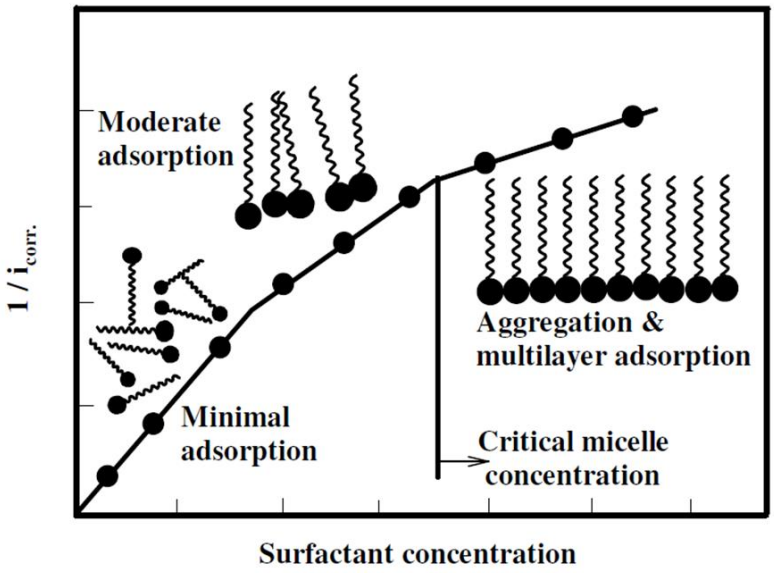

Figure 1. 20: Relationship between concertation of the surfactant and corrosion current, after [95].

The most accepted inhibition mechanism is based on adsorption on the metal surface on one side and on the formation of a hydrophobic layer of the metal carboxylate on the other. In fact, the interaction with metallic ions from the substrate determines the formation of insoluble carboxylates that, once precipitated on the surface provide excellent hydrophobic properties. In the literature, both anodic and cathodic processes are found to be affected by the presence of carboxylates.

The formation of superhydrophobic surfaces due to formation of a metal-carboxylate surface layer is described by Xu et al. [96] on bare copper after treatment with different carboxylic acids in aqueous solution (an organic amine has been added to allow solubility of the otherwise water insoluble fatty acid). The surface hydrophobic layer is identified as copper carboxylate and the reactions leading to its formation are proposed (Equation 6):

$$2Cu + O_2 = 2CuO$$

$$2CuO + H^+ = Cu^{2+} + H_2O \qquad (6)$$

$$Cu^{2+} + 2(HC16)^- = Cu(HC16)_2$$

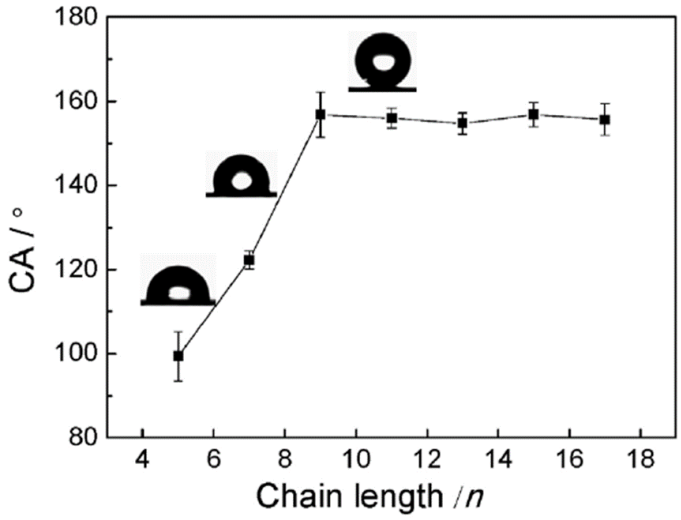

Figure 1. 21: Contact angle variations based on different chain lengths of the carboxylic acid used for treatment, after [96].

Where $(HC16)^-$ represents the carboxylic acid with 16 carbon atoms in its deprotonated form. Results of the potentiodynamic polarization highlight that the cathodic action is inhibited by the surface modification. In the same study (Figure 1.21), the hydrophobic properties are related to chain length of the carboxylic acid: increased hydrophobicity is measured from 5 to 9 carbon atoms and with 9 carbon atoms, superhydrophobicity is reached (CA=160°), which remains constant even by increasing chain length.

Carboxylates have been first studied for (mainly temporary) protection of iron [97] and other metals such as copper [98] and bronze [93], lead [99], [100], zinc [101] with several studies, especially in recent years, targeting cultural heritage applications.

The use of carboxylic acids and sodium carboxylate for the protection of heritage objects has been developed during the PROMET project (2004-2008). Hollner et al. [102] studied the efficiency of sodium decanoate (0.1M NaC10) in aggressive solution on artificially corroded copper coupons. Micrometric copper decanoate crystals form on the coupons surface after treatment with NaC10 and the treatment is suggested as a temporary protective.

Elia [103], [104] has studied the efficiency on copper of electrochemically deposited CuC10 and CuC12 from decanoate and dodecanoate acid solutions: in both cases potential is shifted towards more negative values indicating that the main effect of the layer formation is reducing the cathodic process and, in particular, the access of water on the metal surface. The author suggests that the high standard deviation among measurements could be due to the softness of the layer formed, that makes it

subjected to mechanical removal. The author also points out that an application based on simple immersion does not provide homogeneous coverage in any of the conditions tested.

For application to heritage objects exposed outdoors, myristic acid (HC14) at different concentrations (0.005, 0.01, 0.04, 0.06, 0.1 M in ethanol for 3 to 10 days immersion) for the protection of copper and phosphor bronze has been investigated by Milošev et al. [105]. The immersion in the chosen solutions induces the formation of surface nanostructures and platelets. The authors remark differences in both morphology and inhibition efficiency based on the composition of the substrate: copper is covered by "nano-flowers or knitted-like pattern" (Figure 1.22), while bronze is covered by nanoparticles showing regular patterns. Inhibition efficiency is lower in the case of bronze samples when using a 0.06M HC14 solution after several days of immersion (Table 1.5).

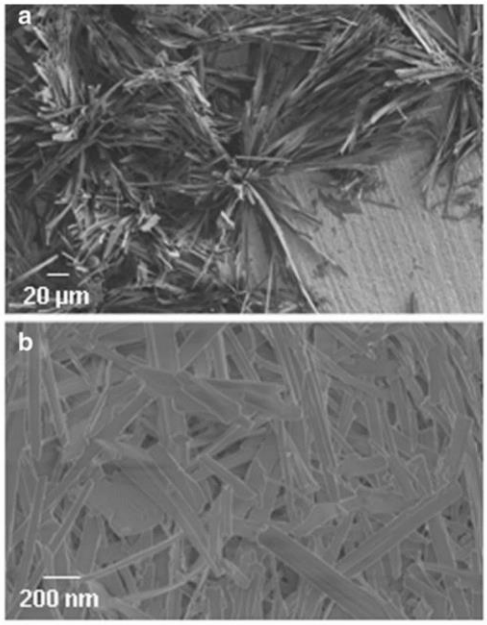

Figure 1. 22: Copper surface after immersion in 0.06 M HC14/ethanol solution after a) 3 days and b) 10 days.

Table 1. 5: Results of Potentiodynamic Polarization for HC14-treated copper and bronze samples in 0.014 M solution Na_2SO_4/0.024 M solution $NaHCO_3$, after [105].

Time of immersion/days	E_{corr}/V	j_{corr}/(A cm^{-2})	IE/%
Cu			
Bare	0.022	7.5×10^{-7}	
3	−0.005	3.1×10^{-7}	58.7
7	0.018	4.5×10^{-8}	94.0
10	−0.046	2.0×10^{-8}	97.3
15	−0.012	7.5×10^{-8}	90.0
Cu-6Sn			
Bare	−0.079	1.3×10^{-6}	
3	−0.057	4.2×10^{-7}	67.7
7	−0.038	4.9×10^{-7}	62.0
10	−0.027	9.1×10^{-7}	34.6
15	−0.089	8.5×10^{-7}	30.0

Based on the promising results obtained on iron and copper using carboxylic acids, Apchain [19], [106] used decanoic acid for the protection of copper. Apchain studies the efficiency and durability of a treatment based on 30 g/L decanoic acid hydro-alcoholic solution and compares it to the traditional microcrystalline wax treatment. The experiments are carried out on naturally corroded copper surfaces and several application strategies are tested for the decanoic acid: by brush (one or multiple layers) and immersion (at different immersion times). Results of the Raman investigation in cross-section show that the carboxylic acid interacts with the brochantite outer layer by partially converting it into insoluble copper decanoate. The presence of the decanoate is detected deeper inside the corrosion layer until the cuprite layer by detecting ^{13}C-marked molecules. These results are confirmed in a complementary study conducted by L'héronde and co-workers [107] using Scanning Auger Microscopy in cross-section: copper decanoate is detected within the brochantite layer while it was not detected within the cuprite layer.

The efficiency and durability of the decanoic acid treatment are shown to be related to the application method [106]: a better penetration and protection (under rain leaching conditions) are connected and achieved when samples are immersed in solution even after short time (1 minute).

3. Study of protectives for copper-based artefacts

3.1 Historical overview

Since the introduction of chemical products in conservation of heritage materials, and particularly of metals, several projects have been undertaken to investigate and propose new protectives. Despite these studies, Degrigny [108] points out how in the context of conservation science, the development of conservation treatments represents a secondary aspect, also in term of budget, compared to the scientific investigation of works of art dedicated to collect artistic, historical and technological information.

A new awareness of the need of protecting outdoor metallic artefacts, among which bronze statues are the most iconic, started in the 1960s with the set-up of large-scale restauration programs such as that of the horses of San Marco in Venice and the Statue of Liberty in New York. At this time, atmospheric pollution started to be recognized as an issue to the preservation of exposed artefacts. The conservation campaigns coupled with the need of understanding of the corrosion phenomena, were accompanied by scientific analysis and studies on new protective strategies. In 1991, Marabelli proposed a double-film coating for outdoor bronzes. The most relevant research programs undertaken in recent years for the preservation of copper-based artefacts are summarized in Figure 1.23.

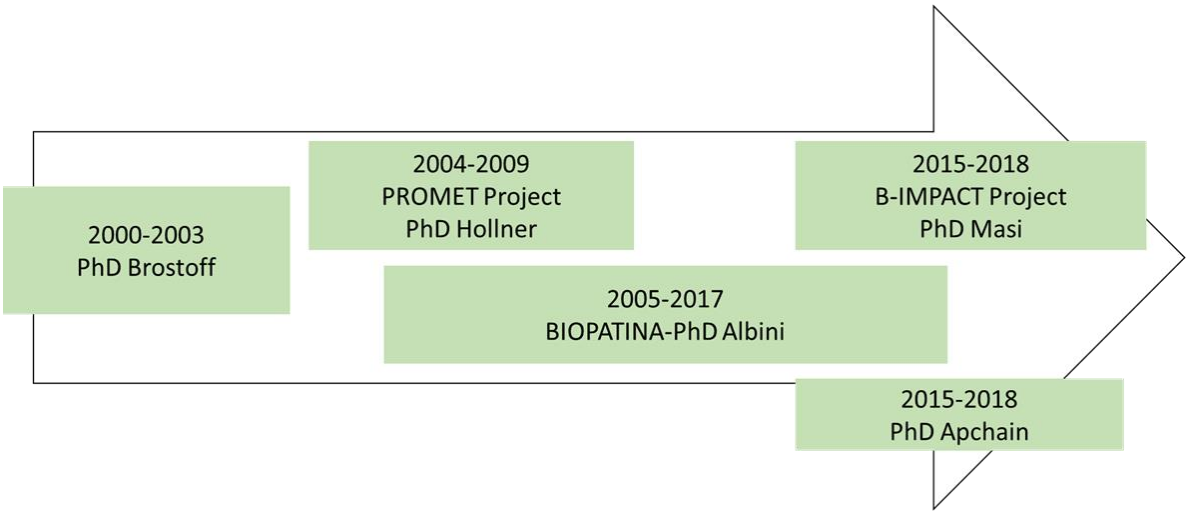

Figure 1. 23: Projects and relative PhD works addressing the protection of outdoor copper and copper alloys in the last 20 years.

In the 2000s up to recently, several projects involving PhD thesis have been carried out especially targeting outdoor bronze sculptures.

In the previously-cited study, Brostoff investigated 29 coatings for outdoor bronzes and, as already seen, a part was devoted to the study of benzotriazole [57]. The PROMET project, a collaboration among different institutions in the Mediterranean basin, focused on the protection of iron and copper. Hollner discussed the main outcomes of this project in her PhD work [109]. The BIOPATINA project launched in 2005 at the He-Arch in Switzerland led Albini to propose a protective based on a biological treatment [51]. In parallel, a new coating based on the organo-silane PropS-SH for outdoor bronzes was developed in the framework of the B-IMPACT project and as part of the PhD work of Masi [110]. In 2018, Apchain [19] discussed her thesis work on the protection of copper based objects using a decanoic acid solution.

As for corrosion inhibitors specifically, the experiments on natural compounds such as plant extracts or natural molecules for heritage applications are increasing [111] following a more general trend in the field of corrosion inhibitors.

3.2 Research methodology in heritage related studies

As it is evident from the analysis of the literature on corrosion inhibitors especially when applied on heritage objects or with the final objective to protect heritage artefacts, no specific and widely accepted protocol exists making the comparison between different studies particularly difficult.

The protection to the substrate is influenced not only by the kind of inhibitor or protective chosen, but also by the application protocol and the substrate used in the study [38]. Application methods can vary from the immersion in solution, for evident practical reasons commonly reserved to small objects, to the application by spray or brush and application in the vapor phase.

The most usual substrates are bare metal copper or bronze samples, sometimes reproducing historic or archaeological alloy composition but also naturally or artificially corroded samples.

A large majority of studies proposing eco-friendly corrosion inhibitors as alternatives to benzotriazole is carried out using immersion of bare metallic samples and is referred as “preliminary” investigations. As an example, Varvara et al. [112] compared cysteine and alanine (0.1 mM) on uncorroded bronze with an alloy composition comparable to that of archaeological bronzes. Channouf [113] proposed the extract from the juniper plant as inhibitor for bronze. In the case of plant extracts, it is sometimes impossible to know whether one or more molecules are responsible for the protective effect [114].

Other studies prefer the preparation of artificially corroded coupons. This choice is determined on one side by the difficulty to find suitable and corroded specimens to be sacrificed to the research and, on

the other, by the necessity of studying flat, reproducible corrosion layers that reflect the typical aspects of outdoor exposed metals. Several procedures are followed by researchers to prepare artificial patinas: immersion in solution, electrochemical corrosion, but also wet and dry cycles and simulated acid rain dropping. Some recent studies reporting artificial ageing are reported in Table 1.6 and represent an example of the variety of methods available.

Table 1. 6: Different methodologies to produce artificial corrosion layers on bronze and copper.

Study	Method	Reactants	Patina structural components
Di Carlo et al. 2007	1) Exposure to vapor 2) Immersion 3) Cotton swab 4) 2-solutions successive immersion	1) HCl 5% in water (vapor) 2) 1 M $CuCl_2$ 3) 0.5 M $CuCl_2$ + 0.1 M HCl 4) 17 mM $CuSO_4$ +50 Mm $CuSO_4$	1) Cuprite + anatacamite 2) Cuprite + clino/atacamite 3) Cuprite + clino/atacamite 4) Cuprite + antlerite + brochantite
Marušić et al. 2009	1) Immersion 2) Successive brush applications 3) Electrochemical	1) 15 mM $CuSO_4$ 2) 33%wt NH_4Cl 3) 0.2 g/L Na_2SO_4 + 0.2 g/L $NaHCO_3$	1) Cuprite + brochantite 2) Atacamite + cuprite/tin oxide (?) 3) Cuprite/tin oxide + malachite + amorphous copper sulfate
Mennucci et al. 2012	Immersion at 50°C for 14 days	5 g/L $CuSO_4$ + 6 g/LNa_2SO_4	Cuprite + brochantite
Chiavari et al. 2011 Chiavari et al. 2013 Masi et al. 2017	1) Dropping 2) Wet and Dry cycles	Synthetic acid rain	1) Mixture cuprite, tenorite, chalcocite (?) + tin oxide 2) Cuprite + posnjakite
Albini et al. 2018	Immersion of corroded copper samples	NaCl + $Cu(NO_3)_2{\cdot}3H_2O$	Cuprite + atacamite + brochantite (traces)

A double-structured cuprite-brochantite artificial patina (Figure 1.24) is produced and investigated by Mennucci and colleagues [115] who conclude that the corrosion layer formed at 50°C in immersion for 14 days did not produce an electrochemically uniform layer

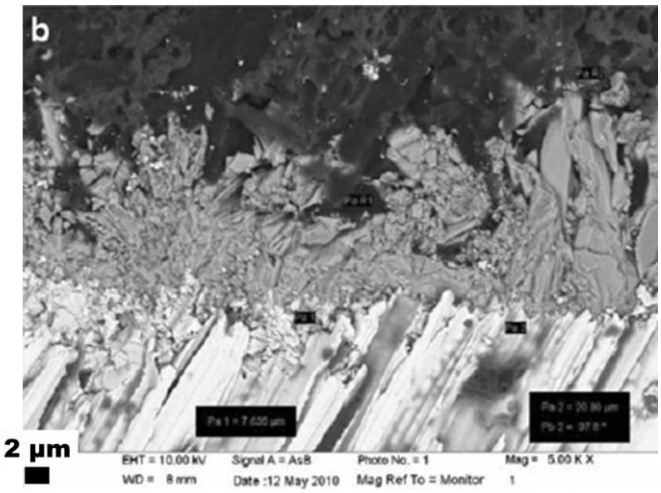

Figure 1. 24: Example of the double-layered patina obtained on copper by Mennucci et al. [115].

Surface-covering, continuous artificial patinas are hard to obtain in the short term and their transport properties might not reflect the situation on real samples. A procedure to obtain patinas more representative of real objects exposed outdoors has been developed by Chiavari and her research group [116]–[118]. The methodology reflects actual outdoor conditions (dropping, wet-dry cycles in synthetic rain) and corrosion layers of few µm in thickness are formed on the metallic substrate.

Finally, in some case, naturally corroded copper-based samples are preferred as they are more easily accessible in the form of corroded tiles from historical buildings [57], [106], [107], [119].

In cultural heritage related studies, when the objective is determining the efficiency of a protective system, several parameters need to be taken into consideration. In fact, not only the efficiency of the protective, but also the impact on the surface colour, the ideal reversibility of the treatment, its durability over time and, its safety for the operator and the environment, are all factors that play an important role when proposing new solutions to the community of conservators. For this reason, and for the complexity of the system under investigation, a multi-analytical approach is generally preferred.

For the assessment of efficiency and durability of inhibitors and coatings, electrochemical methods such as Potentiodynamic Polarization (PP) and Electrochemical Impedance Spectroscopy (EIS) are the most employed. These testing methods usually provide information on the corrosion system and how it evolves after application, with impedance being more adapted for the study of thin coatings and resistive samples such as outdoor exposed metals. EIS is often reported in heritage studies as a powerful tool to evaluate both corrosion processes and coatings properties [120]. The technique offers several advantages:

- It can be performed in-situ (Figure 1.25) directly on the surface thanks to portable and specifically designed cells containing either liquid or jellified electrolyte,
- It is non-destructive as no sampling is required and a small voltage (10-20 mV) is applied in a way not to destabilize the metallic substrate nor the corrosion layer.

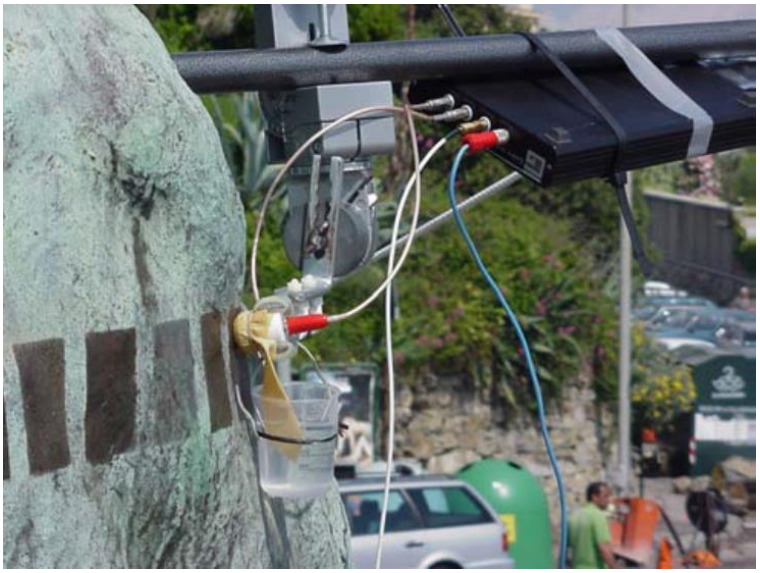

Figure 1. 25: In-situ EIS measurements on different coated and uncoated areas, Monument dei Mille, Genova, after [121].

Most studies on inhibitors follow a methodology already employed in industry for the evaluation of organic compounds in aggressive solution. The methodology has been applied on pre-treated samples that are tested in a corrosive environment and some examples have been cited in the previous part of this review.

Other analytical techniques that aim at investigating the interaction between the inhibitor and the corrosion layer are SEM-EDS, spectroscopic techniques such as Infra-Red [53], [62], [119] and Raman spectroscopy [60], [106]. Auger spectroscopy has been recently used in cross-section [107] for the study of copper decanoate.

4. Conclusion and scope of the research

The bibliographic study allows to have a general understanding of the atmospheric corrosion of copper from the early stages of corrosion to long-term exposures, specifically in urban environment. In addition, the most relevant results present in the literature concerning interactions between inhibitors and reactive substrate have been presented.

The bibliographic study pointed out several aspects.

First, the complexity of long-term corroded samples is pointed out. The copper surface is covered by multiple layers of mineral phases that present different transport properties and can evolve in time based on several parameters among which external atmospheric composition.

Secondly, it is clear that organic molecules can interact with the metallic or oxidized surfaces by forming chemical and/or physical bonds and in particular, by forming new compounds as an effect of such interaction that can have a positive role by inhibiting corrosion. In addition, in the field of inhibitors, there is a need for developing new treatment strategies that are atoxic for the users and the environment.

Based on these considerations is the choice of working with naturally corroded samples which morphological, structural and transport properties are more representative for real long-term outdoor exposed artefacts. The need for understanding what is the substrate with which the inhibitor will interact and that will determine the protection to the underlying metal.

One strategy to slow down corrosion reaction consists in the application of corrosion inhibitors. Inhibitors can act on one or both redox reactions involved in the corrosion process and are classified accordingly (anodic, cathodic or mixed-type inhibitors). Among the corrosion inhibitors studied for applications in conservation, benzotriazole and carboxylic acids have been reviewed. Benzotriazole is a widely employed inhibitor for copper and copper-based metals. It has been proven as an efficient inhibitor in different conditions and on both bare and oxidized copper, although, the precise mechanism of inhibition is still questioned. In conservation, benzotriazole is applied as a pre-treatment in general before coating application, as it is not considered stable over time. In addition, the use of this compound is mostly discouraged because of its toxicity but it remains one of the few inhibitors employed by conservators. The results on efficiency of a treatment based on benzotriazole are contradictory and the durability has not been addressed when only the inhibitor is applied (without a coating) and therefore it remains unclear.

Decanoic acid has been recently studied and it seems a promising, non-toxic alternative to benzotriazole. It acts by transformation of insoluble copper decanoate, which provides good hydrophobic properties to the corrosion layer limiting water and oxygen access. Although, doubts about the adhesion of the carboxylate layer are expressed and a possible role as temporary protection has been suggested.

In general, the review on inhibitors pointed out the presence of a multitude of studies using different parameters and the difficulty in reaching a common conclusion. In addition, the lack of studies addressing specifically corroded surfaces with naturally formed corrosion layers that are representative of real objects is pointed out.

The aim of this PhD research is to address the study of inhibitors considered separately from a final coating in order to understand their role in protection. Secondly, the investigation is based on the use of natural ancient samples of copper taken as simplified model system for copper-based objects. This decision is linked on one side to the samples' availability and on the other to the conviction that, as inhibitors interact with the material surface by forming chemical bonds, the surface characteristics have to be as more representative as possible to real samples when the final goal is the application to naturally corroded surfaces. The aim is to investigate the possible changes that the interaction with the inhibitors have on the properties of the corrosion layer such as transport (permeability) and if they can play a role in supporting passivity of the corrosion layer.

Methodology

Methodology

In this chapter, a description of the methodology followed during the study with regards of the protocols established for each experiment is reported. Materials and characterization techniques employed are detailed.

1. Methodological approach

The main research question concerns the understanding of the main physico-chemical modifications due to the application of an inhibitor as a pre-treatment on a surface that is representative of outdoor corrosion of copper.

As physicochemical changes are involved, a decision is made to adopt a methodological approach able to unveil the physico-chemical properties of substrate after treatment, by directly analysing the physico-chemical changes or by setting up experiments able to provide the information wanted.

Such physico-chemical approach has been used in parallel to study two systems. The first is a relatively simple system as synthetic mineral phases, representative of the composition of the corroded samples, are investigated during and after reaction with the inhibitors solutions.

The second constitutes the complex system as a naturally long-term corroded substrate is treated and investigated after treatment and after outdoor exposure.

The complementarity of the information acquired in this way is important especially when considering that specific analysis, such as those at the nanoscale, are not feasible when considering only the corrosion layer, while the physical properties of the corrosion layer cannot be investigated if only considering the synthetic mineral phases.

The methodology followed for the investigation of the mineral phases after treatment with the inhibitor is schematized in Figure 2.1.

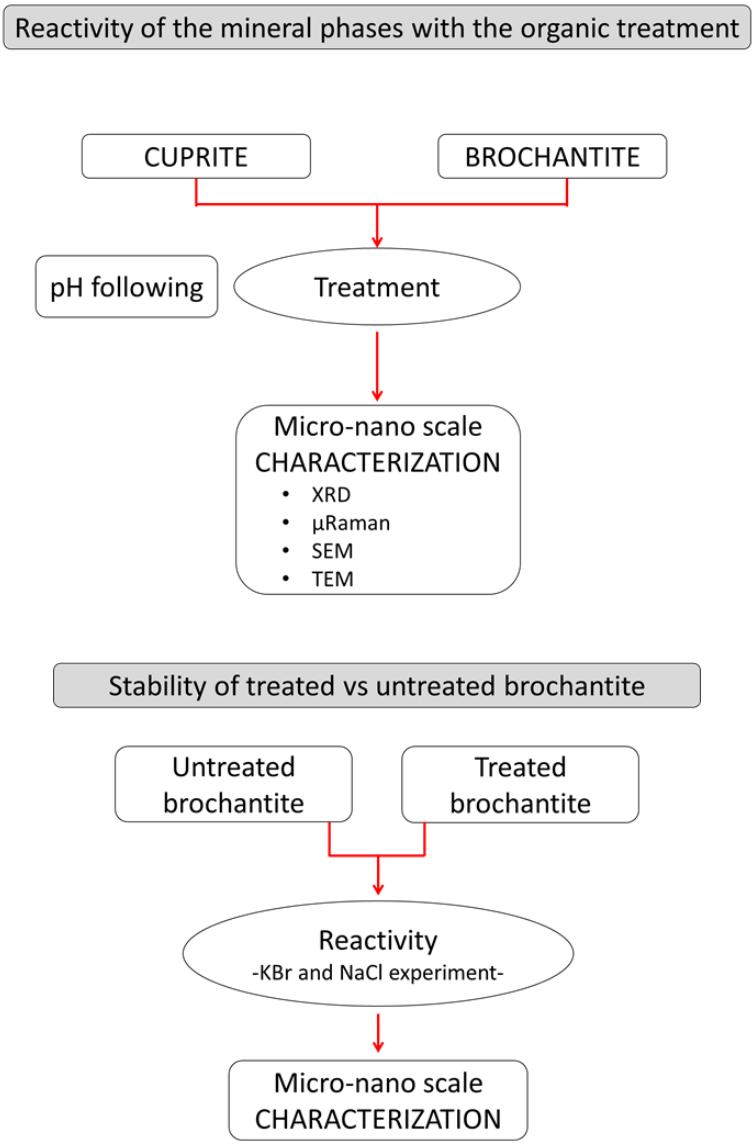

Figure 2. 1 : Schematic view of the experiments carried out on the mineral phases.

First, the reactivity and reaction mechanism are evaluated by separately treating the two minerals with a solution containing the inhibitor. During the reaction, pH of the solution is constantly monitored in order to have a global information on the reaction mechanism involved. During the reaction and after 24 hours, the insoluble reaction product is withdrawn from the solution and systematically studied following a multi-analytical and multi-scale procedure. The analytical protocol includes structural analysis (XRD and µRaman) for all the samples. Further characterization on the compositional and morphological properties of the reaction products are performed by TEM analysis, in alternative SEM analysis has been employed when the specimen is soluble in ethanol.

Based on the information acquired during the first part of the investigation on the synthetic minerals, a second experiment has been added. The objective is to investigate the stability and the change in

reactivity of a treated brochantite for 2 hours, a reaction time chosen as it represents the protocol used for pre-treatment of the real samples. The methodology is based on the chemical reaction observed when untreated brochantite is in contact with a solution containing concentrated NaCl. As it will be presented in the results, brochantite undergoes a transformation and atacamite is formed. The same procedure has been used to evaluate the reactivity of treated brochantite and different pH have been tested.

The methodology employed for the study of the inhibitors on the naturally corroded samples is summarized in Figure 2.2.

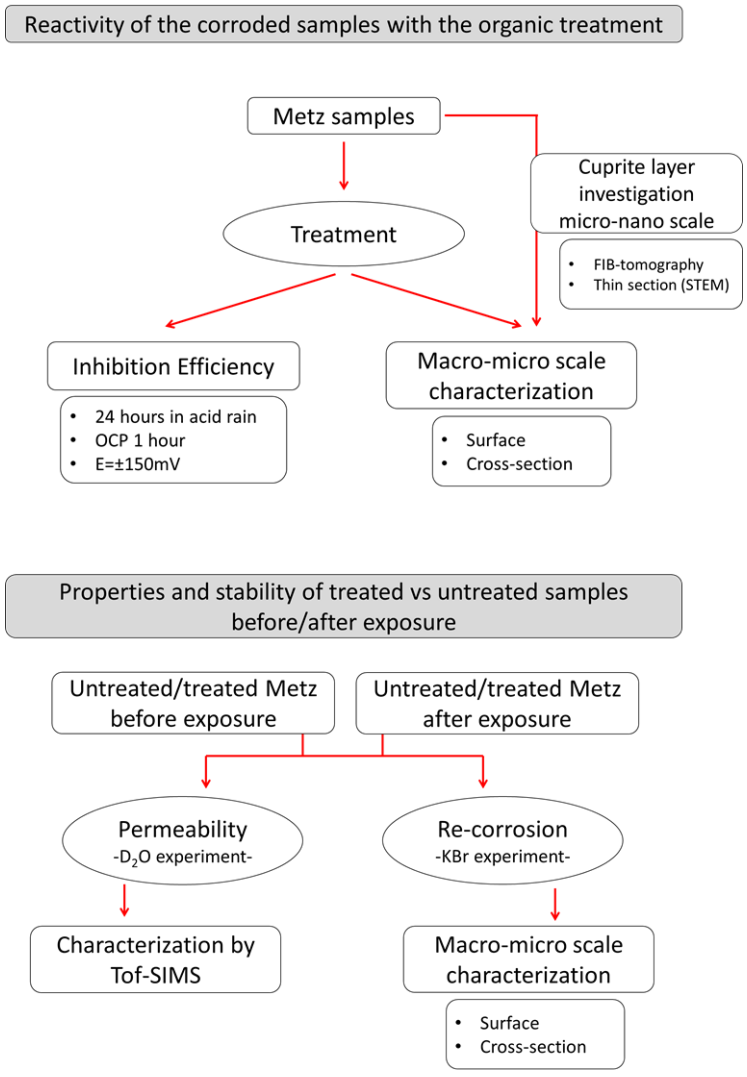

Figure 2. 2 : Schematic overview of the experiments carried out on naturally corroded samples also referred to as Metz samples.

First, the samples before and after treatment are analysed using a well-established protocol characterized by electrochemical and physico-chemical techniques to evaluate inhibition efficiency

and global (colour, surface tension), morphological and structural properties of the corrosion layer after treatment. The techniques employed for characterization are listed in Table 2.1.

Table 2. 1: Analytical protocol followed during the research on naturally corroded samples.

		Property	Technique
macro	Global	Inhibition efficiency	Potentiodynamic polarization
↓	Surface	Colour change	Spectrophotometry
		Surface tension	Drop test
		Surface morphology/structure	OM/SEM/µRaman
micro	Cross-section	Morphology/elemental distribution	SEM-EDS
		Penetration of the treatment	µRaman mapping

The techniques are complementary as they allow to investigate different properties of the corrosion layer at different scales. Electrochemical measurements are employed as preliminary test to evaluate the global efficiency of the treatments. Surface properties of the samples such as colour, surface tension and morphology are studied, while morphological, elemental and structural characterization of the corrosion layer are investigated in cross-section by SEM-EDS and Raman analysis.

In parallel to this more conventional protocol, some advanced characterization has been carried out on the untreated samples in order to better understand the system under investigation and especially the cuprite layer morphology (FIB-tomography and thin section observations).

In a second time, the treated samples are studied for specific properties such as permeability to water (with immersion in D_2O), passivity of the cuprite layer after treatment (KBr re-corrosion experiment) and durability (6-months outdoor exposure).

The principles behind these last experiments are further detailed.

Permeability to water has been assessed by measuring the deuterium adsorbed within the porosity of the corrosion layer after a certain time of immersion in deuterated water. The abundance of the isotope is assessed by Tof-SIMS analysis directly in cross-section and an enrichment can be calculated. The results are used as comparative values among treated and untreated samples.

The evaluation of an effect on cuprite and on its passive behaviour is assessed by exposing the sample to a corrosive environment (KBr solution) for a relatively long time (30 days).

After immersion, the samples have been studied in order to determine structural and morphological changes. In particular, SEM-EDS analysis is used to identify the loss of passivity and the re-corrosion of the metallic substrate. Again, the results are based on the comparison between the untreated sample and the treated ones.

A series of samples is also exposed outdoors for a short time (6 months) and the effects on the stability and durability of the treatment are evaluated following the same protocol described for the samples after treatment.

The next part of the chapter is dedicated to exposing in detail the experimental procedure followed. The analytical techniques employed and reference phases obtained are detailed.

2. Experimental

2.1 Corrosion inhibitors and reference complexes

Three organic compounds have been tested as inhibitors for the naturally corroded copper samples. The main characteristics of each compound are listed in Table 2.2. The three compounds were purchased from Sigma-Aldrich and used as received.

Table 2. 2: Organic compounds used as inhibitors in the study. The molecular structure, purity and the aspect of the compounds as received are also reported.

Compound	Acronym	Molecular structure	Purity	Aspect
Benzotriazole	BTAH	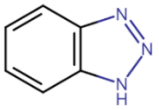	99%	White powder
Benzotriazole-5-carboxylic acid	5CBT	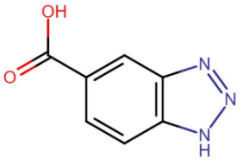	99%	Light-brown powder
Decanoic acid	HC10	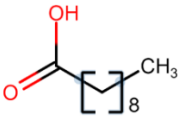	≥98%	Pale-yellow crystals

Additional physico-chemical and hazard information for the three inhibitors is reported in Table 2.3.

Table 2. 3 : Physico-chemical properties and hazard statements for the three inhibitors selected for the study. Size of the BTAH molecule is reported in [122] *and length of the decanoic acid molecule is calculated based on data reported in* [123].

	BTAH	5CBT	HC10
Molecular weight	119.12 g/mol	163.13 g/mol	172.26 g/mol
Molecule length	0.556 nm	n.d.	3 nm
Solubility in water	25 g/L at 25°C	n.d.	Almost insoluble (62 mg/L)
pKa	8.3	3.5	4.9
Vapor pressure at 25°C	$4 \cdot 10^{-2}$ mmHg	$4.18 \cdot 10^{-9}$ mmHg	$3.66 \cdot 10^{-4}$ mmHg
Hazard statements (Sigma-Aldrich 2021)	H302 Harmful if swallowed; H319 Causes serious eyes irritation; H411 Toxic to aquatic life with long lasting effects.	H315 Causes skin irritation; H319 Causes serious eyes irritation; H335 May cause respiratory irritation	H315 Causes skin irritation; H319 Causes serious eyes irritation; H412 Toxic to aquatic life with long lasting effects.

The compounds have a comparable molecular weight, while the molecules have different sizes: length is higher in the case of HC10 (3 nm in length) and lower for BTAH (0.5 nm). The compounds have a different solubility in water with BTAH being the most soluble, while 5CBT and HC10 are almost

insoluble in water and soluble in organic solvents. The acidic equilibrium constant is reported for the three compounds and acidity increases as BTAH<HC10<5CBT.

The pure compounds have been characterized by XRD and µRaman spectroscopy and results of these analysis are presented later in this chapter.

In order to produce reference phases reflecting the interactions between the organic compounds chosen and copper ions, soluble copper sulphate pentahydrate is employed as source of copper ions for the synthesis of copper-inhibitor complexes.

Cu-BTA complex

The reference phase is synthetized at room temperature. To a 0.04 M $CuSO_4 \cdot 5H_2O$ solution (0.2 g in 20 mL distilled water), an aqueous 0.08 M solution of benzotriazole (0.19 g in 20 mL) is added dropwise. The reaction is carried out under continuous magnetic stirring for 24 hours. The insoluble precipitate is then separated by centrifugation, washed with distilled water and oven-dried for 24 hours at 60°C. The water-insoluble phase separated from the solution is analysed by XRD analysis and the crystalline compound $[Cu(BTA)_2(H_2O)]_n$ previously reported in [124] is identified.

Cu-5CBT complex

The same protocol described in the previous paragraph is applied to produce a reference Cu-5CBT complex phase. Considering the low solubility in water, a 50% v/v ethanol/water solution is employed for dissolving the pure 5CBT. To a 0.015 M $CuSO_4 \cdot 5H_2O$ solution (0.07 g in 20 mL distilled water), a 0.03 M solution of 5CBT (0.1 g in 20mL ethanol/water) is added dropwise. Magnetic stirring is applied over 24 hours when the precipitate is recuperated by centrifugation. Characterization of the precipitate is presented later in this chapter. The resulting insoluble powder is amorphous and no match can be found with phases present in the database, although Raman analysis provides comparable results with the Cu-BTA complex.

Copper decanoate

Copper decanoate was available in the laboratory where it has been previously synthetized using the protocol described in [125]. The synthesis involves two steps: a first reaction to form sodium decanoate (Equation 1) and a second one to form, from sodium decanoate, the copper decanoate (Equation 2).

$$HC10 + NaOH \rightarrow NaC10 + H_2O \quad (1)$$

$$2NaC10 + CuSO_4 \cdot 5H_2O \rightarrow Cu(C10)_2 \quad (2)$$

2.2 Mineral phases

Experiments are performed on the two main mineral phases found on outdoor copper in urban areas after long-time of exposure, namely cuprite and brochantite. The characteristics of the two minerals and their synthesis are exposed in the next paragraphs.

Cuprite

Mineral cuprite (Cu_2O) is purchased from Merck as powder (>99.99%) and used as such. This particular high-purity mineral is stored under nitrogen atmosphere prior to use in order not to be subjected to oxidation after exposure to the environment. In other cases, commercially available cuprite is treated with a not-specified organic compound to avoid oxidation, which would have compromised the experiments.

Brochantite

According to the reaction (Equation 3), brochantite, $Cu_4SO_4(OH)_6$, is synthetized. The protocol used has been previously followed by [19], [126].

$$4CuSO_4 \cdot 5H_2O + Na_2CO_3 \rightarrow Cu_4SO_4(OH)_6 + Na_2SO_4 + 2H_2SO_4 + 15H_2O + CO_2 \quad (3)$$

At room temperature, 50 mL of 0.1M Na_2CO_3 solution are added dropwise to 200mL of a 0.1M $CuSO_4 \cdot 5H_2O$ and magnetic stirring is maintained during the reaction. A light-green water-insoluble precipitate is separated by centrifugation and washed three times in deionized water before drying at 60°C for 24 to 48 hours. A yield of approximately 0.55 g of brochantite is obtained and the precipitate is analysed by X-Ray diffraction (XRD) and µRaman spectroscopy after each synthesis.

2.3 Reactions with synthetic minerals

The reactivity of the two mineral phases, brochantite and cuprite, with the solution containing each of the inhibitors is studied following a specific procedure. Table 2.4 represents the ratio between organic inhibitor and mineral chosen for the experiments based on possible complex formation. First, the inhibitor is solubilized in a hydro alcoholic (50%v/v) solution without the mineral. When solubilisation is complete, pH is measured and chosen amount of mineral is then added to the solution, magnetic stirring is constantly applied.

Table 2. 4 : Molar ratio used for the experiments based on the supposed complex formed by reaction with the mineral.

	Molar ratio	**Supposed compound**
BTAH:brochantite	8:1	$Cu(BTA)_2$
BTAH:cuprite	2:1	Cu(BTA)
5CBT:brochantite	8:1	$Cu(5CBT)_2$
5CBT:cuprite	2:1	Cu(5CBT)
HC10:brochantite	8:1	$Cu(C10)_2$
HC10:cuprite	4:1	$Cu(C10)_2$

After adding the water-insoluble mineral to the inhibitor's solution, the pH is followed using an Apera PH820 pH Meter: pH measurements are taken every 3 minutes up to 2 hours and a measurement after 24 hours is also recorded. At different reaction time, 5 mL of the solution are collected to study the precipitate. The insoluble precipitate is separated by centrifugation and washed three times with distilled water before drying for 24 to 48 hours at 60°C.

The precipitate is then characterized from the micro to the nanoscale by X-ray diffraction (XRD), µRaman spectroscopy. SEM-EDS analysis is performed on the reaction products of decanoic acid, while TEM analysis is performed on the reaction products resulting from BTAH and 5CBT reactions. The reason is that the reaction product resulting from the reaction of decanoic acid is soluble in ethanol, therefore it is not possible to prepare the sample for TEM observations. An additional experiment is performed on 2 hours-treated brochantite in order to evaluate its reactivity in 1.3M NaCl aqueous

solution at different pH: 7, 5, 2, 1. The solution is acidified by the addition of hydrochloric acid dropwise. The immersion (0.2 g of powder in 15 mL solution) lasts for 30 days after which the insoluble precipitate is again separated by centrifugation, 3-times washed in distilled water and oven-dried at 60°C. A characterization of the precipitate is carried out by XRD, µ-Raman spectroscopy and TEM analysis.

2.4 Reactions with the naturally corroded samples

2.4.1 Substrate investigated

For the investigation, naturally corroded copper plates originally belonging to the roof cladding of the église Saint Martin in Metz (Figure 2.3), located in the eastern part of France, are employed.

Figure 2. 3 : The bell tower of S. Martin's church with the original copper tiles before restauration.

In 2009, the church underwent a conservation intervention that concerned, among other aspects, the roofing of the building: in that occasion, original and damaged copper plates have been substituted and some of them have been made available for research. The precise date corresponding to the first exposure of the copper plates is not known, although as the bell tower was built in 1887, the copper roof might also be contemporary to the tower.

Advantages of using these samples are multiple: first, no artificially corroded samples needed to be produced, which would have constituted a time-consuming operation and, secondly, the naturally-formed corrosion layer can be considered as more representative for long-term corrosion.

The samples have been previously described in E. Apchain's PhD thesis work [19]. In particular, Apchain investigated the metal microstructure by chemical attack and the porosity of the corrosion layer by

Hg-injection porosimetry. The substrate is constituted by micrometric polygonal grains characteristic of unalloyed copper (Figure 2.4).

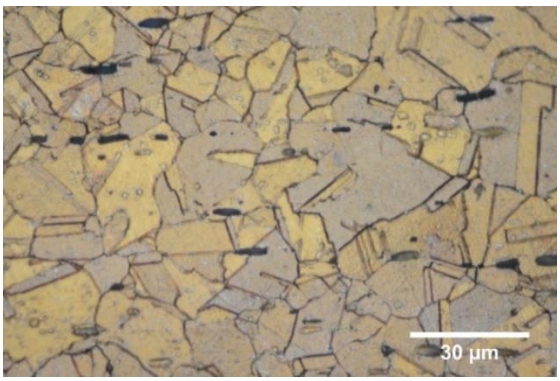

Figure 2. 4 : Microstructure of the Metz sample after [19].

Considering the corrosion layer, it shows the typical structural characteristics of long-term copper corrosion as pointed out in the literature study, with an external layer constituted by brochantite and an internal layer of cuprite. The Hg-injection porosimetry results (Figure 2.5) again obtained by Apchain provide a global information concerning the porosity of the whole corrosion layer.

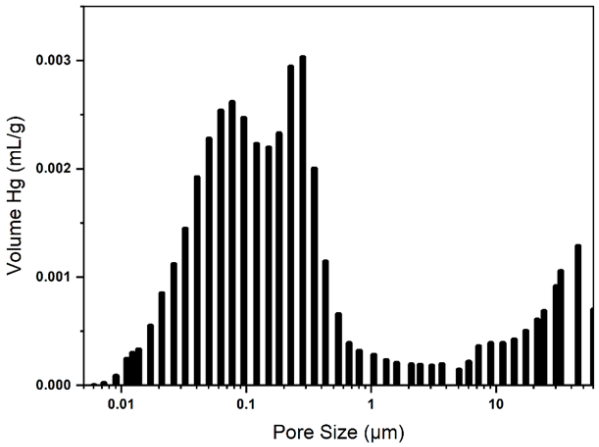

Figure 2. 5 : Pore distribution resulting from Hg injection porosimetry, adapted from [19].

Based on this analysis, the corrosion layer can be described as a meso to macroporous[12] material with the largest majority of pores having a diameter between 30 nm and 1 µm. Large pores (>10 µm) are also present.

The Metz samples before treatment will be described in more detail in Chapter 3.

2.4.2 Treatment protocol

The Metz plate is first gently cleaned by distilled water and a cotton swab in order to remove all dust and loose particles from the surface. It is then let dry in air before cutting it into smaller pieces of approximately 2x2 cm. Each sample is enveloped into a commercial polyurethane resin[13] in a way only the external surface (1.5x1.5 cm) is left in contact with the treatment solution. Samples are prepared in triplets.

For the treatment, a procedure based on immersion is chosen as it constitutes a simple and more reproducible method, although it is less representative of applications to outdoor large monuments' surfaces.

Immersion in each of the inhibitors' solutions lasts for 2 hours. Solutions concentration and solvents are specified in Table 2.5. After immersion, the samples are rinsed in water and oven-dried at 60°C for 24 hours.

Table 2. 5: Concentration and solvent mix used for the treatment.

Compound	Concentration (mol/L)	Solvent
BTAH	0.25	Ethanol/water 50% v/v
5CBT	0.25	
HC10	0.17	

[12] According to the IUPAC definition. A microporous material is characterized by pores of diameter <2nm; mesoporous material 2-50nm and macroporous >50nm.
[13] Bi-component resin from Rougier®.

2.4.3 Analytical protocol and sample preparation

A preliminary evaluation of the inhibition efficiency of the treatment is performed by measuring Potentiodynamic polarization after immersion in synthetic acid rain.

Physico-chemical modifications following the treatment are evaluated by multi-scale analyses both on the surface and in cross-section (Table 2.1).

Cross-sections are prepared by embedding the samples in epoxy resin (Epofix® from Struers). After polymerization of the resin, the sample is polished by means of Si-C abrasive papers with decreasing grain size (30 to 5 µm) using ethanol for the untreated sample and distilled water for the treated samples. A final polishing using a diamond-paste suspension down to ¼ µm is also realized. Samples are cleaned in distilled water ultrasonic bath.

Permeability to liquid water

As the treatment might influence the access of water within the corrosion layer, an experiment concerning the permeability to liquid water was adapted from the one described in [106]. The Metz treated and untreated samples were immersed in heavy water (100% D_2O) for 30 days after which the samples were oven-dried at 60°C for 24 hours. This operation will remove the majority of not-chemically bond deuterated water and the one present in the macropores of the corrosion layer. samples were then prepared as cross-sections and analysed by Tof-SIMS in order to identify the deuterium present and evaluate the enrichment compared to the not immersed corresponding sample.

The data treatment differs from the one previously described as the treatment affects the amount of hydrogen present in the corrosion layer: it was therefore decided not to compare untreated and treated samples but only treated samples before and after immersion in deuterated water.

Depassivation in aggressive solution (KBr experiment)

The objective of this experiment is to produce a relatively rapid perturbation of the corrosion system and understand the impact of immersion in stagnant aggressive solution on the differently treated samples when compared to the untreated sample before and after outdoor exposure. In order to induce such perturbation and produce corrosion, a concentrated solution containing 1.3 M KBr was employed. The bromine salt was preferred to chlorine salt as it can be detected by EDS analysis without overlapping with the chlorine already present in the naturally formed corrosion layer. Moreover, previous studies have shown that a solution containing Br^- ions behaves in a similar way to one containing Cl^- ions on passivated copper and zinc surfaces [127], [128]. A slightly difference was

observed between the two halide-containing solutions: the aggressiveness towards the oxide layer is higher for chlorine than bromine solution. This is possibly due to the difference in ionic radius (0.181 nm for Cl^- and 0.196 nm for Br^-), allowing chlorine ions to better penetrate the oxide layer [129].

The protocol consisted in the immersion of untreated and treated samples (protected with polyurethane resin) in the aggressive solution for 30 days. After this time, they were gently rinsed with water and oven-dried at 60°C for 48 hours. The samples were studied following the protocol previously described for treated samples. In particular, the study in cross-section allowed to evaluate the possible initiation of anodic dissolution of the metallic substrate as well as the ions migration through the corrosion layer. An evaluation of the samples was done by comparing the untreated samples to the treated ones.

Short-term evaluation of the treatment (outdoor exposure)[14]

An evaluation of the treatment was performed by exposing triplets of untreated and treated samples in the proximity of the laboratory on a rack at 45° facing west. The exposure lasted from October 2020 to March 2021. Temperature and relative humidity (RH) have been recorded at 4-hours intervals using a KIMO® KISTOCK KH200 and average monthly results are reported in Annex 1 (pg.258).

After exposure, the analytical protocol described for freshly treated samples has been applied.

Despite the short term, this experiment contributed to the understanding of the protection mechanism.

3. Characterization techniques

3.1 Potentiodynamic Polarization

The inhibition efficiency of the three selected compounds is tested by performing Potentiodynamic Polarization on the treated samples after immersion for 24 hours in synthetic acid rain [130].

Untreated samples (1 cm^2) are preliminary prepared in triplets as working electrodes: the back side is polished with abrasive paper and the electric connection is made by welding a copper wire to the surface. The sides and the back of the sample are protected from the solution using a commercial

[14] This part was carried out in the framework of a Master internship and most of the characterization work was carried out by Mathias Clement.

varnish. The samples are then treated with the inhibitors' solutions following the established protocol before being exposed for 24 hours to an aggressive solution simulating acid rain [80]: its composition is summarized in Table 2.6.

Table 2. 6 : Composition of the synthetic rain. pH of the resulting solution is equal to 3.1

Compound	Concentration (mmol/L)	Brand/purity
H_2SO_4	0.325	Prolabo ≥95%
HNO_3	0.250	Fisher ≥65%
NaCl	1.452	Sigma ≥99%
$NaNO_3$	0.250	Prolabo ≥99%
Na_2SO_4	0.225	Sigma ≥99%
$(NH_4)_2SO_4$	0.325	Sigma ≥99%

Measurements are carried out using an SP-200 Bio-Logic potentiostat controlled by the EC-Lab® software. A three-electrode cell mounting includes the sample as working electrode, a platinum spiral wire (0.6/250mm) as counter electrode and an Ag/AgCl/KCl (3M) as reference electrode.

The potential is followed in the open circuit potential mode for 1 hour before applying the external potential of ±150 mV with a scan rate of 1 mV/s. Measurements are carried out in the acid rain aerated solution without stirring.

The Tafel curves obtained are analysed using the dedicated software in order to obtain the potential and the current parameters. In particular, the current density parameters are used to calculate inhibition efficiency (IE%) (Equation 4):

$$IE\% = \left(\frac{j_{corr} - j_{corrINH}}{j_{corr}}\right) \cdot 100 \qquad (4)$$

In the equation, j_{corr} and $j_{corrINH}$ represent the corrosion current densities of the untreated and treated samples respectively.

3.2 Colorimetry

Colour measurements are performed using a portable CM-2300d spectrophotometer (Konica-Minolta). The reflectance spectra are collected between 360 and 740 nm using the D65 standard

illuminant at a 10° observer angle on an 8 mm diameter surface. The measurement is the result of an average of 5 flashes. The data are elaborated using the SpectraMagic NX® software and expressed as CIEL*a*b* parameters. The colour difference parameters and the colour difference among untreated and treated samples (ΔE_{94}) is calculated from Equations 5 and 6 [131]:

$$\Delta L^* = L^* - L^*_{INH}$$

$$\Delta a^* = a^* - a^*_{INH}$$

$$\Delta b^* = b^* - b^*_{INH}$$

$$C = \sqrt{(a^*)^2 + (b^*)^2} \qquad (5)$$

$$C_{INH} = \sqrt{(a^*_{INH})^2 + (b^*_{INH})^2}$$

$$\Delta C^* = C - C_{INH}$$

$$\Delta H^* = \sqrt{(\Delta a^*)^2 + (\Delta b^*)^2 - (\Delta C^*)^2}$$

$$\Delta E_{94} = \sqrt{\left(\frac{\Delta L^*}{S_L}\right)^2 + \left(\frac{\Delta C^*}{S_C}\right)^2 + \left(\frac{\Delta H^*}{S_H}\right)^2} \qquad (6)$$

Where $S_L = 1$, $S_C = 0.045 \cdot C$ and $S_H = 0.015 \cdot C$

L*, a*, b* represents the average colour parameters obtained for the untreated sample, while the L^*_{INH}, a^*_{INH} and b^*_{INH} the average obtained for the treated samples.

Colour measurements are performed on three samples after treatment and on one sample after 6 months outdoor exposure.

3.3 Surface tension

The drop test is performed by measuring the contact angle of a 5 µL distilled water drop placed on the surface of the sample (Figure 2.7). The measurement of the angle is carried out after 10 seconds after the drop has been placed on the surface and 5 measurements are realized for each sample. The test is performed using an OCA 20EC DataPhysics Instrument equipped with a SCA20 software. Prior to test, the samples are oven-dried for 48 hours at 60°C.

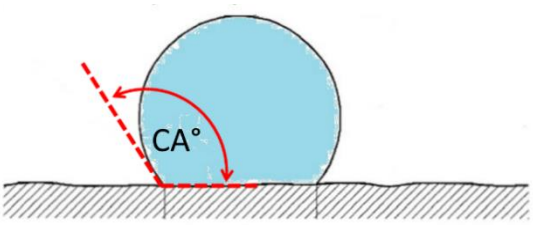

Figure 2. 6: Graphical representation of the static contact angle CA°, modified from [132].

3.4 Optical microscopy

Optical microscopy in bright and dark field is carried out using a Zeiss Axio Imager Vario optical microscope (OM) equipped with an Axiocam 305 Color camera. Images are collected and elaborated with the ZenCore 2.6 ® software.

3.5 X-Ray Diffraction

3.5.1 Technique overview

X-ray diffraction (XRD) is a characterization technique based on the interaction of atomic electron clouds and a monochromatic x-ray radiation. In the case of a crystalline material, atoms are periodically arranged in space: their interaction with the radiation produces scattering in specific directions giving constructive waves. In this case the Bragg's law is respected (Equation 7):

$$2dsin\theta = n\lambda \qquad (7)$$

Where *d* is the distance between diffraction planes, θ is the incident radiation angle, *n* is an integer and *λ* is the incident beam wavelength. The latter is in the same order of magnitude as *d* (1-100 Å).

Concerning amorphous materials, their atoms are randomly distributed in space and the interaction with an incident x-ray beam leads to scatter in many directions: what is observed are halos giving rise to low intensity humps in the diffraction pattern.

3.5.2 Operational mode

A Rigaku RU200B rotating anode is used to perform powder X-ray diffraction. X-rays are produced at the molybdenum tube and monochromatized around the Kα emission lines (λ = 0.7093 Å) using a FOX-2D (Xenocs) toroidal mirror. The beam is focalised on the sample with a beam size of a 100 µm surface and the sample is irradiated by a flux in the order of $20 \cdot 10^6$ photons/second. The obtained diffraction images are collected on photosensitive screens on different apparatus: first, a photosensitive screen scanned by an Amersham Biosciences Storm 820 Phosphor imager, then replaced by a Pilatus 300K (Dectris) or RebirX-70S (Cegitek) hybrid pixel detectors in transmission mode with a 2θ range from 2-35°. 2D images are integrated using the Fit2D [133] or the PyFAI (ESRF) [134] software. Phase identification of the diffraction patterns is performed using the DiffracEVA (Bruker AXS) software interfaced with the databases ICDD (PDF 2003) and the Crystallography Open Database (CDD) [135]. Finally, diffraction pattern are elaborated using OriginPro2021 software.

In some cases, a quantitative estimation concerning the occurrence of crystalline phases have been performed using the Reference Intensity Ratio method based on data *I/Icor* cited in PDF files from the ICDD database.

3.5.3 Characterization of reference phases

Cuprite

Diffraction pattern of synthetic cuprite is reported in Figure 2.7 and compared to the reference cuprite.

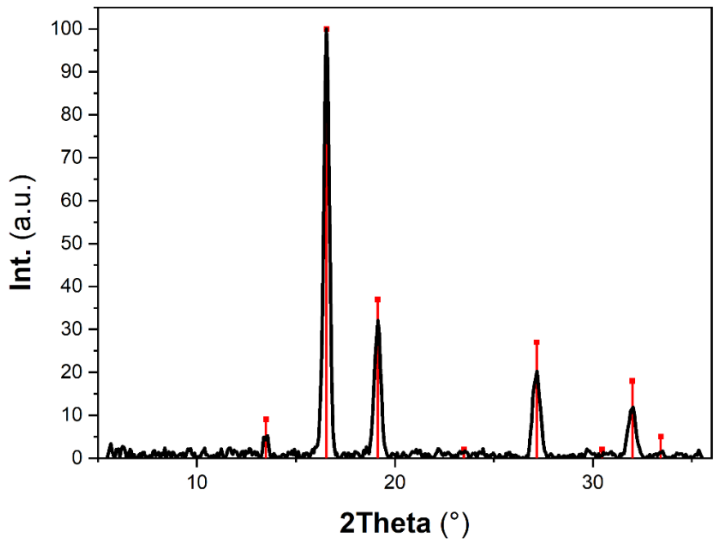

Figure 2. 7 : Diffraction pattern of synthetic cuprite and reference peaks (PDF 05-0667).

Brochantite

XRD analysis is performed at every new synthesis of brochantite. Figure 2.8 shows a representative pattern of the powdery sample obtained. The pattern is in agreement with the one reported in the database.

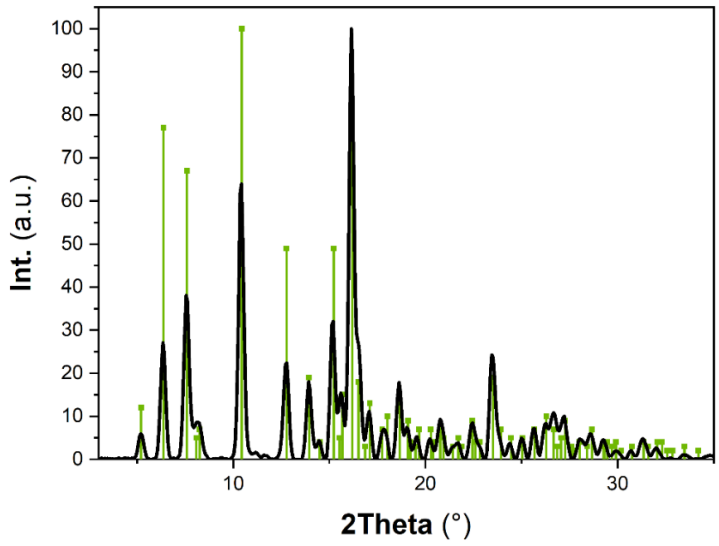

Figure 2. 8 Diffraction pattern of synthetic brochantite and reference peaks (PDF 87-0454).

Benzotriazole

Figure 2.9 shows the diffraction pattern of pure benzotriazole. The compound is a crystalline compound [39], [40].

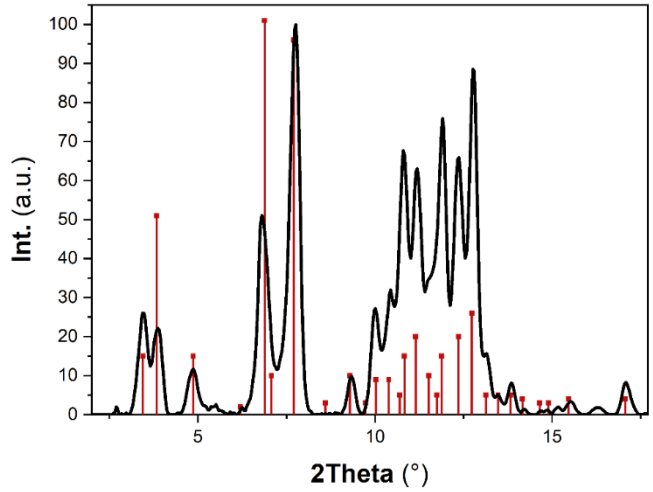

Figure 2. 9 : Diffraction pattern of pure BTAH and reference peaks (PDF 32-1536).

Cu-BTA complex

A diffraction pattern showing the crystalline nature of the synthetized phase is obtained (Figure 2.10).

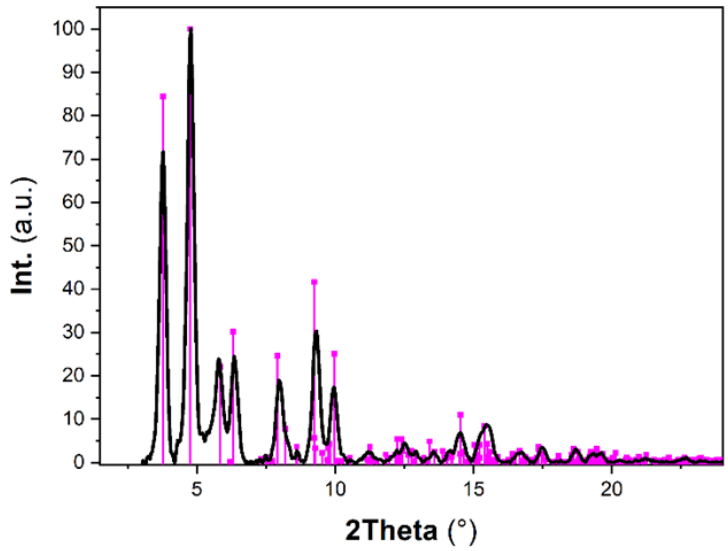

Figure 2. 10 : Diffraction pattern of Cu-BTA and reference peaks (COD 2211909).

Benzotriazole-5-carboxylic acid

5CBT also gives a distinct diffraction pattern and, as BTAH, it exhibits a crystalline structure in its pure form (Figure 2.11). No reference XRD pattern has been found in the available databases.

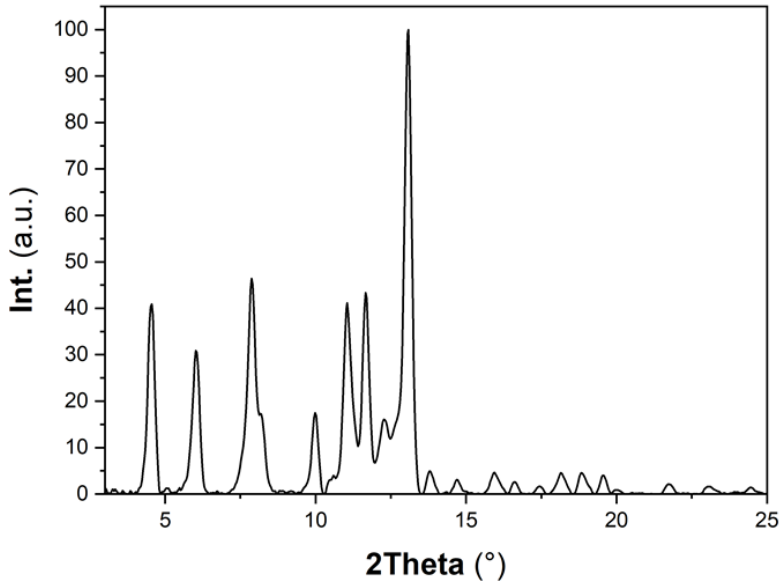

Figure 2. 11 : Diffraction pattern of pure 5CBT.

Cu-5CBT complex

XRD analysis shows the amorphous nature of the compound as the diffraction pattern obtained is characterized by large humps (Figure 2.12).

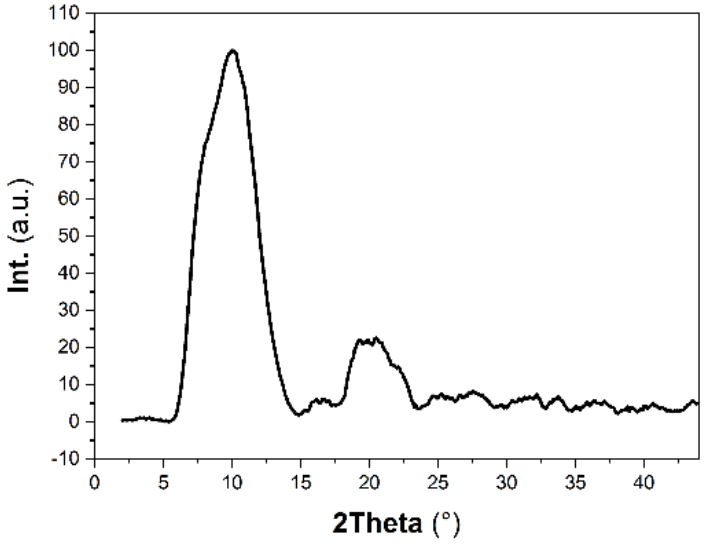

Figure 2. 12: Diffraction pattern of Cu-5CBT complex (not identified).

Decanoic acid

Decanoic acid's diffraction pattern is reported and compared to the corresponding reference in Figure 2.13.

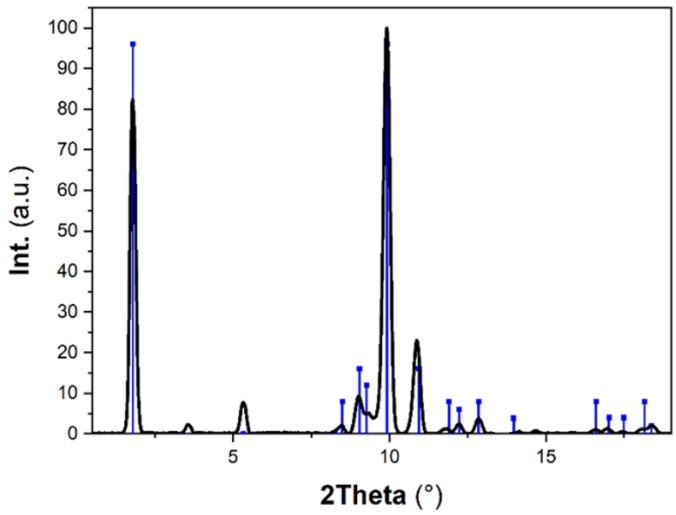

Figure 2. 13 : Diffraction pattern of pure HC10 and reference peaks (PDF 08-0527).

Copper(II) decanoate

Synthetic copper decanoate was clearly identified by XRD (Figure 2.14).

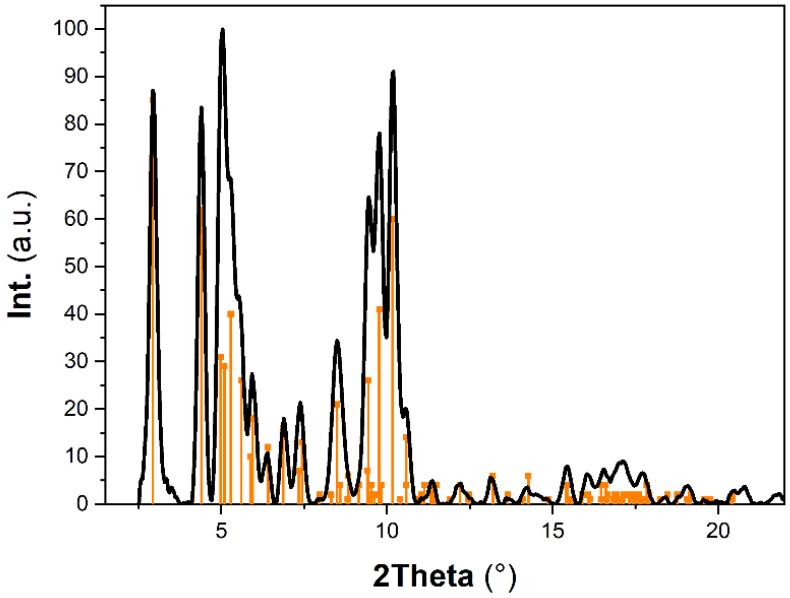

Figure 2. 14 : Diffraction pattern of pure HC10 and reference peaks (COD 4512487).

3.6 SEM-EDS

Surface morphology, morphology and elemental composition of the corrosion layer are studied by scanning electron microscopy coupled with energy dispersive X-ray spectroscopy (SEM-EDS) analysis. For this purpose, a JEOL JSM-7001F scanning electron microscope equipped with an Oxford SDD detector and an energy dispersive spectrometer (EDS) producing energy spectra with a resolution of 124 eV is used.

The surface morphology is assessed by secondary electron images by placing the sample at a working distance of 5 mm and using an acceleration voltage of 5 KeV.

For the acquisition of secondary electron and backscattered electron images of samples in cross-section, a 10 mm working distance and 10 to 15 keV acceleration voltage are the parameters employed.

The EDS analysis is performed using a working distance of 10 mm and an acceleration voltage of 15 keV and 10keV. Elemental maps with a resolution of 1024x1024 pixels and acquisition time equal to

~10 ms/pixel are collected and processed using the dedicated microanalysis Aztec 4.3® software from Oxford Instruments. The analysis of the spectra allows a semi-quantitative evaluation of the elements present: the semi-quantitative data are normalized and reported as atomic or mass percentages.

All samples are metallized by applying a thin (10-20 nm) carbon layer on the surface prior to the analysis.

3.7 SEM-FIB

3.7.1 Technique overview

The morphological properties of the cuprite layer of the untreated sample have been investigated at a sub-micrometric scale by preparation and observation of thin sections of the cuprite layer and by performing FIB-tomography.

FIB-tomography is realized by volume reconstruction starting from successive images of a selected cuprite volume. In order to obtain the images, a SEM equipped with a focus ion beam (FIB) gun is employed. In a selected area including the interfaces metal-cuprite-brochantite, the sample is successively abraded by gallium ions and imaged with electrons to reveal the underlying 3D structures (Figure 2.15-a). The second operation consists in post-processing of the images obtained (Figure 2.15-b): this operation allows to reconstruct the abraded volume and, by image contrast, locate porosity and estimate the total pore volume within the cuprite [136].

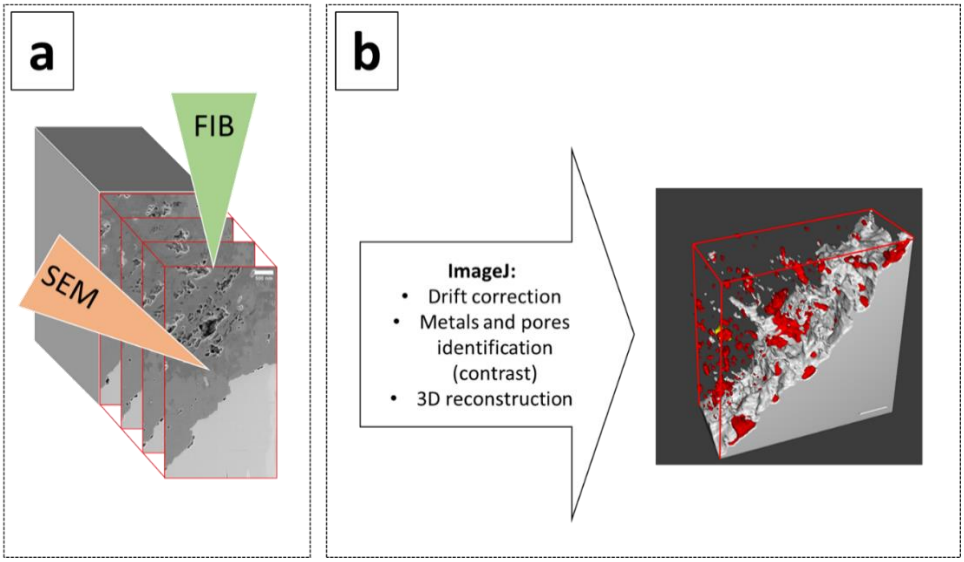

Figure 2. 15: Scheme of tomographic volume reconstruction using FIB. A first step (a) consists in slicing the sample by FIB abrasion and taking a series of SE images. The second step (b) consists of image treatment and 3D reconstruction using ImageJ software.

3.7.2 Operational mode

Thin section preparation and image acquisition were carried out at the CIMAP laboratory in Caen. The apparatus used is a FEI Helios NanoLab 660 equipped with a gallium ions gun (FIB) as well as an electron gun (SEM). The Ga^+ ions are accelerated within the FIB column and abrades the sample by removing a slice of material which thickness depends on the ionic current. At the ionic current of 80 pA employed, slices of 10.5 nm thickness were successively removed. Each new cross-section was imaged at the following conditions: secondary electron detector, 2 keV acceleration voltage, 50 pA current, and 4 mm working distance. The secondary electron images pixel size corresponds to 2 nm. The process is successively repeated (~100 times) in order to obtain a representative volume of the interface.

The 3D volume reconstruction is performed using the software ImageJ.

3.8 µRaman spectroscopy

3.8.1 Operational mode

Raman spectra are collected using a Renishaw Invia Reflex Raman µ-spectrometer equipped with a Leica LM/MD optical microscope. The 50 × long working distance objective is employed to analyse the powdery samples and the sample surfaces, while the conventional 50 x objective is used for the Raman analysis in cross-section. The samples are excited by a 532 nm Nd:YAG laser with an energy <300 µW. When performing spot analysis, an accumulation time of 60 s/scan is employed, while 20 s/scan is used for mapping. The lateral resolution is 1 µm. The spectrometer is calibrated using a silicon wafer having a characteristic Raman shift at 520.5 cm^{-1}. Spectral resolution is 2 cm^{-1} and spectra are collected and treated with the software Wire 3.4®. Spectra presented in this work have been elaborated using OriginPro2021 software.

3.8.2 Characterization of reference materials

Cuprite

The representative spectrum obtained on the synthetic cuprite powder is presented in Figure 2.16 (black line). Characteristic shifts reported in Table 2.7 are comparable to those reported in the literature [137]. The higher intensity peak at 218 cm^{-1}, corresponding to the stretching vibration of the Cu-O bond, was used for the mapping characterization of cuprite in cross-section.

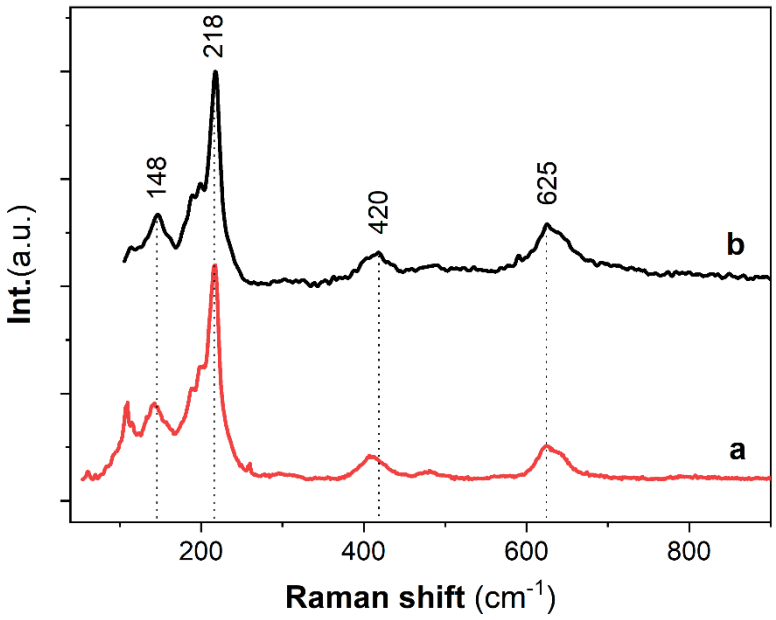

Figure 2. 16: Raman spectra of (a) reference cuprite (RRUFF R050384) and (b) synthetic cuprite. Main shifts are reported.

Table 2. 7 : Main Raman peaks reported in the literature and those obtained on the synthetic cuprite. Cuprite (*) refers to the shifts reported in [138]

Cuprite (*)	Cuprite RRUFF R050384	Synthetic cuprite
93	109	
148	145	148
186	188	189
195	198	199
218	**218**	**218**
495	407	420
638	625	625

Brochantite

Figure 2.17 shows the representative spectrum on the synthetized brochantite. Main shifts are reported in Table 2.8 and compared to the literature. The stronger Raman vibration corresponds to the sulphate group stretching mode at 973 cm^{-1}.

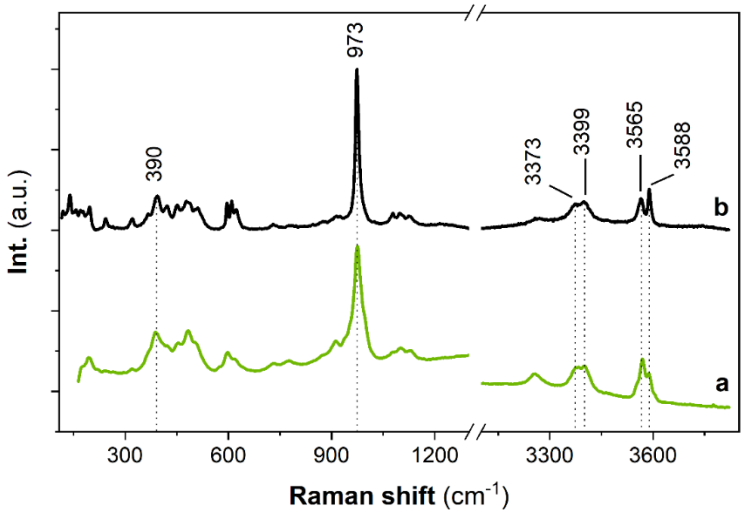

Figure 2. 17: Raman spectra of (a) reference brochantite (RRUFF R100199) and (b) synthetic brochantite.

Table 2. 8 : Main Raman peaks reported in the literature and those obtained in this study on the synthetized brochantite. (*) refers to the brochantite shifts reported in [138].

Brochantite (*)	Brochantite RRUFF R100199	Synthetic brochantite (this study)
171	-	170
195	194	197
243	-	243
319	321	320
366	-	367
389	388	390
429	-	421
449	452	450
506	505	511
597	598	596
611	-	611
621	621	622
911	911	-
974	**973**	**973**
1078	1077	1077
1098	1100	1098
3252	3255	3255
3369	3373	3373
3398	3399	3399
3563	3565	3565
3585	3588	3588

Benzotriazole

Reference spectra of pure benzotriazole is reported in Figure 2.18. The band assignment based on literature studies [61], [68], [139], [140] is proposed in Table 2.9.

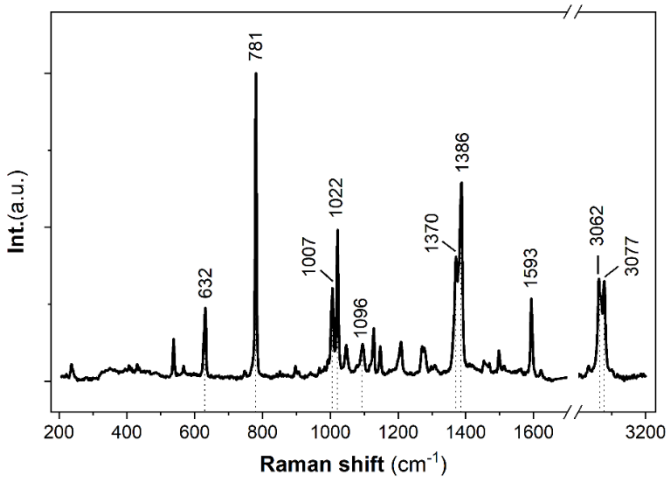

Figure 2. 18: Raman reference spectrum of pure BTAH.

Table 2. 9 : Main Raman bands and assignment proposed in the literature.(r), (c), (t), (k) correspond to references.

Benzotriazole	Benzotriazole (this study)	Assignment
235 [136]	236	Skeletal torsion
538 [136]	538	triazole ring bending
631 [137] , 628 [136]	632	Triazole ring torsion
779 [137], [137], **783** [61]	**781**	**Benzene ring breathing**
1008 [136],1009 [61]	1007	Benzene skeletal bending
1020 [136],1017 [137], 1027 [61]	1022	In plane ring breathing
1049 [68]	1047	Ring stretching
1095 [68], [136]	**1096**	**NH bending in plane**
1128 [163], 1125 [61]	1129	CH bending in plane
1145 [136]	1148	CH bending in plane
1208 [136]	1208	Triazole ring stretching + NH bending
1278 [136]	1272	Combination band (skeletal stetching +
1278 [136]	1277	Combination band (CH in plane bending + CC stretching)
1370 [136]	1370	Fermi resonance with 1386 cm^{-1} band
1385 [136], **1388** [137], **1387** [61]	**1386**	**Triazole ring stretching [17], benzene skeletal stretching + CH bending in plane [16]**
1498 [136]	1497	Skeletal stretch
1594 [68], 1595 [61]	1593	C-C stretching
	3062	Aromatic CH stretching
3078 [61]	3077	CH stretching

Cu-BTA complex

The spectrum and reference shifts for the reference Cu-BTA compound are reported in Figure 2.19 and Table 2.10 respectively.

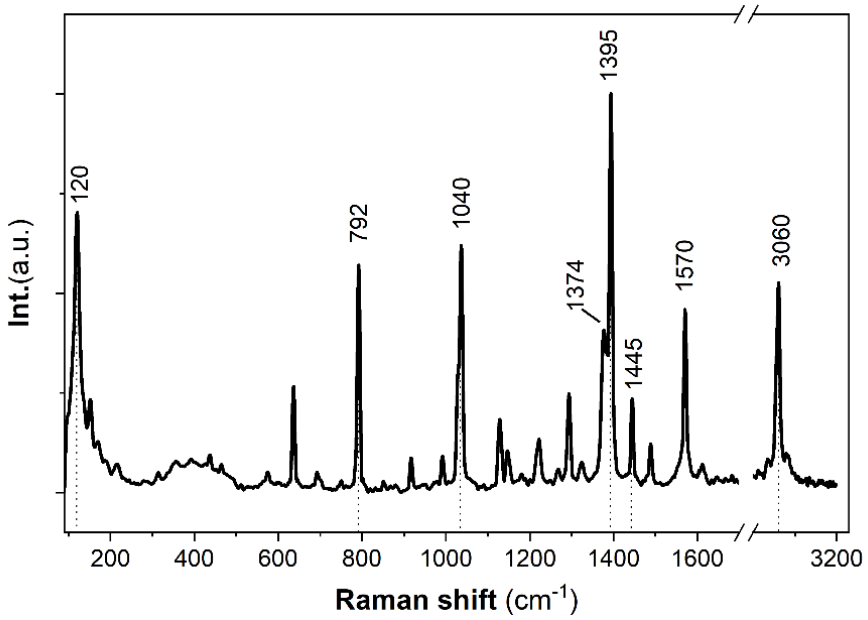

Figure 2. 19: Raman reference spectrum of reference Cu-BTA.

In particular, it can be noticed that the shift at 1096 cm^{-1}, corresponding to the NH bending vibration in BTAH is absent in the complex. Other high intensity peaks are shifted in the complex compared to the pure compound: the benzene ring breathing at 781 cm^{-1} is shifted to 791 cm^{-1}; the combination band at 1986 cm^{-1} is shifted to 1395 cm^{-1} and the C-C stretching mode at 1593 cm^{-1} is shifted to 1570 cm^{-1}. A new peak is detected at 1445 cm^{-1}.

The blue-shifts (to high wavenumbers) and red-shift (to low wavenumbers) indicating a different vibrational frequency of functional groups in BTAH molecule are observed and have been associated to the adsorption of the inhibitor and bond formation with copper atoms [83], [139]. The interaction between the electrons in copper and those in the organic compound can also generate peak broadening in the observed peaks in the Raman spectrum [23].

Table 2. 10: Main Raman bands for the complex Cu-BTA compared to those of pure BTAH.

Benzotriazole	Cu-BTA (this study)	Assignment
235 [136]	120	Cu-N ?
538 [136]	151	Cu-N ?
631 [137] , 628 [136]	636	Triazole ring torsion
779 [137], [137], **783** [61]	**792**	**(Shifted) Benzene ring breathing**
1008 [136],1009 [61]	918	Benzene skeletal bending
1020 [136],1017 [137], 1027 [61]	992	In plane ring breathing
1049 [68]	1040	Ring stretching
1095 [68], [136]	**-**	**NH bending in plane**
1128 [163], 1125 [61]	1128	CH bending in plane
1145 [136]	1146	CH bending in plane
1208 [136]	1220	Triazole ring stretching + NH bending
1278 [136]	1294	Combination band (skeletal stetching +
1278 [136]		Combination band (CH in plane bending + CC stretching)
1370 [136]	1374	Fermi resonance with 1386 cm^{-1} band
1385 [136], **1388** [137], **1387** [61]	**1395**	**(Shifted) Triazole ring stretching [17], benzene skeletal stretching + CH bending in plane [16]**
1498 [136]	**1445**	
1594 [68], 1595 [61]	1490	Skeletal stretch
	1570	(Shifted) C-C stretching
3078 [61]	3060	Aromatic CH stretching

Benzotriazole-5-carboxylic acid

Raman spectrum of reference 5CBT is reported in Figure 2.20. For this compound, no reference was found in the literature to determine the assignment of bands, although some similarities can be found with BTAH.

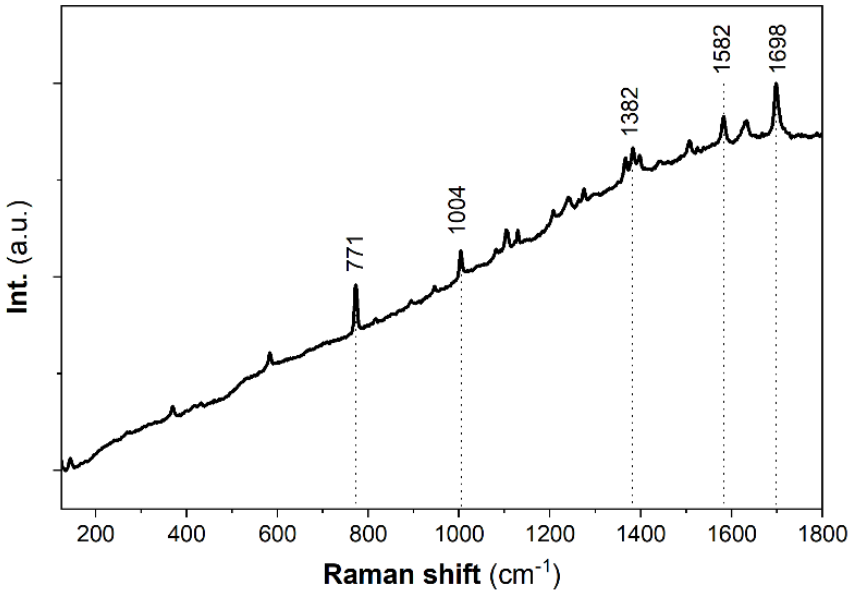

Figure 2. 20: Raman reference spectrum of pure 5CBT. The spectrum is characterized by high fluorescence.

Cu-5CBT complex

As for 5CBT, no reference has been found in the literature for this compound; the spectrum obtained is shown in Figure 2.21 and the main Raman shifts are compared to those of the pure inhibitor in Table 2.11.

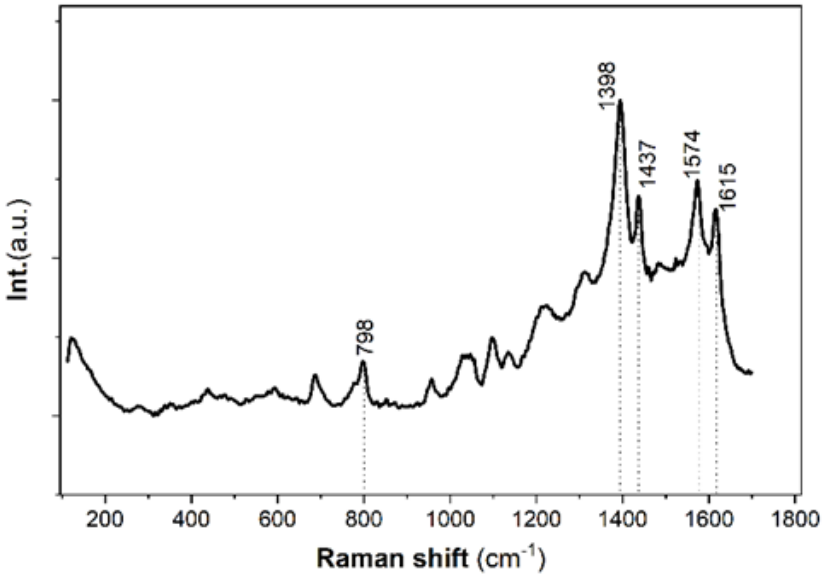

Figure 2. 21: Raman reference spectrum of Cu-5CBT.

Table 2. 11 : Main Raman bands for pure 5CBT and those of the supposed Cu-5CBT.

5CBT	Cu-5CBT
144	
370	434
582	
771	**798**
1007	956
1004	**1027, 1038, 1047**
1081	1096
1104	
1129	1136
1207	1212
1241	1222
1264	
1275	1311
1367	
1382	**1398**
	1437
1506	
1582	**1574**
1633	1615
1698 (C=O stretching)	

Decanoic acid

Figure 2.22 shows the Raman spectrum of reference decanoic acid; in Table 2.12, the main band and their assignment based on [141] are reported.

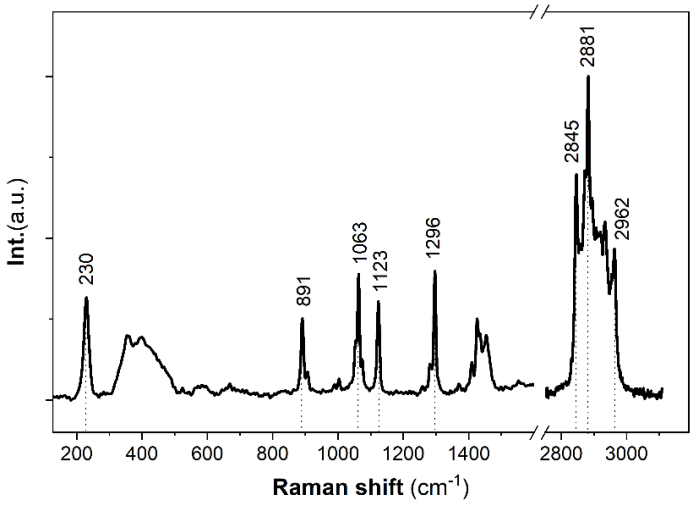

Figure 2. 22: Raman reference spectrum of pure HC10.

Table 2. 12: Main Raman bands for pure HC10 and bands assignment. Reference frequencies are reported from [141].

Decanoic acid	Decanoic acid (this study)	Assignment
	230	
	355	
488	400	
893	**891**	**CH bending in plane + C-C stretching**
908	907	
1065	1063	C-C stretching + C-C-C bending
1075		
1126	1123	
1299	**1296**	**CH bending in plane**
	1410	
	1426	
	1434	**CH bending in plane**
	1454	
1640		
	2845	CH symmetric stretching
	2872	
	2881	**CH asymmetric stretching**
	2893	
	2906	
	2939	
	2954	
	2962	

Copper decanoate

Spectrum of synthetic copper decanoate is presented in Figure 2.23 and main shifts are listed in Table 2.13 and compared to those of the acid.

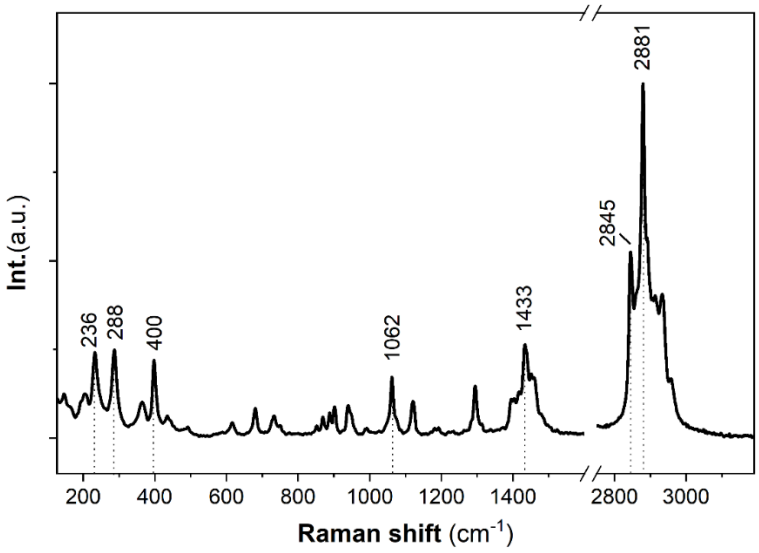

Figure 2. 23: Raman spectrum of copper decanoate.

Table 2. 13: Main Raman bands for copper decanoate (CuC10) compared to decanoic acid.

Decanoic acid (this study)	Copper decanoate	Assignment
230	234	
	288	Cu-O stretching
355	356	
400	400	
891	**850, 868, 888, 903**	**CH bending in plane + C-C stretching**
907	941	
1063	1062	C-C stretching + C-C-C bending
1123	1122	
1296	**1294**	**CH bending in plane**
1410	1397	
1426	1418	
1434	1433	**CH bending in plane**
1454	1450	
2845	2843	CH symmetric stretching
2872		
2881	**2881**	**CH asymmetric stretching**
2893		
2906	2915	
2939	2933	
2954		
2962	2960	

3.9 TEM

3.9.1 Technique overview

Morphology, crystal structure and elemental composition at the nanometric level of the modified mineral phases are studied by Transmission electron microscopy (TEM) and Scanning Transmission Electron Microscopy (STEM). In TEM microscopy, a high energy electron beam illuminates the specimen: part of the electrons is transmitted through the sample and an objective lens will form the image of the sample that is projected on the detector. The image contrast is given by thickness and electron transparency of the sample. In STEM microscopy, the beam is focused on the sample it scans the area of interest. The intensity of the transmitted beam is recorded with different detectors to form the image.

Selected area electron diffraction (SAED) can also be performed using a principle similar to XRD, although here the incident beam is constituted by electrons. In a crystalline solid, part of the electrons is scattered by the atoms to specific angles based on the structure of the material: these electrons will then form a diffraction pattern.

In general, the technique requires thin sections (<100 nm) or good dispersed powdery samples as the material has to be transparent to, at least, part of the electrons.

3.9.2 Operational mode

TEM analysis has been performed at the ICMPE laboratory (UPEC) in Thiais. Powdered samples preparation includes a first ethanol dispersion in ultrasonic bath and successive deposition of a drop of the dispersed phase on top of a C-coated molybdenum grid and let dry.

Observations are carried out on a FEG Tecnai F20 microscope equipped with an EDAX Octane T Optima EDS-SDD detector using an acceleration voltage of 200 keV. The electron beam is produced by an emission field gun and the polar pieces allow to obtain high resolution images. Micrographs are acquired via the Digital Micrograph software from Gatan while EDS analysis are acquired and processed using the EDAX Team® software.

Electron diffraction (SAED) is also performed in order to identify crystalline phase and/or reveal the amorphous nature of the powdery samples.

3.10 Tof-SIMS

3.10.1 Technique overview

Time-of-flight Secondary Ion Mass Spectrometry (Tof-SIMS) is a technique that allows the detection of elemental and molecular ions with a high sensitivity (in the order of the ppm to ppb). Despite being a surface characterization technique as only the first nanometres of the sample are investigated, it has been used to the study of the samples' cross-section (previously prepared as described in paragraph 2.4.3).

In particular, the technique has been employed to detected deuterium within the corrosion layer after immersion in deuterated water.

3.10.2 Operational mode

Analysis have been performed at the Surface Analysis platform of the Lille University of Villeneuve d'Ascq. The apparatus used is a TOF.SIMS 5 from IONTOF. Acquisition and data treatment are done using the dedicated Surface Lab 7.0® software. The first step consists in surface sputtering by Cs^+ ion beam for 5 to 10 minutes. The ions are accelerated using a voltage of 2 keV at a current of 130 nA; this operation is carried out on a large area of 500x500 μm^2 in order to clear the surface from any contamination. Within this area, a smaller (90x90 μm^2) region of interest (ROI) is selected. Primary ion beam used for analysis is a Bi^+ with an acceleration voltage of 25 keV which scans the surface with short pulses (1ns). For each sample, 3 regions of interest including the whole corrosion layer are analysed. Each ROI has a resolution of 256x256 pixels and between 300 and 1000 scans are recorded in order to have statistically representative data. After each scan of Bi^+, a cleaning (1s) of the surface using the Cs^+ ion beam is performed (non-interlaced mode).

The samples after treatment and those after outdoor exposure are analysed in two different periods.

3.10.2 Data treatment

The differences in the corrosion layer composition allows to separate the outer and inner layer: in particular, an overlay of the two fragments of S^- (characteristic of the presence of brochantite) and CuO^- (for cuprite) is used to create two different regions of interest within the corrosion layer (Figure 2.24).

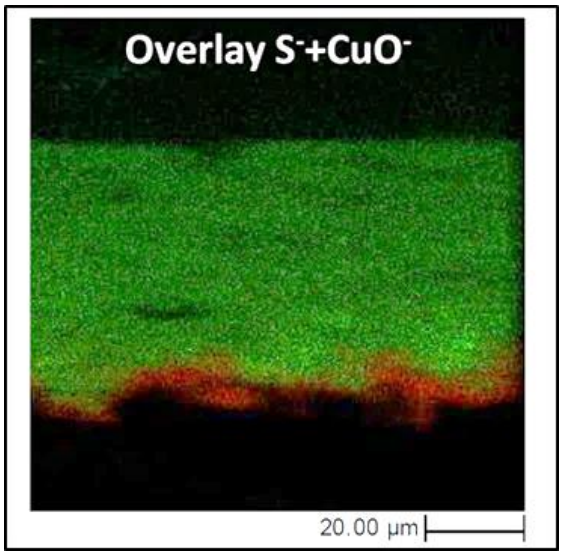

Figure 2. 24: Image resulting from the overlay of the S-rich (in green) and CuO-rich (in red) fragments areas.

A choice has been made not to calculate the deuterium enrichment based on hydrogen as the enrichment generally expressed as D/H is not comparable when analysing different materials, characterized by different hydrogen content. This is the case of the corrosion layer treated with the inhibitors as the interaction gives rise to a different substrate and data are difficult to compare. The ratio D/Cu is therefore privileged as copper is supposed to remain stable even after treatment.

Within the two regions, the intensity of the two fragments D^- and Cu^- is extracted from the mass spectrum and the ratio D/Cu is calculated for both the untreated and the treated samples. The enrichment in deuterium is calculated as in Equation 7:

$$\delta_{\left(\frac{D}{Cu}\right)} = \left(\frac{\left(\frac{D}{Cu}\right)_{imm}}{\left(\frac{D}{Cu}\right)_{notimm}} - 1 \right) \cdot 100 \qquad (7)$$

Where $\left(\frac{D}{Cu}\right)_{imm}$ represents the deuterium enrichment calculated for the immersed sample and $\left(\frac{D}{Cu}\right)_{notimm}$ the enrichment in the not immersed sample.

Finally, the enrichment value is normalized to the S/Cu ratio (R_b) in brochantite (Equation 9) and to the ^{18}O/Cu ratio in cuprite (R_c) (Equation 10).

$$R_b = \left(\frac{\left(\frac{S}{Cu}\right)_{imm}}{\left(\frac{S}{Cu}\right)_{ni}}\right) \quad ; \quad R_c = \left(\frac{\left(\frac{^{18}O}{Cu}\right)_{imm}}{\left(\frac{^{18}O}{Cu}\right)_{ni}}\right) \tag{8}$$

$$\delta_n = R_b \cdot \delta_{\left(\frac{D}{Cu}\right)} \tag{9}$$

$$\delta_n = R_c \cdot \delta_{\left(\frac{D}{Cu}\right)} \tag{10}$$

The calculation of the error (σ) was calculated as follows:

$$\sigma\,(\boldsymbol{D}) = \sqrt{\frac{N \cdot D}{N - D}} \tag{11}$$

$$\sigma\left(\frac{\boldsymbol{D}}{\boldsymbol{Cu}}\right) = \left(\frac{D}{Cu}\right) \cdot \sqrt{\left(\frac{\sigma(Cu)}{Cu}\right)^2 + \left(\frac{\sigma(D)}{D}\right)^2} \tag{12}$$

$$\sigma\boldsymbol{\delta}_{\left(\frac{\boldsymbol{D}}{\boldsymbol{Cu}}\right)} = \delta_{\left(\frac{D}{Cu}\right)} \cdot \sqrt{\left(\frac{\sigma(Cu)}{Cu}\right)_{imm}^{2} + \left(\frac{\sigma(D)}{D}\right)_{imm}^{2} + \left(\frac{\sigma(Cu)}{Cu}\right)_{ni}^{2} + \left(\frac{\sigma(D)}{D}\right)_{ni}^{2}} \tag{13}$$

$$\sigma\,(\boldsymbol{\delta_N}) = \boldsymbol{\delta}_{\left(\frac{\boldsymbol{D}}{\boldsymbol{Cu}}\right)} \cdot \sigma(\boldsymbol{R}) + \boldsymbol{R} \cdot \sigma\boldsymbol{\delta}_{\left(\frac{\boldsymbol{D}}{\boldsymbol{Cu}}\right)} \tag{14}$$

Results

Results

In the next chapter, the results collected from the experimental part are presented. The first part is dedicated to the results obtained by reacting the synthetic minerals, cuprite and brochantite, with the inhibitors' solution. In the second part, the natural corrosion layer is investigated without treatment, after treatment and after outdoor exposure.

1. Investigating the inhibitor-mineral reactivity from the global to the nanoscale

In this first part of the results, the interaction between each organic compound and the two mineral phases, cuprite and brochantite, is investigated to better understand the reaction mechanism. Specifically, experiments in solution with a synthetic commercially available cuprite and brochantite synthetized in the laboratory have been conducted. During each experiment, the evolution of pH has been measured at intervals of 3 minutes in the first 2 hours and pH after 24 hours is also recorded. During the reaction and after 24 hours, part of the insoluble precipitate has been separated from the liquid phase and further investigated to understand morphological and structural modifications.

The three organic compounds are presented separately and, for each inhibitor, results concerning the reactivity with cuprite and brochantite are described. The final paragraph details the results of the experiments carried out on the 2-hour reacted brochantite in aggressive solution containing NaCl at different pH.

1.1 Reactions with benzotriazole

1.1.1 Reaction benzotriazole-cuprite: pH evolution and precipitate analysis

Figure 3.1 represents the evolution of pH as a function of time for the first 2 hours of reaction between a solution containing BTAH and the corresponding amount of cuprite added at time "0". The initial pH of pure BTAH solution is equal to 4.61 ± 0.11, comparable to the calculated pH for the 0.08 M BTAH solution (4.7) using pKa equal to 8.4. The graph shows a stable pH over the whole-time interval. The pH after 24 hours is one pH unit lower and corresponds to 3.7.

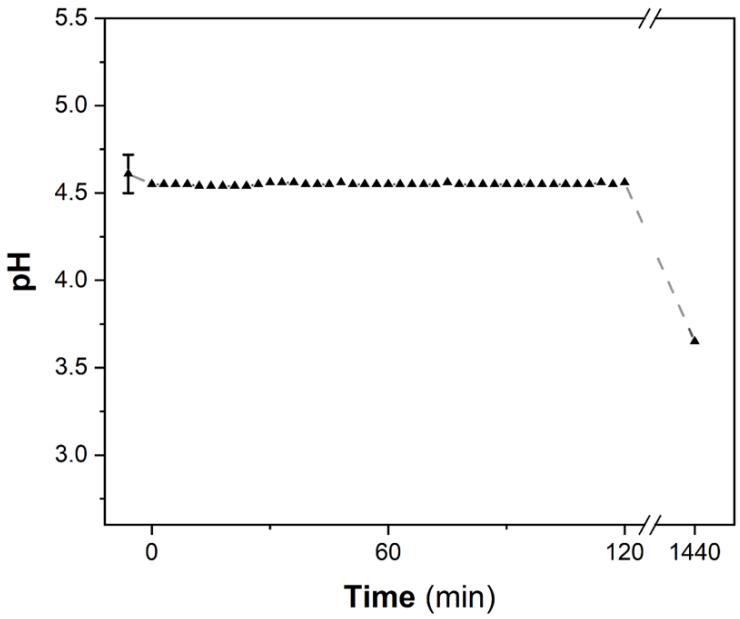

Figure 3. 1: pH evolution for the reaction between BTAH and cuprite. Cuprite is added at time=0 and pH is measured every 3 minutes.

The insoluble precipitate collected after 24 hours has a similar colour to unreacted cuprite (Figure 3.2).

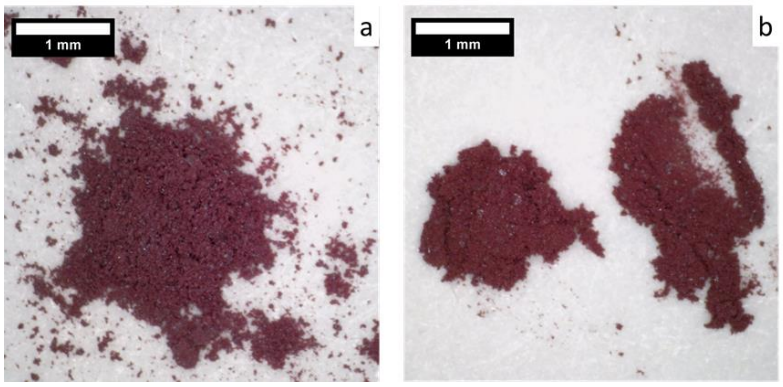

Figure 3. 2: Visual appearance of cuprite before (a) and after (b) immersion in BTAH solution for 24 hours.

When analysing the precipitate, at 2 and 24-hour reaction time, only cuprite is identified by XRD (Figure 3.3) and Raman analysis (Figure 3.4).

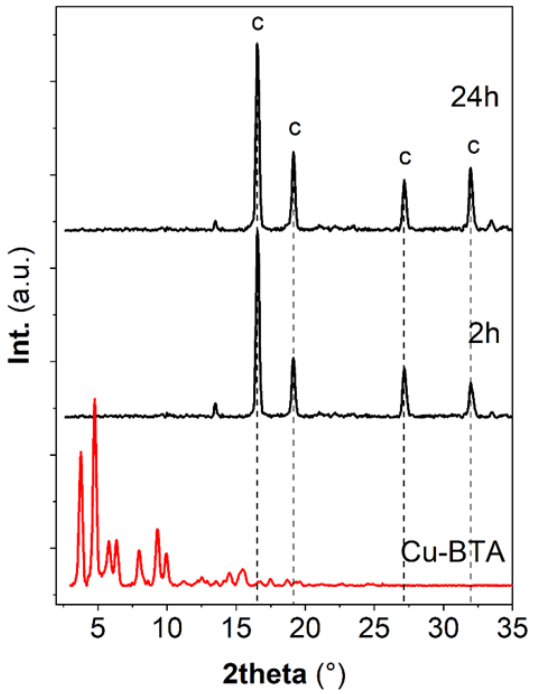

Figure 3. 3: Diffraction patterns obtained after 2- and 24-hours immersion of cuprite in BTAH solution. The red diffraction pattern corresponds to the reference Cu-BTA.

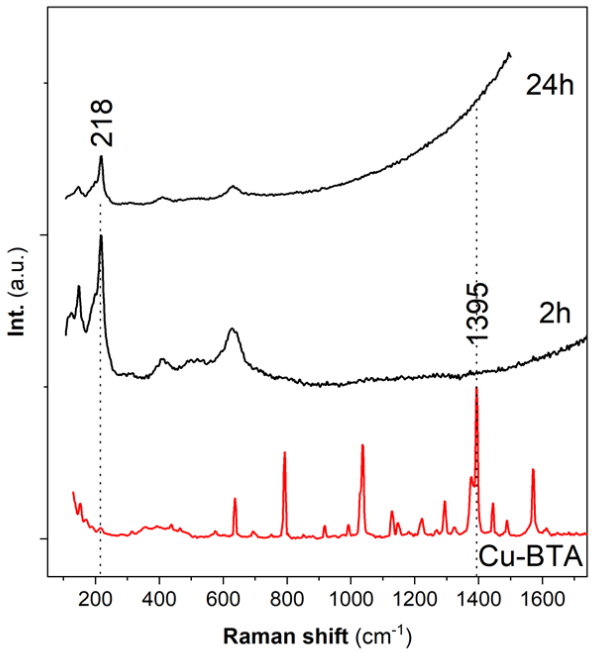

Figure 3. 4: Raman spectra after 2- and 24-hours immersion of cuprite in BTAH solution. The red spectrum corresponds to the reference Cu-BTA.

The nanometric scale analysis and, in particular, HR-TEM images collected on the 2-hours treated cuprite powder show the presence of large grains characterized by crystalline planes with a measured interplanar distance of 2.5 Å, corresponding to cuprite. In addition, a thin layer on the outer surface of the grains is present and, in the layer, no crystalline planes are observed (Figure 3.5), suggesting that the layer is amorphous.

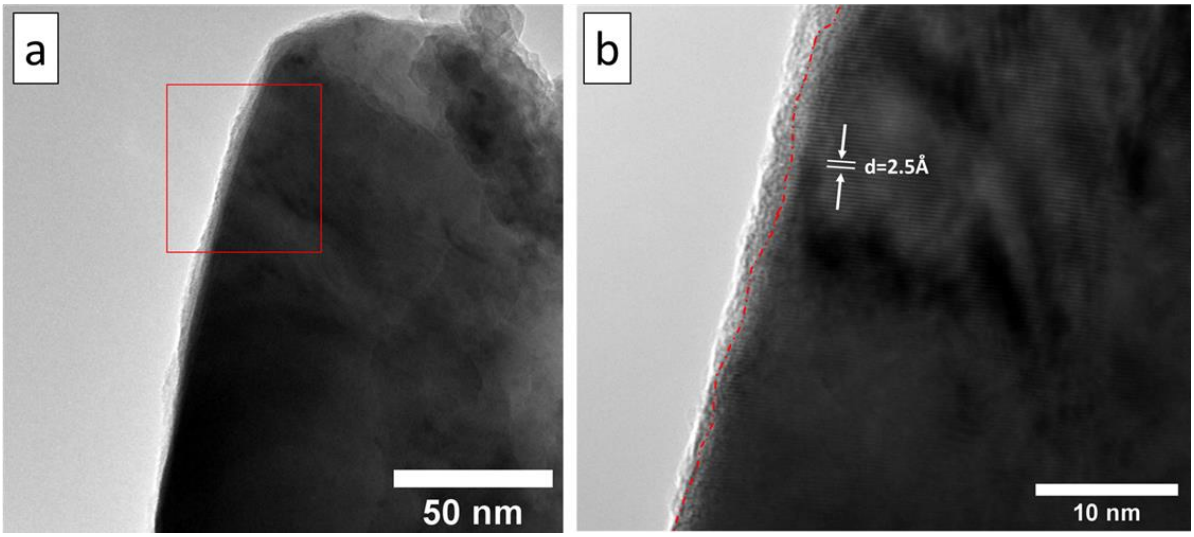

Figure 3. 5: HR-TEM images of a 2-hour treated cuprite grain after BTAH treatment. Image (b) is obtained by zooming on the area highlighted in red on image (a).

The thickness of the outer layer corresponds to 3 ± 2 nm[15]. A similar morphology is observed on the 24-hours treated cuprite. The average measured thickness is higher, although characterized by an important variability (15 ± 14 nm), indicating a certain inhomogeneity of the layer thickness.

1.1.2 Reaction benzotriazole-brochantite: pH evolution and precipitate analysis

When evaluating the evolution of pH with brochantite as a reactant (Figure 3.6), the situation is different compared to cuprite. Again, the initial pH of the solution, corresponding to 4.86 ± 0.02, is measured before adding the solid brochantite (at time "0" in the graph). In the minutes immediately following the addition of brochantite, a drastic drop in pH is registered. The drop is followed by a rapid stabilization of the pH value that, after 20 minutes is equal to 2.5 and remains constant from 20 minutes until the end of the experiment with a pH of 2.48 measured after 24 hours.

[15] The thickness is evaluated by measuring the distance between the grain and the amorphous layer using the software ImageJ. Average values are calculated on 50 measurements taken on several particles.

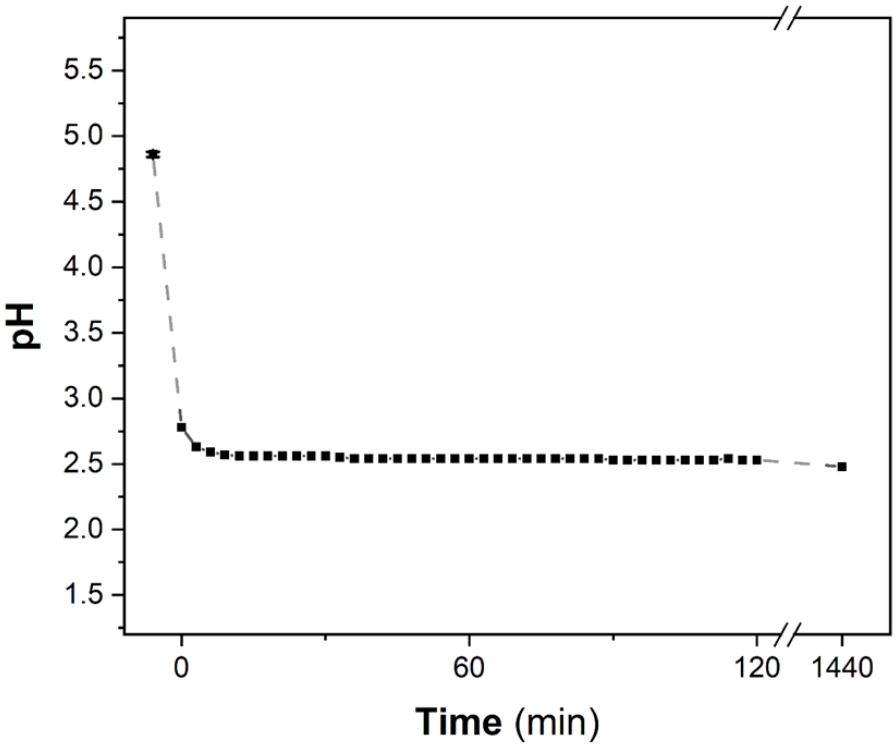

Figure 3. 6: pH evolution over 24 hours for the reaction between BTAH and brochantite. Brochantite is added at time=0 and pH is measured every 3 minutes.

The precipitate collected after 24 hours, is of a dark green colour (Figure 3.7).

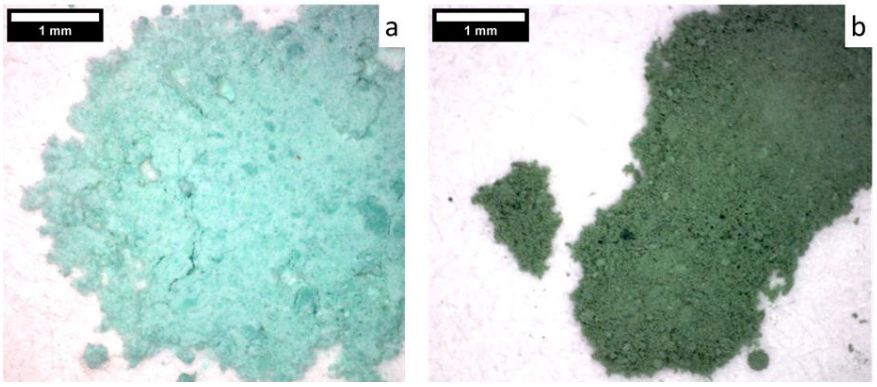

Figure 3. 7: Visual appearance of brochantite before (a) and after (b) immersion in BTAH solution for 24 hours.

The diffraction patterns obtained on the precipitate after 2 and 24 hours (Figure 3.8 a) present the characteristic peaks of brochantite as main feature. Additionally, a broad hump at low angle (2θ=3.4°) is observed at low angles (Figure 3.8 b).

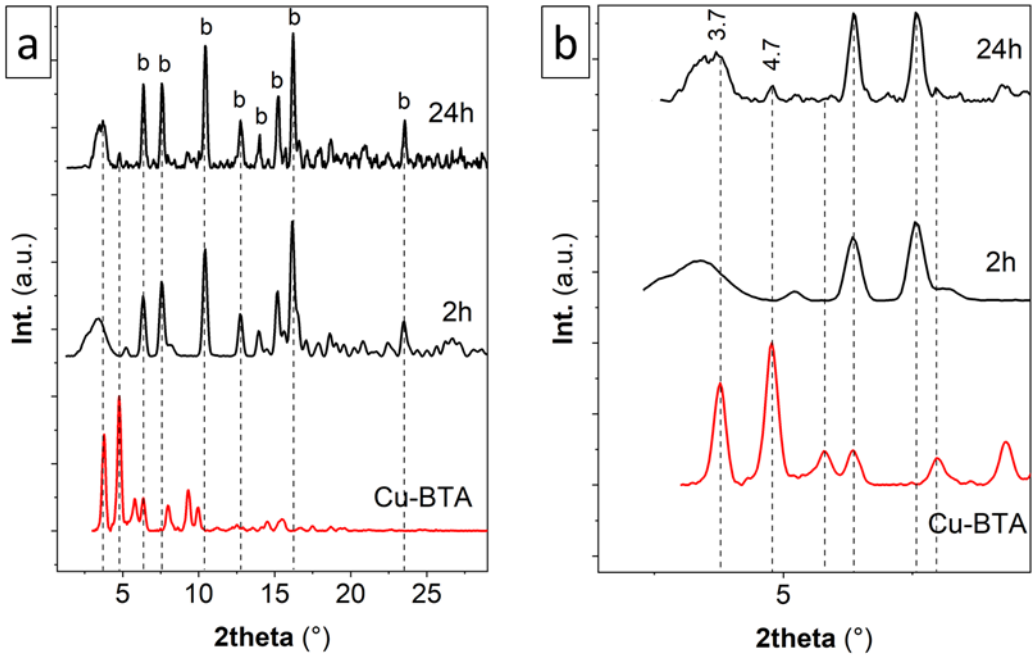

Figure 3. 8: (a) Diffraction pattern obtained for the precipitate after 2 hours and 24 hours reaction. Brochantite is detected and indicated by a 'b'. The XRD of Cu-BTA is also reported. (b) Zoomed pattern at low angles.

The comparison with the diffraction pattern of the reference Cu-BTA suggests that the hump observed after 2 hours reaction, does not precisely correspond to the two intense bands at 2θ corresponding to 3.7° and 4.7°. The presence of broad humps at low angles in the diffraction pattern is usually associated to the presence of poorly crystalline polymeric materials. After 24 hours, the two bands at 3.7° and 4.7° are present, although at a low intensity together with the large hump at 3.4°. This suggests that together with the amorphous material, some crystalline Cu-BTA has formed.

The analysis by Raman spectroscopy (Figure 3.9) again confirms the presence of brochantite thanks to the Raman shift at 973 cm^{-1}. The peak is present but at a lower intensity after 24 hours. Additionally, the shifts previously related to the formation of a Cu-BTA complex, and, in particular, the strong peak at 1395 cm^{-1} are identified. In this case, the peaks corresponding to the complex after 2 hours reaction are broader compared to the reference, while after 24 hours they are narrower. This confirms the results obtained from XRD after 24 hours.

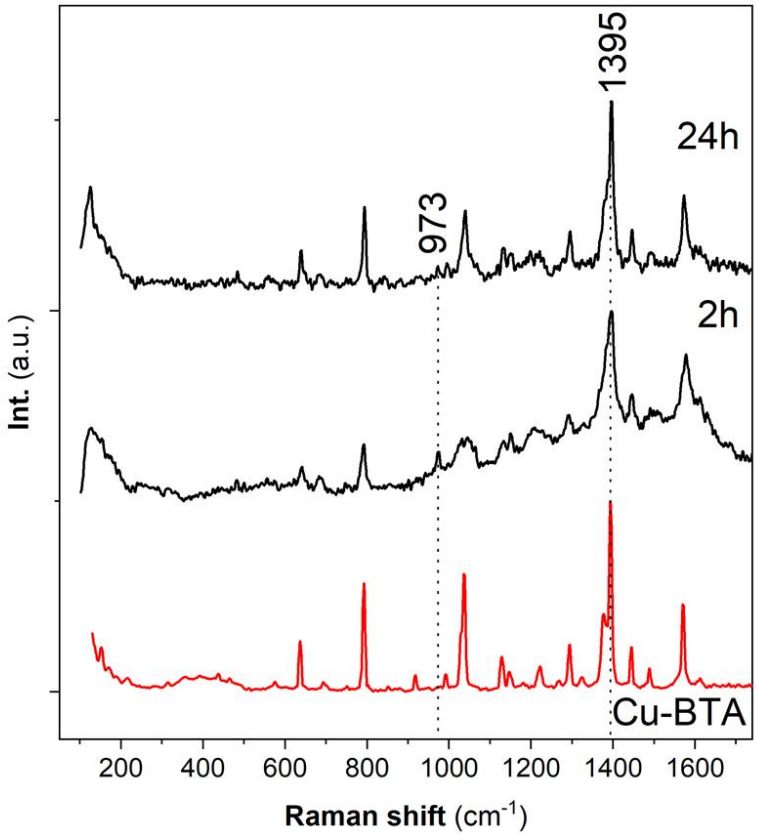

Figure 3. 9: Raman spectra of the precipitate after 2 and 24 hours of reaction. The reference spectrum of Cu-BTAH is reported and the main shifts allowing brochantite and Cu-BTA identification are reported.

At the microscopic scale, the results presented up to now evidence that an interaction of brochantite with the inhibitor-containing solution has occurred leading to a partial transformation of brochantite into an amorphous or, after 24 hours, partly crystalline Cu-BTA complex.

The TEM analysis allows to better understand these results. When observing the precipitate formed after 2 hours under the electron microscope, a specific morphology is found: brochantite grains (crystalline) are covered by an external layer, which amorphous nature is confirmed by SAED analysis as no diffraction spots are detected (Figure 3.10).

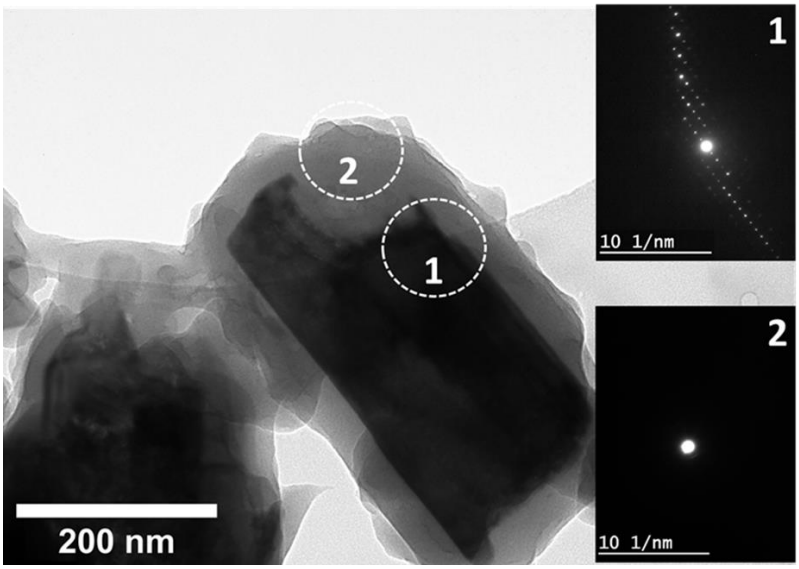

Figure 3. 10: HR-TEM image of a particle showing the core-shell structure. SAED diffraction results are included for the inner crystalline core (1) and the outer amorphous layer (2).

Figure 3.11 represents the TEM-EDS results performed on one particle.

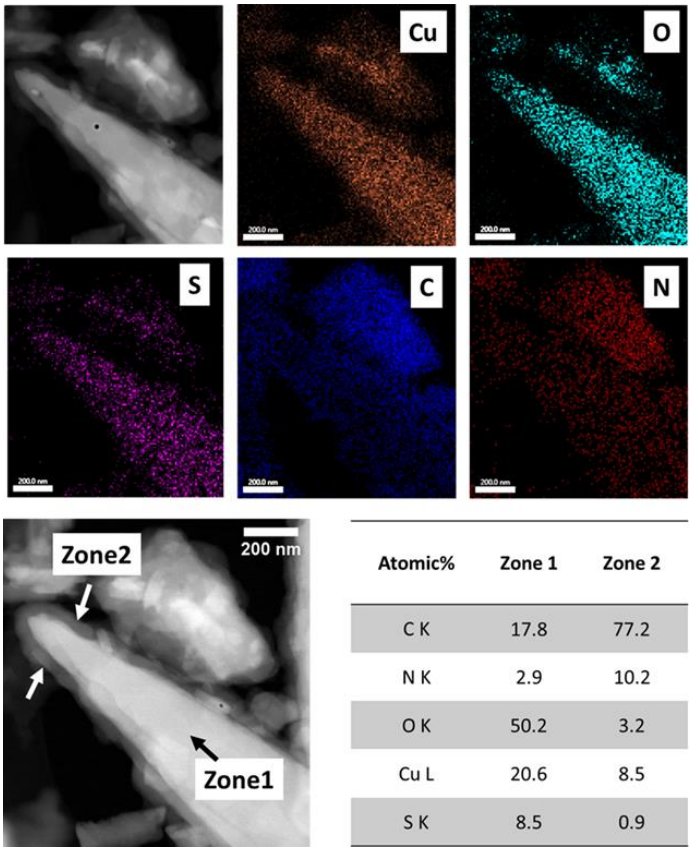

Atomic%	Zone 1	Zone 2
C K	17.8	77.2
N K	2.9	10.2
O K	50.2	3.2
Cu L	20.6	8.5
S K	8.5	0.9

Figure 3. 11: Elemental mapping performed on one particle showing the characteristic core-shell structure. Atomic % obtained at the inner (Zone 1) and outer (Zone 2) layer are reported in the table.

The image shows that the external layer is rich in nitrogen and carbon (Zone 2), while the internal part of the particle is rich in sulphur and oxygen (Zone 1). In Zone 1, the calculated atomic ratio O/Cu, equal to 2.5 in brochantite, well correspond to the ratio calculated for this area and corresponding to 2.4.

It can be assumed that the external nanometric layer corresponds to the Cu-BTA complex previously detected on the precipitate by μRaman spectroscopy and that the mineral and the newly formed phase give a core-shell structure, similar to the one observed for cuprite.

HR-TEM images of the particles allow to measure the layer thickness after different reaction intervals: measurements are reported in Table 3.1.

Table 3. 1: Mean thickness of the outer amorphous layer. Results are an average on 60 measurements on several particles observed by TEM.

Reaction time (h)	Thickness Cu-BTA (nm)
0.5	16 ± 6
2	29 ± 14
3	27 ± 12
6	40 ± 17
9	43 ± 20
12	47 ± 26
18	52 ± 22
24	59 ± 22

After 24 hours, only few particles analysed retain the core-shell structure, while for the majority we observe elongated amorphous structures (Figure 3.12).

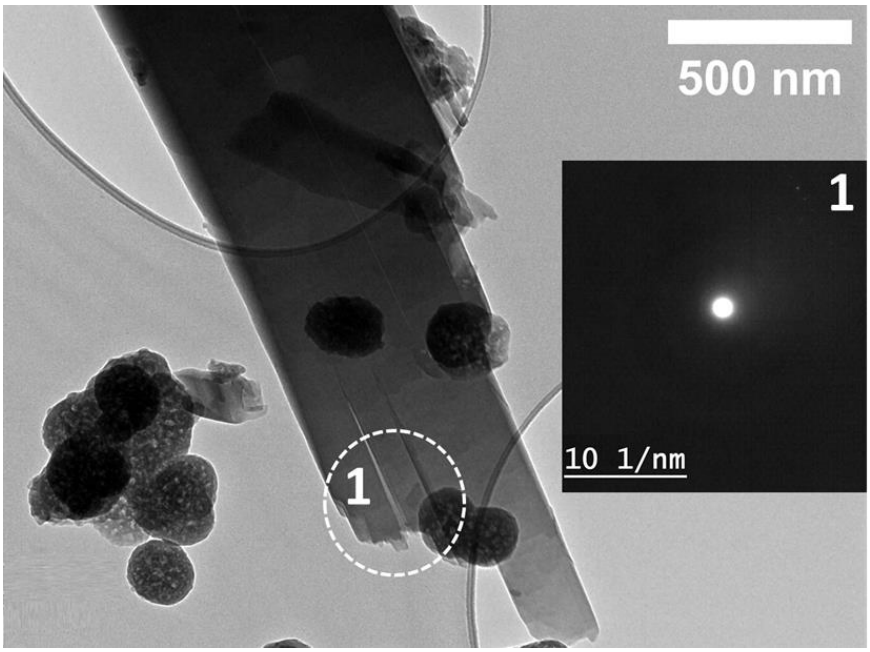

Figure 3. 12: Typical morphology of particles observed after 24 hours immersion of brochantite in BTAH solution. The large, elongated particle is amorphous as shown by the SAED image (1).

1.1.3 Permeability of the amorphous layer

In order to understand the diffusion properties of the outer amorphous layer formed on brochantite, immersion in KBr solution lasted for a duration of 30 days, followed by the investigation of the layer after immersion again at the nanometric scale.

TEM-EDS analysis is performed on the solid phase after immersion. The results on a representative particle analysed by EDS are presented in Figure 3.13: the sulphur in violet highlights the presence of the inner-brochantite core surrounded by the amorphous outer layer rich in nitrogen and carbon. The superposed elemental maps of sulphur and bromine (in grey) and sulphur and nitrogen (in red) show that the external area (Zone 2), characterized by high N concentration, is also the one where Br is detected in higher concentration (6.2%wt.).

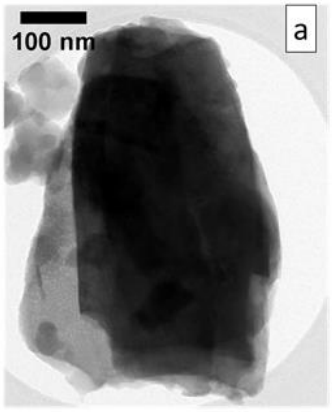

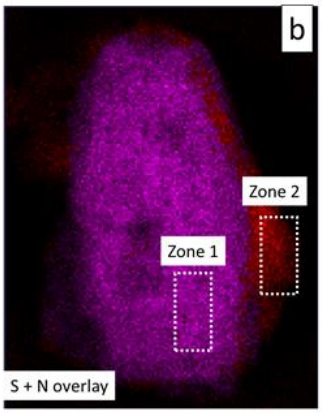

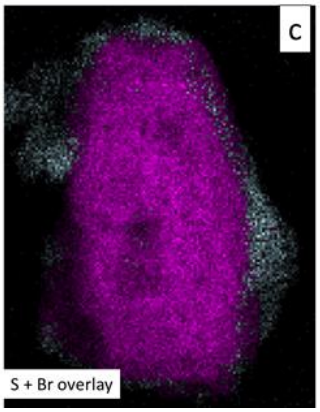

	Zone 1 %wt	Zone 2 %wt
C K	5.9	39.5
N K	2.7	11.8
O K	31	9.5
Br L	0.4	6.2
S K	5.8	0.6
Cu K	54	32.3

Figure 3. 13: Elemental mapping performed on one particle after immersion in KBr solution. The particle shows the characteristic core-shell structure. Weight % obtained at the inner (Zone 1) and outer (Zone 2) layer are reported in the table.

1.2 Reactions with benzotriazole-5-carboxylic acid

1.2.1 Reaction 5CBT-cuprite: pH evolution and precipitate analysis

The evolution of pH for the reaction between 5CBT solution and cuprite (Figure 3.14) is marked by an increase in pH in the first 10 minutes of the reaction: pH increases from 2.6 of the pure 5CBT solution to 3.3. For the next 2 hours, the pH remains constant and slightly decreases to 2.4 after 24 hours.

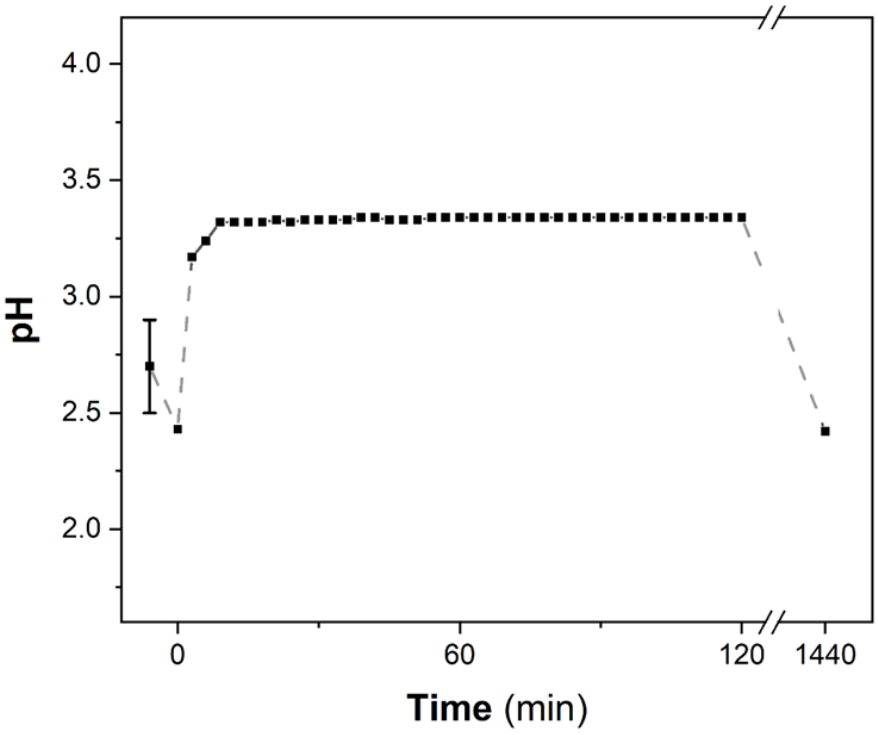

Figure 3. 14: pH evolution over 2 hours for the reaction between 5CBT and cuprite. Cuprite is added at time 0 and pH is measured every 3 minutes.

The precipitate after 24 hours appears visually unchanged compared to the cuprite (Figure 3.15).

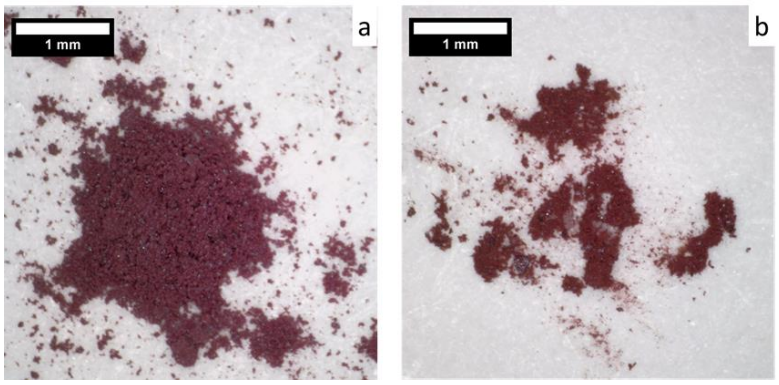

Figure 3. 15: Visual appearance of cuprite before (a) and after (b) immersion in 5CBT solution for 24 hours.

Cuprite is the only detected crystalline phase identified by XRD after 2 and 24 hours (Figure 3.16).

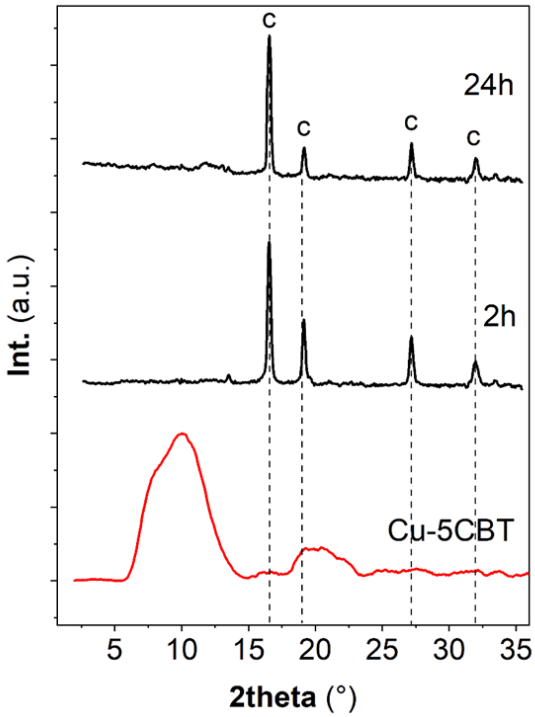

*Figure 3. 16: Diffraction pattern obtained for the precipitate after 2 hours and 24 hours reaction. Cuprite is detected and indicated by a '**c**'. The XRD of Cu-5CBT is reported (red trace).*

The Raman analysis (Figure 3.17) on one side confirms the presence of cuprite at both reaction time (main peak at 218 cm^{-1}) and, on the other, suggests the formation of a Cu-5CBT complex due to the broad peak at 1398 cm^{-1}.

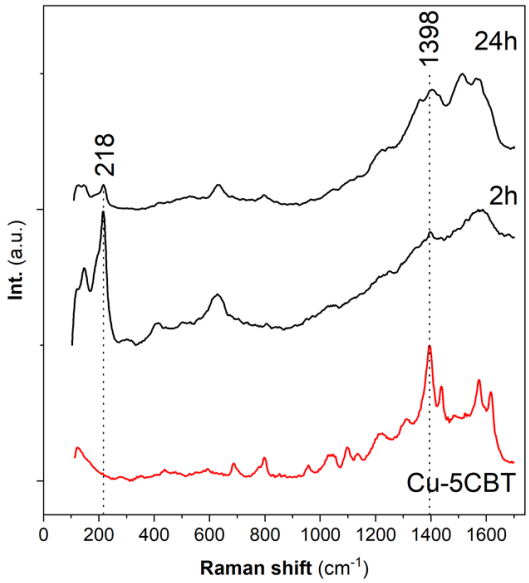

Figure 3. 17: Raman spectra after 2- and 24-hours immersion of cuprite in 5CBT solution. The red spectrum corresponds to the reference Cu-5CBT.

Again, to clarify the reactivity, analysis of the precipitate after 2 and 24 hours is performed at the nanoscale by TEM. Figure 3.18 shows part of the outer surface of a grain after 2-hour reaction.

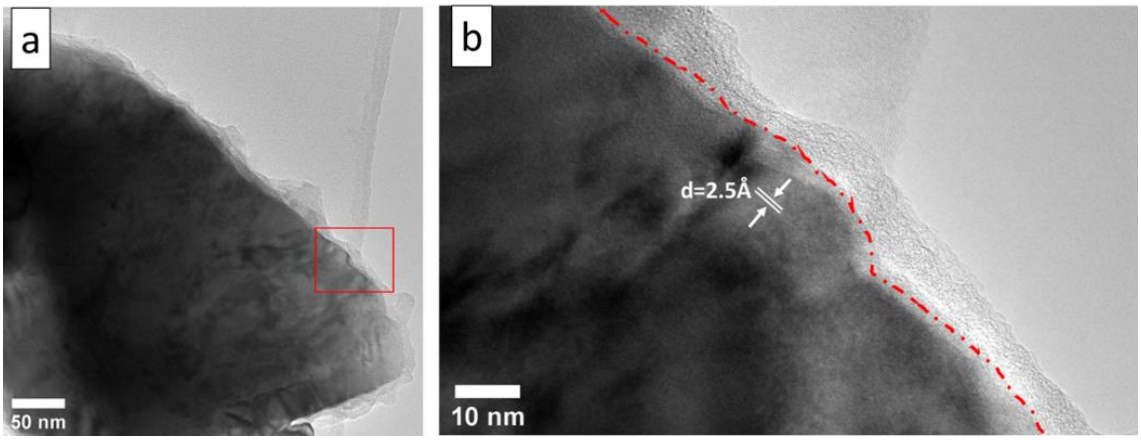

Figure 3. 18: HR-TEM images of a 2-hour treated cuprite grain after 5CBT treatment. Image (b) is obtained by magnifying the area highlighted in red on image (a).

The grain is characterized by crystalline planes with d=2.5 Å, confirming that they are constituted by cuprite. At the outer surface, crystalline planes are no more recognized, indicating the formation of an amorphous nanometric layer, which average thickness after 2 hours corresponds to 11 ± 9 nm.

After 24 hours, the outer layer is only slightly thicker (average thickness 14 ± 9 nm). In addition to the previously described core-shell structure, completely amorphous clusters are present in the powder after 24 hours reaction (Figure 3.19).

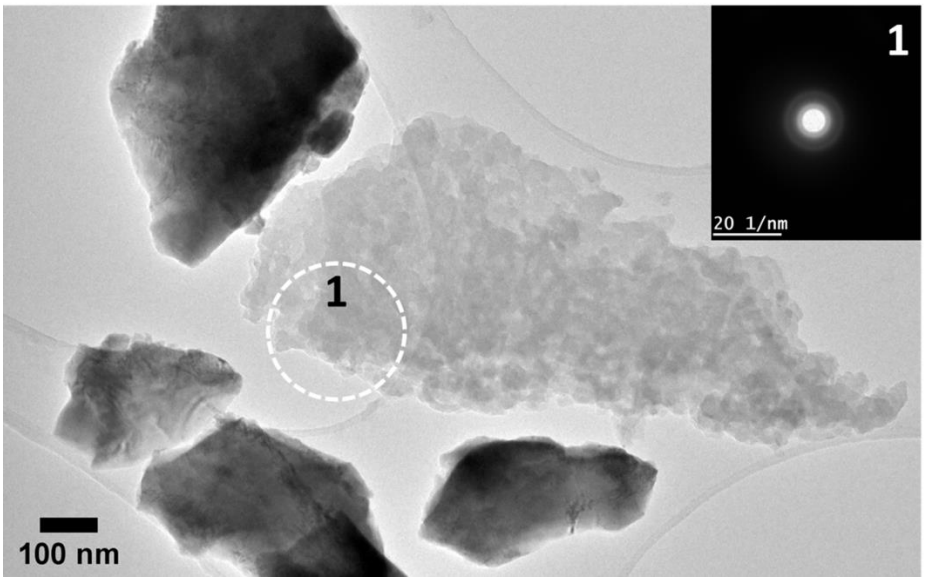

Figure 3. 19: HR-TEM images on the reaction product of cuprite immersion in 5CBT solution after 24 hours. Dark particles are cuprite grains while the lighter particle in the centre of the image is amorphous (1).

1.2.2 Reaction 5CBT-brochantite: pH evolution and precipitate analysis

When studying the reactivity of 5CBT with brochantite, the pH varies during the reaction time (Figure 3.20). First, a decrease from 2.5 to 2.3 is noticed as soon as brochantite is added to the solution. pH remains stable at this value for the next 30 minutes. Another pH variation, this time an increase of pH is detected between 30 and 80 minutes, after which pH reaches a stable value (2.9) between 80 and 120 minutes and the same value measured again at the end of the experiment (2.86).

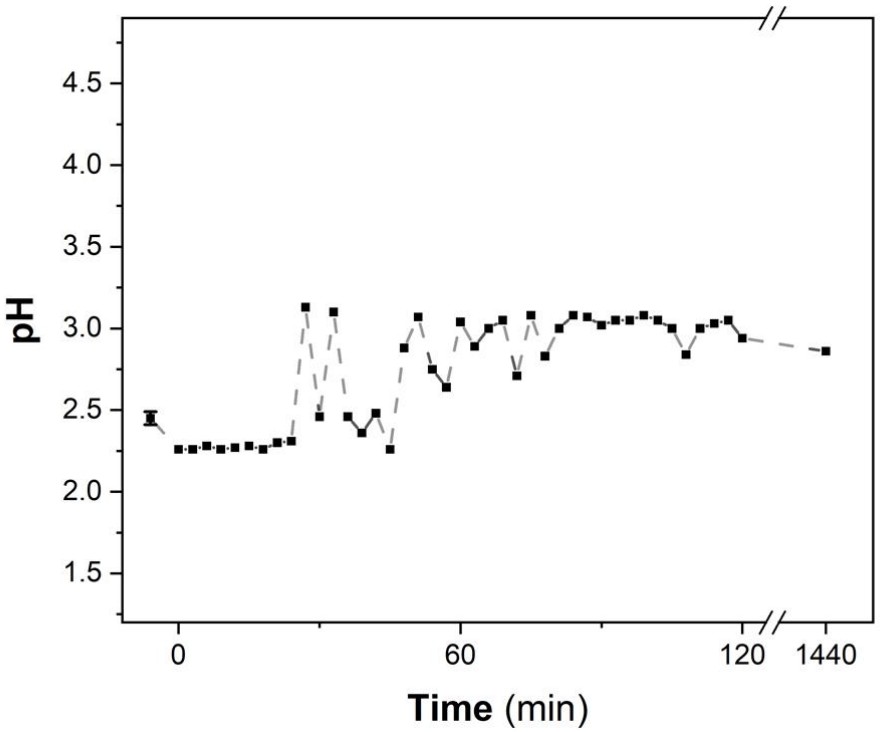

Figure 3. 20: pH evolution over 2 hours for the reaction between 5CBT and brochantite. Brochantite is added at time 0 and pH is measured every 3 minutes.

The compound separated from the solution after 24 hours appears dark green in colour (Figure 3.21).

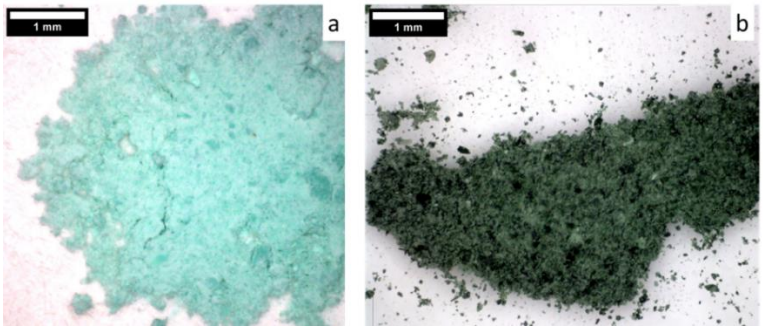

Figure 3. 21: Visual appearance of brochantite before (a) and after (b) immersion in 5CBT solution for 24 hours.

Brochantite is clearly identified by XRD analysis (Figure 3.22 a). The diffraction patterns of the precipitate obtained after 24 hours show the presence of a low-intensity broad hump at low angles (2θ=4.4°) that does not correspond to the reference Cu-5CBT compound (Figure 3.22 b).

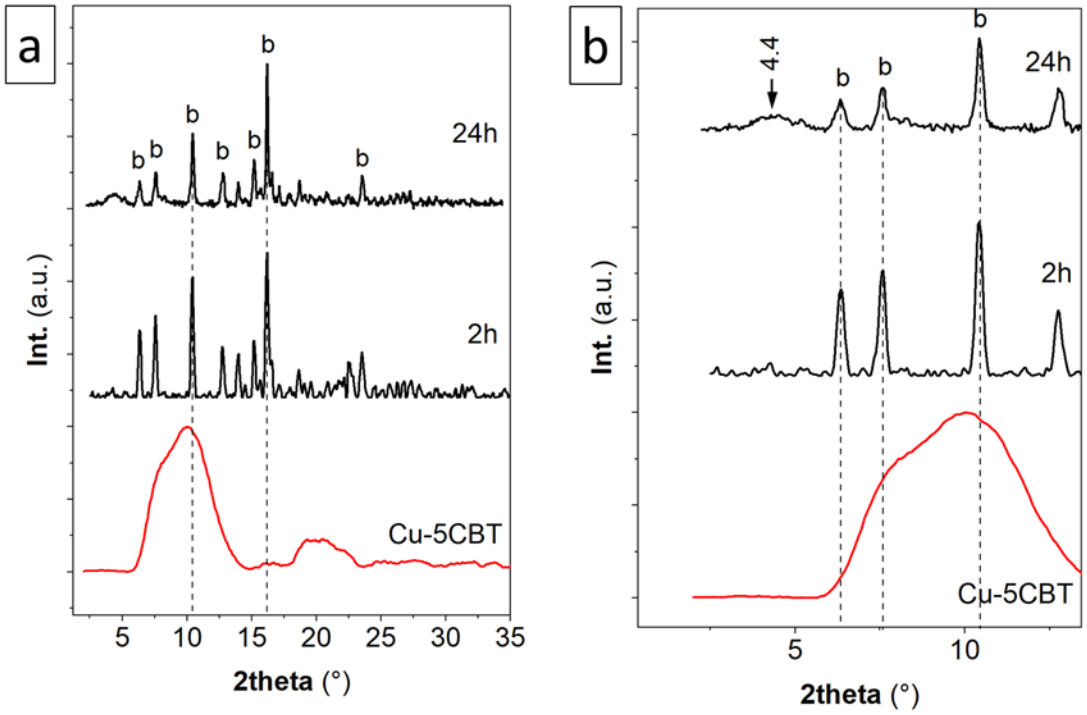

*Figure 3. 22: (a) Diffraction pattern obtained for the precipitate after 2 hours and 24 hours reaction in 5CBT solution. Brochantite is detected and indicated by a '**b**'. The XRD of Cu-5CBT is also reported. (b) Zoomed pattern at low angles.*

By Raman analysis, the characteristic shift corresponding to brochantite is again identified (Figure 3.23) together with the characteristic frequencies attributed to a Cu-5CBT complex, in particular the high-intensity peak at 1398 cm^{-1} is clearly detected after 2 and 24 hours. The peak is broader after 24 hours, while the otherwise intense peak of brochantite at 973 cm^{-1} exhibits a low intensity.

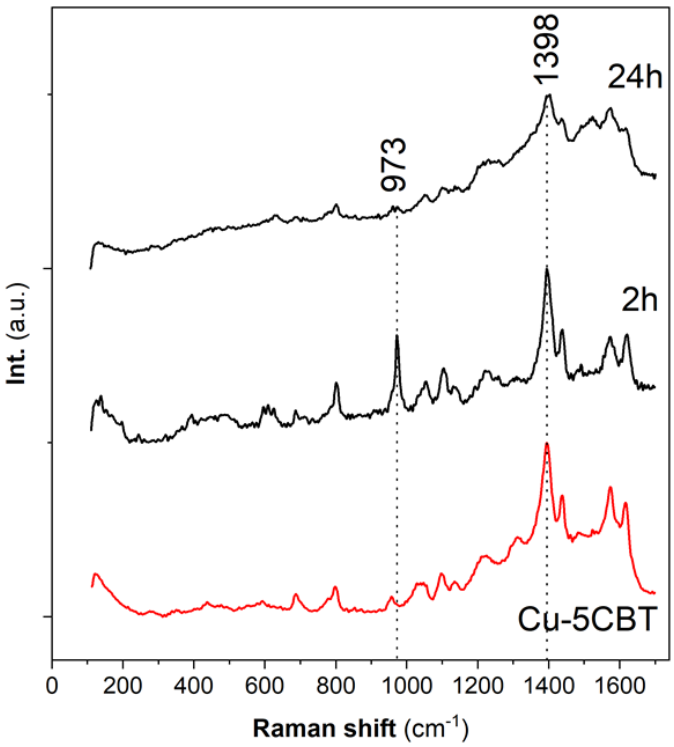

Figure 3. 23: Raman spectra of the precipitate after 2 and 24 hours of reaction. In red, the reference spectrum of Cu-5CBT is reported as well as main shifts allowing brochantite and Cu-5CBT identification.

TEM analysis using SAED diffraction is performed and a similar morphology compared to the BTAH-treated brochantite is identified. After 2 hours, crystalline particles are detected (Figure 3.24 Zone 1) surrounded by an amorphous layer (Figure 3.24 Zone 2).

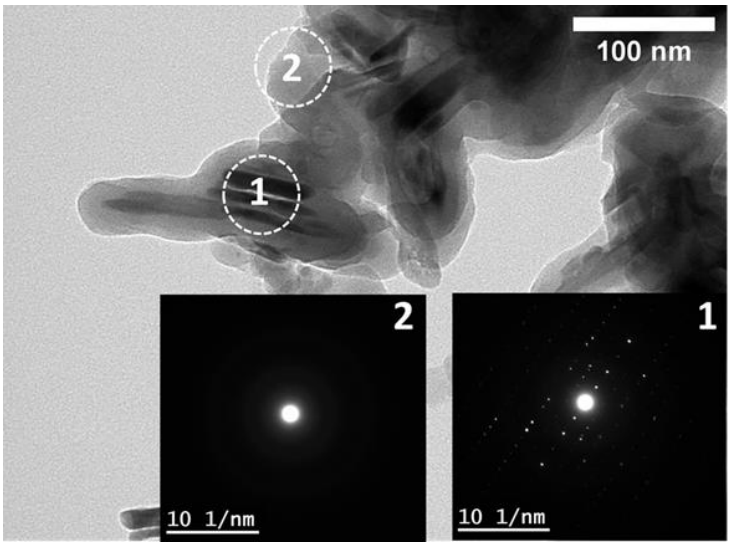

Figure 3. 24: HR-TEM image of a particle showing the core-shell structure. SAED diffraction results are included for the inner crystalline core (1) and the outer amorphous layer (2).

The outer amorphous layer is rich in nitrogen and carbon, while the internal part is rich in S, Cu and O with a O/Cu ratio equal to 2.5 and corresponding to the ratio present in the mineral brochantite: EDS analysis on a representative particle after 2 hours reaction is reported in Figure 3.25.

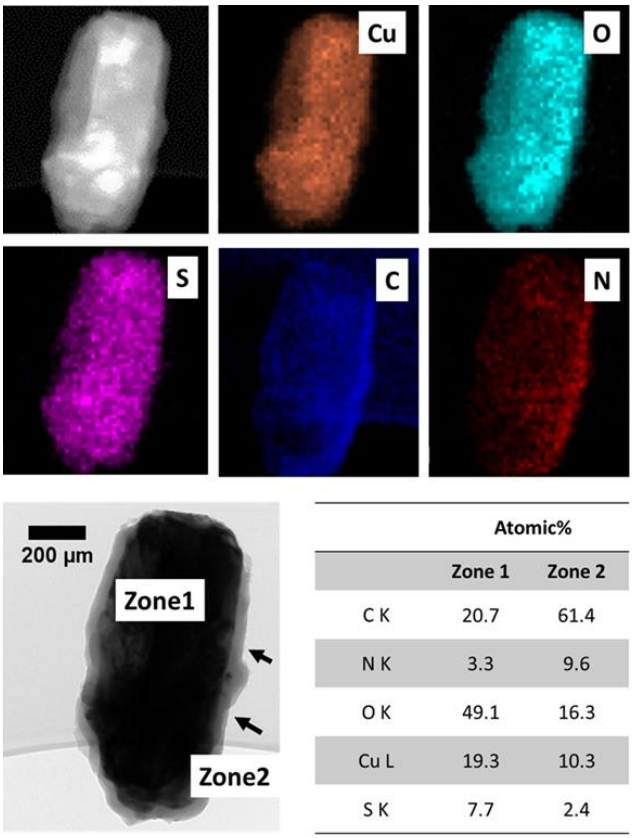

	Atomic%	
	Zone 1	Zone 2
C K	20.7	61.4
N K	3.3	9.6
O K	49.1	16.3
Cu L	19.3	10.3
S K	7.7	2.4

Figure 3. 25: Elemental mapping performed on one particle showing the characteristic core-shell structure after 2-hour reaction with 5CBT. Atomic % obtained at the inner (Zone 1) and outer (Zone 2) layer are reported in the table.

TEM imaging of the particles allows to measure the external layer thickness at different reaction intervals (Table 3.2).

Table 3. 2: Mean thickness of the outer amorphous layer. Results are an average on 60 measurements on several particles observed by TEM.

Reaction time (h)	Thickness Cu-5CBT (nm)
2	9 ± 4
3	11 ± 4
6	12 ± 4
12	16 ± 5
18	19 ± 7
24	23 ± 7

Thickness increases over time while, after 24 hours, the precipitate is mainly constituted by spherical amorphous particles (Figure 3.26).

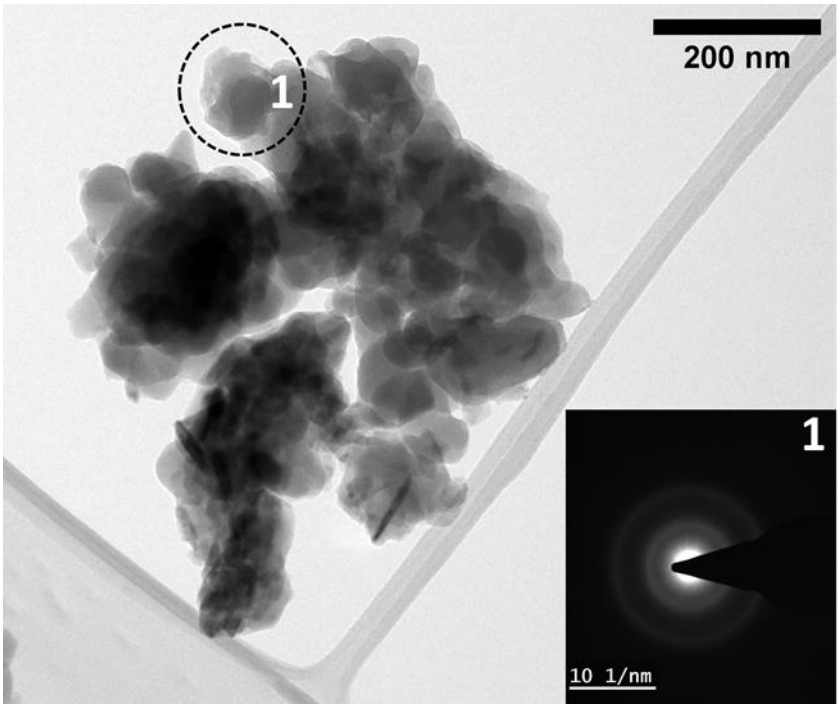

Figure 3. 26: Typical morphology of particles observed after 24 hours immersion of brochantite in 5CBT solution. A majority of amorphous particles is identified by electron diffraction (1).

1.3 Reactions with decanoic acid

The protocol used to analyse the precipitate when decanoic acid is used as reactant differs from the one previously employed. Here, nanoscale analysis by TEM was not feasible due to the solubility of the products in ethanol used for sample preparation. SEM analysis was therefore preferred, always coupled with bulk (XRD) and microscale vibrational spectroscopy (µRaman).

1.3.1 Reaction HC10-cuprite: pH evolution and precipitate analysis

The initial experimental pH of the decanoic acid solution is 2.62 ± 0.07, close to the calculated pH (2.8). Figure 3.27 shows the evolution of pH. pH increases as soon as the cuprite is added to the solution and keeps on augmenting for the first 20 minutes of the reaction. After this time, pH stabilizes at a value of 3.7 and, after 24 hours, the measured pH is slightly higher (3.9).

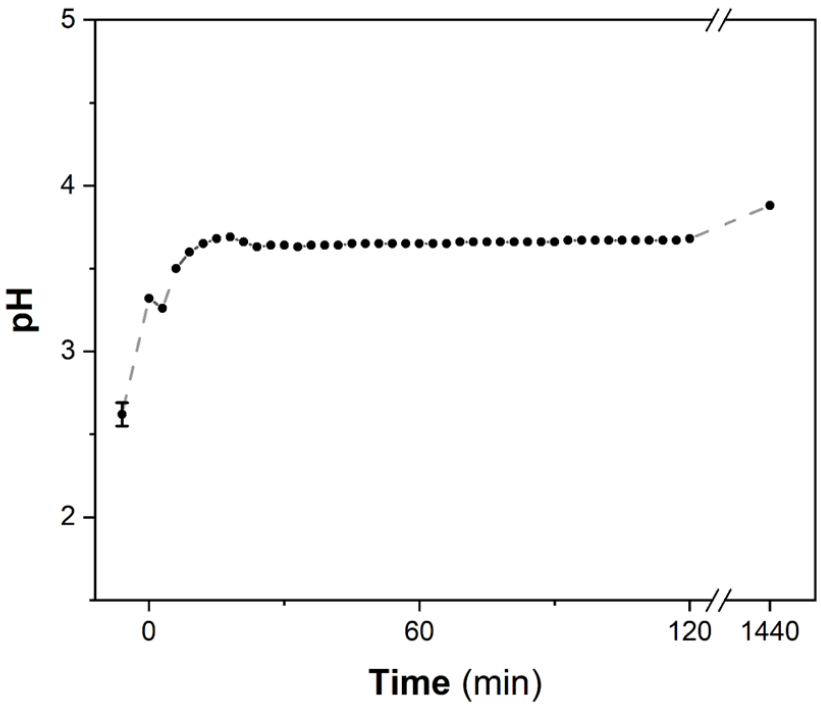

Figure 3. 27: pH evolution over 2 hours for the reaction between HC10 and cuprite. Cuprite is added at time 0 and pH is measured every 3 minutes.

Interestingly, the initial colour of cuprite shifts to a bright blue and localized areas characterized by blue crystals are observed after 2 hours. After 24-hour reaction, the majority of particles observed are blue in colour (Figure 3.28).

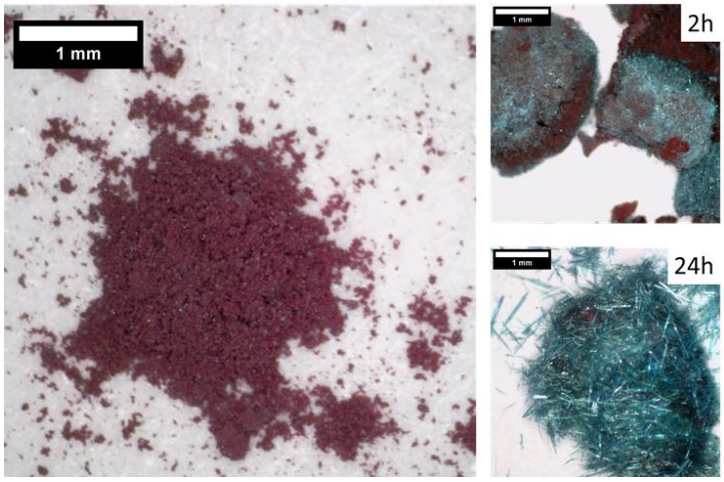

Figure 3. 28: Visual appearance of cuprite before (left) and after (right) immersion in HC10 solution at 2 and 24 hours.

The insoluble precipitate resulting from the reaction is examined by SEM-EDS analysis. In Figure 3.29 a, the precipitate after 2-hours reaction is observed in the backscattered mode: bright and dark particles can be recognized, reflecting a different elemental composition. The EDS spectra representative for dark particles (Sp.1) and bright particles (Sp.2) are reported together with the corresponding elemental composition. Despite the samples were carbon-coated prior to analysis, a relative higher amount of carbon is detected when pointing the darker particles (Sp.1) compared to the brighter ones. The bright particles are mainly composed by copper and oxygen with an atomic ratio comparable to the one of cuprite (O/Cu=0.5).

Similar observations are made after 24 hours of reaction (Figure 3.29 b). In this case, elongated darker crystals are observed together with few bright particles. The elemental composition measured on the dark (Sp.1) and bright (Sp.2) components of the precipitate are reported in the table. As previously observed, a higher amount of carbon characterizes the darker elongated particles while bright prismatic grains exhibit an elemental composition comparable to the one of pure cuprite.

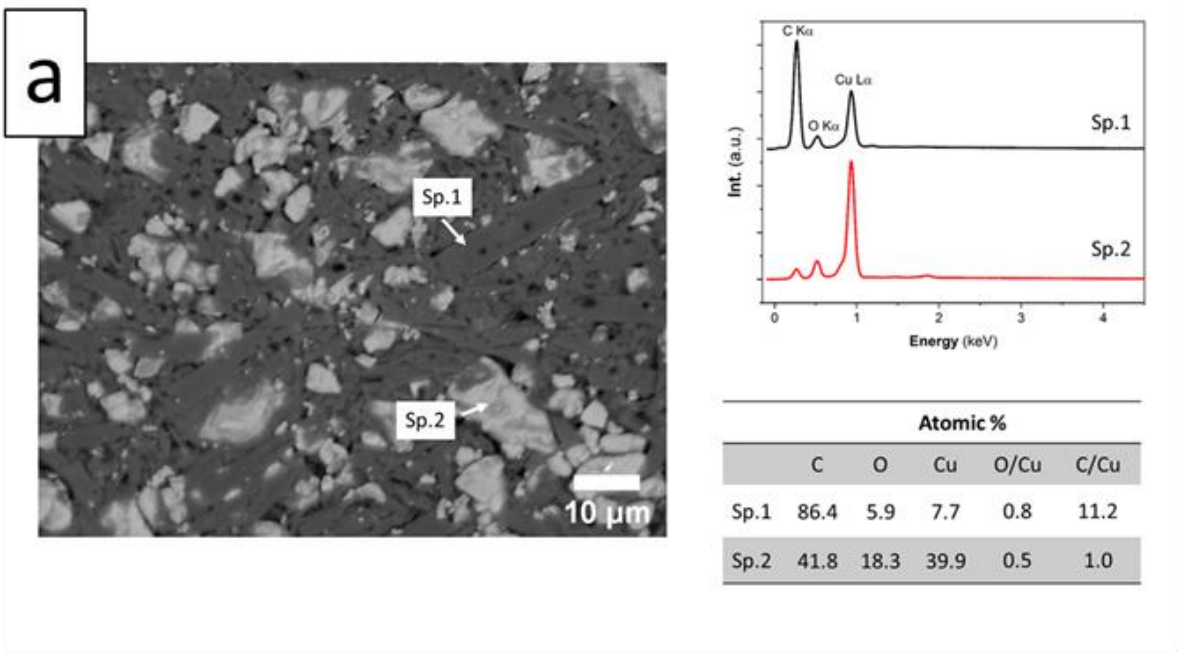

Atomic %					
	C	O	Cu	O/Cu	C/Cu
Sp.1	86.4	5.9	7.7	0.8	11.2
Sp.2	41.8	18.3	39.9	0.5	1.0

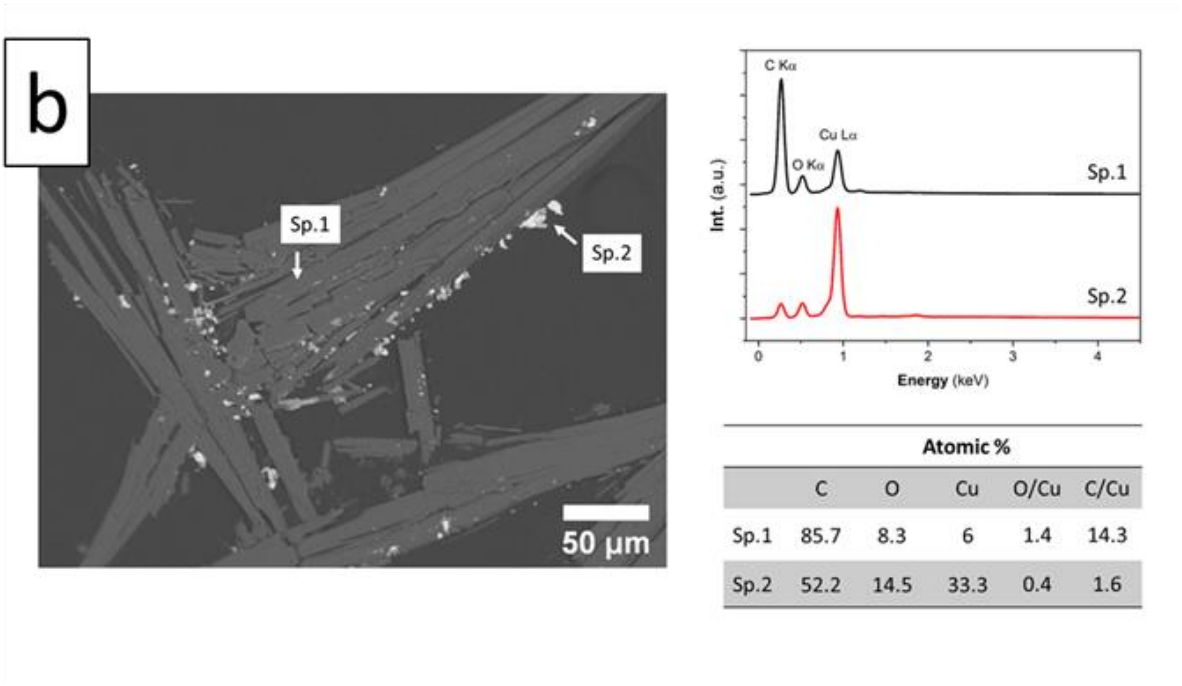

Atomic %					
	C	O	Cu	O/Cu	C/Cu
Sp.1	85.7	8.3	6	1.4	14.3
Sp.2	52.2	14.5	33.3	0.4	1.6

Figure 3. 29: Backscattered image and results of EDS analysis on the powder obtained as insoluble product of the reaction between cuprite and HC10 solution after 2 hours (a) and 24 hours (b).

After 2 hours, the precipitate analysed by XRD analysis (Figure 3.30) is composed by cuprite and crystalline copper decanoate. Cuprite is still present after 24 hours, although the low intensity of the corresponding diffraction bands testifies that it is present at a lower concentration. The evolution of the relative amount corresponding to the two crystalline phases, cuprite and copper decanoate can be measured based on the diffraction patterns.

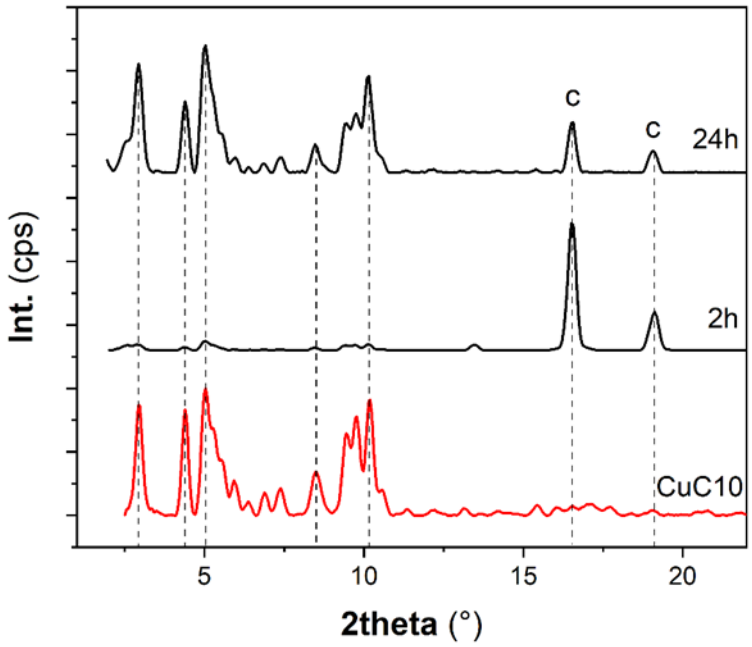

Figure 3. 30: Diffraction patterns obtained after 2- and 24-hours immersion of cuprite in HC10 solution. The red diffraction pattern corresponds to the reference copper decanoate (CuC10).

Results are reported in Table 3.3 and show that copper decanoate is the major phase present after 24 hours thus indicating a nearly complete transformation of cuprite.

Reaction time (h)	CuC10%
0.5	6.7
1	11.9
2	15
3	24.1
24	92.8

Table 3. 3: Estimated percentage of copper decanoate obtained at different reaction times. The only other crystalline phase detected by XRD is cuprite, which % decreases over time.

The presence of cuprite and copper decanoate is further confirmed by µRaman spectroscopy (Figure 3.31). Here, cuprite is identified only after a 2-hour reaction, while copper decanoate is the only phase detected after 24 hours.

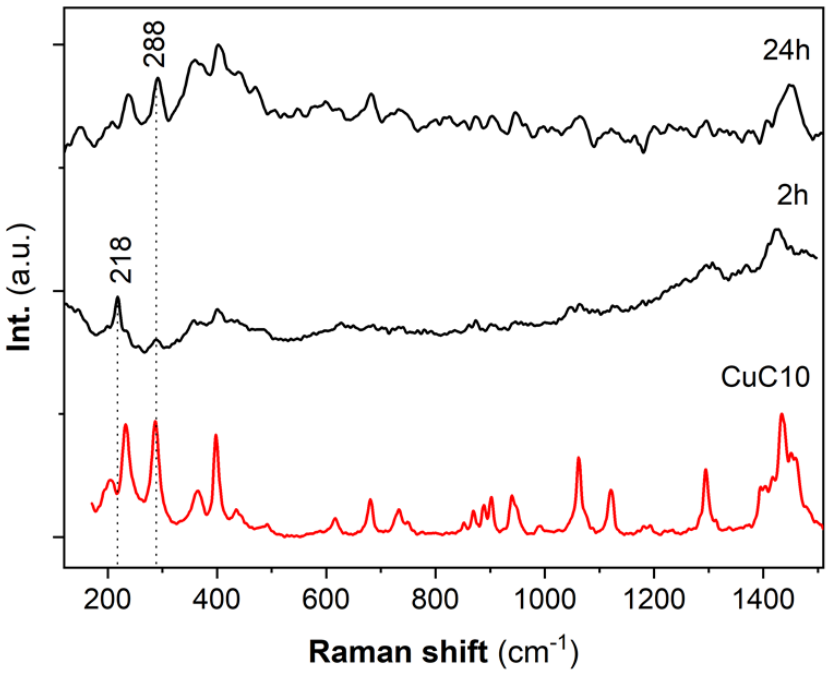

Figure 3. 31: Raman spectra after 2- and 24-hours immersion of cuprite in HC10 solution. The red spectrum corresponds to the reference CuC10.

1.3.2 Reaction HC10-brochantite: pH evolution and precipitate analysis

In this experiment, initial measured pH is equal to 2.96 ± 0.2. The evolution of pH with time is presented in Figure 3.32: after the addition of brochantite to the solution (time "0"), pH decreases gradually over time and reaches, after 2 hours, a value of 1.8. At the end of the experiment, pH did not vary considerably as a value of 1.6 is measured.

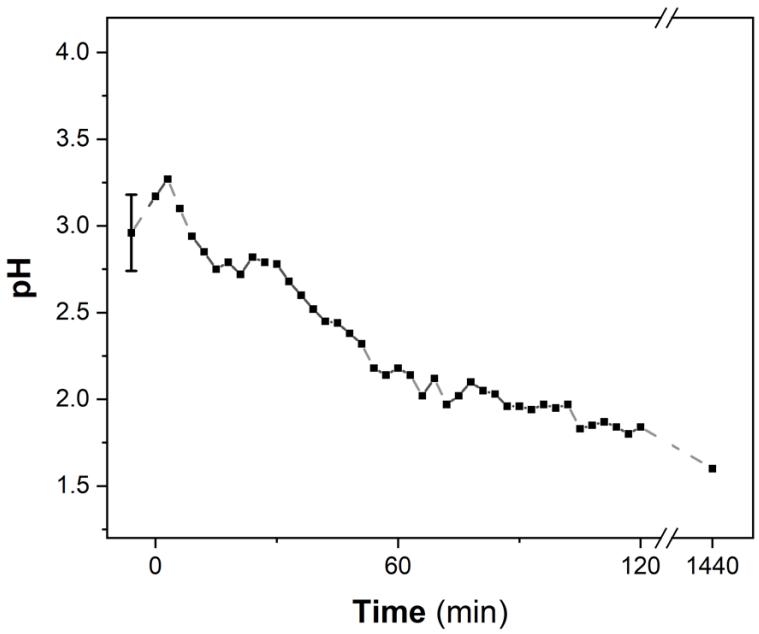

Figure 3. 32: pH evolution over 2 hours for the reaction between HC10 and brochantite. Brochantite is added at time 0 and pH is measured every 3 minutes.

The precipitate after 24 hours is mainly composed by bright blue elongated crystals (Figure 3.33-b).

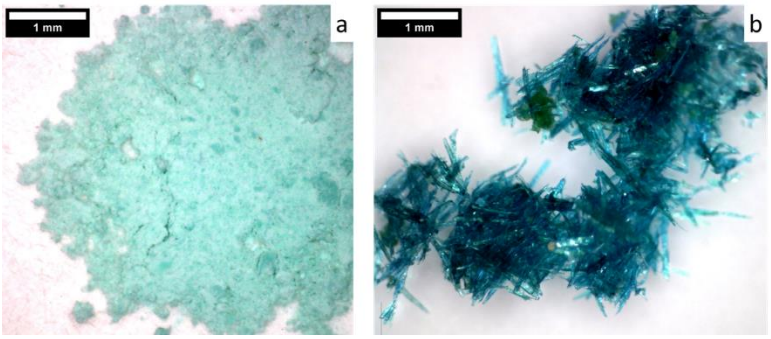

Figure 3. 33: Visual appearance of brochantite before (left) and after (right) 24-hours immersion in HC10 solution.

The elongated particles are detected by SEM analysis after short and long immersion time (Figure 3.34 a-b).

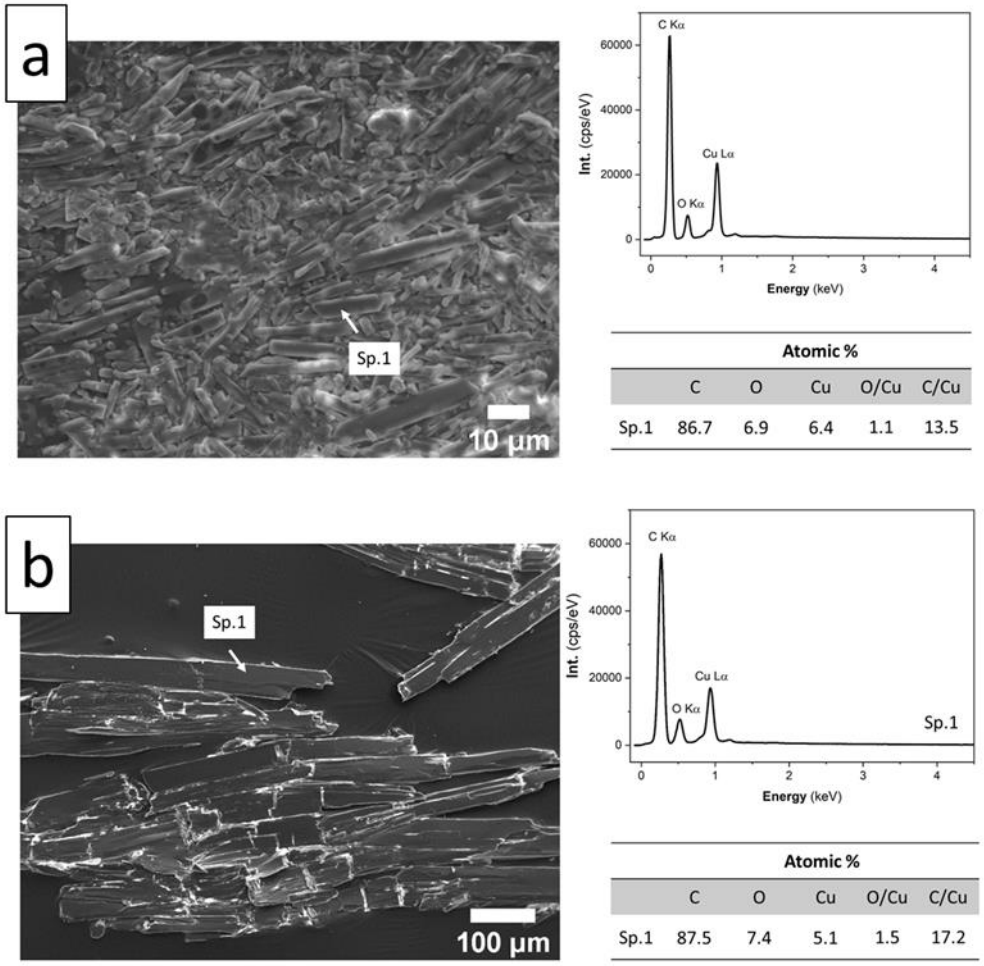

Figure 3. 34: Secondary electron image and results of EDS analysis on the powder obtained as insoluble product of the reaction between brochantite and HC10 solution after 2 hours (a) and 24 hours (b).

The elemental composition performed on the precipitate after different reaction times, highlights the high amount of carbon present while no specific phase can be distinguished based on elemental composition. The size of the crystals increases as the reaction proceeds over time with an average length of about 11 µm after 2 hours to 491 µm after 24 hours.

Both XRD (Figure 3.35) and Raman analysis (Figure 3.36) are performed on the precipitate. The results confirm the presence of copper decanoate as the only phase detected already after 2-hour reaction. In particular, in Raman spectra, the Cu-O bond characteristic of the metallic carboxylate is detected at 288 cm^{-1}.

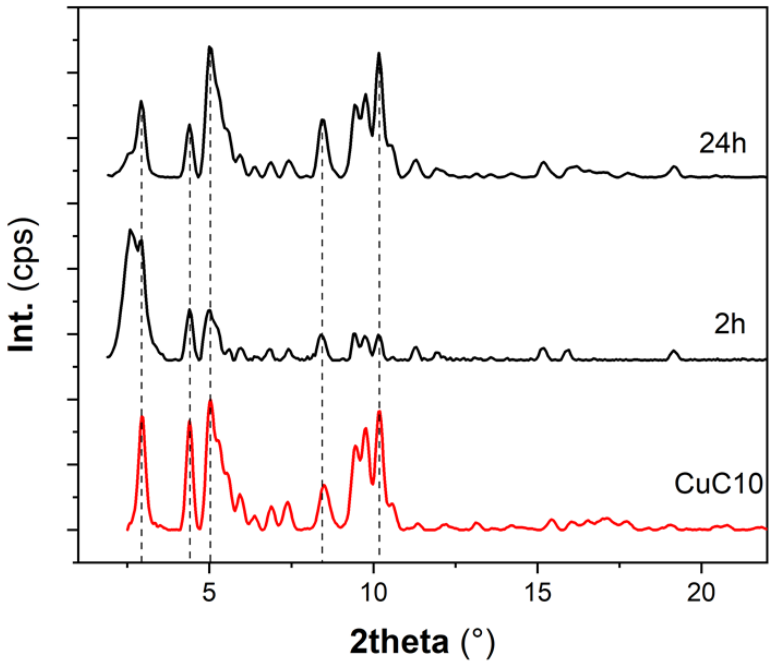

Figure 3. 35: Diffraction patterns obtained after 2- and 24-hours immersion of brochantite in HC10 solution. The red diffraction pattern corresponds to the reference CuC10.

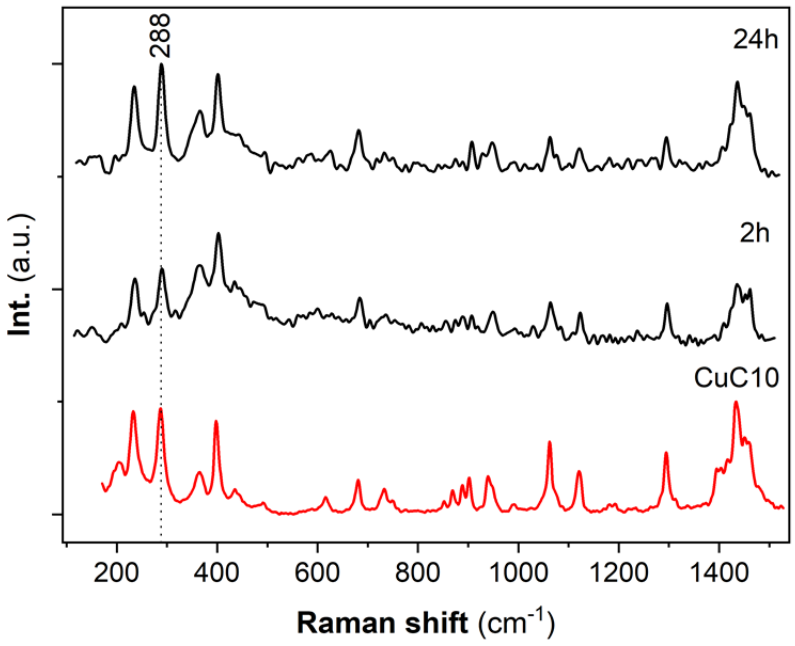

Figure 3. 36: Raman spectra after 2- and 24-hours immersion of brochantite in HC10 solution. The characteristic peak corresponding to CuC10 (red trace) at 288 cm^{-1} is identified at all reaction times.

1.4 Summary of the reactions

The reactions between the two synthetic phases and the solutions containing the inhibitors have been studied by following pH and by analysing the reaction products. A summary of the results and observations is presented in Table 3.4.

Table 3. 4: Summary of the main results from the reactions of the inhibitors with the synthetic mineral phases.

	Cuprite	**Brochantite**
BTAH	Cuprite+? Core-shell structure Surface amorphous layer not detectable at the bulk- to microscopic scale (only cuprite detected)	Brochantite+Cu-BTA Core-shell structure Surface amorphous layer detectable at the microscopic scale
5CBT	Cuprite+Cu-5CBT Core-shell structure Surface amorphous layer detectable at the microscopic scale	Brochantite+Cu-5CBT Core-shell structure Surface amorphous layer detectable at the microscopic scale
HC10	Cuprite+CuC10 Separate cuprite and copper decanoate crystals	CuC10 Elongated crystals well recognizable

For all inhibitors the formation of a new compound due to the interaction between copper and the inhibitor is detected at the microscopic scale. In the case of BTAH-treated cuprite, the interaction is not detectable at the bulk/microscopic scale and the nanometric scale is necessary to detect an interaction that occurs at the mineral's surface.

1.5 Stability of the 2-hour treated brochantite

The inhibitor-modified brochantite powders obtained after the 2-hour reaction from the previous experiments are studied to define their stability in severe conditions. In fact, brochantite undergoes a transformation after immersion for 30 days in concentrated stagnant NaCl solution at different pH (7,

5, 2, 1). In fact, diffraction patterns (Figure 3.37) and Raman spectra (Figure 3.38) show that brochantite is no more present regardless the pH of the solution and the new phase atacamite, $Cu_2Cl(OH)_3$, is clearly identified.

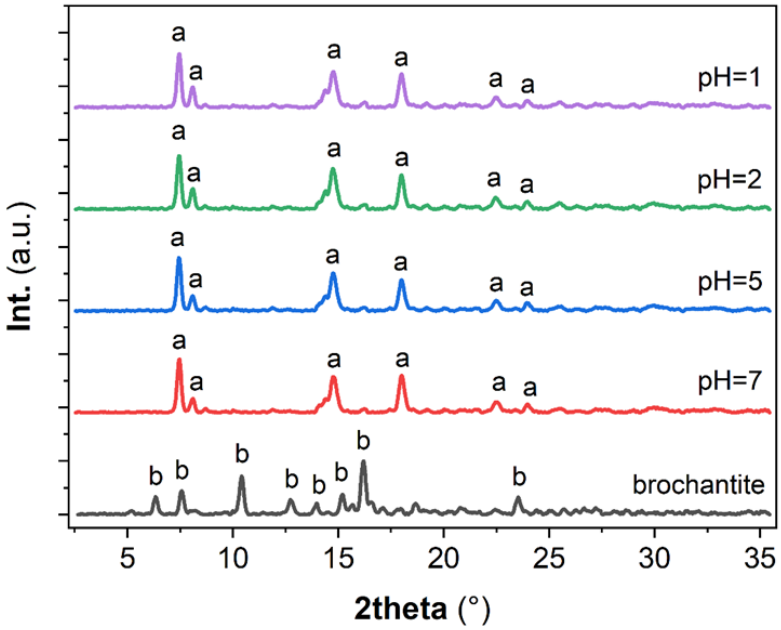

Figure 3. 37: Diffraction patterns obtained on brochantite (black trace) upon immersion in NaCl solution at different pH. The letter 'b' and 'a' indicate characteristics bands of brochantite and atacamite respectively.

The Raman shifts that allow to identify atacamite are, among others, the strong peaks in the hydroxyl-stretching region at 3347 and 3430 cm^{-1} and the Cu-O stretching mode at 511 cm^{-1} [142].

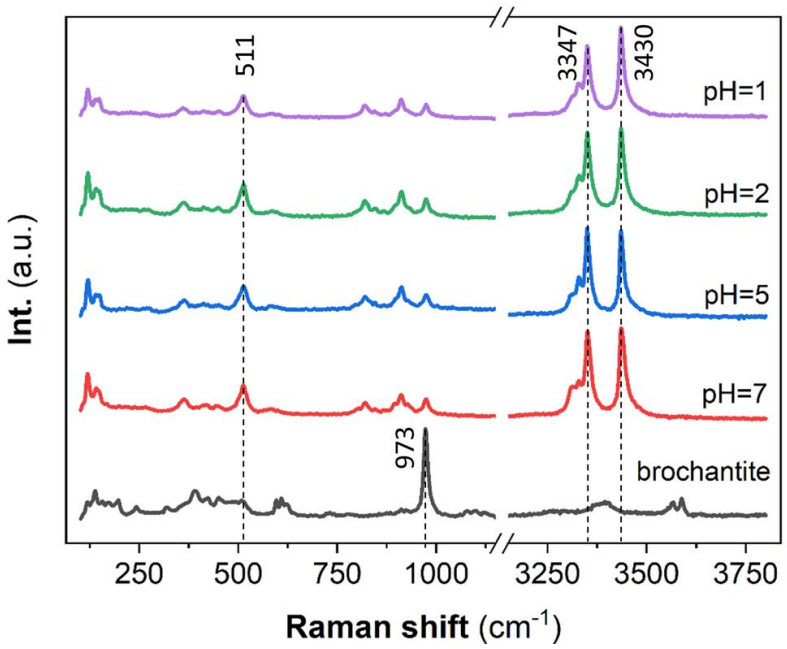

Figure 3. 38: Raman spectra obtained upon immersion of synthetic brochantite (black trace) in NaCl solution at different pH. Characteristic shifts corresponding atacamite (511, 3347, 3430 cm^{-1}) are identified after immersion.

The same protocol used for untreated brochantite is employed to evaluate the effects of the solution on the 2-hour treated brochantite. The insoluble precipitate from each solution is characterized by XRD and Raman analyses in order to identify the presence of atacamite or any other phase change.

Results of the diffraction and spectroscopic characterization of the BTAH-treated brochantite after immersion are presented in Figure 3.39 and Figure 3.40 respectively. Both the diffraction pattern and the Raman spectra indicate the presence of atacamite when the BTAH-treated brochantite reacted with the acidic solution (pH 2 and 1). Brochantite is still detected using both techniques at pH 2. Atacamite is clearly identified after reaction at pH 1.

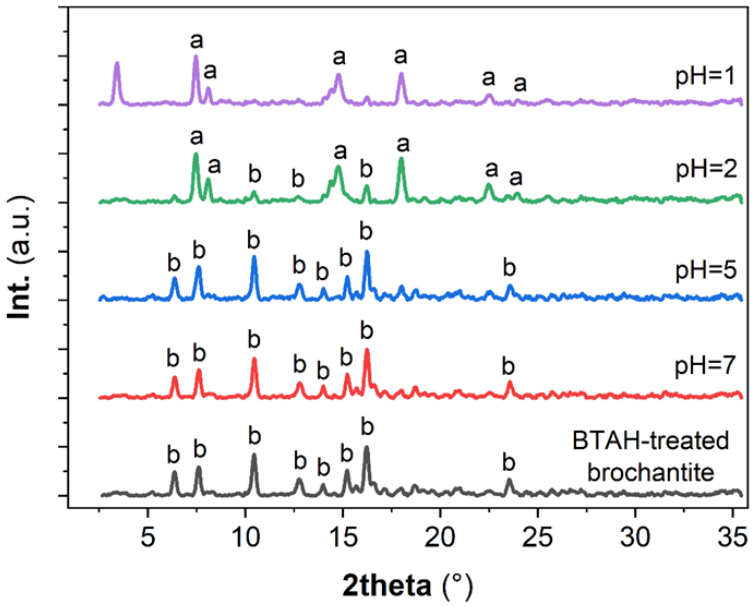

*Figure 3. 39: Diffraction patterns obtained on BTAH-treated brochantite (black trace) upon immersion in NaCl solution at different pH. The letter '**b**' and 'a' indicate characteristics bands of brochantite and atacamite respectively.*

Interestingly, the shift at 1395 cm^{-1} that allows to identify the Cu-BTA complex is detected in by µRaman spectroscopy (Figure 3.40) after reaction at all pH values.

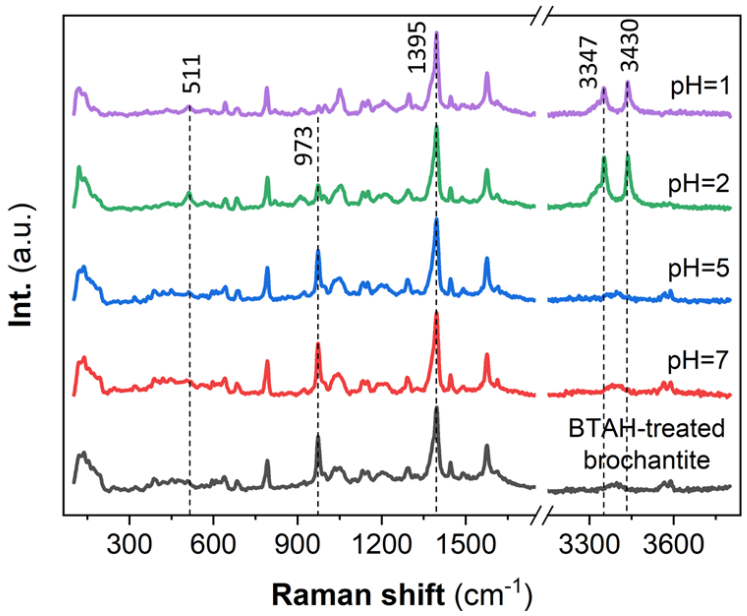

Figure 3. 40: Raman spectra obtained upon immersion of BTAH-treated brochantite (black trace) in NaCl solution at different pH. Characteristic shifts corresponding atacamite (511, 3347, 3430 cm^{-1}) are identified after immersion in acidic solution (pH 2 and 1). The strong peak at 1395 cm^{-1} characteristic of Cu-BTA is always identified.

Complementary TEM observations are performed on the BTAH-treated brochantite after 30 days of immersion at pH 2. When observed at the nanometric scale, the particles retain the previously described morphology with a crystalline core and an amorphous layer (Figure 3.41 a). The thickness of the amorphous outer layer is not drastically reduced compared to that before immersion with a mean thickness of 21 ± 7 nm compared to the 29 ± 14 nm before immersion in aggressive solution. Other particles present a hollow structure with an outer amorphous layer retaining the morphology of the previously present mineral (Figure 3.41 b). These hollow structures have been named “ghost structure”. The present of such morphology testifies that in some cases, brochantite solubilizes and disappears form the core-shell structure, while the Cu-BTA complex layer remains in position.

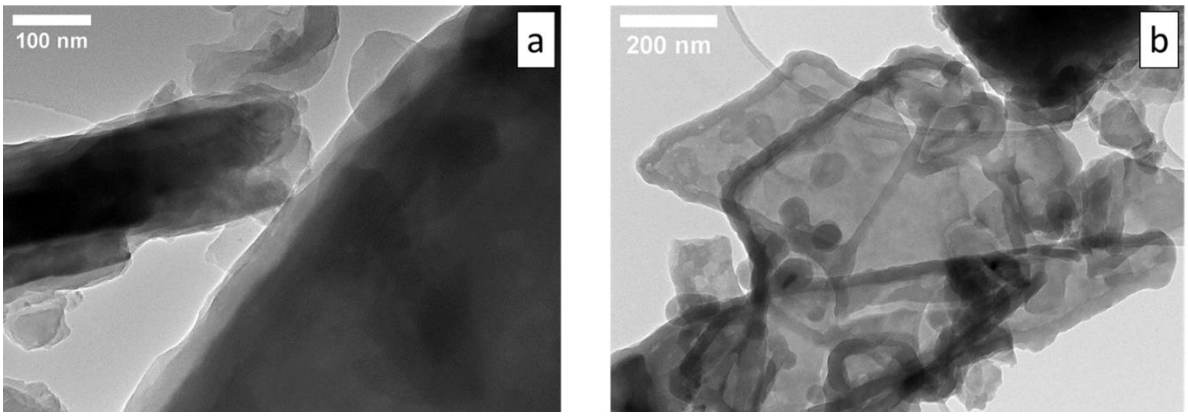

Figure 3. 41: TEM analysis on the BTAH-treated brochantite after immersion in NaCl solution at pH 2. The powder is characterized by different morphologies with core-shell structures (a) and “ghost structures” (b).

Regarding the 5CBT-treaed brochantite, at neutral and near-neutral pH, only brochantite is identified by both XRD and µRaman spectroscopy (Figure 3.42 and Figure 3.43). Brochantite and atacamite are detected at pH 2 and, in these conditions, brochantite is still detected. The peak at 1398 cm^{-1}, detected by structural Raman analysis and characteristic of the Cu-5CBT complex, is present after immersion in NaCl solution for pH 7, 5 and 2.

At pH 1, a non-identified crystalline phase is detected by XRD analysis, which does not correspond to pure 5CBT. The corresponding Raman analysis (Figure 3.43) does not provide any information due to the high fluorescence in the spectrum, although the fluorescence suggests that an organic phase might be present.

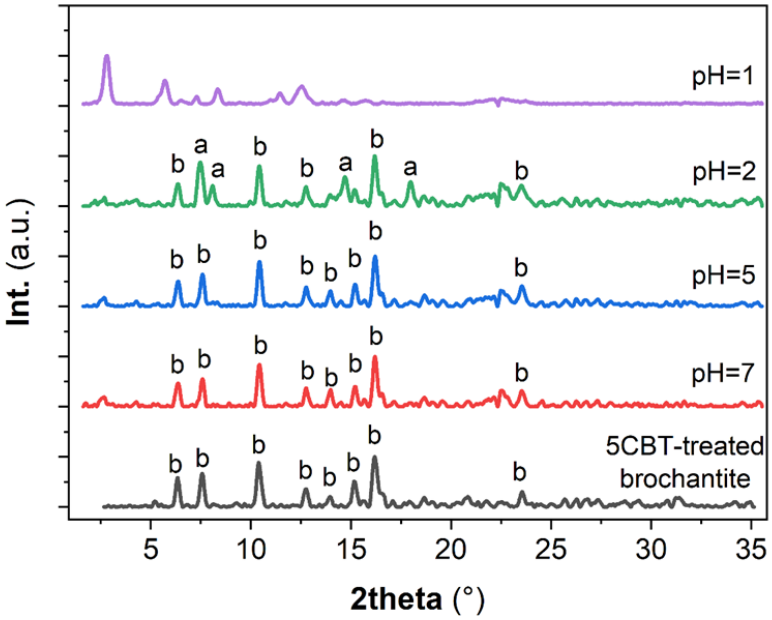

*Figure 3. 42: Diffraction patterns obtained on 5CBT-treated brochantite (black trace) upon immersion in NaCl solution at different pH. The letter '**b**' and '**a**' indicate characteristics bands of brochantite and atacamite respectively.*

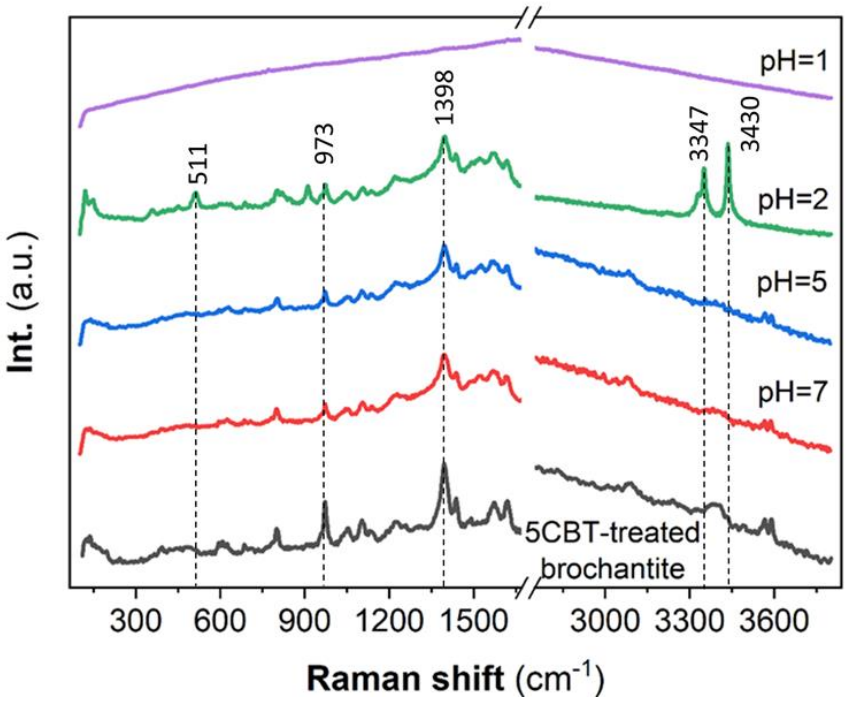

Figure 3. 43: Raman spectra obtained upon immersion of 5CBT-treated brochantite (black trace) in NaCl solution at different pH. Characteristic shifts corresponding atacamite (511, 3347, 3430 cm^{-1}) are identified after immersion in acidic solution (pH 2). The strong peak at 1398 cm^{-1} characteristic of Cu-5CBT is always identified. At pH 1, strong fluorescence is present.

5CBT-treated and immersed brochantite exhibits similar morphological features to the BTAH one. Figure 3.44-a shows part of a particle's surface with the characteristic core-shell structure.

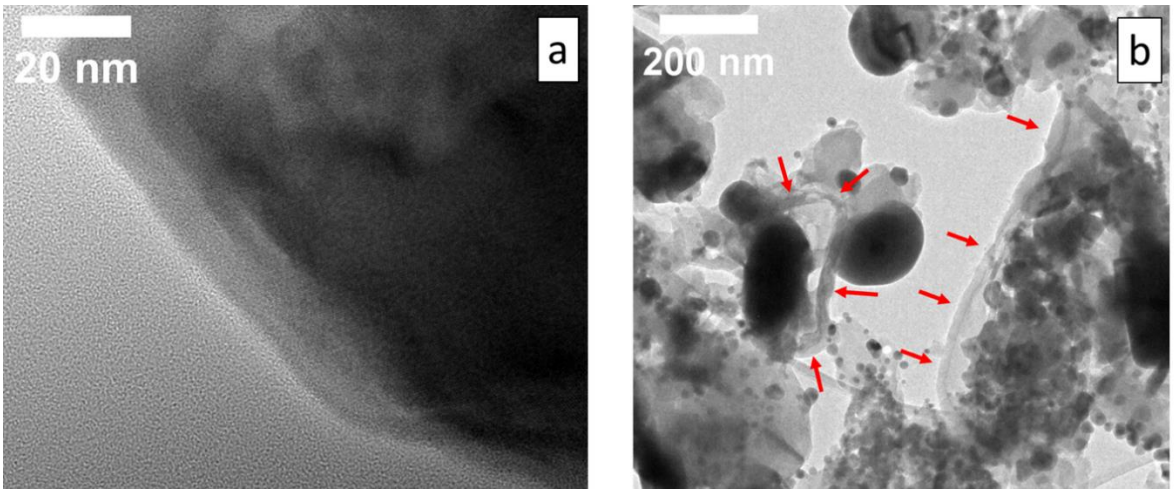

Figure 3. 44: TEM analysis on the 5CBT-treated brochantite after immersion in NaCl solution at pH 2. The powder is characterized by different morphologies with core-shell structures (a) and "ghost structures" indicated by the red arrows (b).

The thickness of the Cu-5CBT layer (11 ± 6 nm) did not vary compared to the one measured before immersion (9.3 ± 3.9 nm). Similarly to BTAH, the "ghost structures" are also identified in this sample (Figure 3.44-b). The spherical particles that can be observed in the image formed as an effect of the incident electron beam.

As reported previously in this chapter, after 2 hours, brochantite treated with decanoic acid completely transformed into copper decanoate. Therefore, it can be considered that the stability of copper decanoate in NaCl at different pH has been investigated. Copper decanoate is clearly identified by both XRD and Raman analysis (Figure 3.45 and Figure 3.46) until pH 2. At pH 1, the decanoic acid is detected. It is possible to conclude that in strongly acidic conditions (below pH 2), the copper decanoate is not stable and the acidic form is favoured.

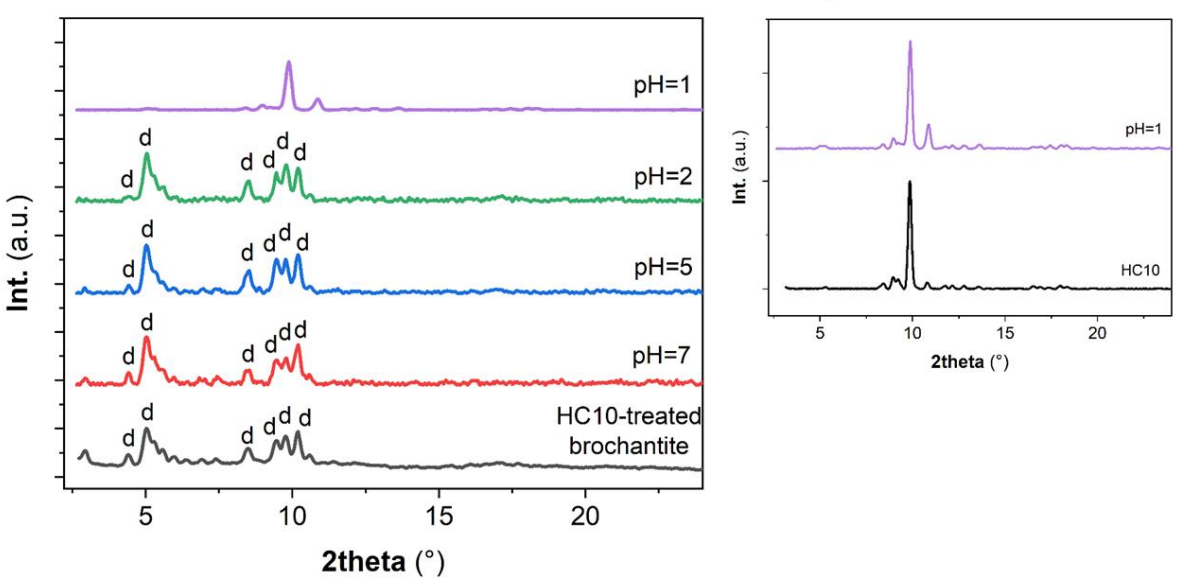

Figure 3. 45: Diffraction patterns obtained on HC10-treated brochantite (black trace) upon immersion in NaCl solution at different pH. Only copper decanoate I identified ('d') at all pH, except at pH 1when decanoic acid is identified.

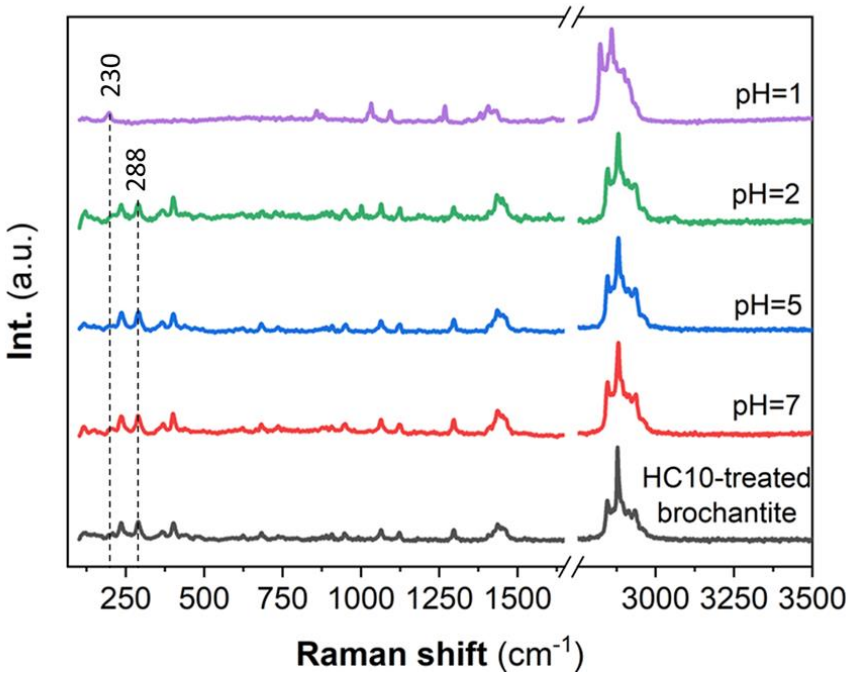

Figure 3. 46: Raman spectra obtained upon immersion of HC10-treated brochantite (black trace) in NaCl solution at different pH. Copper decanoate is detected up to pH 2. After immersion in even more acidic solution, decanoic acid is identified.

2. Metz samples before treatment

2.1 General description

Naturally corroded copper tiles are used as coupons for the experimentation, they are referred to as "Metz samples" further in the text. Based on their visual appearance, a distinction between sheltered (internal) and unsheltered (external) surfaces can be made based on their visual appearance: the unsheltered surface exhibits a uniform light-green colour while the internal part of the roof tile is darker (Figure 3.47). Parallel lines of different colours evidence the direction of water percolation on the internal side. For the present work, only the external part has been investigated.

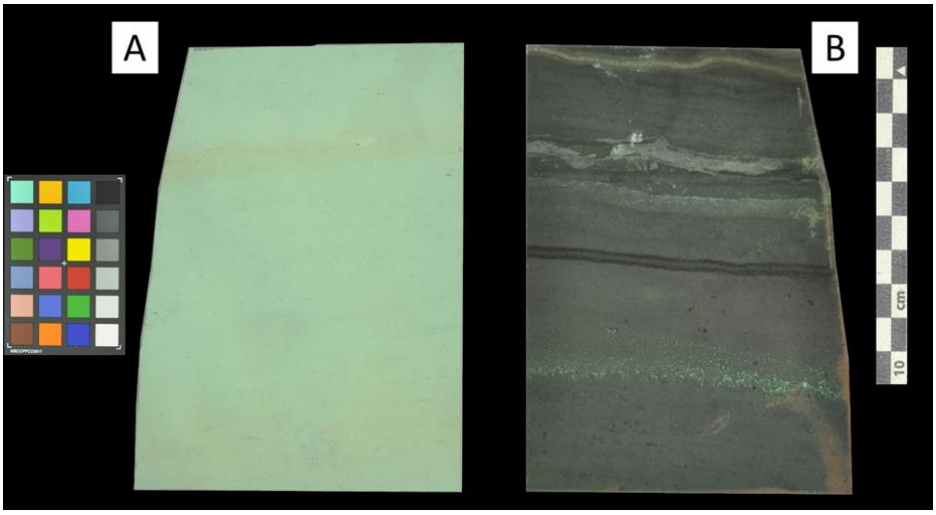

Figure 3. 47: Verso (A) and recto (B) of one of the copper plates used in this study. The unexposed side (B) clearly shows the signs of run-off in form of parallel lines characterized by different colouration. The exposed surface (A) is uniform.

2.2 Metallic substrate

The average thickness of the metallic substrate, evaluated on SEM micrographs, is uniform and equal to 510 ± 23 µm (Figure 3.48).

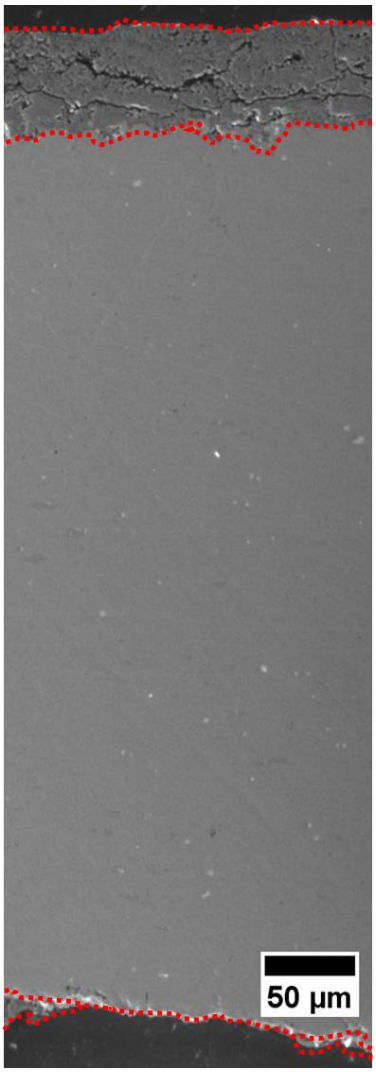

Figure 3. 48: Overview cross-section of the whole Metz sample with the external corrosion layer in the upper part of the image. SEM, 15kV.

As already mentioned earlier, the copper microstructure of the Metz samples has been studied elsewhere [2] and is characterized by the presence of equiaxed grains of several tenth micrometres.

2.3 Non-metallic inclusions

The metallic substrate is characterized by the presence of non-metallic inclusions (Figure 3.49). The number of inclusions is calculated using SEM micrographs the density corresponds to 59 ± 10 inclusions on a 200x200 µm area, results are average of the measurements on 4 different areas in the metal.

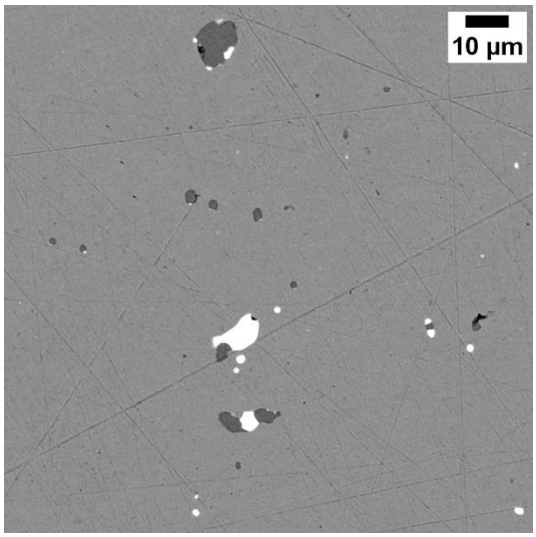

Figure 3. 49: Inclusions (dark grey and white) in the metallic matrix (grey). SEM-BSE, 15kV.

Based on their elemental composition, two types of inclusions are distinguished (Table 3.5).

Table 3. 5: Elemental composition of the inclusions (calculated as average on 8 inclusions), SEM-EDS.

%wt	Type 1	Type 2	Inclusions inside the CL
O	11.5±0.6	9.3±0.2	12.8±0.9
Cu	5.2±4.4	90.5±0.3	5.3±2.8
Pb	66.9±3.7	-	64.6±3.9
As	16.3±0.3	-	15.8±1.3
Sb	-	-	3.3±0.4 (2 of 8)
Ni	-	-	1.3±1.2 (2 of 8)
O/Cu	**3.6**	**0.10**	**3.1**
As/Pb	**0.24**	**-**	**0.24**

Lead, arsenic, oxygen and copper are the main elements identified for the “Type 1” inclusions. “Type 2” inclusions are composed of oxygen and copper and the mass ratio calculated (O/Cu=0.10) is comparable to the one calculated for pure cuprite (O/Cu=0.13); the slight difference is reasonably due to the presence of the copper matrix, leading to an overestimation of copper. Structural analysis is performed on the two types of inclusions and Raman spectra obtained on “Type 2” inclusions confirm that they are composed by cuprite. Figure 3.50 shows the Raman spectra characteristic of the two types of inclusions.

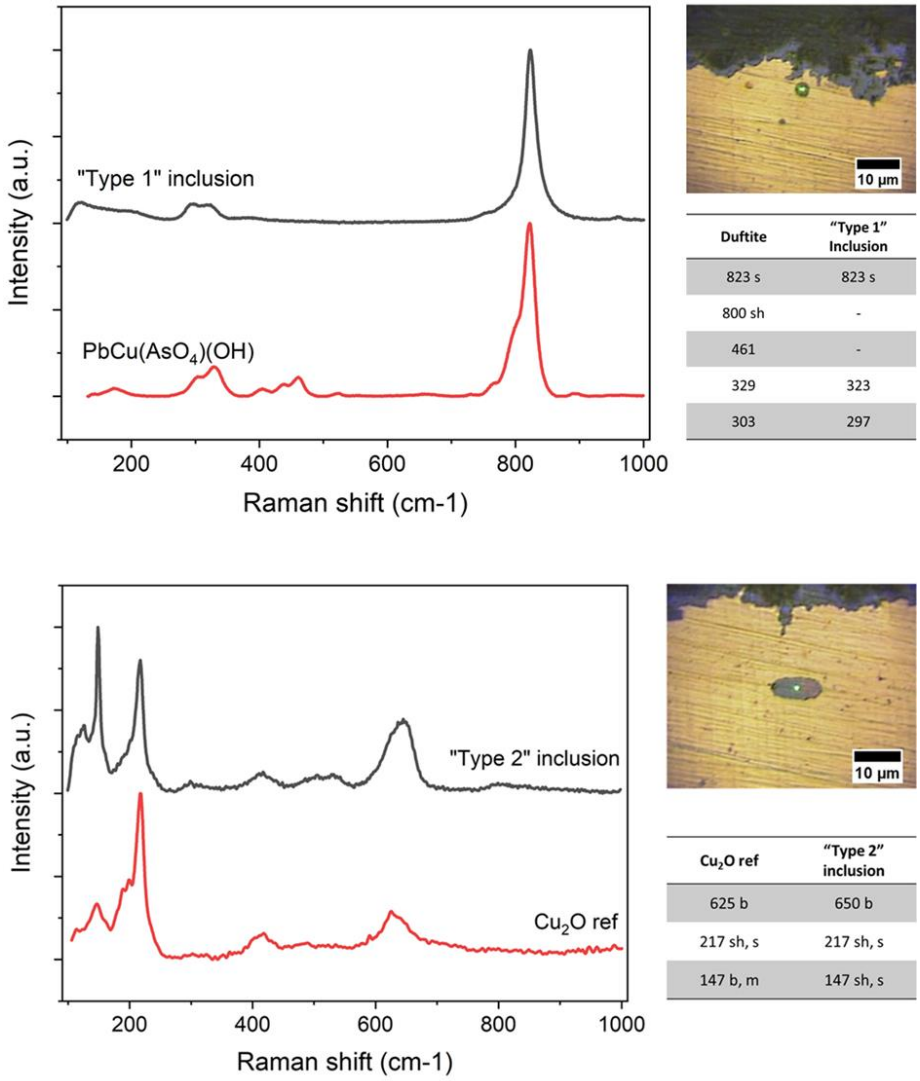

Duftite	"Type 1" Inclusion
823 s	823 s
800 sh	-
461	-
329	323
303	297

Cu_2O ref	"Type 2" inclusion
625 b	650 b
217 sh, s	217 sh, s
147 b, m	147 sh, s

Figure 3. 50: Structural characterization on two different types of inclusions, Raman spectroscopy.

Concerning the "Type 2" inclusion, the Raman spectrum corresponds to the mineral cuprite. Interestingly, a difference in intensity of the peak at 147 cm^{-1} is observed: the peak is more intense in the inclusions compared to the reference spectrum (powder Cu_2O, Sigma-Aldrich) indicating a higher crystallinity of the cuprite in the inclusions [3].

More problematic is the structural identification of the "Type 1" inclusions as no mineral phase corresponds to the elemental mass ratios from EDS analysis. The strong shift identified by Raman spectroscopy at 823 cm^{-1} and the presence of both oxygen and arsenic indicate a possible arsenate group [4] such in the Pb-Cu arsenate duftite, $CuPb(AsO_4)(OH)$.

Only "type 1" inclusions are identified in the corrosion layer (Figure 3.51) and their elemental composition does not vary considerably compared to those found in the sound metal (Table 3.5).

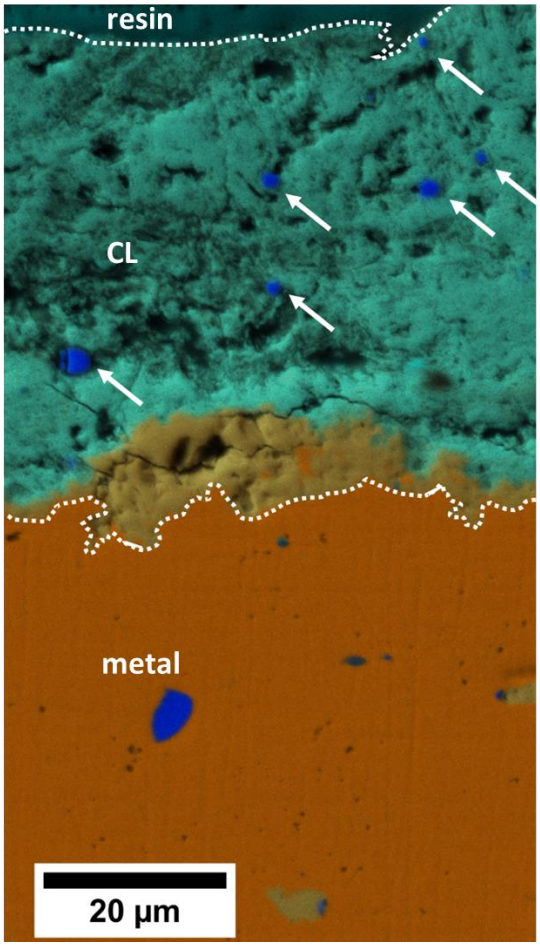

Figure 3. 51: Elemental mapping in cross-section. Cu is represented in orange, O in light blue, Pb in dark blue and the white arrows indicate Pb-rich inclusions within the corrosion layer. SEM-EDS.

2.4 Corrosion layer characterization

The investigation of the morphological and physico-chemical properties of the corrosion layer of Metz samples represents an essential starting point for the further research on inhibitors. After an evaluation of the global colour of the surface, structural and morphological features of the corrosion layer are studied in cross-section by SEM-EDS and Raman spectroscopy.

2.4.1 Surface colour

As previously mentioned, the copper plaques are covered by a light-green external corrosion layer. The colour and colour homogeneity of the external layer is investigated by spectrophotometric measurements in different parts of the copper plaque. The colour parameters (L* a* b*), resulting from such measurements, are summarized in Table 3.6.

Table 3. 6: Colour parameters from measuring the surface of the copper plate.

	L*(D65) Lighter-darker	a*(D65) Red-green	b*(D65) Yellow-blue
Metz untreated	72,2	-14,9	11,2
	71,8	-14,6	12,1
	74,7	-14,3	11,2
	73,3	-14,3	11,8
	72,8	-13,5	14,5
	73,6	-14,8	11,4
	71,0	-12,0	14,9
	71,1	-12,3	14,0
	72,3	-12,1	14,5
	72,8	-11,7	14,3
	71,0	-12,4	14,1
	71,9	-12,5	13,5
	72,5	-12,2	13,6
	72,8	-13,5	14,5
Mean	**72,4**	**-13,2**	**13,2**
SD	**1,0**	**1,2**	**1,4**

With a standard deviation between 1 and 1.4 among the different measurements, it can be concluded that none of the parameters varies considerably in different parts of the tile. Although, a certain variability does exist. In fact, by plotting the L* a* b* parameters (Figure 3.52), two groups having similar a*b* values can be distinguished: “Group 1” (black dots) is characterized by high a* and b* values with a tendency towards a less blue and more yellow hue, while “Group 2” (red dots) has lower a* and b* indicating the opposite tendency.

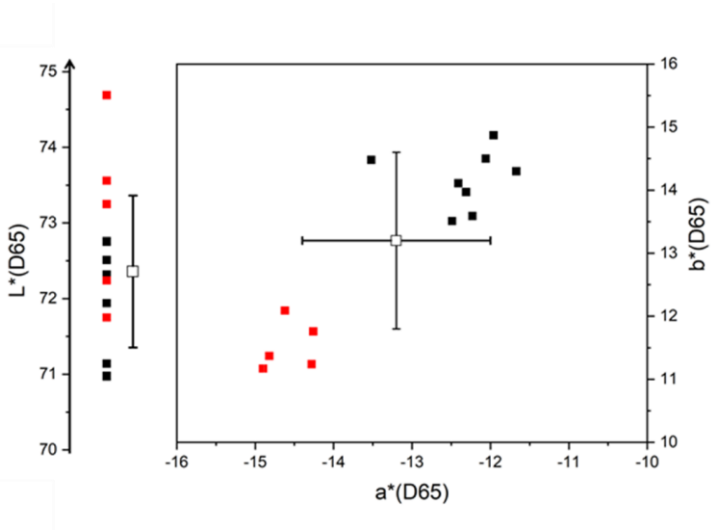

Figure 3. 52: L*a*b* plot. Two groups are identified based on similar a*b* values: in black "group 1", in red "group2".

2.4.2 Corrosion layer general overview and thickness

In Figure 3.53, the corrosion layer is observed under optical microscope in bright and dark field.

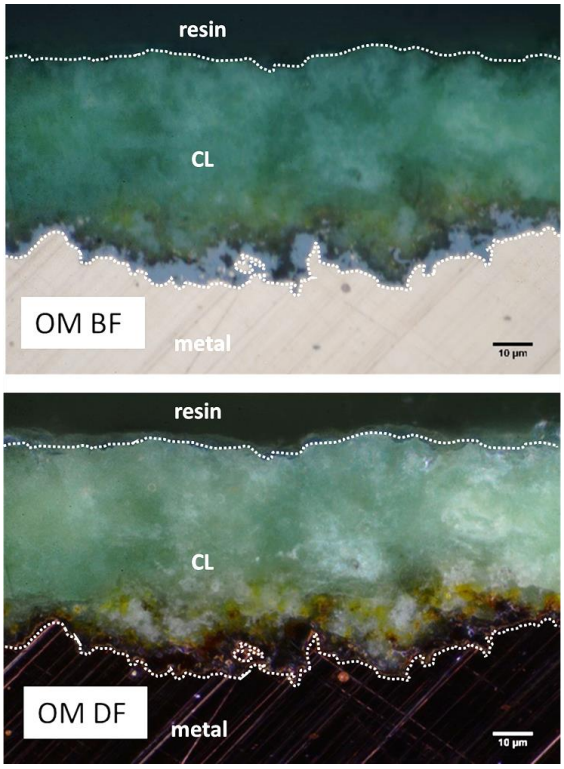

Figure 3. 53: Overview of the corrosion layer, Optical Microscope in bright field (OM BF) and dark field (OM DF).

In both images, the corrosion layer can be easily identified on top of the metal. Additionally, two different parts of the corrosion layer can be distinguished: an external green layer and, in contact with the metal, a more irregular grey layer. On the dark field image, a grey-yellow coloured area is also visible in the innermost part of the outer green layer.

SEM micrographs obtained in cross-section confirm the two-layered morphology of the corrosion layer and the thickness of both layers is evaluated based on image contrast between internal and external layer as observed on backscattered electron images. Results are plotted in Figure 3.54.

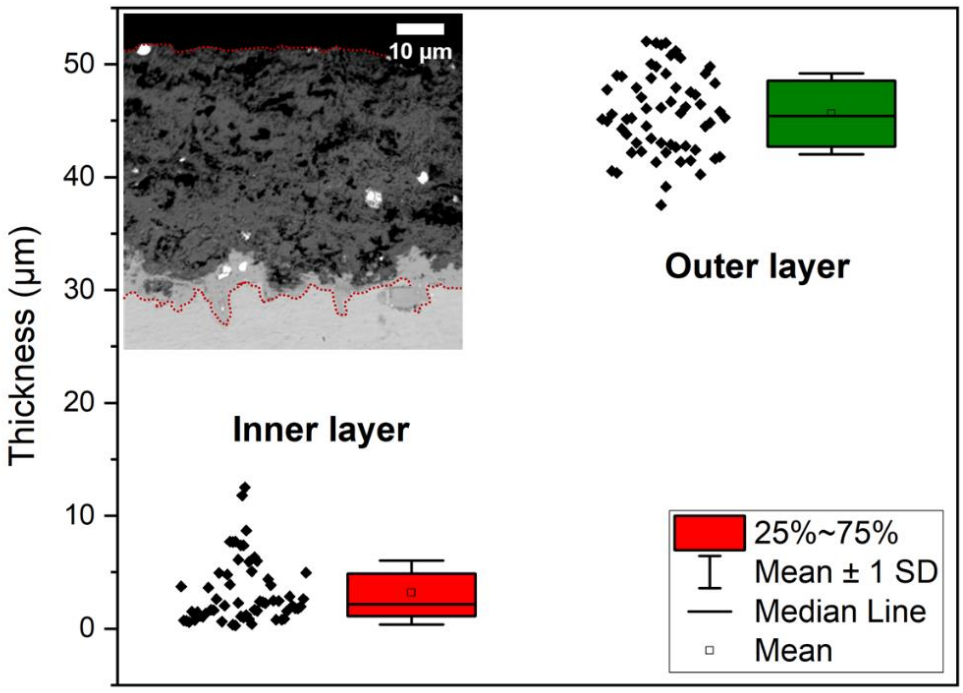

Figure 3. 54: Thickness measurements plotted for cuprite (red) vs brochantite layer (green). The man value is an average of 60 measurements.

The inner layer measures 3.2 ± 2.8 µm in thickness and it is characterized by a high variability with a maximum thickness measured of 12 µm and a minimum thickness of 0.3 µm. In contrast, the outer layer is thicker (45.6 ± 3.4 µm on average) and exhibits a lower variability.

2.4.3 Elemental and structural characterization

The elemental composition of the corrosion layer is studied in cross-section by SEM-EDS analysis. Figure 3.55 shows EDS maps of the main elements detected on the corrosion layer. In particular, the

presence or absence of sulphur (in violet in the coloured maps), marks the distinction between the outer, thicker layer and the inner, thinner layer where S is absent.

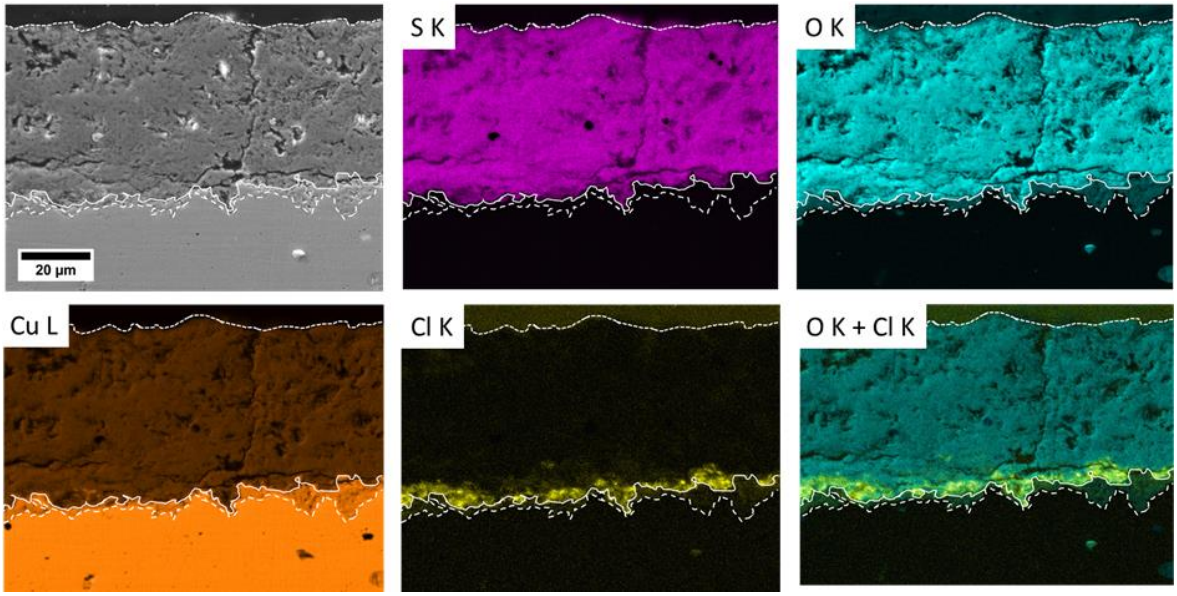

Figure 3. 55: EDS elemental distribution of the main elements identified in the corrosion layer. SEM-EDS.

Main elements distribution inside the corrosion layer is reported in Table 3.7.

Table 3. 7: Average elemental composition (in %wt.) and mass ratios for the three different zones identified. The results are an average on three areas of the sample analysed. SEM-EDS, 15kV. The mass ratios corresponding to reference minerals found in the literature are also reported for comparison.

%wt	O	Cu	S	Cl	O/Cu	S/Cu	Cl/Cu
Outer layer	27.3±0.3	62.9±0.7	7.7±0.1	**0.3**±0.1	**0.43**	**0.12**	-
Interfacial layer	23.5±1.5	69.5±2.9	4.5±0.9	**2.1**±0.4	**0.34**	**0.06**	**0.03**
Inner layer	9.3 ±0.8	89.9±1.3	0.3±0.1	**0.5**±0.2	**0.10**	**0.00**	**0.01**

		O/Cu	S/Cu	Cl/Cu
Brochantite	$Cu_4SO_4(OH)_6$	**0.63**	**0.13**	-
Antlerite	$Cu_3SO_4(OH)_4$	**0.67**	**0.17**	-
Posnjakite	$Cu_4SO_4(OH)_6 \cdot H_2O$	**0.69**	**0.13**	-
Clinoatacamite	$Cu_2(OH)_3Cl$	**0.73**	-	**0.38**
Cuprite	Cu_2O	**0.13**	-	-

Three areas can be distinguished:

1. An external layer characterized by the presence of sulphur. The mass ratio S/Cu is equal to 0.12 and it is comparable to the calculated mass ratio of the copper hydroxyl sulphate mineral brochantite.
2. In contact with the metal the continuous and thin layer is mainly composed by copper and oxygen with a mass ratio O/Cu of 0.10, in agreement with the corresponding mass ratio in the mineral cuprite (0.13).
3. Finally, EDS mapping points out the presence of an intermediate area located between the previous ones. This area is characterized by a relatively higher amount of chlorine (2.1 %wt. ± 0.4) when compared to both external (0.3 %wt. ± 0.1) and internal layer (0.5 %wt. ± 0.2). By plotting the mean profile of chlorine, the thickness of such layer is estimated at 6.9 ± 1.8 µm. Figure 3.56 shows a profile along the whole thickness of the corrosion layer from the resin to the metal substrate. In the outer layer (1), the ratios O/Cu (black line) and S/Cu (red line) remain constant. At about 40 µm from the surface, the values for the ratios start changing giving two slopes. At the same time, chlorine (grey bars) is detected in significantly higher amounts (zone 2). The last zone (3) is characterized by the absence of sulphur and a constant O/Cu ratio.

   The mass ratios obtained in the interfacial layer do not allow a precise phase identification of the Cl-containing phase.

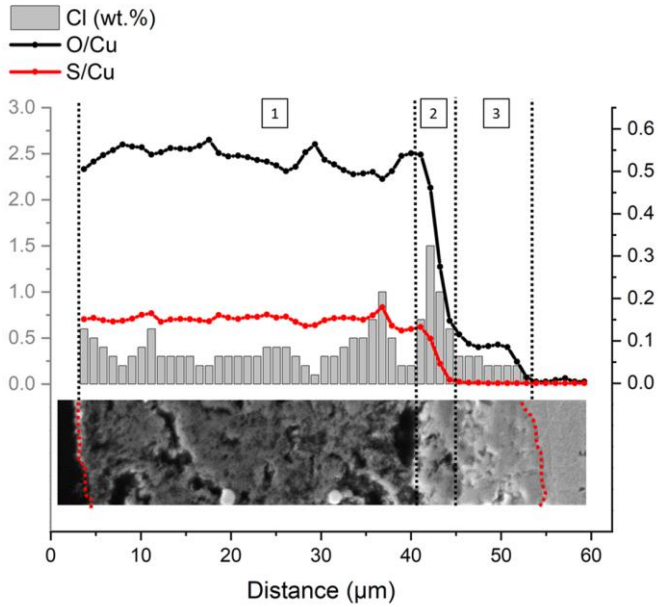

Figure 3. 56: Mean profile plot of Cl %wt. (grey bars) variation within the corrosion layer. The black line indicates the mass ratio O/Cu; the red line the mass ratio S/Cu.

The structural characterization of the different components of the corrosion layer is achieved by performing µRaman spectroscopy as mapping in cross-section. An example of typical Raman mapping obtained on the cross-section of the corrosion layer is presented in Figure 3.57.

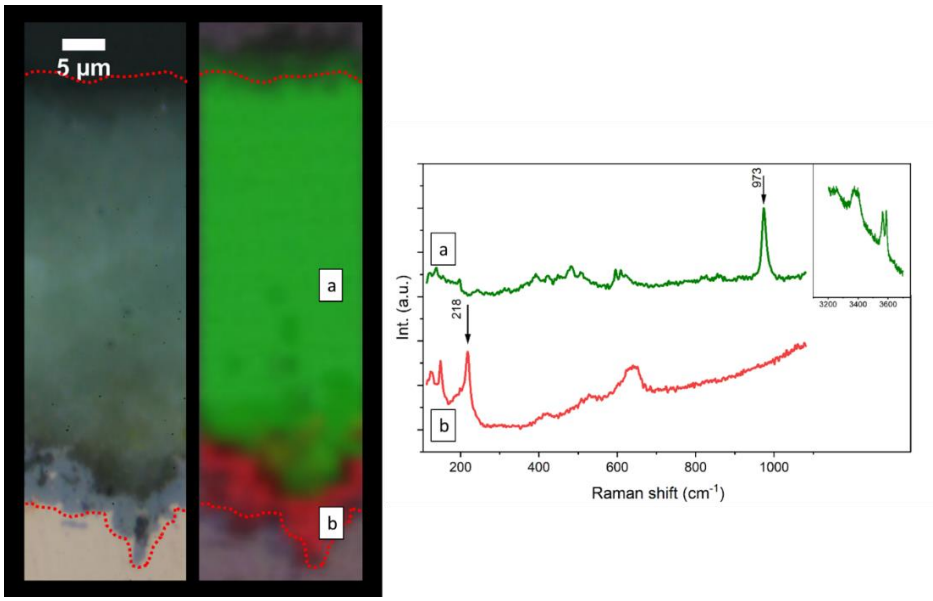

Figure 3. 57: Raman mapping of the corrosion layer and representative spectra from the outer (a) and inner (b) layer. The green area is characterized by the peak at 973 cm^{-1}, in red the area of the corrosion layer characterized by the peak at 218 cm^{-1}.

In the outer part of the corrosion layer (in green), Cu(II) hydroxy sulphate brochantite ($Cu_4SO_4(OH)_6$) is identified thanks to the strong shift at 973 cm^{-1} corresponding to the sulphate group stretching mode. Other shifts, characteristics of this basic copper sulphate, are identified, such as the typical doublet at 3587-3397 cm^{-1} assigned to the -OH stretching vibrations (Table 3.8). Concerning the internal layer, the strong shift at 218 cm^{-1}, associated with shifts at 146, 198 and 640 cm^{-1}, is attributed to Cu(I) oxide.

Table 3. 8: Main Raman shift identified on the external and internal part of the corrosion layer. The peaks are compared with reference shifts for brochantite and cuprite reported in [137].

Reference brochantite (Bouchard2003)	Outer corrosion layer
Raman shift (cm^{-1})	
3585	3587
3398	3397
3369	3370
3252	3254
974	**973**
911	
621	620
611	609
597	596
506	505
483	482
449	
429	
389	392
366	
319	
243	
195	196
171	

Reference cuprite (Bouchard2003)	Inner corrosion layer
Raman shift (cm^{-1})	
638	639
218	**218**
195	198
186	
148	149
	124

The relative intensity of the two characteristic peaks is measured and plotted as a profile along the thickness of the corrosion layer (Figure 3.58).

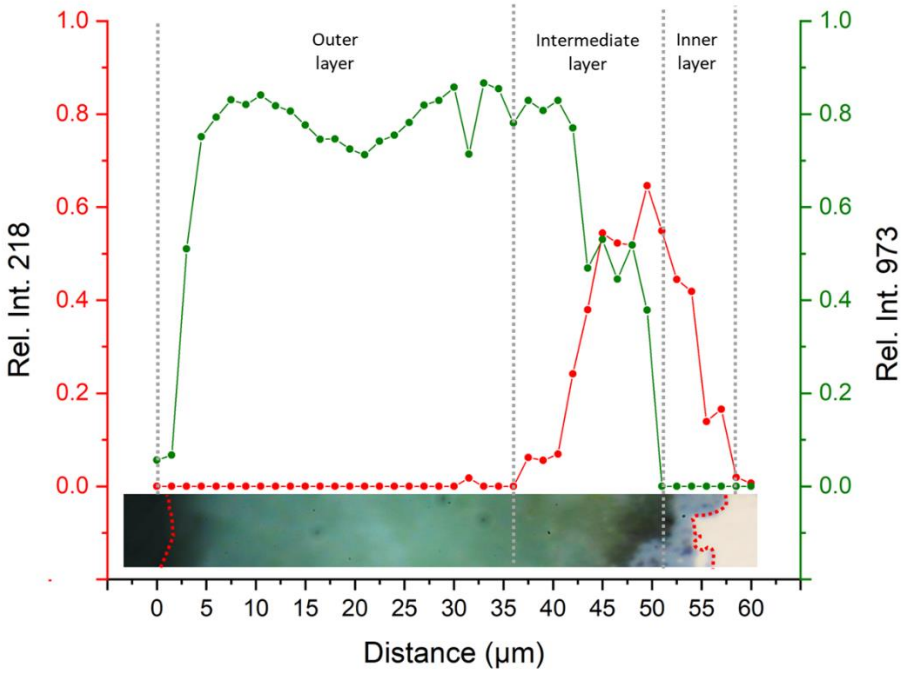

Figure 3. 58: Peak relative intensity profile for the peak at 973 cm^{-1}, relative to brochantite, and the peak at 218 cm^{-1} identifying cuprite. An overlap of brochantite and cuprite can be observed between the two layers suggesting the common presence of the two phases.

The profile shows an outer layer where only the peak at 973 cm^{-1} is present and an inner layer where the main peak is at 218 cm^{-1}. The two peaks overlap over approximately 10 to 15 µm in thickness, indicating the presence of both mineral phases at the interface.

2.4.4 Morphology and porosity

The morphology and porosity of the corrosion layer are investigated. By observing SEM micrographs, it is evident that the outer layer is highly porous at the micrometric scale. Pores and perpendicular cracks running perpendicularly or parallel to the surface are a common feature (Figure 3.59). The area occupied by pores and cracks is estimated on secondary electron images using image contrast. Results show that pores' surface represents more than 30% of the outer corrosion layer, thus confirming visual observations.

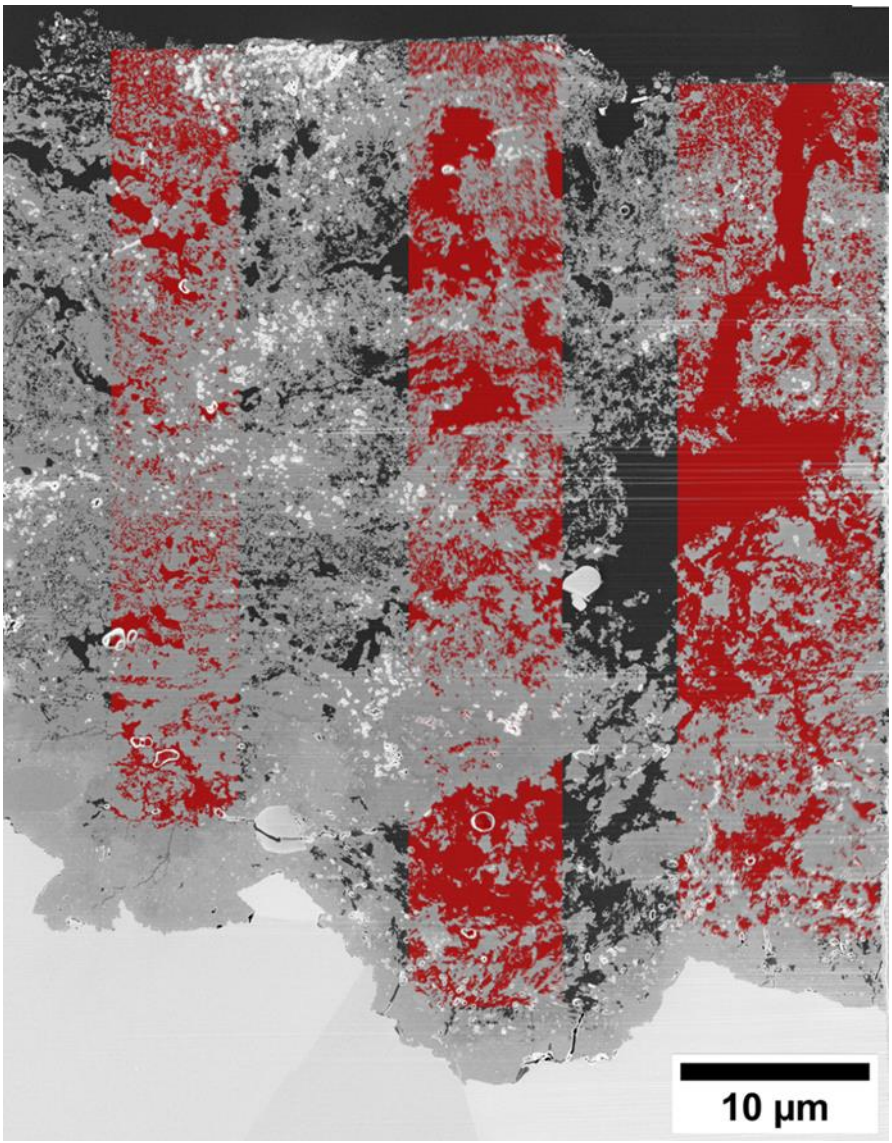

Figure 3. 59: SE image of the corrosion layer after FIB abrasion. In red, the porosity within the brochantite layer for calculating total pore areas is highlighted.

An examination at higher magnification of the morphology of the cuprite layer is possible by analysing the thin section obtained by FIB abrasion at the metal/cuprite/brochantite interface. The STEM image of the abraded area is shown in Figure 3.60.

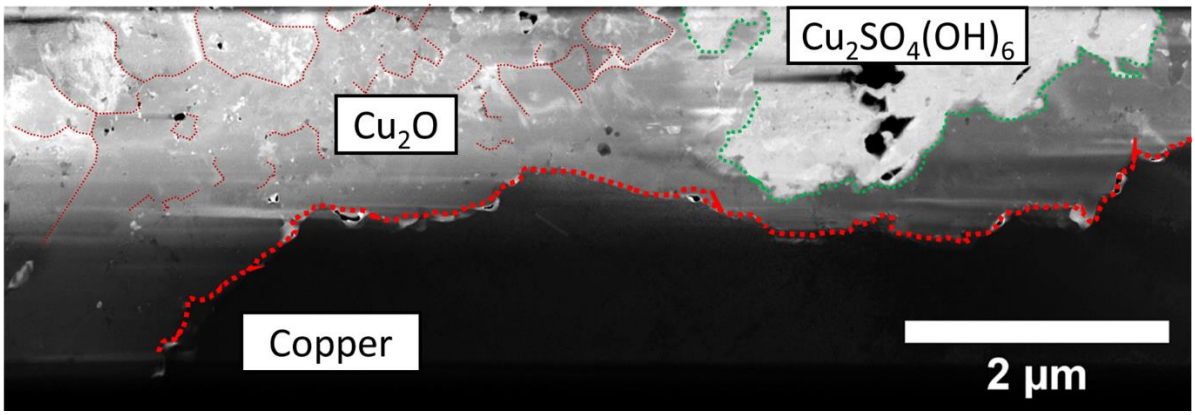

Figure 3. 60: STEM image of the thin section obtained at the Copper/Cuprite/Brochantite interface. The different greyscale corresponds to material density with the metal appearing black, Cu_2O dark grey and $Cu_4SO_4(OH)_6$ light grey.

As it is obtained in transmission mode, the denser copper substrate in the lower part of the image appears black, while less dense areas such as brochantite are brighter. In the left side of the image, a thicker cuprite layer is found. This part of the layer is characterized by the presence of a continuous compact and uniform area in contact with the metal of about 0.5 to 1 µm where no grain boundaries can be recognized. In the upper part, an area characterized by well recognizable polygonal-shaped grains boundaries is observed. Part of the grains is characterized by a lighter colour compared to bulk cuprite. The right side of the image shows an area where cuprite layer is thinner (less than 500 nm) on top of which a lighter area corresponding to brochantite is highlighted by the green dotted line.

The porosity of the inner compact cuprite layer (Figure 3.61) is investigated by FIB-tomography in order to understand its porosity and the eventual connectivity among the pores at the nanometric scale.

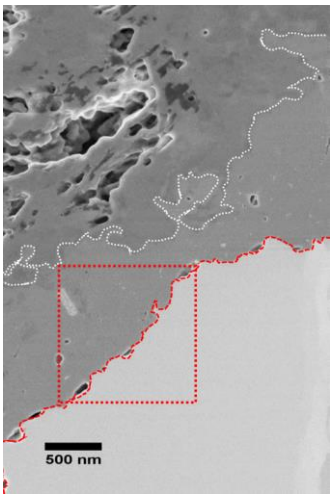

Figure 3. 61: Image of the area selected (red square) for the data treatment. Pixel size of the SE images is 2 nm.

This methodology allows to define pores of a minimum size of 10 nm. Figure 3.62 shows the volume reconstruction.

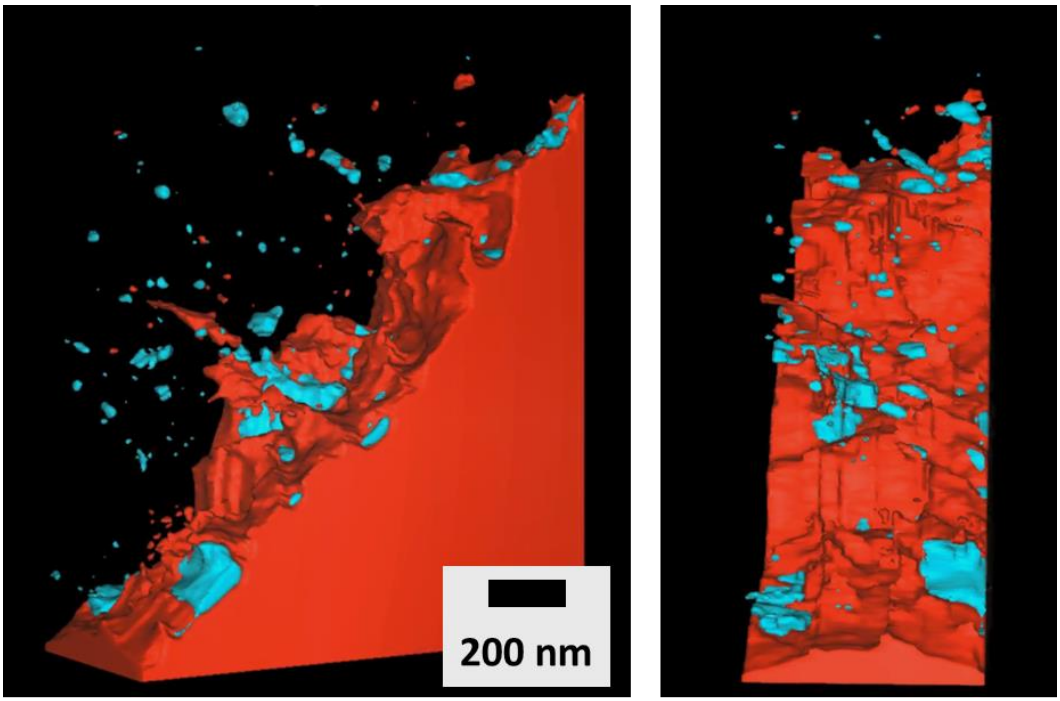

Figure 3. 62: FIB-tomography reconstruction of the area selected. The metal is represented in red while the porosity within the cuprite in light blue.

The metallic substrate is represented in red, while the light-blue shapes represent the pores within the cuprite layer. The total volume occupied by voids in the area analysed corresponds to 1.25% of the total cuprite volume, which represents a value considerably lower compared to the outer layer. Moreover, it is observed how larger pores (~100 nm) are located at the interface with the metal, while within the cuprite the pores are of smaller dimensions (few tenths of nm).

Finally, no network channels connecting pores is identified. As it is an imaging technique, the limit of the image resolution must be considered and the presence of smaller channels of less than 10nm cannot be completely excluded.

2.5 Summary of the results

In general, the structural and morphological characteristics of the Metz corrosion layer are typical of outdoor long-term exposed copper as in numerous studies the double-layered structure with inner cuprite and outer brochantite layer is described [8], [9]. One peculiar characteristic specified for the Metz samples is the interfacial layer where both cuprite and brochantite are present. Interestingly,

chlorine is also detected at the interface where it is present at a higher concentration compared to the other parts of the corrosion layer. The results will be further discussed in Chapter 4.

3. Metz samples after treatment

The next part includes the results obtained after the application of the treatments on the Metz samples. In particular, the changes in the physico-chemical properties before and after treatment are investigated.

3.1 Evaluation of the inhibition efficiency

A preliminary study by electrochemical analysis allow to determine the efficiency of the selected inhibitors solutions after being applied as pre-treatments and compare their protection upon immersion in synthetic acid rain. Part of the results included in this paragraph have been published in a recent paper, which is a result of a collaboration carried out during the PhD work [130]. Before performing Potentiodynamic polarization, the open circuit potential is followed over 1 hour before starting the experiment. Representative curves of potential vs time in open circuit conditions are presented in Figure 3.63.

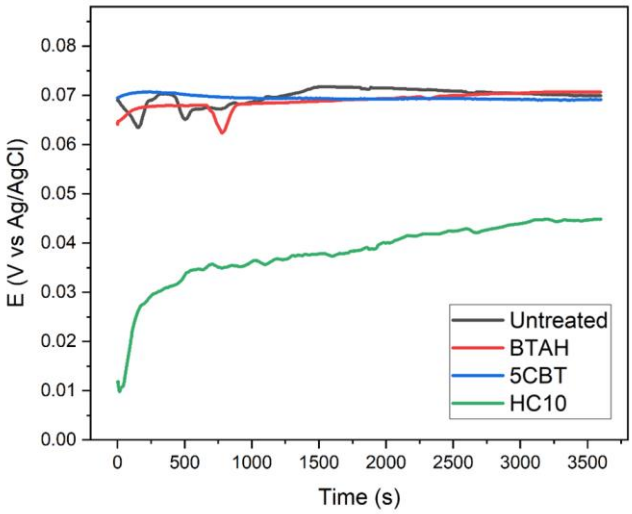

Figure 3. 63: Representative OCP measurement followed for 1 hour in acid rain solution for the different pre-treated samples.

At 1 hour the OCP potential value around 66 to 67 mV is comparable for the untreated, BTAH-treated and 5CBT-treated samples, while it is lower in the case of the HC10-treated sample.

Representative Tafel plots are shown in Figure 3.63 and the results of the interpolation and the calculated inhibition efficiency (IE%), are summarized in Table 3.9.

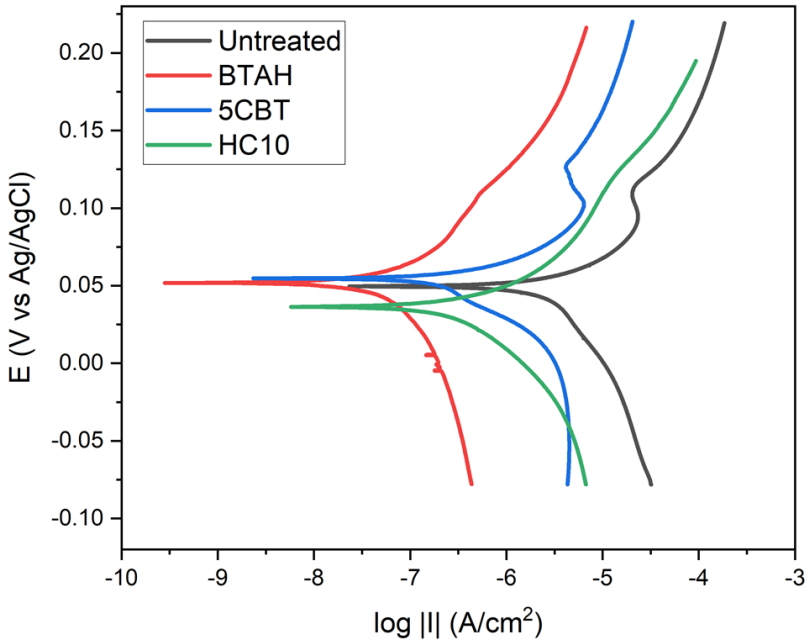

Figure 3. 64: Representative Tafel plots obtained for the untreated Metz sample (black), BTAH (red), 5CBT (blue) and HC10 (green).

Table 3. 9: Results obtained from the Potentiodynamic polarization experiment. Inhibition efficiency is calculated by comparison with the values obtained for the untreated sample.

	Eoc (mV)	Ecorr (mV)	Icorr (µA/cm²)	IE%
Untreated	66 ± 2	51 ± 2	2.38±0.07	
BTAH	66 ± 2	56 ± 3	0.032±0.002	98.8
5CBT	67 ± 3	55 ± 1	0.36±0.001	85
HC10	43 ±3	39 ± 2	0.14 ±0.01	94.2

All the compounds protect the sample from corrosion with a lower efficiency for the 5CBT (IE%=85%) and a higher performance for the BTAH-treated sample (IE%=99%). A high inhibition efficiency corresponding to 94% is calculated for the HC10-treated sample. A different behaviour can be observed for the different treatments concerning the potential: the two azoles shift the potential

towards the anodic values, while a shift towards cathodic values is observed for the HC10-treated samples.

Nevertheless, the shift is too small to proper categorize the inhibitors as having a cathodic or anodic influence on the corrosion reaction and a mixed-type behaviour is suggested especially for the two azoles.

The results confirm the efficiency of the three chosen compounds in limiting corrosion in the tested conditions. BTAH and HC10 as pre-treatments prove to be particularly efficient.

3.2 Physico-chemical characterization of the system after treatment

In this part, the results of the investigation of the Metz samples after immersion in solution containing the inhibitor are exposed. The first section includes surface and cross-section analysis, while the second focuses on the system description after a certain perturbation has been applied: immersion in D_2O water for the study of permeability (paragraph 3.2.3) and immersion in KBr solution for the study of passivity breakdown (paragraph 3.2.4).

3.2.1 Surface properties

The aesthetic aspect of the surface is often one of the first parameters that conservators consider when it comes to validate a conservation treatment.

Colour change of the treated samples is evaluated as a difference of colour measurement compared to the untreated Metz sample. The L*a*b* colour parameters as well as the colour difference (ΔE_{94}) are reported in Table 3.10 and are plotted in Figure 3.65.

Table 3. 10: L, a*, b* parameters before and after treatment. The colour difference is calculated based on the values of the samples before treatment.*

		L*	a*	b*	ΔL*	Δa*	Δb*	ΔE_{94}
BTAH	Untreated	72.2±1.1	-12.5±0.6	13.8±0.7				
	Treated	59.4±0.4	-18.0±0.6	16.1±0.2	12.8±1.5	5.5±0.6	-2.2±0.7	**13.3±1.4**
5CBT	Untreated	71.6±1	-12±0.4	14.4±0.3				
	Treated	59.3±1.9	-16.4±1.6	15.6±0.7	12.3±1.2	4.4±1.2	-1.2±0.9	**12.6±1.2**
HC10	Untreated	72±0.6	-12.1±0.4	14.2±1				
	Treated	65.5±0.6	-24.2±0.9	4.8±0.5	6.5±1	12.2±1.1	9.3±1.1	**13.3±1.1**

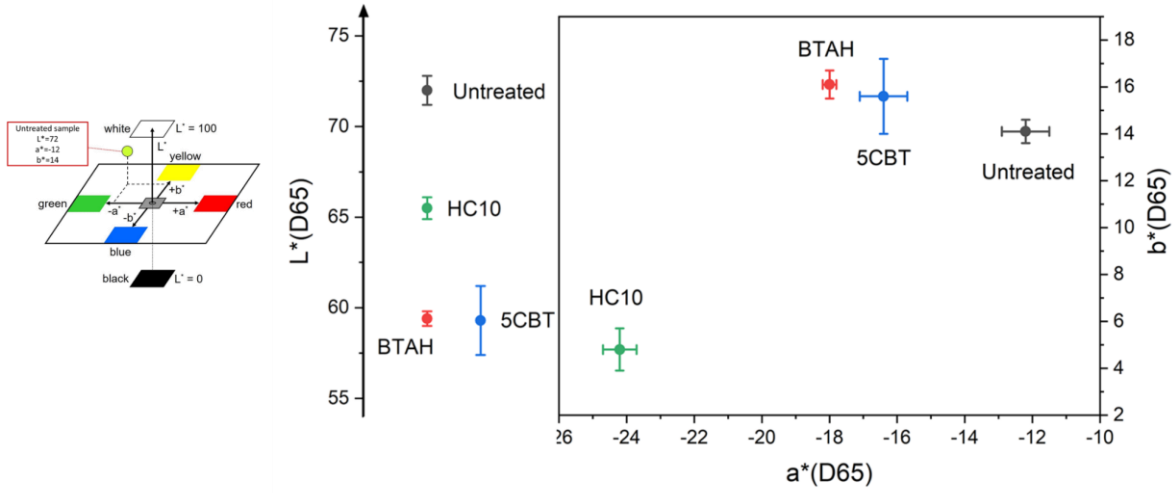

*Figure 3. 65: L*a*b* plot representing the mean value and relative standard deviation for each treatment.*

For all the treatments, a perceivable colour change of about 13 is measured, although different tendencies can be highlighted for BTAH and 5CBT vs the carboxylate treatments. Considering HC10 treatment, both a decrease in a* and b* parameters are observed: the a* variation testifies a shift to a greener hue, while a decrease in b* value indicates a shift towards a blue hue. The variation of brightness expressed by the L* parameter is less important compared to the azole treatments. BTAH and 5CBT treatments both lead to a comparable tendency in the colour parameters' variation: if a*

and b* values are not particularly affected, L* is considerably reduced (more than 10 units) resulting in an important darkening of the (green) surface colour.

After treatment, an evaluation of the wettability of the surface is performed by the sessile drop method (Figure 3.66).

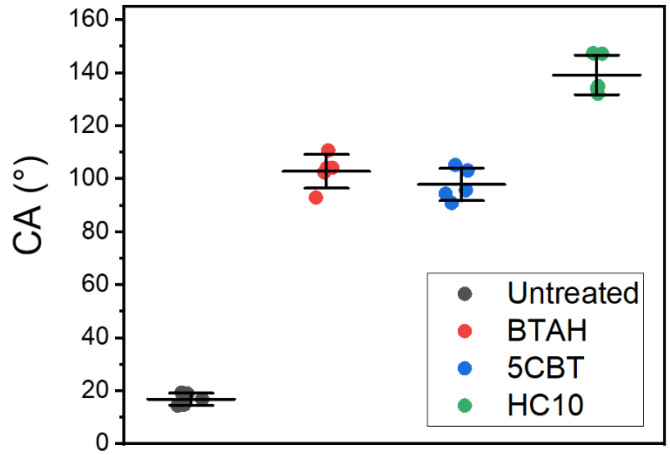

	Contact angle (°)	
Untreated	17 ± 2	
BTAH	103 ± 6	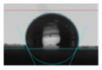
5CBT	98 ± 6	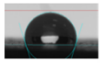
HC10	139 ± 7	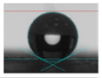

Figure 3. 66: Mean contact angle calculated on 5 measurements for each treated sample.

The contact angle of the untreated sample is below 20°, which testifies the hydrophilic behaviour of the outer surface. After all treatments, the surface contact angles higher than 90° are measured. Contact angle for BTAH and 5CBT treated surfaces are comparable (about 100°), while very high contact angles (~140°) are measured in the case of the HC10-treated surface. The high surface tension for the samples treated with HC10 is evident during the experimental procedure as it is difficult to place the water drop on top of the surface.

The global information obtained on colour and surface tension are particularly interesting when compared to microscopic observations of the surface by secondary electron images.

In Figure 3.67, secondary electron images of the surface at lower (a) and higher (b) magnification are presented.

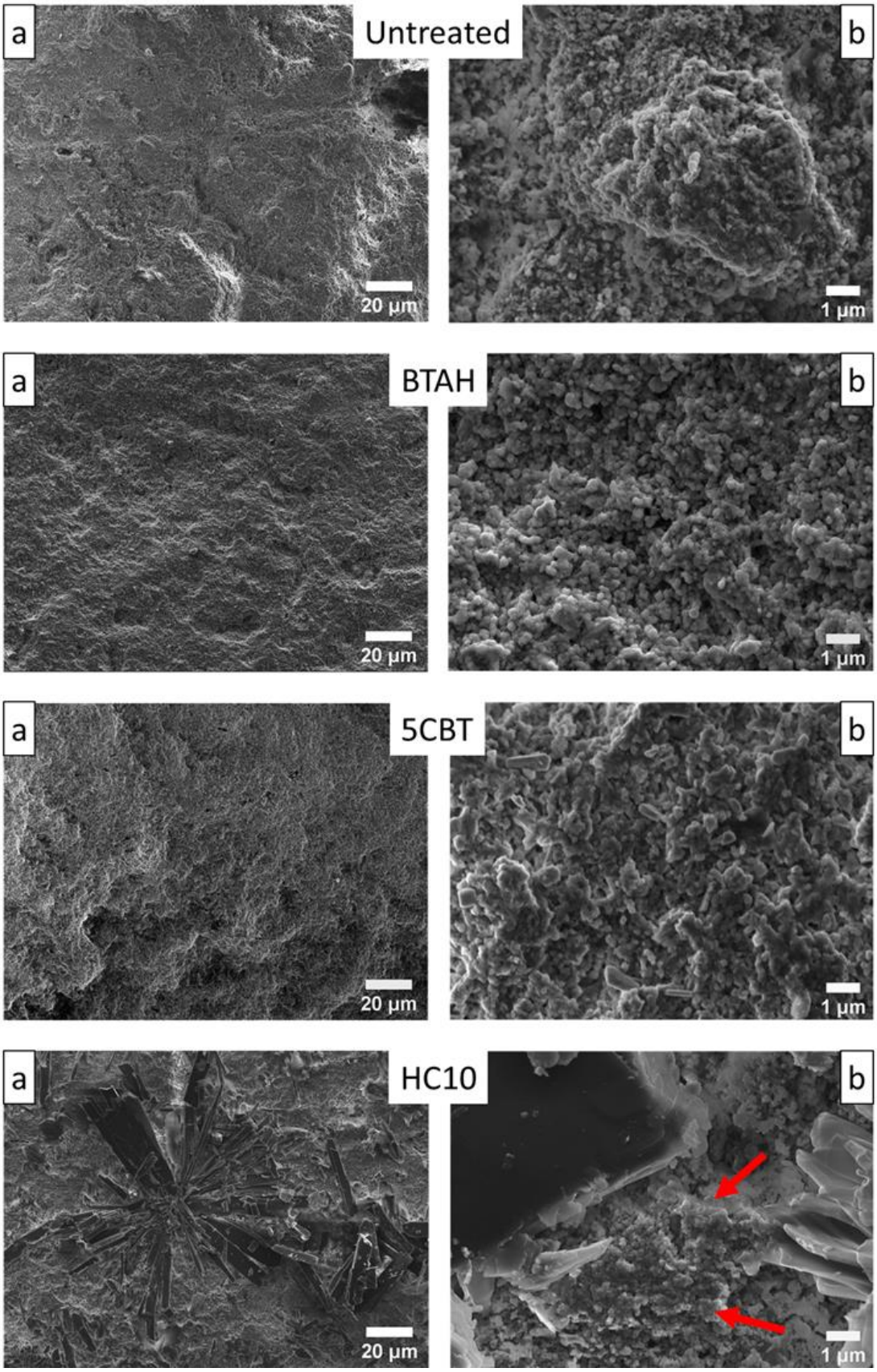

Figure 3. 67: Surface morphology at low (a) and high (b) magnification. SEM-SE, WD=5, 5 kV.

A similar morphology can be observed in the case of the untreated, BTAH-treated and 5CBT-treated samples. At higher magnification (Figure 3.67UT-b), to the untreated sample revealed that the surface is characterized by aggregates of rounded-shaped particles with a diameter of about 0.1 µm. The same morphology is observed after treatment with BTAH and 5CBT. Different considerations can be drawn for the sample treated with HC10 solution. Here, even at lower magnification (Figure 3.68) flower-like shaped crystals aggregates randomly distributed on the surface are observed. The crystals have an elongated shape (41 ± 15 µm in length, 6 ± 2 µm in width). At higher magnification it is possible to observe how the crystals do not entirely cover the surface and the rounded particles like those observed for the untreated sample are still present here (Figure 3.67HC10-b red arrows).

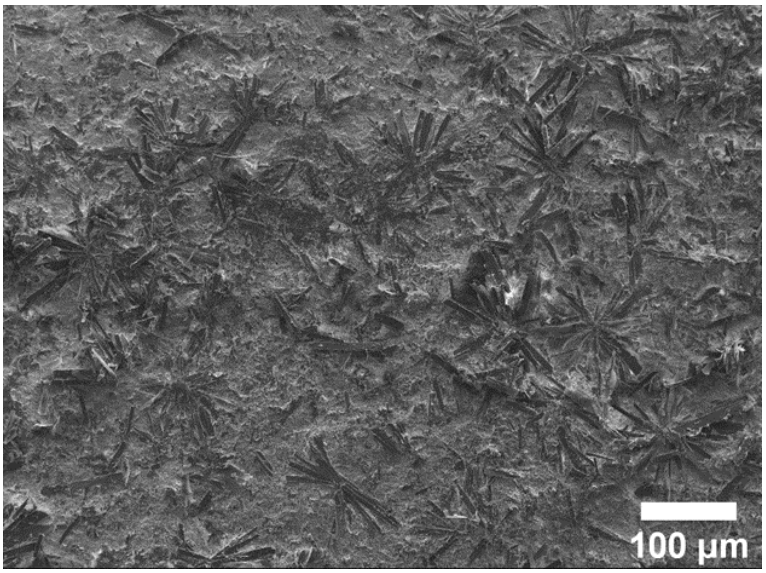

Figure 3. 68: Surface morphology at low magnification of the HC10-treated sample. SEM-SE, WD=5, 5 kV.

The effect of the treatment on the surface structural composition is investigated by µRaman spectroscopy. Representative Raman spectra obtained on the surface (red line) are compared to the respective reference compounds (black line) (Figure 3.69).

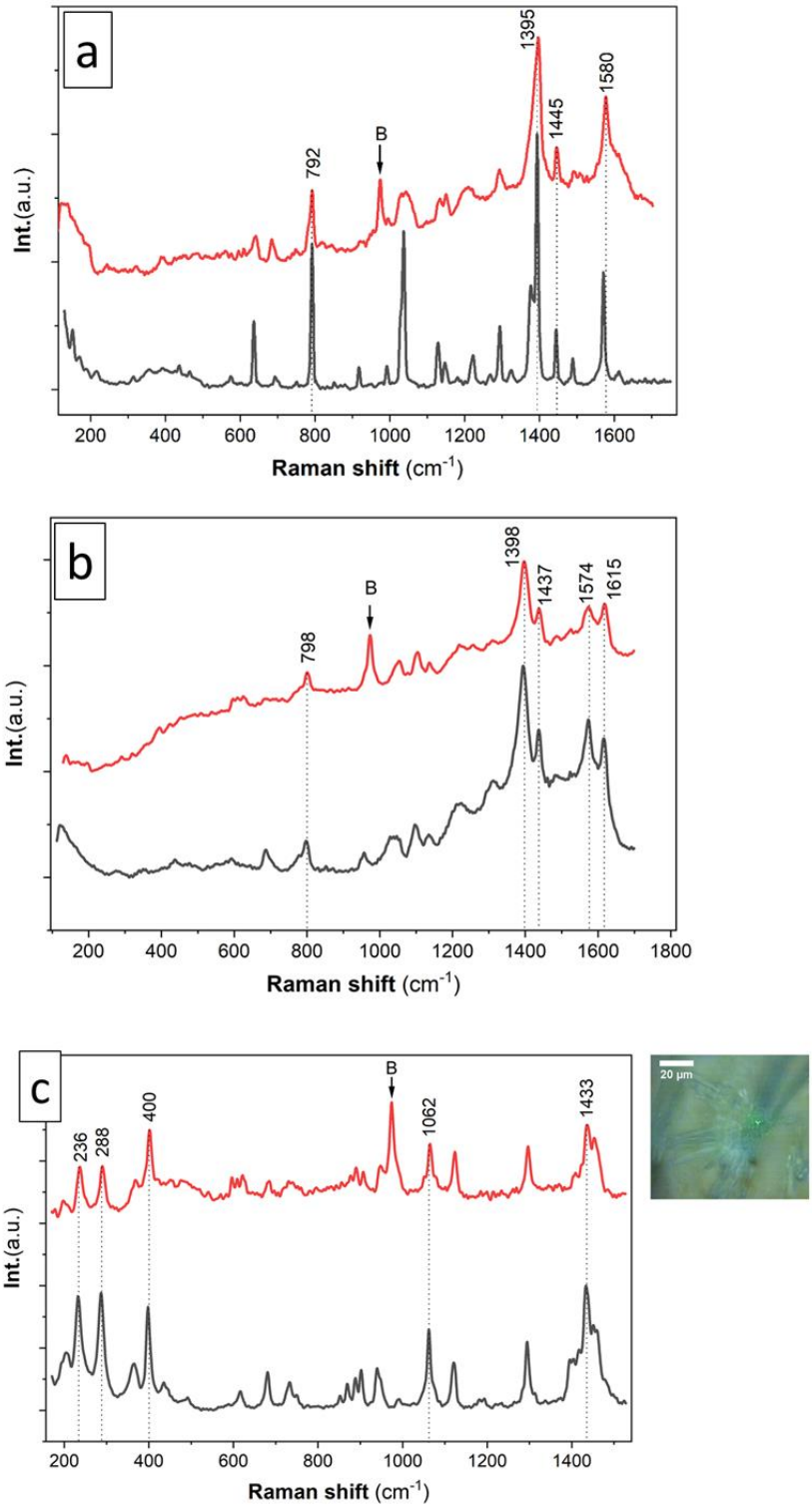

Figure 3. 69: Representative Raman spectra (red trace) obtained on the samples' surfaces of the BTAH-treated (a), 5CBT-treated (b) and HC10-treated samples. Reference spectra of the respective Cu-complex are reported (black trace).

BTAH-treated surface spectrum (Figure 3.69-a) is characterized by the peak at 973 cm^{-1} corresponding to brochantite and other peaks are observed that correspond to the formation of a Cu-BTA coordination compound, in particular, the strong shift at 1395 cm^{-1}. Similar observations are made when analysing the surface spectrum of the 5CBT-treated sample. Brochantite is again detected and other shifts, among which the strong peak at 1398 cm^{-1}, are attributed to the formation of a Cu-5CBT compound (Figure 3.69-b).

The identification of the surface crystals observed on the HC10-treated sample is achieved thanks to their microscopic dimensions as the laser can be directly pointed to at one crystal aggregate for analysis (Figure 3.69-c optical image). The crystals are unambiguously identified as copper decanoate as it results from the comparison with the reference spectrum corresponding to synthetic copper decanoate (Figure 3.69-c blue line).

3.2.2 Morphological and structural properties in cross-section

The cross-section micrographs in backscattered mode allowed to evaluate the morphology of the corrosion layer. Again, as for the untreated sample, a double-layered structure is identified. The distribution of the major elements within the corrosion layer is very similar among the different treatments and reflects what already observed in cross-section for untreated Metz samples (EDS maps after treatment are reported in Annex 2).

The thickness of the outer and inner layers after treatment is evaluated on SEM micrographs and results of these measurements are presented in Figure 3.70.

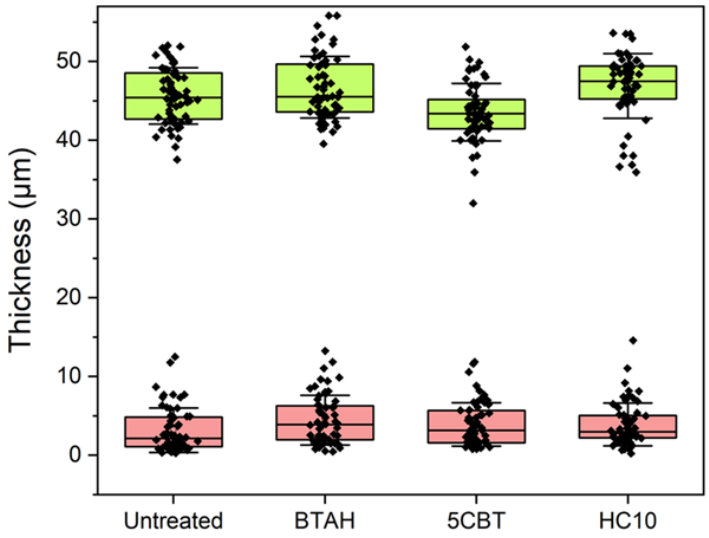

	Untreated	BTAH	5CBT	HC10
Outer layer (µm)	45.6 ± 3.6	46.7 ± 3.9	43.5 ± 3.6	46.9 ± 4.1
Inner layer (µm)	3.2 ± 2.8	4.5 ± 3.1	3.9 ± 2.8	3.9 ± 2.7

Figure 3. 70: Thickness measurements for all the samples compared. Mean thickness values are reported in the table.

The thickness of the inner layer is slightly higher for the treated samples with the high value obtained for the BTAH-treated cross-section (4.5 ± 3.1 µm), while a thickness of about 4 µm is detected for the 5CBT and HC10-treated samples. The high thickness inhomogeneity that characterizes the untreated samples is not affected. The outer layer values are also comparable except for the 5CBT-treated sample where a thickness of the outer layer corresponding to 43.5 ± 3.6 µm is measured against the 46 to 47 µm of the untreated, BTAH and HC10-treated samples. In general, the variations between untreated and treated samples are low and they can reasonably be ascribed to the variability within the naturally formed corrosion layer.

Concerning the outer layer morphology, the porosity and pore network observe for the untreated sample are still present and do not seem to be affected by any of the treatments at the micrometric scale of the analysis (Figure 3.71).

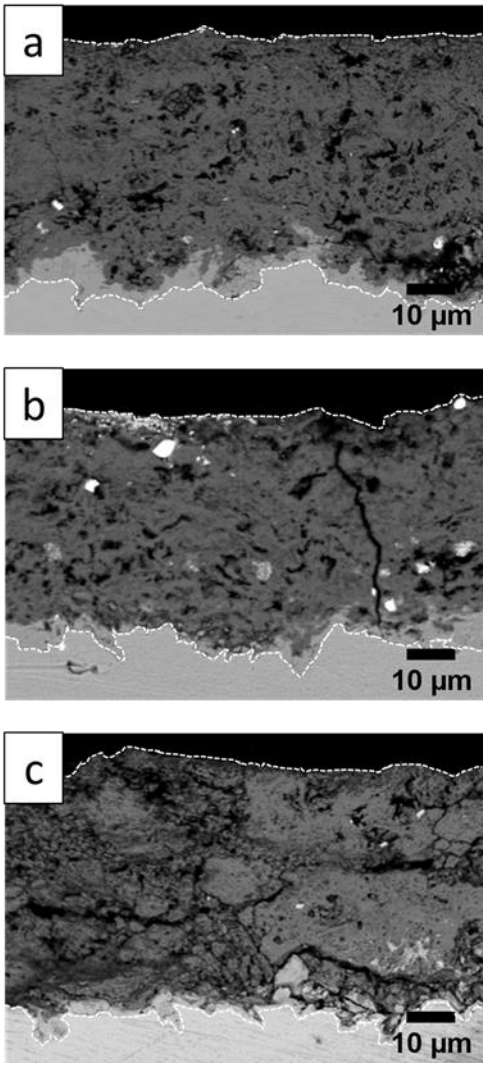

Figure 3. 71: Micrographs of the cross-section relative to a) BTAH-treated sample; b) 5CBT-treated sample and c) HC10-treated sample. 10 kV, SEM-BSE.

Regarding the interaction of the inhibitor and the corrosion layer, on the surface the presence of a new phase in addition to brochantite has been pointed out by surface Raman spectra. The structural analysis in cross-section allows to study and locate structural changes within the corrosion layer after interaction with the inhibitor solution and Raman maps are reconstructed based on selected peaks for each of the compounds detected.

Figure 3.72 shows the optical image (left) and a representative Raman mapping (right) for the sample treated with BTAH.

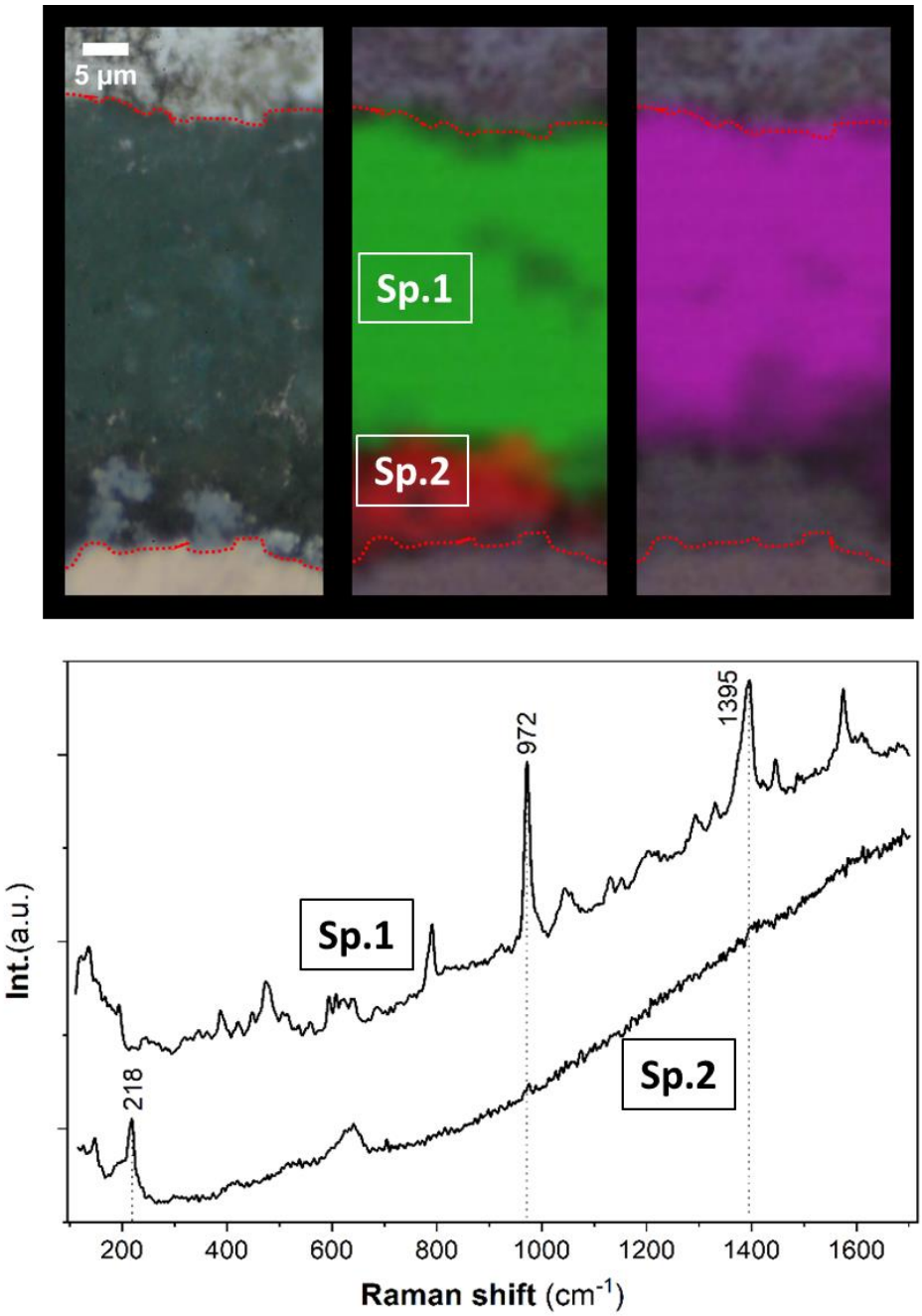

Figure 3. 72: Raman mapping of the corrosion layer (left image). The green and red areas correspond to brochantite and cuprite respectively. The violet area identifies the peak at 1395 cm^{-1}. The spectra are representative of the outer (Sp.1) and the inner layer (Sp.2).

The two mineral phases are identified: the region in red correspond to the peak at 218 cm^{-1} characteristics of cuprite, while the region in green correspond to the peak at 973 cm^{-1} characteristic of brochantite. In addition, as previously observed on the surface, other peaks are identified. The violet map is reconstructed based on the peak at 1395 cm^{-1} representative for the complex Cu-BTA. The maps of brochantite and that of the Cu-BTA overlap. This is confirmed by the intensity profile extracted from peaks representative of each phase (Figure 3.73).

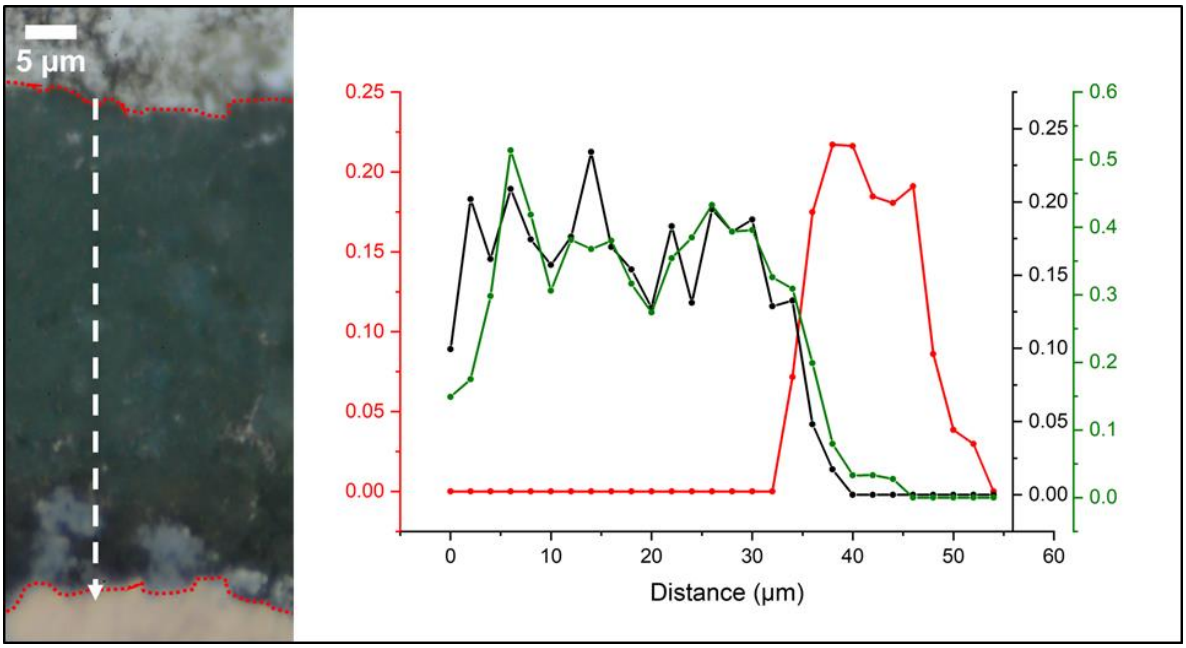

Figure 3. 73: Profiles of the peak intensity profile for the Raman shifts at 218 cm^{-1} (red), 973 cm^{-1} (green) and 792 cm^{-1} (black). The outer surface is considered at 0 µm.

The intensity of the peak at 218 cm^{-1} (red), 973 cm^{-1} (green) and 792 cm^{-1} (black) are plotted as a function of distance from the surface. The shift at 792 cm^{-1} is preferred as it is narrower compared to the one at 1395 cm^{-1}. The relative intensity of the two peaks identifying brochantite and Cu-BTA respectively follow a similar profile confirming the presence of both compounds from the outer zone to the interface with the cuprite.

The Raman analysis in cross-section of the sample treated with 5CBT is presented in Figure 3.74.

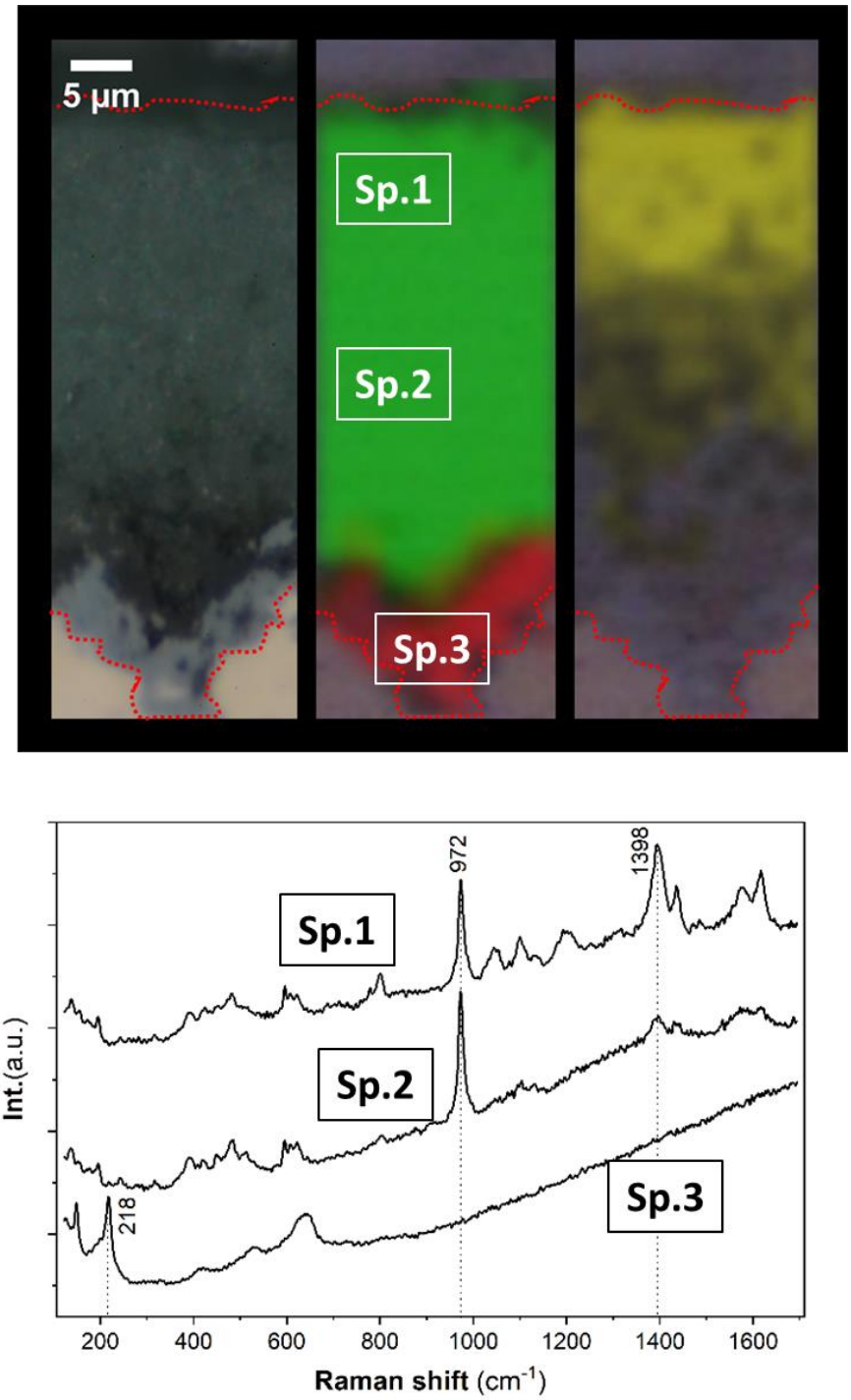

Figure 3. 74: Raman mapping of the corrosion layer (left image). The green and red areas correspond to brochantite and cuprite respectively. The yellow area identifies the peak at 1389 cm^{-1}. The spectra are representative of the outer (Sp.1), mid (Sp.2) and the inner layer (Sp.3).

The double layer cuprite/brochantite is again identified. The shifts corresponding to the newly formed phase Cu-5CBT (in yellow in the map) are only identified in the outer part of the brochantite layer at about 20 µm from the surface. This behaviour is even more evident when considering the intensity profile (Figure 3.75).

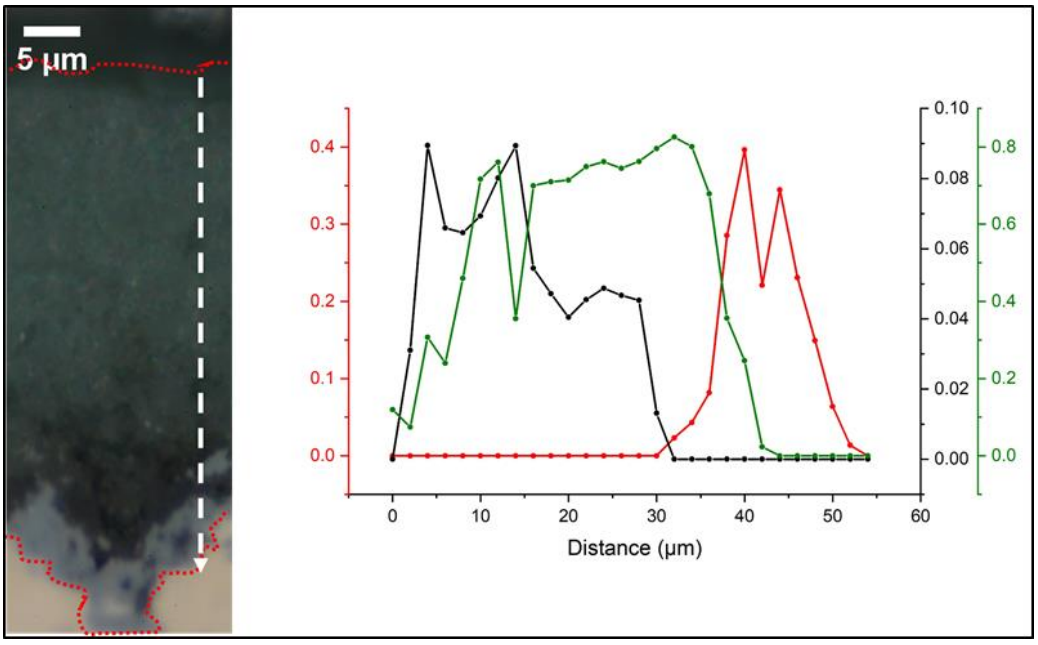

Figure 3. 75: Profiles of the peak intensity profile for the Raman shifts at 218 cm^{-1} (red), 973cm^{-1} (green) and 800 cm^{-1} (black).

Here again, red and green line identify the intensity of brochantite and cuprite main shifts respectively. The intensity of the peak at 800 cm^{-1}, related to the Cu-5CBT, is represented in black and, unlike for BTAH, the profile line intensity decreases at 15 µm from the surface and is absent at 30 µm, inside the brochantite layer.

The results of the Raman analysis on the cross-section of the HC10-treated sample (Figure 3.76) show that the outer and inner layers are identified as the only phases present. Despite the identification of copper decanoate on the surface, the corresponding frequencies are not found inside the corrosion layer.

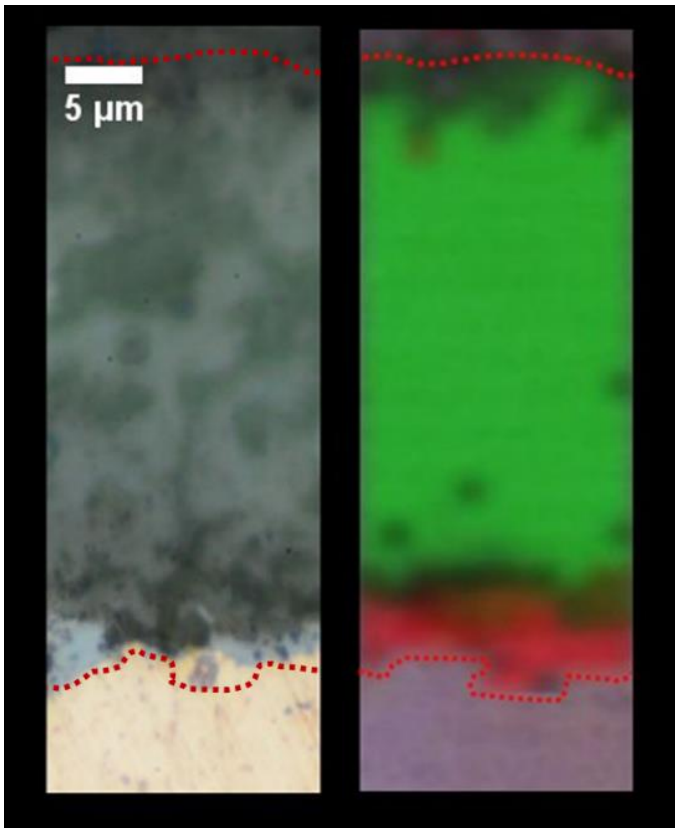

Figure 3. 76: Raman mapping of the corrosion layer (left image). The green and red areas correspond to brochantite and cuprite respectively.

3.2.3 Permeability of the treated samples

The ability of the treated corrosion layer to modify the liquid water intake tendency is studied by immersion in marked (D_2O) solution for 30 days and further Tof-SIMS analysis in cross-section. The outer and inner layer are distinguished thanks to the presence of different negative fragments (S^- for the brochantite layer and CuO^- for the cuprite layer) and the data corresponding to the enrichment in areas corresponding to the outer and inner layer can be extracted from the total map (Figure 3.77 overlay images). An enrichment in deuterium (δ_n) is then calculated for each ROI normalized to the ratio obtained for the corresponding not immersed samples (see methodology in Chapter 2).

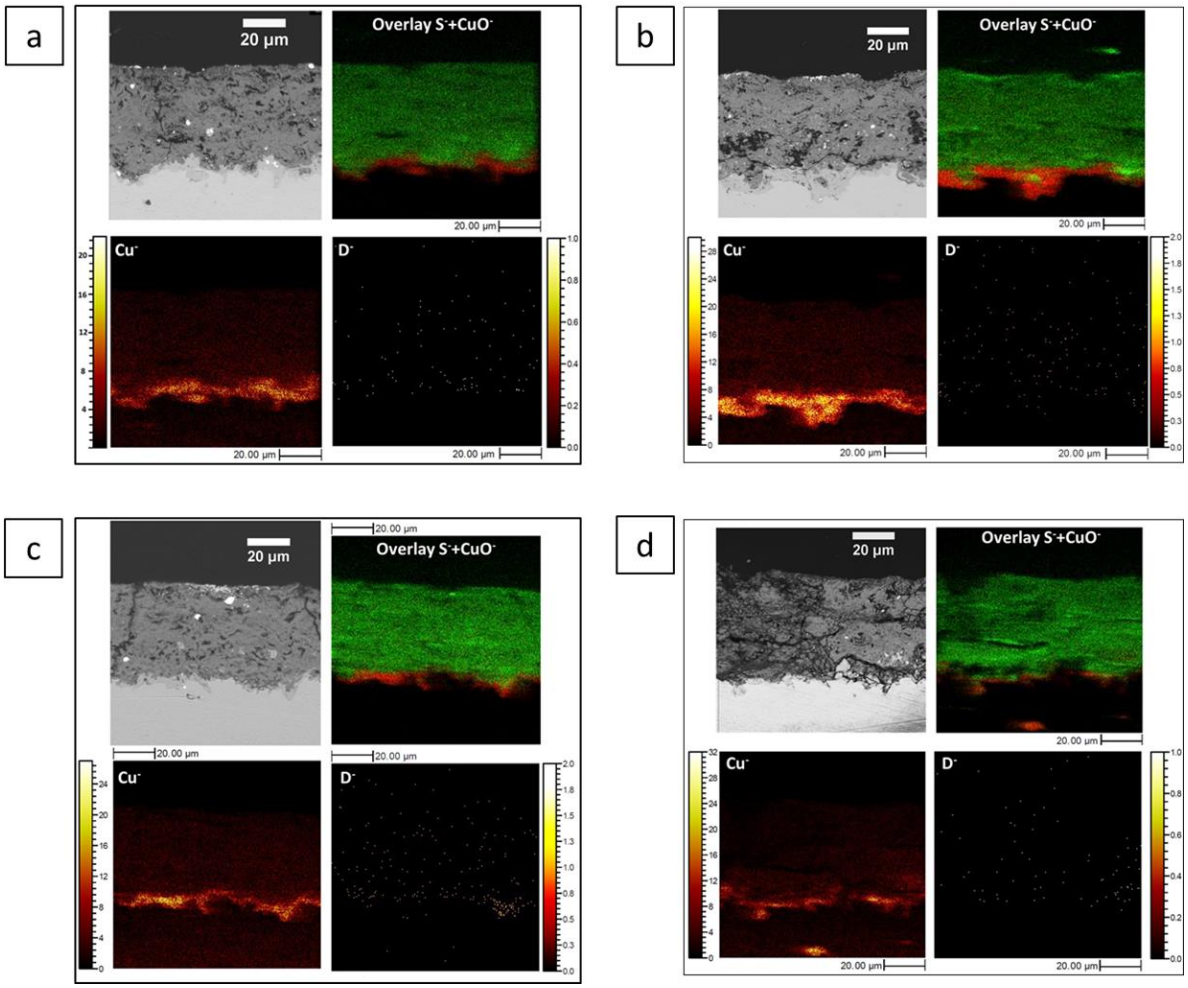

Figure 3. 77: Negative ions images and overlay for the a) untreated, b) BTAH-treated, c) 5CBT-treated and d) HC10-treated samples. Tof-SIMS.

The results for both regions of interest (brochantite and cuprite) are summarized in Table 3.11.

Table 3. 11: Enrichment values calculated in both the outer and inner layer for the untreated and treated samples.

δ_n	ROI brochantite	ROI cuprite
Untreated	1264 ± 148	999 ± 471
BTAH	1014 ± 97	205 ± 104
5CBT	1879 ± 251	1056 ± 703
HC10	1300 ± 131	1842 ± 1246

In the outer brochantite layer (Figure 3.78), the enrichment values of untreated (δ_n=1264 ± 148), BTAH-treated (δ_n=1014 ± 97) and HC10-treated samples (δ_n=1300 ± 131) are comparable; in the case of 5CBT treatment a higher value (δ_n=1879 ± 251) is found.

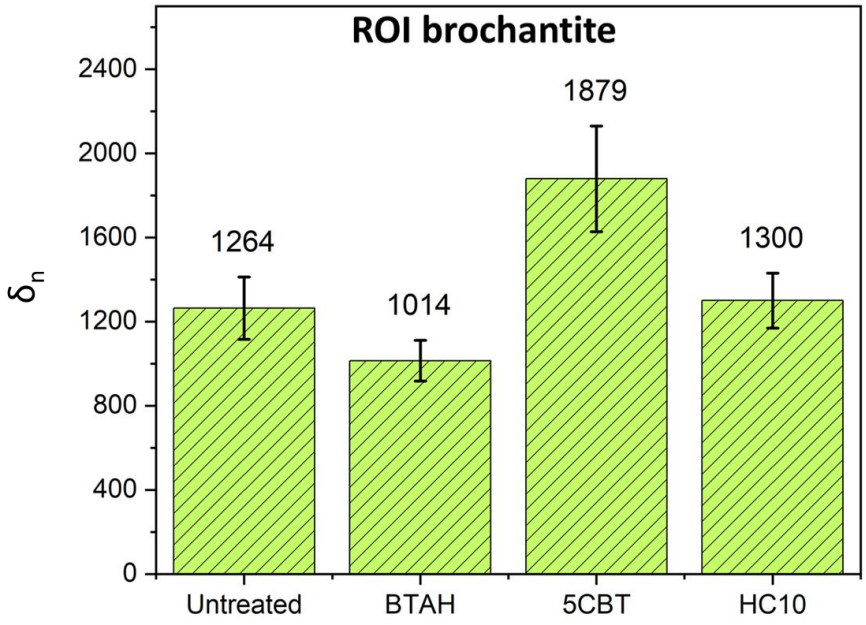

Figure 3. 78: Comparison of the deuterium enrichment (δ_n) within the outer brochantite layer for the untreated and treated samples.

For the cuprite layer (Figure 3.79), similar values of enrichment are found for the untreated (δ_n=999 ± 471) and the 5CBT-treated sample (δ_n=1056 ± 703), although a higher error is registered for the latter. Interestingly, the sample treated with BTAH has a considerably lower enrichment of the cuprite layer (δ_n=205 ± 104), while the HC10-treated sample shows the highest value (δ_n=1842 ± 1246) as well as an important variability.

A consideration must be done on the error found for the cuprite region of interest. The higher values when compared to those obtained for the outer sulphur-rich region can be related to the lower number of counts related to the low area included in the cuprite ROI.

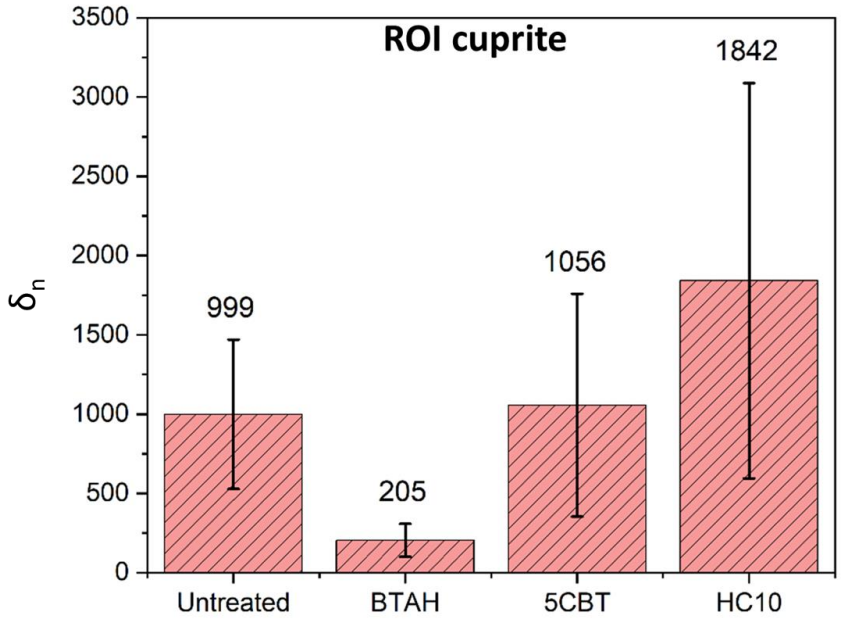

Figure 3. 79: Comparison of the deuterium enrichment (δ_n) within the inner cuprite layer for the untreated and treated samples.

3.2.4 Re-corrosion in aggressive environment

In the following paragraphs, the physico-chemical modifications occurring on the Metz corrosion system untreated and treated with the different inhibitors after a perturbation induced by immersion in 1.3 M KBr solution for 30 days are exposed. The samples have been characterized following a similar procedure on surface and in cross-section to the one employed until now and a comparative approach is used to evidence differences and similarities with the behaviour of the untreated sample.

After immersion, the surface is observed using optical microscopy (Figure 3.80).

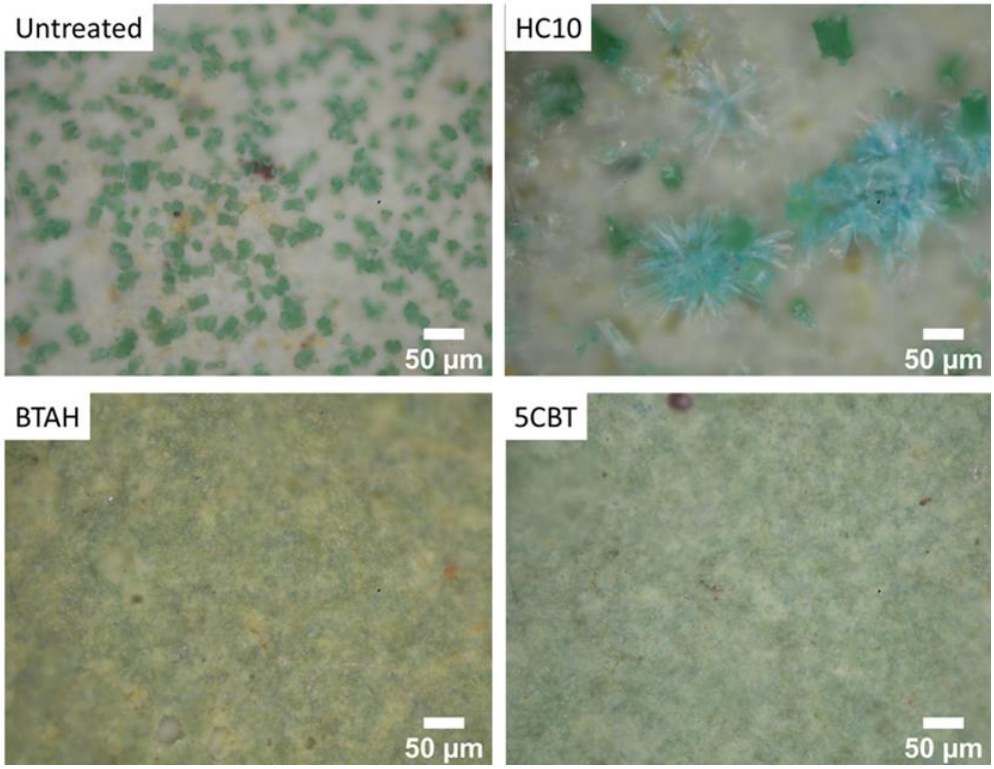

Figure 3. 80: Optical images of the untreated and treated samples' surfaces after KBr immersion.

In the optical images, the presence of dark green crystals is evident for the untreated sample and similar crystals are observed on the HC10-treated sample together with blue crystal aggregate. The green crystals are not visible on the BTAH-treated and the 5CBT-treated samples. By performing µRaman spectroscopy on the surface crystals (Figure 3.81-a), it is possible to identify a new compound. The phase probably corresponds to a copper hydroxy bromide for the similarity to other copper hydroxy halides such as botallackite (red spectrum in Figure 3.81-a). The same compound is identified on the surface of the HC10-treated sample. The blue crystals are identified as copper decanoate (Figure 3.81-b red spectrum).

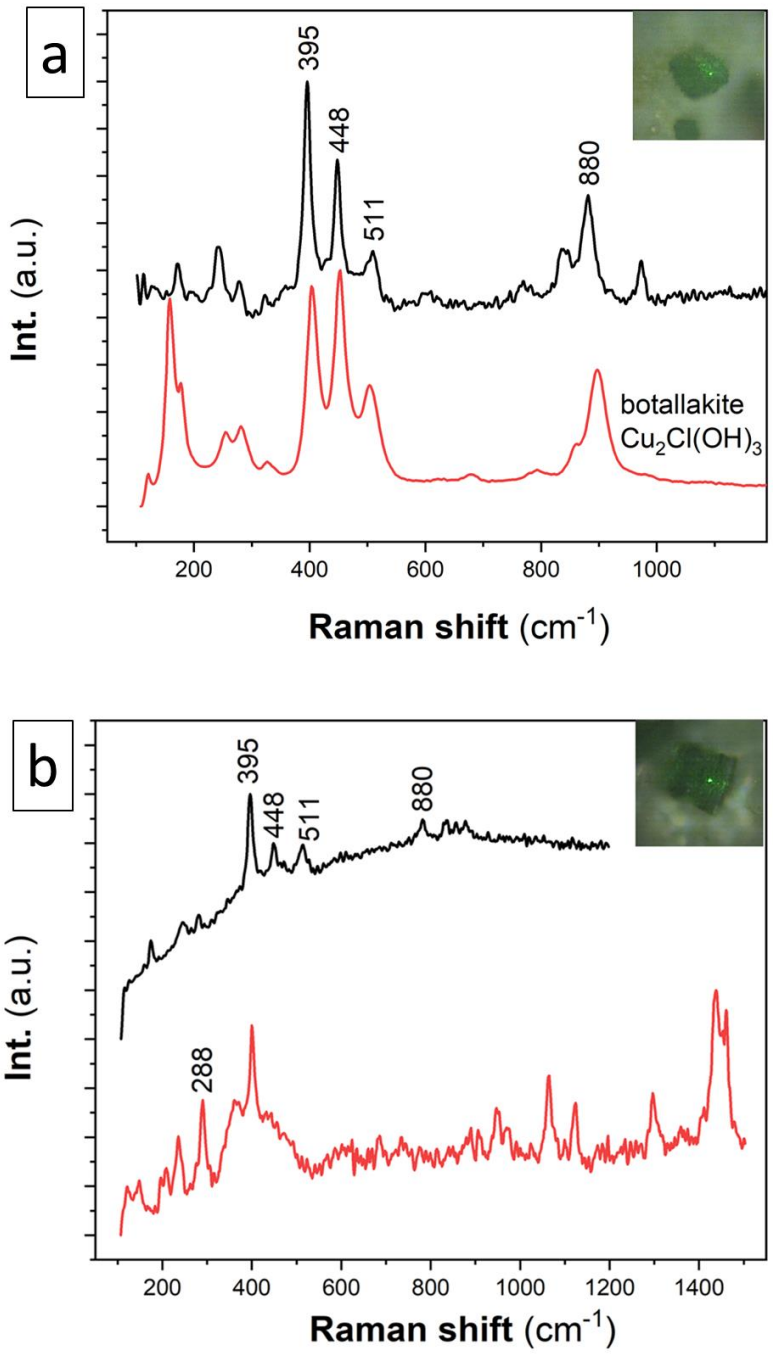

Figure 3. 81: Identification of the surface green crystals by µRaman spectroscopy on the untreated (a) and on the HC10-treated (b) samples. In (b) the red spectrum corresponds to the blue particles and copper decanoate Is identified. The reference botallackite corresponds to the specimen RRUFF-R070066.

The SEM analysis in cross-section allow to identify changes in the morphology and in the elemental composition within the corrosion layer. First, Figure 3.82, shows the backscattered electron images of the samples after immersion in KBr.

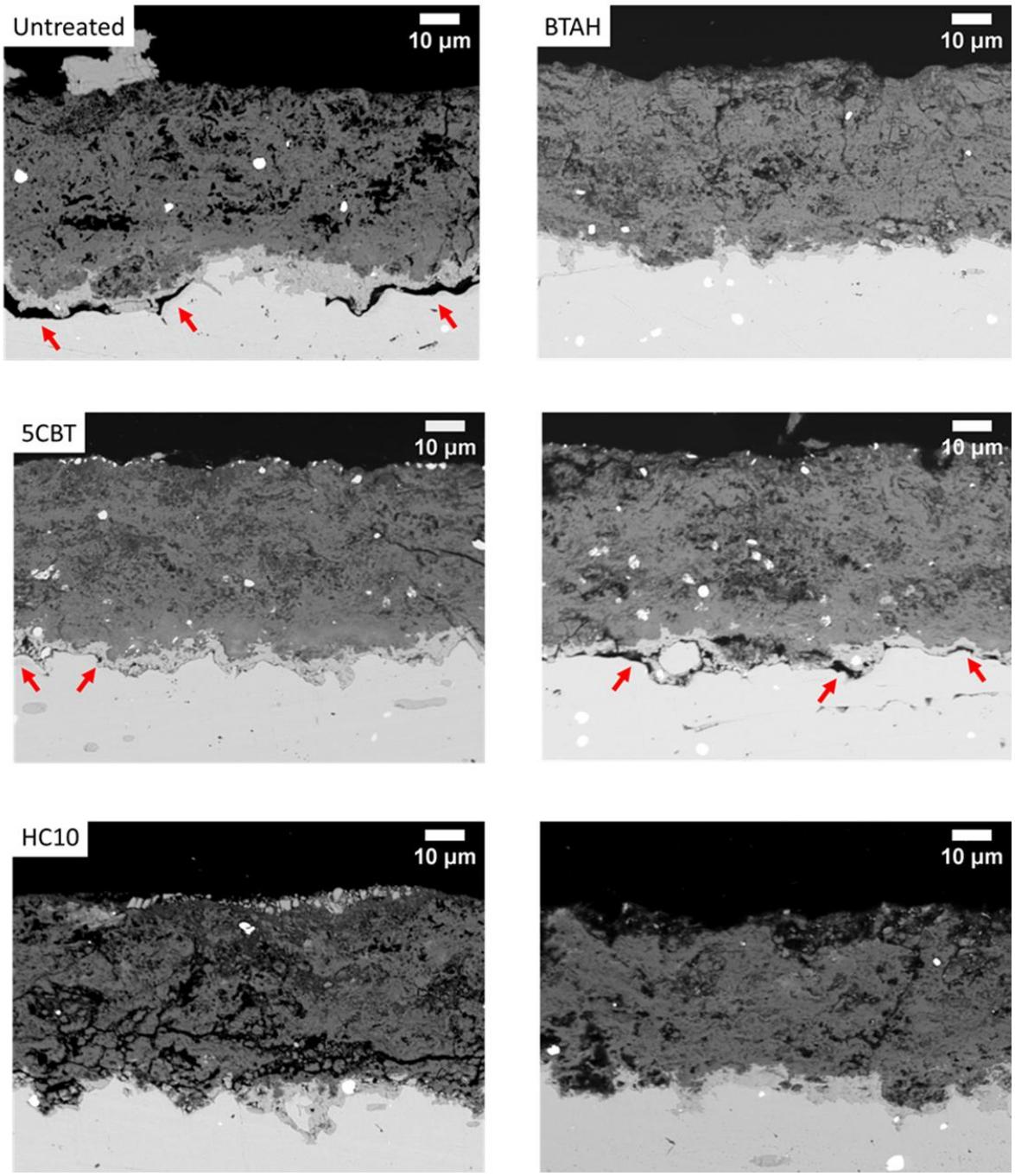

Figure 3. 82: Cross-section backscattered electron images of the samples after KBr immersion. SEM-BSE, 10 kV.

The first picture is representative of the untreated sample: large crystals are identified on the surface and, more interestingly, voiding formation between the metal and the cuprite layer is observed as black areas few micron-thick (red arrows). In some parts, the connection between cuprite and metal is maintained such as in the central part of the image.

The second picture on top, represent the BTAH-treated sample. Here, no morphological changes are detected. The 5CBT-treated sample is similar to BTAH, but some voiding is locally observed at the interface between metal and cuprite. Their thickness is limited compared to the untreated sample.

The HC10-traeated sample exhibits surface crystallization as previously determined and, at the same time, no voiding is observed at the interface. Locally, the outer layer appears more porous (left image).

The distribution of elements in cross-section is studied by EDS analysis. Figure 3.83 shows the results for each sample with an overlay of the secondary electron image and the map of bromine (left side) and the maps corresponding to the major elements (right side). The distribution of S, O, Cu and Cl are similar to what previously observed. The new element bromine is detected at different positions inside the corrosion layer. As it is reasonable, the crystals on the surface of the untreated and HC10-treated samples present a high concentration of bromine as highlighted in the overlay images. A relatively higher amount of bromine is detected at the brochantite/cuprite interface: 1.8%wt of bromine is present at the interface in the untreated sample and 2.4%wt is detected at the same interface in the 5CBT-treated sample. The enrichment is not detected for the BTAH-treated and the HC10-terated samples. A very low amount of bromine characterizes the brochantite layer in all samples (Table 3.12).

Table 3. 12: Results of the bromine identification inside the brochantite layer (left) and at the interface cuprite/brochantite (right) calculated from three EDS maps for each sample.

Outer layer			Interfacial layer		
	Br L %wt	**K K %wt**		**Br L %wt**	**K K %wt**
Untreated	0.15 ± 0.02	0.23 ± 0.03	**Untreated**	1.84 ± 0.7	0.28 ± 0.01
BTAH	0.39 ± 0.25	0.32 ± 0.12	**BTAH**	0.32 ± 0.10	0.30 ± 0.03
5CBT	0.28 ± 0.11	0.17 ± 0.05	**5CBT**	2.36 ± 0.37	0.17 ± 0.08
HC10	0.34 ± 0.15	0.24 ± 0.01	**HC10**	0.41 ± 0.05	0.28 ± 0.01

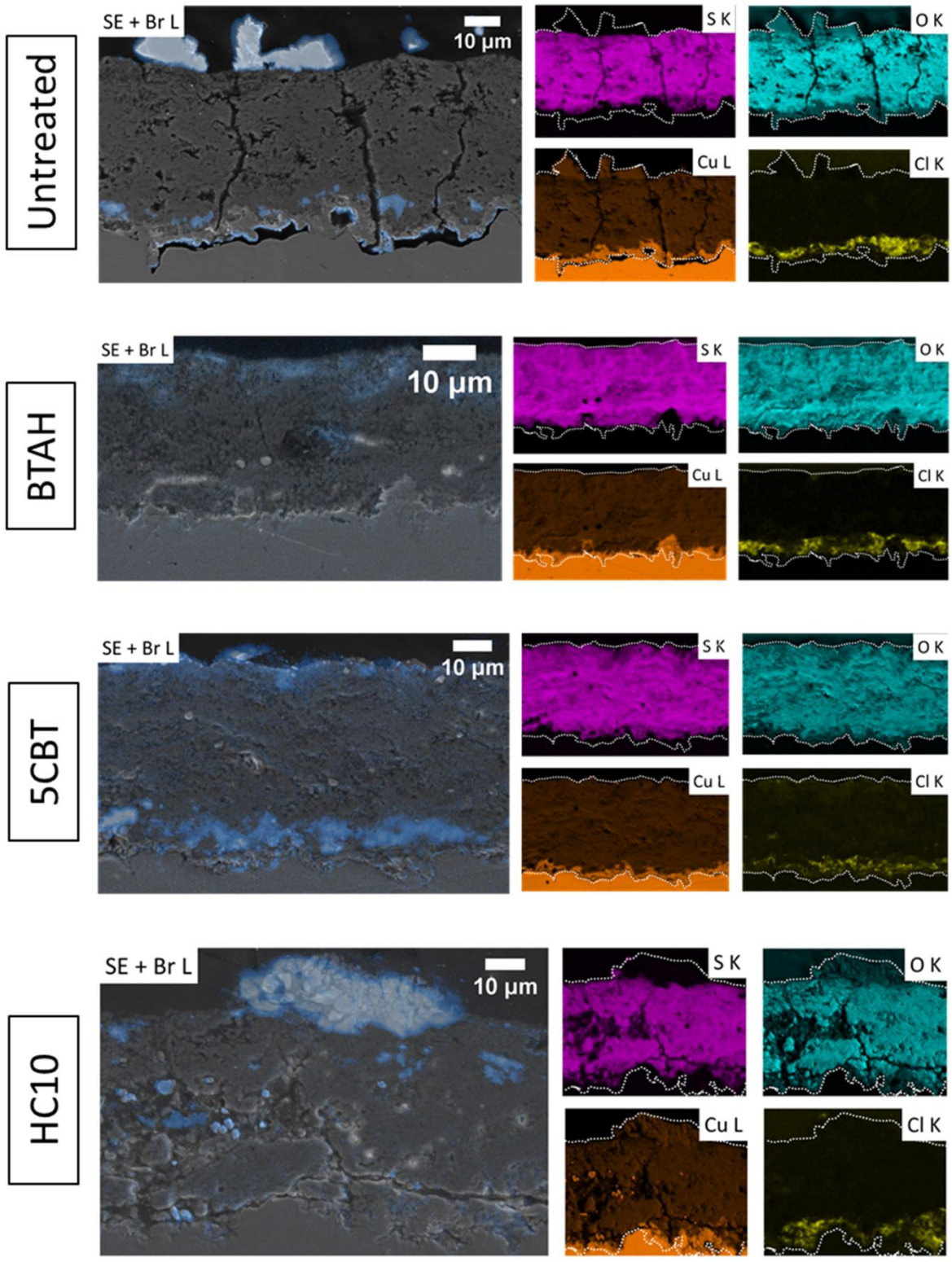

Figure 3. 83: Elemental mapping in cross-section after KBr immersion for untreated and treated samples. The left image represents the overlay of the secondary electron image and the Br-Lα distribution map.

To summarize, three main phenomena are observed on the untreated and on some treated samples after one month of immersion in a concentrated KBr solution (Table 3.13):

- Formation of a new mineral phase on the surface (untreated, HC10).
- Dissolution of the metal (untreated and 5CBT).
- Localized distribution of elemental Br within the corrosion layer not assigned to the formation of a copper hydroxy bromide (untreated and 5CBT).

Table 3. 13: Summary of the different observations of the KBr experiment.

	New crystalline phase	Metal dissolution	Br enrichment at brochantite-cuprite interface
Untreated	Yes	Yes, diffuse	Yes
BTAH	No	No	No
5CBT	No	Yes, locally	Yes
HC10	Yes	No	No

4. Metz samples after exposure

4.1 Surface properties

As for the samples analysed after treatment, surface properties (colour change, surface tension and surface morphology) are studied after 6 months of outdoors exposure.

Colour change is evaluated on one sample for each treatment and the variation of colour parameters (ΔL*, Δa*, Δb*). The calculated colour change (ΔE_{94}) is obtained by comparing the results with the untreated exposed sample. An additional colour change is also measured between the untreated samples before and after exposure to determine a possible evolution of the colour during the 6-months of outdoor exposure of the untreated Metz sample. Results including the L*a*b* parameters, their variations and the colour change are summarized in Table 3.14 and represented graphically in Figure 3.84.

Table 3. 14: L, a*, b* parameters after 6 months outdoor exposure. The measurement is performed only on one of the three exposed samples. The ΔE_{94} of the exposed sample is calculated based on the reference untreated and unexposed sample.*

	L*	a*	b*	ΔL*	Δa*	Δb*	ΔE_{94}
Untreated before exposure	**72,4**	**-13,2**	**13,2**				
Untreated exposed	68.0	-13.9	17.1	-4.4	-0.7	3.9	**5.0***
BTAH	54.7	-10.1	13.9	-13.3	3.8	-3.2	**13.6**
5CBT	53.3	-14.8	19.1	-14.7	-0.9	2.0	**14.7**
HC10	68.7	-14.3	16.1	0.7	-0.4	-1.0	**1.0**

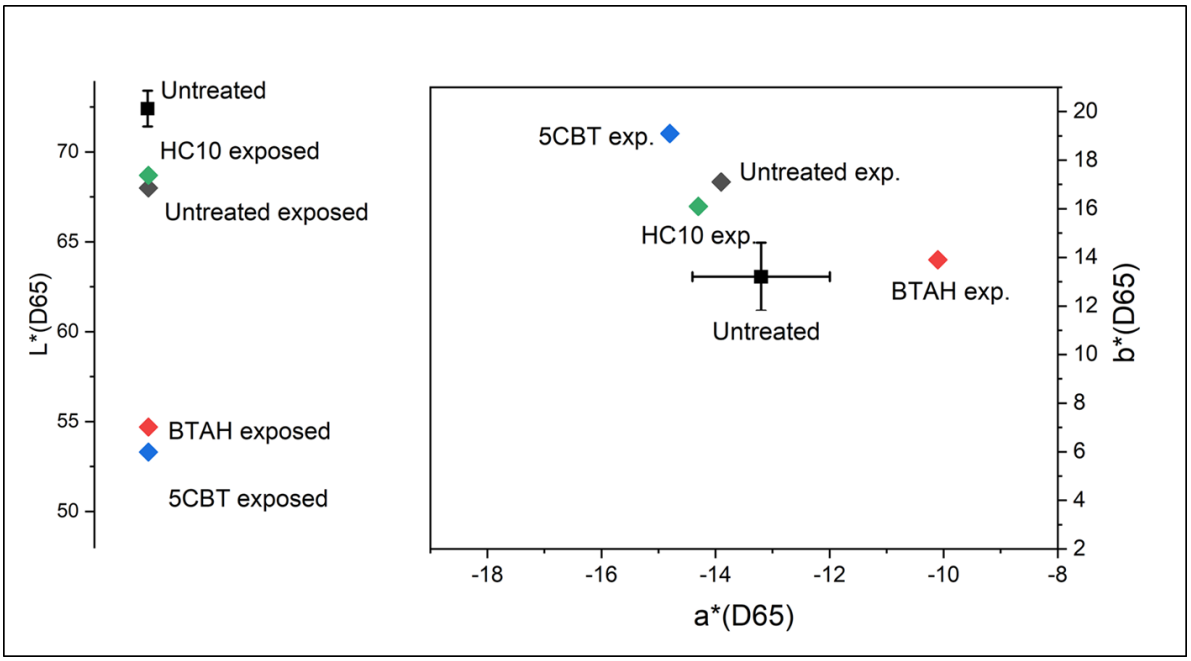

*Figure 3. 84: L*a*b* plot for the samples after 6 months exposure. The values corresponding to the untreated unexposed sample is also reported.*

The untreated sample presents a colour variation corresponding to a ΔE_{94} = 5.0 when compared to the unexposed copper tile. This change is at the limit of the visual appreciable change by human eye.

The treated samples are studied in relation to the exposed sample. High and similar colour change is observed for the BTAH-treated (13.6) and 5CBT-treated (14.7) samples. In both samples, a decrease of the surface's brightness is registered: the L* value corresponds to 54.7 for the exposed BTAH and 53.3 for the exposed 5CBT, while a L* equal to 68 is measured on the exposed untreated sample. Interestingly, an important variation (3.8) of the a* parameter is also observed on the exposed BTAH sample with a shift towards the red hue.

The sample treated with HC10 and exposed 6 months exhibits a ΔE_{94} corresponding to 1.0 testifying no difference in colour with the untreated exposed sample.

As for the colour, the contact angle is also measured after exposure and the values obtained are presented Figure 3.85.

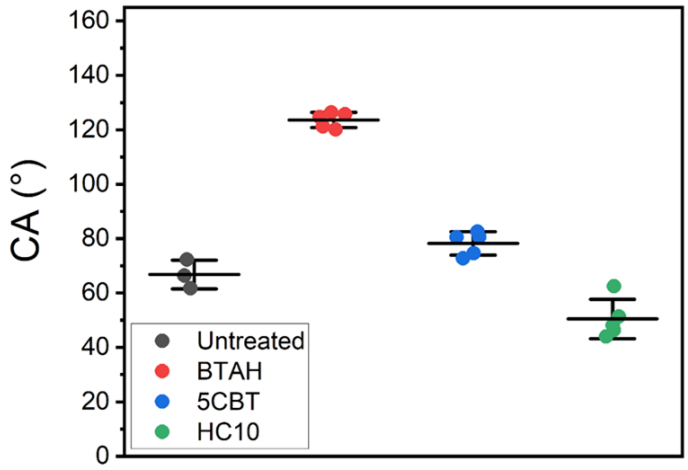

	Contact angle (°)
Untreated	67 ± 5
BTAH	124 ± 3
5CBT	78 ± 4
HC10	51 ± 7

Figure 3. 85: Graphical representation and mean contact angle calculated on 5 measurements for each treated sample after 6 months exposure.

The contact angle measured for the untreated (67 ± 5°), 5CBT-treated (78 ± 4°) and HC10-treated (51 ± 7°) is below 90°, indicating a hydrophilic surface, while exposed BTAH-treated sample is hydrophobic (124 ± 3°).

When analysing the surface by SEM analysis (Figure 3.86), the morphology of the treated samples is similar to the one observed for the exposed untreated sample. In particular, it is important to point out that the sample treated with HC10 does not show the flower-like crystals observed on the surface before exposure.

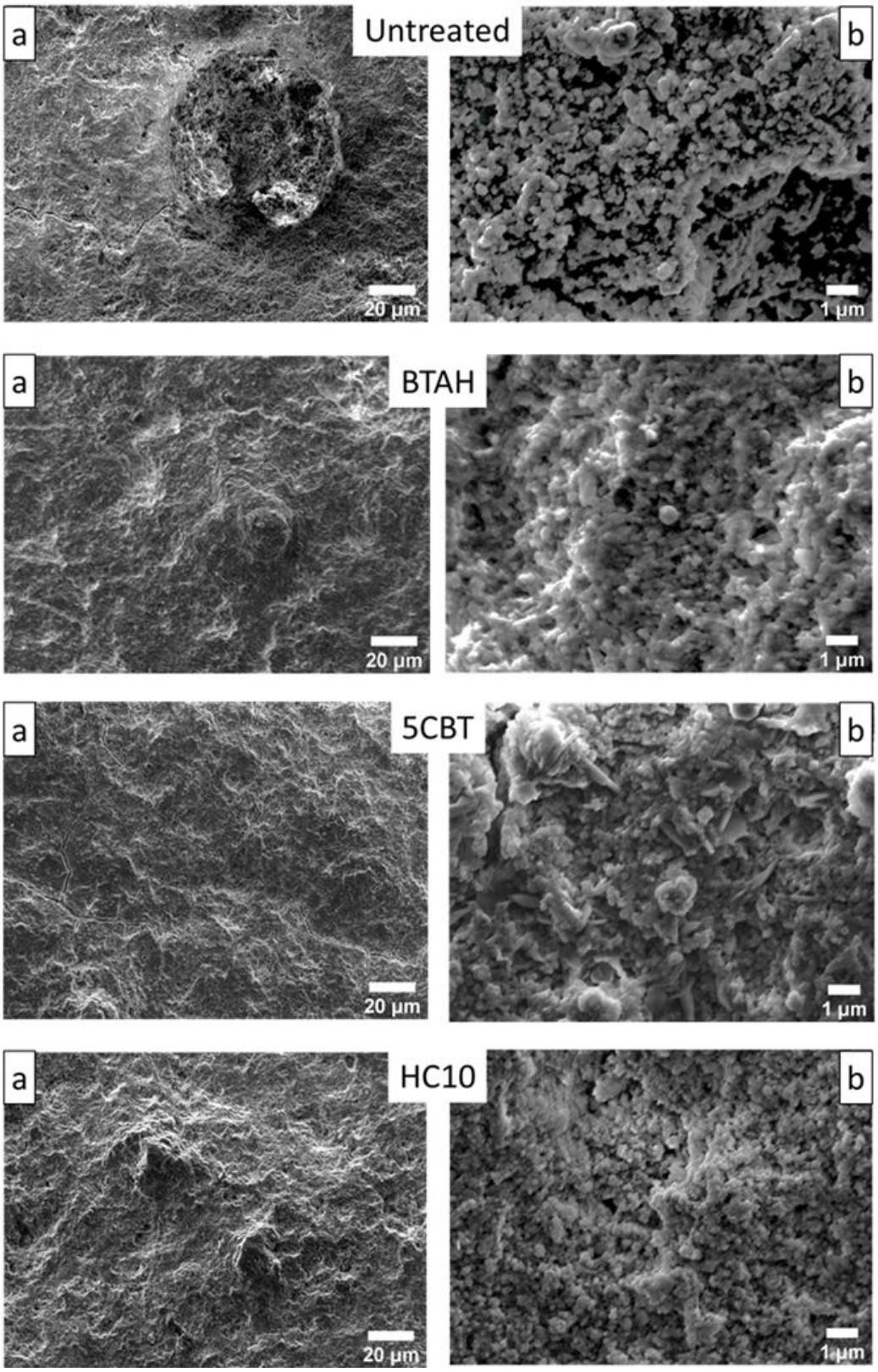

Figure 3. 86: Surface morphology at low (a) and high (b) magnification. SEM-SE, WD=5, 5 kV.

Raman analysis associated to the HC10-treated and exposed sample surface confirms the presence of brochantite and the absence of copper decanoate (Figure 3.87-d). In the case of BTAH and 5CBT-treated and exposed samples, the strong peak at 1395 cm^{-1} and 1398 cm^{-1} is detected respectively (Figure 3.87-b and Figure 3.87-c), which confirms that the complex formed before exposure is still present on the outer surface of the azoles-treated samples.

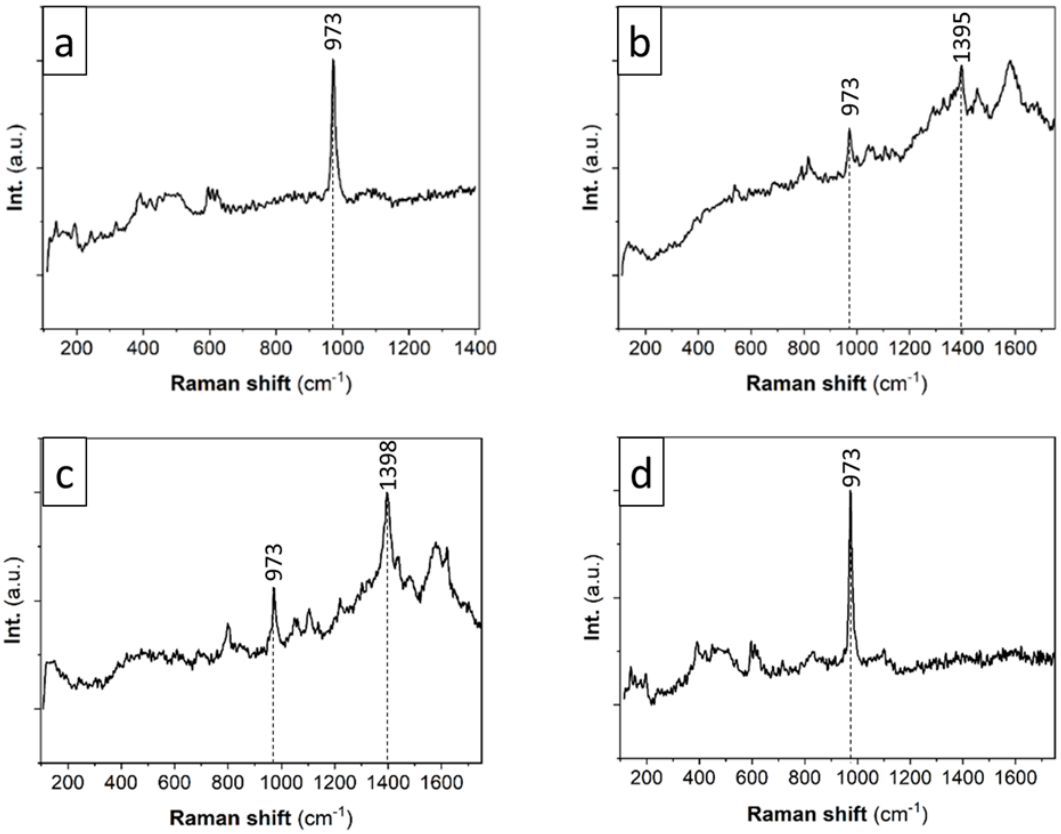

Figure 3. 87: Representative Raman surface spectra after exposure of the (a) untreated, (b) BTAH-treated, (c) 5CBT-treated and (d) HC10-treated samples.

4.2 Morphological and structural properties in cross-section

The samples are investigated in cross-section. The corrosion layer morphology is evaluated at the micrometric scale observed by OM and SEM microscopy: Figure 3.88 shows the backscattered electron images of the corrosion layer for all the exposed samples. In all cases, the double-layer structure with an outer porous layer and an inner compact and thinner layer is found again after exposure.

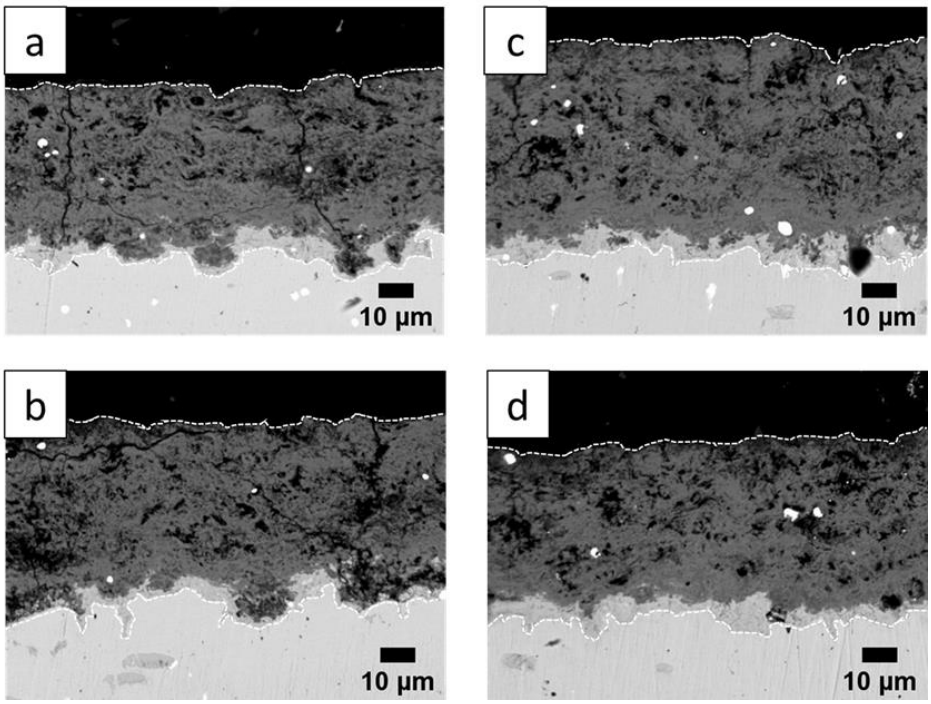

Figure 3. 88: Cross-section in backscattered electron images of the cross-section of the (a) untreated, (b) BTAH-treated, (c) 5CBT-treated and (d) HC-10 treated samples exposed outdoors. The white dotted lines indicate the upper and lower limit of the corrosion layer.

The thickness of the two layers is measured and results are presented in Figure 3.89.

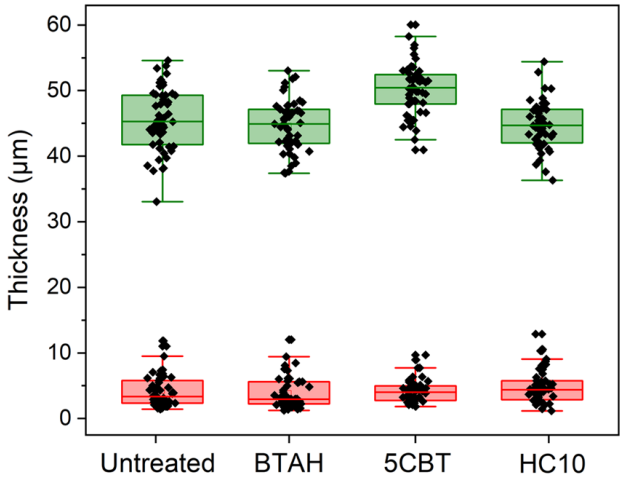

	Untreated	BTAH	5CBT	HC10
Outer layer (µm)	45,5 ± 4,8	44,7 ± 4	50,2 ± 4	44,8 ± 3,6
Inner layer (µm)	4,2 ± 2,5	3,9 ± 2,4	4,1 ± 1,8	4,9 ± 2,6

Figure 3. 89: Thickness of the cuprite (red) and brochantite (green) layer. The table reports the mean values and standard deviation obtained on 60 measurements per sample.

In general, no major change is observed among the samples with the inner layer measuring 4 to 5 µm, and the outer layer 45 to 50 µm. The distribution of the main elements within the corrosion layer is assessed by EDS analysis and no change compared to results before exposure are detected. Elemental maps are presented in Annex 3.

Representative Raman maps are obtained for the cross sections of the outdoor exposed samples: the results are presented in Figures 3.90 to Figure 3.93. The typical double layer with cuprite in contact with the metal and brochantite in the outer part of the corrosion layer is confirmed for the untreated sample after 6 months exposure (Figure 3.90).

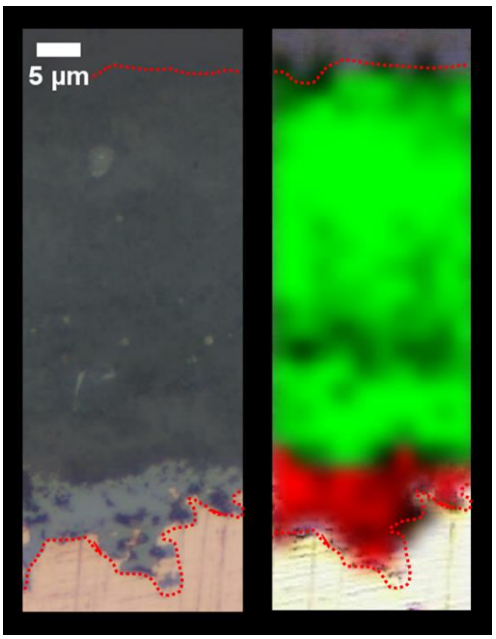

Figure 3. 90: Raman mapping of the untreated Metz corrosion layer (left image) after 6 months exposure. The green and red areas correspond to brochantite and cuprite respectively.

The treated samples also exhibit the same dual structure. Additionally, the complex Cu-BTA is detected together with brochantite within the outer layer and until the cuprite layer in the BTAH-treated sample, (Figure 3.91).

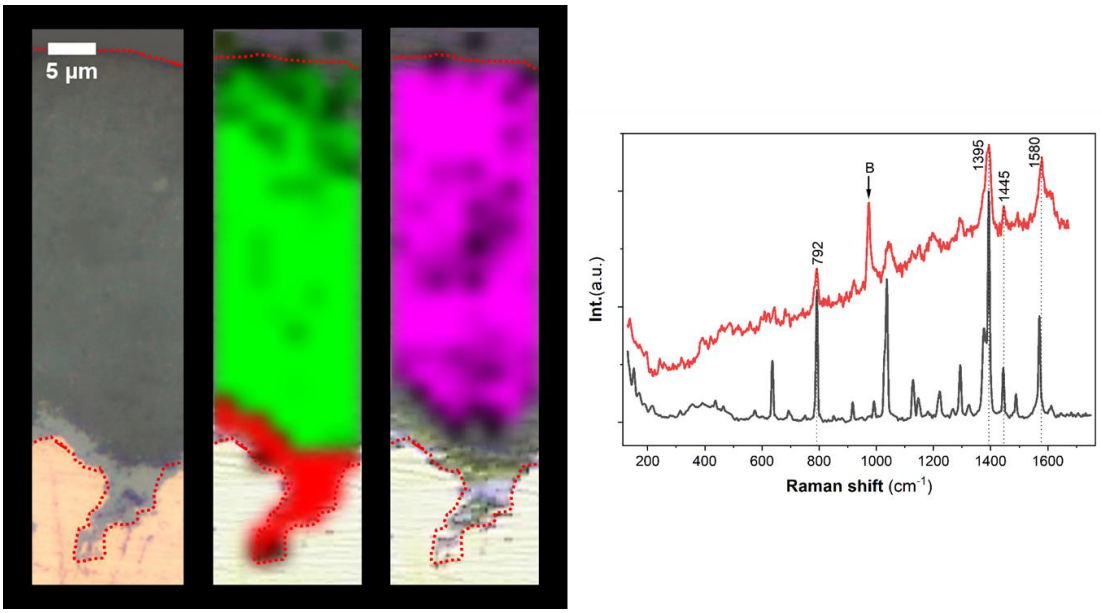

Figure 3. 91: Raman mapping of the BTAH-treated corrosion layer (left image) after 6 months exposure. The green and red areas correspond to brochantite and cuprite respectively. The violet area identifies the peak at 1395 cm^{-1}. To the right, a representative spectrum (red trace) recorded inside the brochantite layer is compared to the Cu-BTA reference spectrum.

Figure 3.92 corresponds to the Raman map representative of the 5CBT-treated and exposed sample.

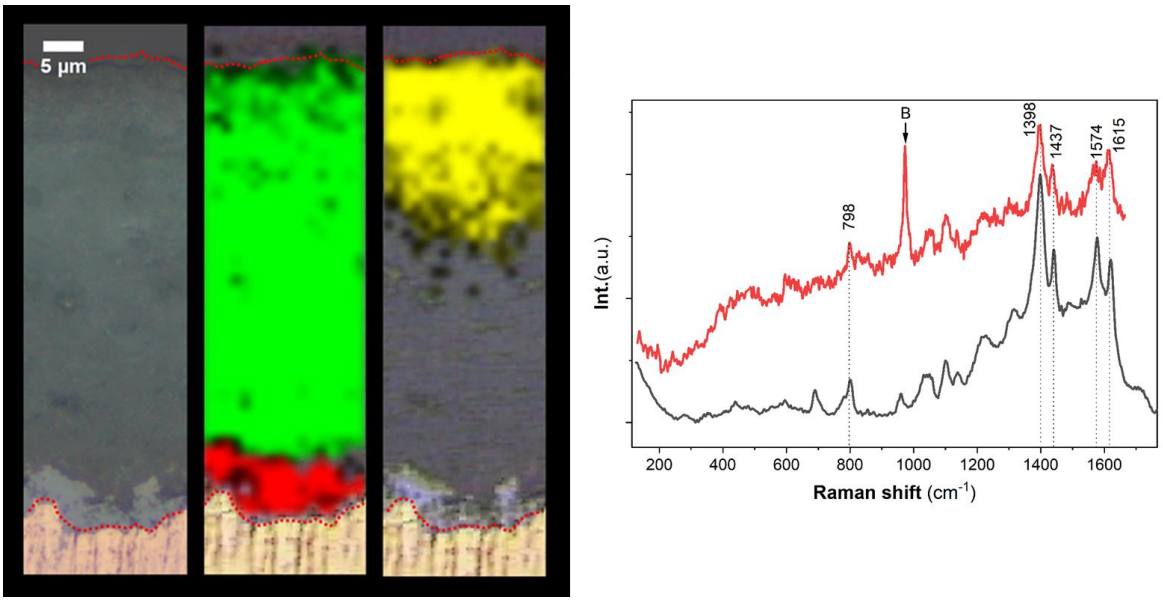

Figure 3. 92: Raman mapping of the 5CBT-treated corrosion layer (left image) after 6 months exposure. The green and red areas correspond to brochantite and cuprite respectively. The yellow area identifies the peak at 1398 cm^{-1}.

The complex identified as Cu-5CBT is detected (yellow area) and, similarly to before exposure, the signal is more intense and can be clearly identified in the outer part of the brochantite layer (20 µm approximately).

The only phases detected in cross-section for the HC10-treated and exposed sample are cuprite and brochantite (Figure 3.93).

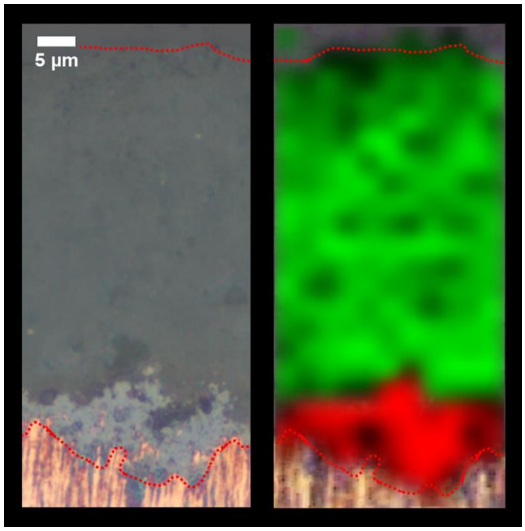

Figure 3. 93: Raman mapping of the HC10-corrosion layer (left image) after 6 months exposure. The green and red areas correspond to brochantite and cuprite respectively.

4.3 Permeability of the exposed samples

The permeability has been evaluated thanks to immersion in a deuterated water for 30 days. Results of the immersion in D_2O for the samples exposed 6 months outdoor are summarized in Table 3.15.

Table 3. 15: Enrichment values calculated in both the outer and inner layer for the 6 months-exposed samples.

δ_n	ROI brochantite	ROI cuprite
Untreated	2302 ± 140	2778 ± 836
BTAH	667 ± 40	666 ± 220
5CBT	748 ± 83	1496 ± 806
HC10	2136 ± 176	2523 ± 1514

Differently from what has been previously observed on the freshly treated compounds, a reduction of permeability is measured for the BTAH-treated and 5CBT-treated samples in the outer brochantite layer (Figure 3.94). In this area, the enrichment is approximately three times lower compared to the untreated sample (δ_n=2302 ± 140) and δ_n corresponds to 667% and 748% for BTAH and 5CBT respectively. The value obtained for the HC10-treated sample is 2136%, comparable to the untreated sample.

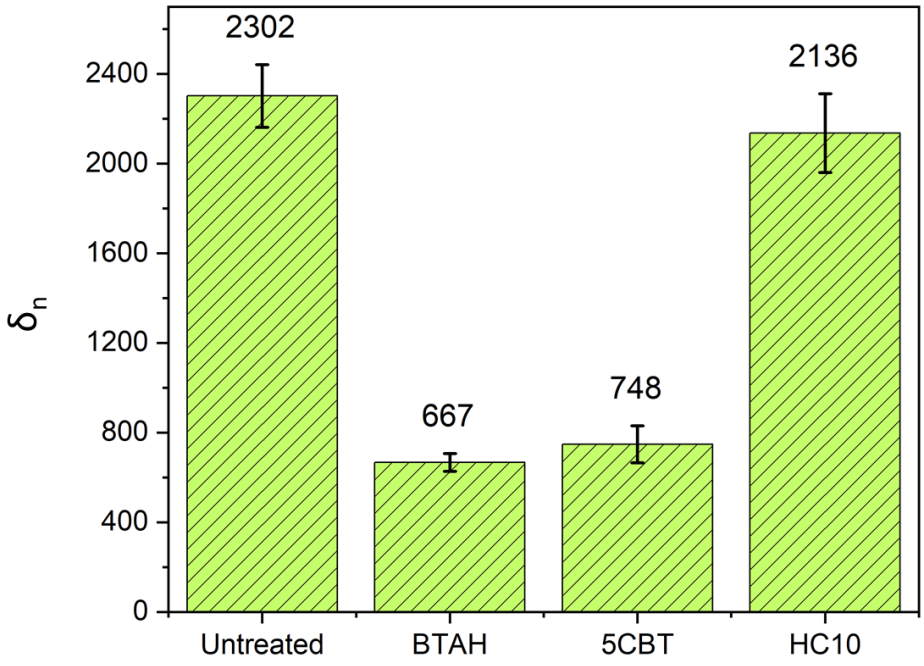

Figure 3. 94: Comparison of the deuterium enrichment (δ_n) within the outer brochantite layer for the 6 months exposed samples.

When evaluating the deuterium enrichment within the cuprite layer (Figure 3.95), the lowest values is calculated for the BTAH-treated sample (δ_n=666 ± 220), about four times lower than the untreated one (δ_n of 2778 ± 836). The 5CBT-treated sample also shows a lower enrichment in cuprite, about half compared to the untreated cuprite, but the higher error indicates a higher variability throughout the sample (δ_n at 1496 ± 806). Last, the HC10-treated sample shows a mean enrichment value comparable to the untreated sample (δ_n=2523 ± 1514). Also in this last sample, a high variability is registered among the three zones analysed.

Figure 3. 95: Comparison of the deuterium enrichment (δ_n) within the inner cuprite layer for the 6 months exposed samples.

4.4 Re-corrosion in aggressive environment

The exposed samples have been subjected to immersion in stagnant KBr solution for 30 days. Similarly, to the experiment performed after treatment, three main morphological and structural changes are found on the outdoor exposed samples.

The first observation concerns the surface. In Figure 3.96, representative optical micrographs of the samples' surfaces after immersion are presented.

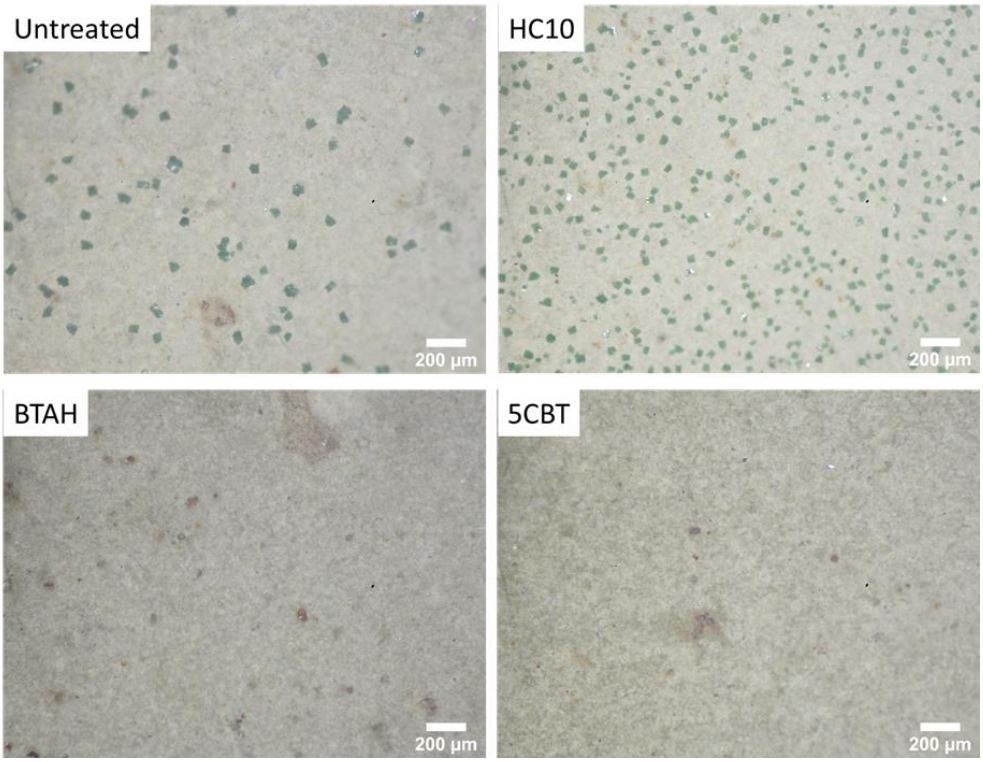

Figure 3. 96: Raman spectrum corresponding to one of the dark green crystals on the untreated sample after immersion in KBr solution.

Microscopic emerald-green crystals are identified on the surface of the untreated and the HC10-treated samples.

µRaman spectroscopy performed by directly pointing the laser on one of the green crystals on the untreated sample's surface allows to identify the new phase as $Cu_2Br(OH)_3$ as shown on Figure 3.97.

The same spectrum is obtained when analysing the green crystals on the HC10-treated sample (Figure 3.97 red trace), while brochantite is detected in the light-green part (Figure 3.97 black trace).

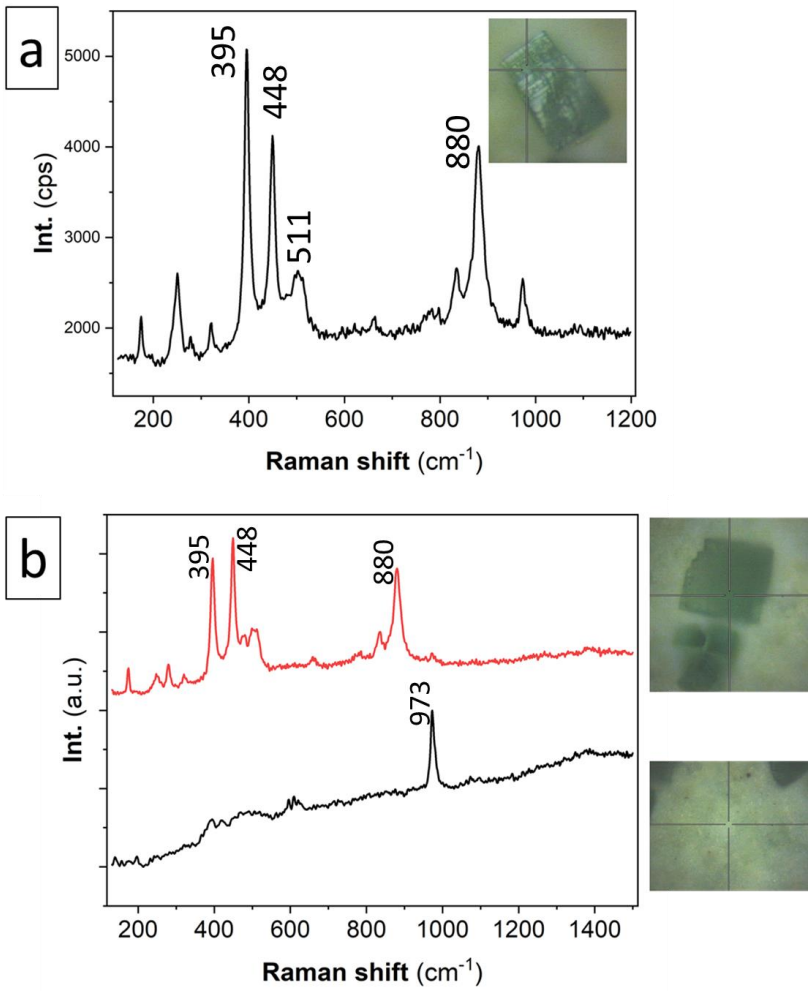

Figure 3. 97: (a) Raman spectrum corresponding to a dark green crystal on the surface of the untreated sample after immersion in KBr solution. (b) Raman spectra obtained on the surface of the HC10-treated and exposed sample after immersion in KBr solution. The red spectrum corresponds to the dark green crystal, the black spectrum is obtained at the sample's surface where no crystals are visible.

SEM analysis in cross-section is performed and representative micrographs are reported in Figure 3.98.

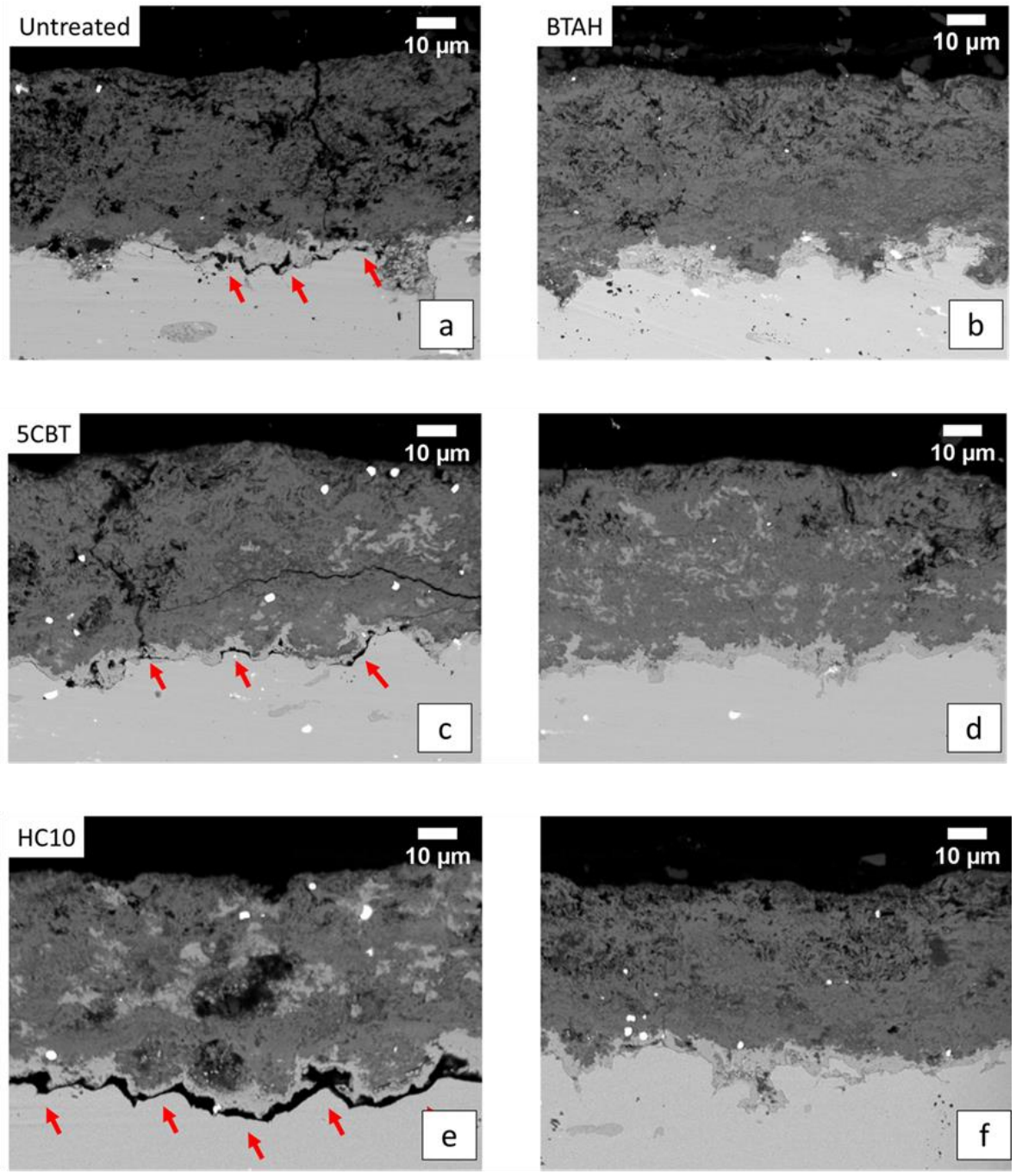

Figure 3. 98: Cross-section backscattered electron images of the exposed samples after KBr immersion. SEM-BSE, 10 kV.

The observation evidence the voiding formation between cuprite and metal in some of the samples analysed. In the backscattered electron images, the voiding appears black (due to the resin) and is highlighted by the red arrows in Figure 3.98. No change is observed for the BTAH-treated sample (Figure 3.98-b). Localized black areas at the metal/cuprite interface are present for the untreated sample (Figure 3.98-a) and for the 5CBT-treated sample (Figure 3.98-c), while a more severe re-

corrosion interests the HC10-treated sample (Figure 3.98-e). Similarly to 5CBT, other parts of the corrosion layer are not affected (Figure 3.98-f).

The results of the EDS analysis in cross-section are presented as elemental maps in Figure 3.99.

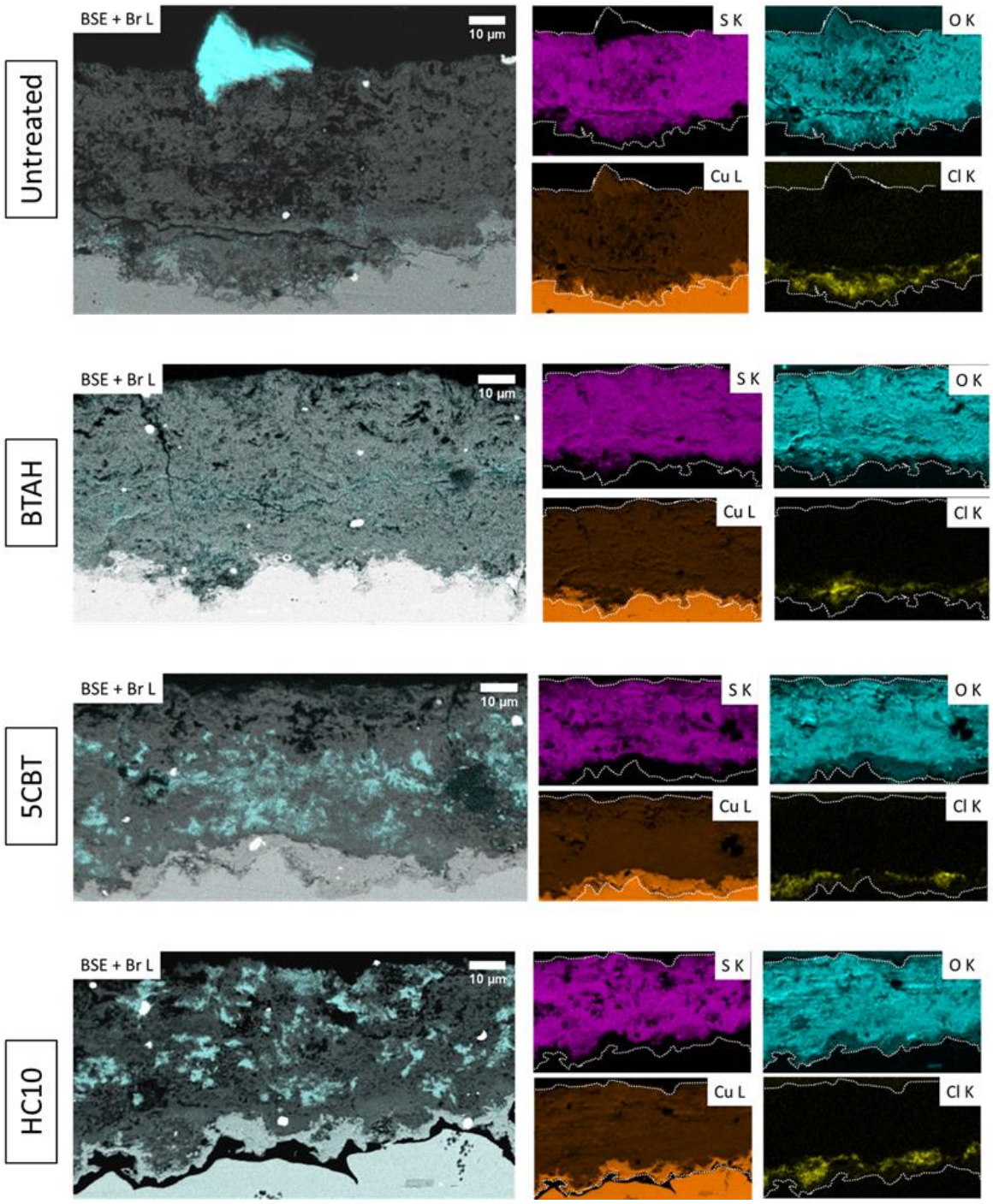

Figure 3. 99: Elemental maps representative for the untreated and treated samples exposed and immersed in KBr solution.

High values of bromine are detected in the outer part of the corrosion layer for the samples 5CBT-treated and HC10-treated (Table 3.16). This result is in agreement with the detection of $Cu_2Br(OH)_3$ by µRaman spectroscopy within the brochantite layer (spectra in Figure 3.100).

Table 3. 16: Mean %wt. resulting from the values of three elemental maps for Br and K in the outer brochantite layer (left table) and in the interfacial layer cuprite/brochantite (right table). SEM-EDS.

Outer layer		
	Br L %wt	**K K %wt**
Untreated	0.39 ± 0.27	0.24 ± 0.13
BTAH	0.79 ± 0.48	1.13 ± 0.88
5CBT	3.91 ± 3.66	0.34 ± 0.07
HC10	5.29 ± 4.30	0.24 ± 0.06

Interfacial layer		
	Br L %wt	**K K %wt**
Untreated	0.76 ± 0.18	0.27 ± 0.06
BTAH	1.77 ± 1.06	1.44 ± 0.96
5CBT	2.00 ± 0.72	0.35 ± 0.13
HC10	2.15 ± 1.49	0.40 ± 0.11

A localized enrichment of bromine at the brochantite/cuprite interface is detected for the 5CBT and HC10-treated samples (2%wt and 2.2%wt respectively) while a lower increase in the area is detected for the untreated sample (0.8%wt). At the interface, a high value of bromine (1.8%wt) is detected on the BTAH-treated sample but the value is similar to the one of potassium (1.4%wt) thus suggesting the presence of the salt probably within the porosity.

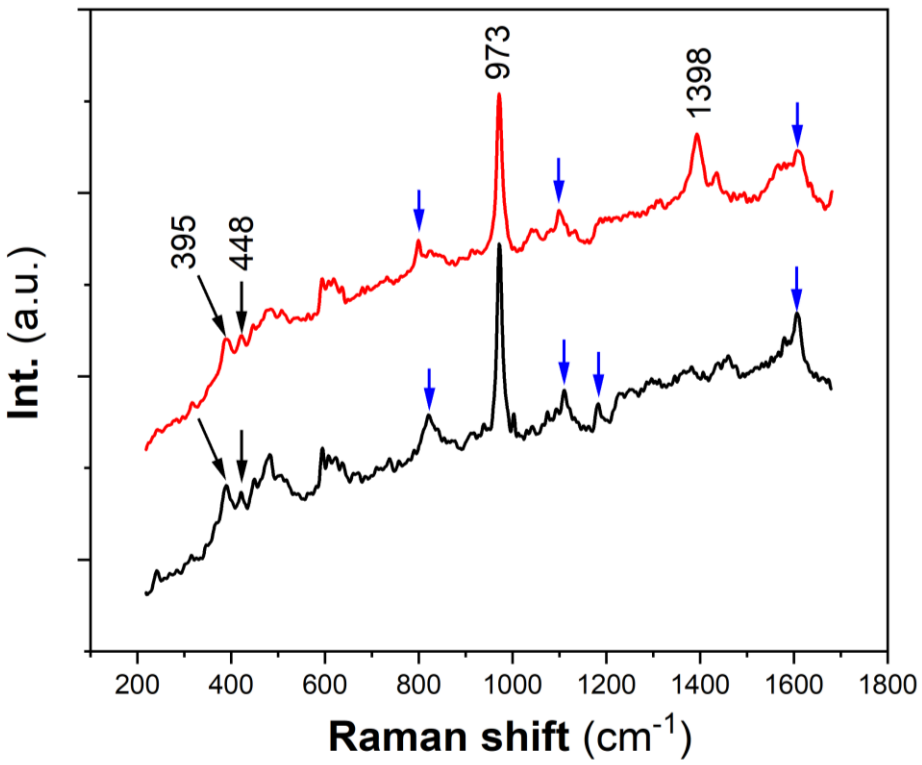

Figure 3. 100: Raman spectra obtained on the bromine-rich zones in cross-section for the 5CBT-treated (red trace) and the HC10-treated (black trace). The shifts at 395 and 448 cm^{-1} might indicate a copper hydroxy bromide. Blue arrows marked correspond to the embedding resin.

A qualitative summary of the observations obtained on the exposed samples after immersion in KBr is proposed in Table 3.17.

Table 3. 17: Summary of the different observations of the KBr experiment after 6-month outdoor exposure.

	New crystalline phase	Metal dissolution	Br enrichment at brochantite-cuprite interface
Untreated	Yes (surface)	Yes, locally	?
BTAH	No	No	No
5CBT	Yes (CL)	Yes, locally	Yes
HC10	Yes (surface+CL)	Yes, locally	Yes

Discussion

Discussion

This chapter includes the discussion of the results obtained in the experimental part. The results concerning the experiments carried out on the synthetic phases are discussed first. A second part is dedicated to the understanding of the complex system, the naturally corroded sample. Lastly, based on the information gained from the previous sections, the results concerning the treatments are discussed and reaction models are proposed for each inhibitor.

1. Reactivity of the inhibitors with synthetic mineral phases

The reactivity of the three inhibitors with synthetic minerals cuprite and brochantite has been investigated in solution. The reaction was monitored over 24 hours by measuring pH and by analysing the reaction product at specific time intervals. By combining the results obtained on global properties during reaction (pH) and the analytical investigation of the reaction product(s) characterized from the bulk down to the nanoscale, reaction mechanisms are proposed for each inhibitor. Similarities and differences among the inhibitors are also discussed.

1.1 Reactivity in Benzotriazole solution

1.1.1 Reactivity of BTAH with cuprite

Complementary results are obtained when analysing the product from the reaction between BTAH and cuprite using bulk, micrometric and nanometric scale analysis.

When characterization was carried out using XRD and µRaman spectroscopy, the only phase detected is cuprite. The observations by HR-TEM confirm the presence of micrometric cuprite grains, and additionally, they reveal that the grains are covered by an amorphous layer measuring few nanometers in thickness. The limited thickness clearly indicates that the newly formed phase is present at a very low amount at the micrometric and bulk scales, which explains the impossibility of being detected by Raman spectroscopy and XRD.

Despite the lack of structural information concerning the nature of this film in the present work, previous studies making use of surface-sensitive techniques such as XPS and SERS, have shown that an

amorphous and nanometric Cu(I)-BTA layer forms on copper covered by thin cuprite layers as a result of immersion in BTAH solution [45], [54], [66], [75], [143].

The analysis of the high-resolution TEM images provides additional information on the thickness evolution of the surface layer and its homogeneity after short (2 hours) and long (24 hours) time. It was observed that a thin, homogeneously thick layer of 3 nm on average is formed at short reaction time, while a thicker layer (14 nm), characterized by a higher thickness variability (thickness ranging from 0.5 to 30 nm), forms after 24 hours. In the short term, the thickness measured is comparable to the Cu-BTA layer thickness reported by Brusic et al. [66] that formed on a native polycrystalline cuprite layer on copper: the authors measured a layer of 2 and 2.3 nm after 10 and 30 minutes respectively. When plotting these measurements together with the one obtained on the synthetic powder (Figure 4.1), the thickness variation trend of the outer amorphous layer follows a logarithmic curve (red dashed line) within the first 2 hours. The same trend is not valid at longer immersion time as the layer is thicker after 24 hours.

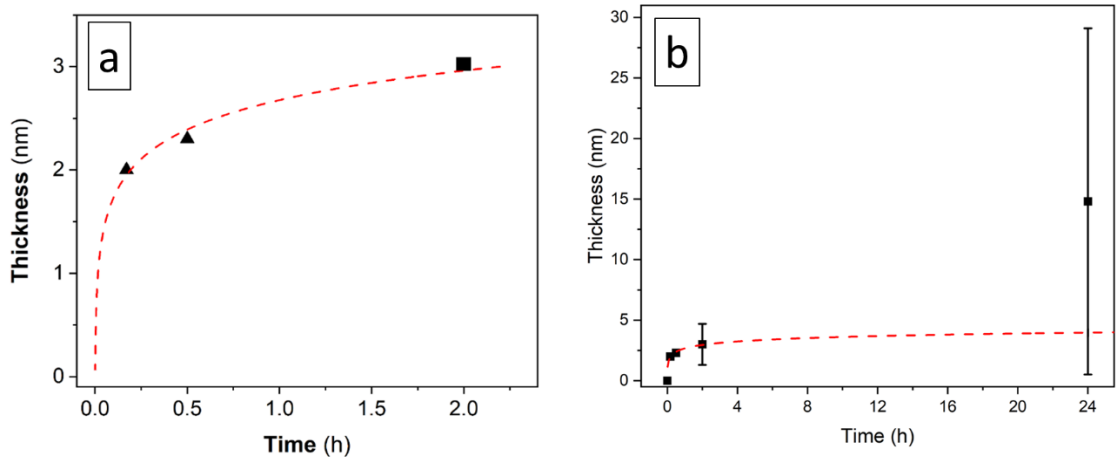

Figure 4. 1: Cu-BTA layer thickness evolution on cuprite. The graph (a) includes data from after 10 and 30 minutes (triangles) and the thickness measured after 2 hours in this study (square). By fitting the data, a logarithmic trend is observed (red line) in the short term, while in the long term (graph b) the value obtained after 24 hours reaction does not match the curve.

The stability of pH during the reaction can be differently interpreted.

By supposing that no oxidation of cuprite took place, at least for short immersion times, the total reaction leading to the formation of Cu-BTA (Equation 1) can be seen as two half reactions, one (Equation 2) involving BTAH deprotonation and the second (Equation 3), the dissolution of cuprite.

$$2BTAH + Cu_2O + H_2O \rightarrow 2CuBTA \downarrow + 2H_2O \quad (1)$$

$$BTAH \rightarrow BTA^- + H^+ \quad (2)$$

$$Cu_2O + H_2O \rightarrow Cu^+ + 2OH^- \quad (3)$$

As it is evident from Equation 1, the reaction does not produce a variation of the bulk pH, confirmed by the experimental data showing a constant pH value (4.6) in the first 2 hours of reaction. This hypothesis, leading to the formation of a Cu-BTA complex with copper is in the first coordination state, is confirmed by literature studies on oxide-covered copper surfaces [4], [47]–[49].

Another hypothesis for the behaviour observed would be the oxidation of cuprite concomitant to film formation (Equation 4 to 6), although further investigation is needed to confirm this hypothesis.

$$Cu_2O + H_2O \rightarrow Cu^{2+} + 2OH^- \quad (4)$$

$$2BTAH \rightarrow 2BTA^- + 2H^+ \quad (5)$$

$$2BTAH + Cu_2O + H_2O \rightarrow 2Cu(BTA)_2 \downarrow + 2H_2O \quad (6)$$

In both cases, the reduced thickness of the film can be attributed to the intermediate step constituted by either the dissolution or the oxidation of cuprite, also considering cuprite stability at pH higher than 4, close to the one of the BTAH solution (4.7).

After 24 hours, the decrease of one pH unit (3.6) might indicate that reaction (2) is favoured over cuprite dissolution. In addition, other phenomena such as cuprite oxidation might also intervene in the long term and modify the equilibrium reached at short immersion time. The high thickness variability of the outer layer after 24 hours seems to confirm this hypothesis.

1.1.2 Reactivity of BTAH with brochantite

The reaction between synthetic brochantite and BTAH has been studied. Differently from the previous results on cuprite, bulk and micrometric-scale analysis indicate, in addition to brochantite, the formation of a new compound. By XRD, the distinctive pattern of brochantite and a broad hump, characteristic of long-chain amorphous polymers, at low angles are observed. µRaman spectroscopy again confirms the presence of brochantite together with a new phase. The interpretation of the Raman spectra indicates that a Cu-BTA complex is present as reaction product.

HR-TEM observations at the nanoscale confirm that a carbon and nitrogen-rich amorphous compound is present and, more importantly, allow to locate the phase at the outer surface of the brochantite grains: the core-shell morphology, already observed on cuprite, is found here. Such morphology is observed at all reaction times. The Cu-BTA surface layer thickness increases with increasing reaction

time. Thickness measurements versus time, resulting from the analysis of HR-images, are reported in Figure 4.2.

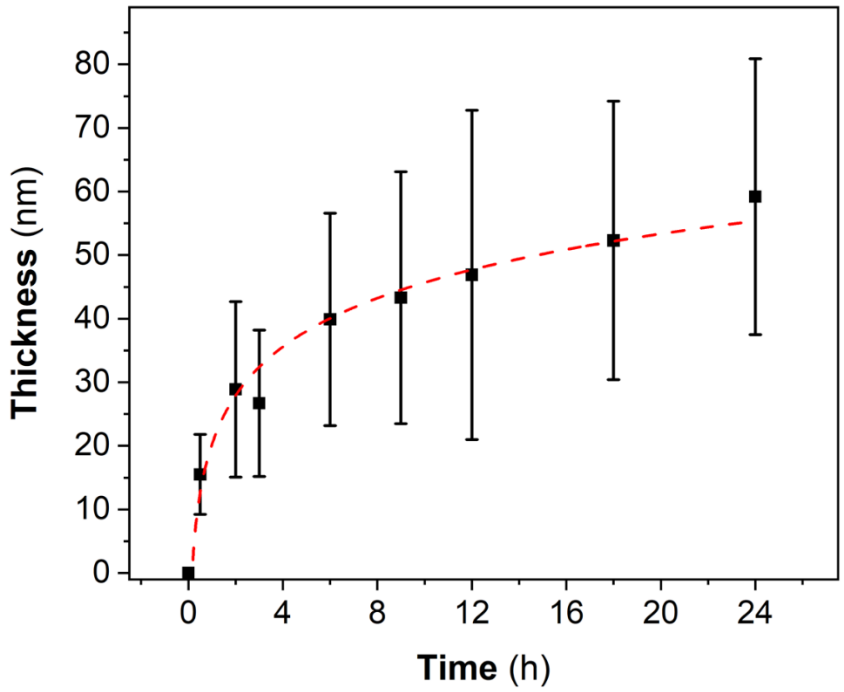

Figure 4. 2: Cu-BTA layer thickness variation with reaction time when brochantite reacts with BTAH. The red dashed line indicates a logarithmic evolution of the thickness.

The thickness variation trend (dotted line) shows that the growth of the Cu-BTA layer follows a logarithmic tendency, and, after an initial fast step, thickness stabilizes progressively. After 24 hours, most particles observed is amorphous, which suggests an almost complete transformation of the mineral into the Cu-BTA complex. This result is confirmed by the low intensity of the shift corresponding to sulphate group vibration in brochantite (at 973 cm^{-1}).

The layer continuous growth up to near complete brochantite consumption implies a certain permeability of the outer layer to the passage of ions. The permeability through the layer was evidenced by the detection of bromine in the Cu-BTA layer formed after 2 hours and immersed in a KBr solution. The Cu-BTA layer is more porous compared to the mineral allowing ions to diffuse through it.

In the light of these results, the reaction between brochantite and BTAH is discussed. The total reaction can be written as in Equation 7 by supposing that the nitrogen atoms from two benzotriazole molecules coordinate to one copper atom in the resulting polymer.

$$Cu_4SO_4(OH)_6 + 8BTAH \rightarrow 4Cu(BTA)_2 \downarrow + H_2SO_4 + 6H_2O \qquad (7)$$

The reaction leads to H_2SO_4 formation with a final calculated pH that corresponds to 1.68. This theoretical pH value is not confirmed by the experimental pH measured in solution. In fact, it was observed that pH changes drastically from that of the initial pure BTAH solution (4.7) to a value of 2.5 after less than 10 minutes from the addition of brochantite. Afterwards the measured pH remains constant for 24 hours.

The question of the nature of chemical bond between the brochantite and the BTAH is crucial. Considering that brochantite is almost insoluble in water (pKs=62.5), the reaction of BTA^- anions and copper ions in solution would not justify alone the decrease in pH obtained experimentally. Taking into account these results and the progressive formation of a surface layer, an initial step consisting into the adsorption of BTA^- ions on the outer surface of brochantite grains is proposed (Equations 8).

$$Cu_4SO_4(OH)_6 + BTAH \rightarrow Cu_4SO_4(OH)_6 + (BTA)^-_{ads} + H^+ \quad (8)$$

The electron-donor tendency of the nitrogen atoms in the azole ring induces the dissociated BTA^- to interact almost instantaneously with the outermost copper atoms present at the mineral surface. This interaction causes further dissociation of BTAH in solution with the pH drop measured. If the brochantite dissolution is neglected in the very beginning of the reaction, the organic molecules that interact with the mineral surface corresponds to a small fraction (3.2mM) of the total BTAH (0.084 M) and protonated BTAH is still present in solution.

Starting from the first chemisorption step, further bond formation is due to the presence of cupric ions from the mineral progressive dissolution. Copper ions diffusing act as bridges between organic molecules inducing polymerization and growth of the surface layer. Other weaker forces such as van der Waals interactions between benzene rings can provide further stability to the surface compound. The polymer growth process takes place at constant pH, which implies an equilibrium between BTAH deprotonation and brochantite dissolution and this situation is possible when considering that the deprotonated form of BTAH is less favoured at lower pH.

As the Cu-BTA is permeable to ions, during the layer growth, BTA^- and H^+ are able to reach the mineral surface and, in the same way, cupric ions can diffuse to the layer/solution interface. As reaction proceeds, the slow increase of the layer thickness can be due to the decrease in available benzotriazole at the surface of the outer layer as it is progressively consumed during the reaction, but also to the increased thickness of the Cu-BTA layer that might hinder ionic species diffusion.

The reaction steps are schematized in Figure 4.3.

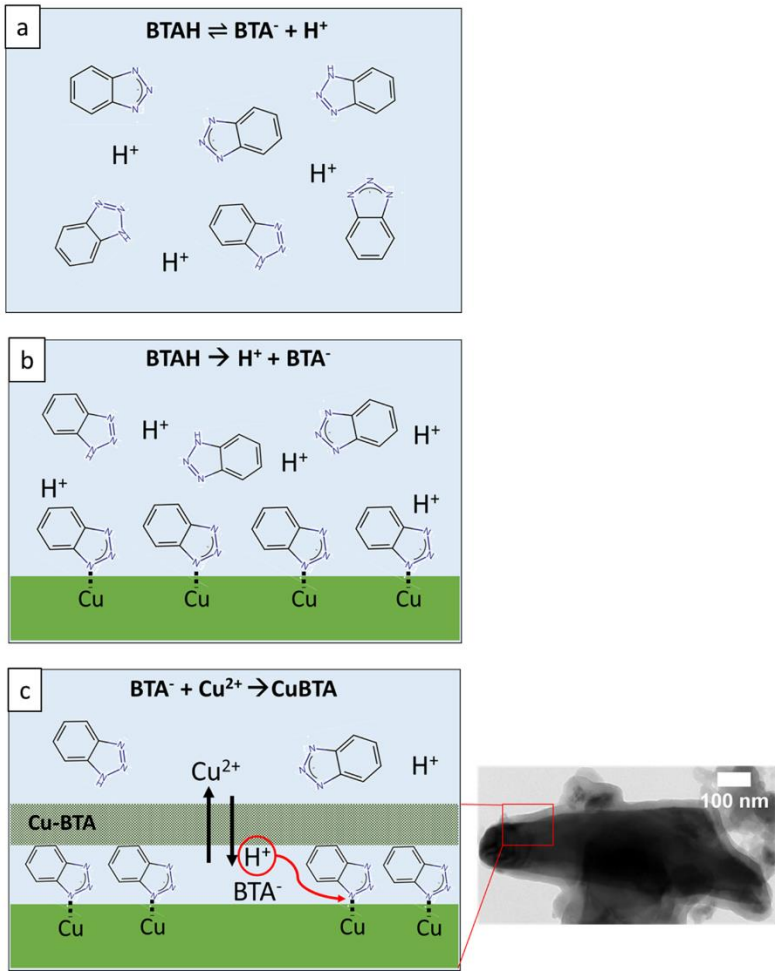

Figure 4. 3: Proposed model for the reaction of BTAH with brochantite. (a) BTAH equilibrium in solution. (b) Formation of a first adsorbed layer right after adding brochantite. (c) Cu-BTA layer growth on brochantite in presence of BTAH in acidic solution.

First, in solution, the amount of dissociated and undissociated BTAH molecules is determined by the pKa of BTAH at the concentration chosen (Figure 4.3 a). The introduction of brochantite in the system causes pH drop due to the adsorption and further BTAH deprotonation (Figure 4.3 b). The Cu-BTA layer continues growing (Figure 4.3 c) as ions can diffuse through and brochantite progressively solubilize providing cupric ions for further polymerization.

Once the layer is formed, the stability of the BTAH-modified brochantite has been investigated. The experiment consisted in immersing the 2-hours treated brochantite in a solution containing NaCl at pH varying from to 7 to 1. The experiment was carried out for 30 days in stagnant conditions.

Untreated brochantite reacts in NaCl solution at all pH solutions tested inducing the precipitation of the compound atacamite (Equation 9).

$$Cu_4SO_4(OH)_6 + 2NaCl \rightarrow 2Cu_2Cl(OH)_3 + Na_2\,SO_4 \quad (9)$$

The 2-hours surface-modified brochantite does not undergo any change at neutral and slightly acidic pH (7 and 5). In these conditions, the presence of chloride ions does not affect the stability of the brochantite core and no new phase forms even though ions are able to diffuse through the Cu-BTA layer, as demonstrated by the detection of bromine after 30 days immersion in neutral solution.

Only at low pH (from pH 2), formation of the new mineral atacamite is detected. By comparing the fraction of brochantite versus atacamite obtained by XRD analysis, 60% of the crystalline components is constituted by atacamite at pH 2 and 72% at pH 1. In parallel, both µRaman and TEM analysis show that the Cu-BTA layer does not dissolve even if the evolution of its porosity and degree of polymerization remains to be determined. The complete dissolution of the brochantite-core is clearly observed for some grains where at the nanometric scale a characteristic "ghost structures" is present: in such hollow structures only the outer Cu-BTA remains of the previously observed core-shell structures. Some hypotheses can be drawn from these observations.

First, the change in reactivity between brochantite treated and untreated is clearly related to the presence of the surface Cu-BTA layer and it is more largely influenced by pH than Cl^- activity. As the Cu-BTA layer is permeable to ionic species, results are evidence of the primary role in changing brochantite stability is played by the very first adsorbed molecules on the mineral surface. At near-neutral pH, the number of protons reaching the surface is low and the copper benzotriazolate is stable. On the contrary, at low pH, the protonated BTAH molecule is more favoured. In particular, the N-Cu bond of the adsorbed BTA molecules on brochantite represents a weaker interaction when compared to the N-Cu one within the Cu-BTA polymer in which Cu is bond to various N atoms. Therefore, we suppose that at low pH, H^+ acts by first destabilizing the adsorbed molecules leaving the Cu-BTA shell practically intact and dissolution of brochantite can proceed.

A parallel can be proposed between this mechanism and the one observed during the process that leads to the formation of the Cu-BTA layer. In presence of chloride ions and in absence of BTAH in solution, once the adsorbed molecules of BTAH are no more in place and BTAH is not present as reservoir in solution, brochantite dissolution can take place as cuprous ions interact with chloride forming soluble compounds. The availability of soluble copper ions in solution will then generate the precipitation of atacamite (Figure 4.4).

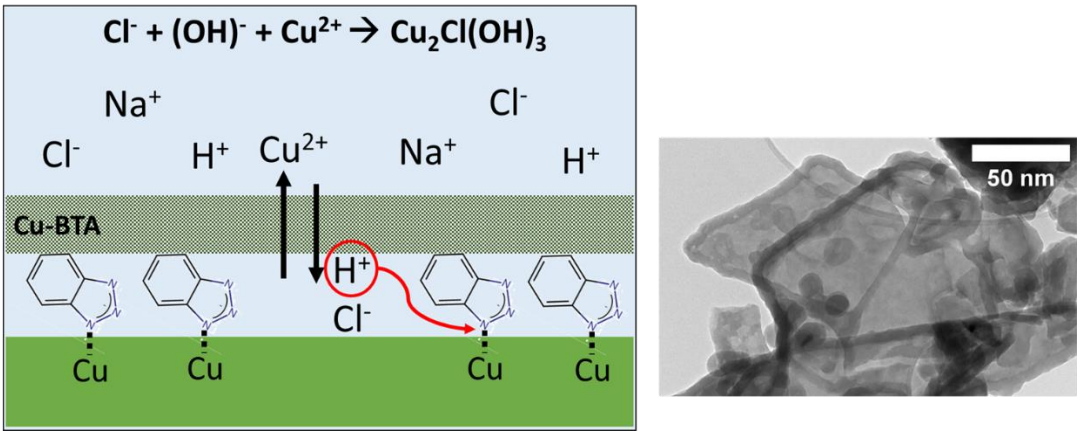

Figure 4. 4: To the left, scheme of the Cu-BTA layer on brochantite in presence of aggressive ions at low pH. To the right, the "ghost structures" observed by TEM.

It remains unknown why at pH 2, only some particles exhibit the hollow structure. According to the previous hypothesis, a stronger bond can be supposed to form on certain particles compared to others for reasons that remain unclear.

The results at low pH confirm, from another perspective, previous studies according to which, BTAH complexes do not form or are less protective at low pH on copper and copper oxidized surfaces in presence of aggressive species. Tromans et al. [41] attribute the non-protective behaviour of BTAH in acidic conditions (pH 1) to the impossibility of forming a polymeric film but also to the "difficulty in producing an initial monolayer of adsorbed Cu-BTA" as, in these conditions, the stable form of BTAH is the protonated one.

In conclusion, pH plays an important role and controls both the formation and the stability of the Cu-BTA layer.

1.1.3 Comparing cuprite and brochantite reactivity

In solution, benzotriazole reacts with synthetic cuprite and brochantite. The reaction induces a surface modification of the mineral at the nanometric scale with the formation of an amorphous outer layer, possibly polymeric, due to the interaction with copper atoms and BTAH molecules. A specific morphology (core-shell structure) is recognized in both cases: the unreacted mineral represents the core embedded in a Cu-BTA shell.

The reaction pathway includes in both cases a rapid growth of the layer in the first minutes of the reaction. For brochantite, an initial adsorption step can be suggested based on the experimental data, followed by continuous polymerization of Cu-BTA at the outer surface as dissolution of the mineral

proceeds. Despite the lack of direct evidence obtained in this work, a process based on a similar adsorption step and successive layer polymerization seems a possible pathway for the growth of the Cu-BTA on cuprite.

Despite the common points, when evaluating the surface layer thickness, the reactivity between the two minerals is different. In the case of brochantite, a thicker layer forms rapidly (30 nm after 2 hours) and reaction is nearly complete after 24 hours, with almost no mineral left. If the fast reactivity with synthetic brochantite is confirmed by Turgoose [144], who affirms that a complex forms after just few seconds.

On cuprite, the layer formed after the first 2 hours of reaction is ten times less thick compared to the one formed on brochantite. After 24 hours, the reaction is not complete and cuprite is still the major phase constituting the precipitate. The different reactivity can be connected to the different pH at which the two reactions take place, with an important acidification of the solution in the case of brochantite, while during reaction with cuprite pH is measured at value at which the mineral is stable.

It can be concluded that complexation is faster in presence of Cu(II) mineral brochantite as cupric ions are more readily available for reaction at the pH reached during the reaction. In the case of cuprite, a higher reactivity can be supposed at lower pH when brochantite is also present, which confirms the results obtained by Brostoff, who was able to identify the complex Cu-BTA by FT-IR spectroscopy after immersion in acidified solutions containing BTAH. The improved reactivity after 24 hours reaction might be also due to the oxidation of cuprous to cupric ions. Further investigation with cuprite at a pH comparable to the one reached during reaction with brochantite would help clarifying this point.

1.2 5CBT reactions

1.2.1 Reactivity of 5CBT with cuprite

The same protocol used for BTAH is followed to study the reactivity of cuprite with 5CBT solution.

Cuprite is identified by both µRaman and X-Ray diffraction analysis after different immersion times (2 and 24 hours). Differently from the experiment with BTAH, µRaman analysis indicates the formation of a Cu-5CBT complex that is detected even at short immersion time (2 hours).

TEM analysis confirms the presence of cuprite grains together with an amorphous layer at the cuprite grains' surface. The average layer's thickness does not vary considerably after 2 (11 ± 10 nm) and 24 hours (14 ± 9 nm).

The layer growth tendency is logarithmic (Figure 4.5) but more measurements are needed to confirm this trend.

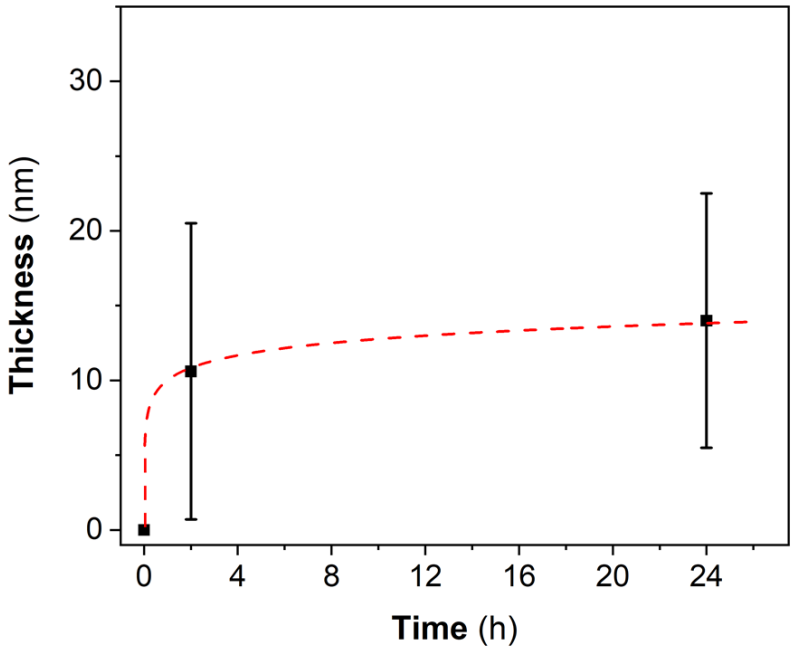

Figure 4. 5: Cu-5CBT layer thickness evolution on cuprite. The red dashed trend line suggests a logarithmic growth.

The high standard deviation recorded indicates that the layer thickness is not homogeneous in both cases. Moreover, after 24 hours in addition to the grains covered by the amorphous film, completely amorphous particles and cuprite grains that are not covered by the surface layer are observed (Figure 3.19 in Chapter 3).

The increase of pH from a value of 2.6 (pH of the pure 5CBT solution) to a pH of 3.3 in the first 10 minutes could be related to the oxidation reaction of cuprite in aerated liquid environment (Equations 10-11). The oxidation might have favoured the formation of Cu(II)-5CBT. Assuming this reaction path, the stability of the pH between 10 and 120 minutes indicates that during this time an equilibrium between cuprite oxidation and 5CBT deprotonation (Equation 12) is reached. The low pH (2.4) measured after 24 hours together with the presence of completely amorphous particles suggests that the equilibrium broke down at some point during the reaction and dissociation of 5CBT prevails on cuprite oxidation.

$$\frac{1}{2}O_2 + H_2O + 2e^- \rightarrow 2(OH)^- \quad (10)$$

$$Cu(I) \rightarrow Cu(II) + 2e^- \quad (11)$$

$$5CBT \rightarrow 5CBT^- + H^+ \quad (12)$$

1.2.2 Reactivity of 5CBT with brochantite

The insoluble compound obtained from the reaction of 5CBT and brochantite is investigated. The analysis of the precipitate in bulk (XRD) and at the microscale (µRaman) pointed out that brochantite is present at all reaction times. In addition, µRaman spectroscopy allowed to identify the Cu-5CBT complex, analogue to the one formed in the reaction with BTAH. The interaction between copper and the inhibitor seems to predominantly involve the nitrogen atoms of the molecule, while the possible bonding between the carboxylic group and copper atoms is not clarified.

The diffraction pattern after 24 hours reaction is characterized by a broad hump at low theta suggesting that the complex is polymeric at this stage of the reaction.

When analysed at the nanoscale by TEM, a similar morphology to the one already observed for BTAH is found: the reaction product exhibits a core-shell morphology with a crystalline core and an amorphous N-rich shell. By measuring the external layer on HR-TEM images, it was possible to evaluate the thickness evolution with time of the outer Cu-5CBT amorphous layer. Results are reported in Figure 4.6.

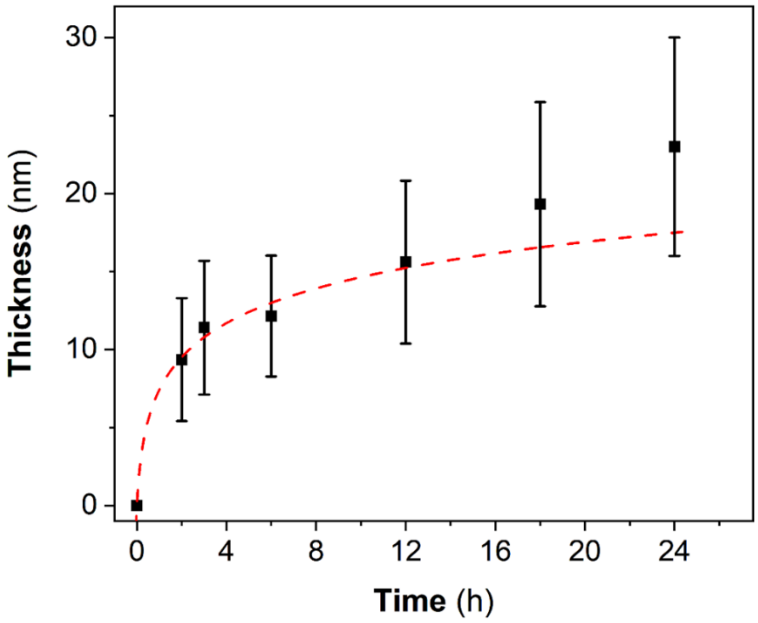

Figure 4. 6: Cu-5CBT layer growth on brochantite. The red dashed trend line suggests a logarithmic evolution of the thickness.

As it is highlighted by the red line, the data follow a logarithmic tendency until 12 hours while, after 12 hours, a variation in the thickness growth tendency is observed.

The thickness of the external layer after 2 hours corresponds to 9 nm. After 24 hours, most of the particles are amorphous and for those exhibiting the core-shell structure, the outer layer measures 21 nanometers-thick on average.

The evolution of pH during the reaction is of complex interpretation. A first step immediately after the addition of the mineral to the solution is characterized by a slight decrease of pH (2.3) compared to the initial pH of the 5CBT solution (2.5). This pH change can be interpreted as due to immediate complex formation (Equation 13) or as an immediate adsorption of $5CBT^-$ to the brochantite surface, followed by further 5CBT deprotonation.

$$Cu_4SO_4(OH)_6 + 8(5CBTH) \rightarrow 4Cu(5CBT)_2 \downarrow + H_2SO_4 + 6H_2O \qquad (13)$$

In a second step (first 30 minutes of the reaction), pH remains stable at 2.3, which suggests that brochantite dissolution is promoted compared to 5CBT deprotonation/complex. Between 30 and 80 minutes, pH increases up to a value of 2.9: at this point, a dissolution of brochantite with release of hydroxide ions not immediately compensated by the dissociation and complexation is suggested. A new equilibrium establishes again between 80 minutes and 2 hours and it is maintained for the next 24 hours as the pH stabilizes at 2.9.

Despite the low pH of the initial solution, brochantite is still observed after long immersion time. This observation is related to the formation of a surface Cu-5CBT complex and demonstrates that the interaction of the mineral with the inhibitor at the surface of the mineral have an influence on the access of the H^+ in solution directly to the mineral surface, thus controlling the dissolution process.

An initial adsorption step can be suggested with successive growth of the film by progressive dissolution of the mineral and polymer formation by a self-assembly process.

In order to evaluate the stability and the protectiveness of the surface layer, the 2-hours surface-modified brochantite was investigated after immersion in NaCl solution at different pH.

Results are comparable to those obtained for BTAH. In fact, brochantite is the only mineral phase detected in the solution at pH 7 and 5 and Cu-5CBT is always identified by µRaman spectroscopy. The new mineral atacamite is detected at pH 2.

Moreover, and again similarly to what has been previously observed on BTAH-treated brochantite, after immersion in solution at pH 2 the “ghost structure” morphology is observed on the HR-TEM

images. Hollow Cu-5CBT amorphous shells are still in place, while brochantite completely dissolved from the inner core (Figure 3.44 in Results).

The presence of a surface complex has a clear influence in the reactivity of the brochantite that is still present as crystalline core after 2 hours reaction with the inhibitor. The mechanism of dissolution in presence of the surface layer that is proposed for 5CBT is similar to the one suggested for the BTAH surface-modified brochantite and relies on the disruption of the bond at the mineral-complex interface when proton concentration is high. Presence of chloride alone does not affect the stability of the amorphous film and the surface bond in particular.

1.2.3 Comparing cuprite and brochantite reactivity

In solution, benzotriazole-5-carboxylic acid reacts with synthetic cuprite and brochantite. The reaction produces an amorphous layer on the minerals' surface due to the interaction with copper atoms and 5CBT giving the same morphology (core-shell structure) previously observed for BTAH.

The thickness of the layer formed on cuprite and brochantite after 2 hours of reaction is comparable as it measures 10 and 11 nm respectively. The layer is more homogeneous in terms of thickness when it forms on brochantite, while a high variability is observed on the cuprite. After 24 hours of reaction, in the case of brochantite most of the mineral is dissolved with amorphous Cu-5CBT aggregates representing the major phase. Different is the case of cuprite where the mineral covered by a thin amorphous film (14 nm) co-exists with amorphous aggregates of Cu-5CBT after 24 hours reaction.

The results suggest a mechanism of reaction in multiple stages: a first adsorption of the inhibitor could be involved and a further growth of the Cu-5CBT polymer on this first adsorbed layer is plausible.

The reaction with cuprite probably involves an additional oxidation step with formation of Cu(II)-5CBT.

1.3 Decanoic acid

1.3.1 Reactivity of HC10 with cuprite

Cuprite reaction in a decanoic acid solution is followed over 24 hours. The precipitate assumes a vivid blue colour that is more notable after 24 hours. Cu(II)-decanoate was unambiguously identified in the precipitate by both bulk (XRD) and micrometric structural analysis (µRaman) at all reaction times. The quantification based on XRD diffraction patterns shows that the formation of copper decanoate follows an exponential trend (Figure 4.7) and the reaction is not complete after 24 hours as 6.2%wt of cuprite is still detected. According to the curve, the reaction is complete after 27 hours.

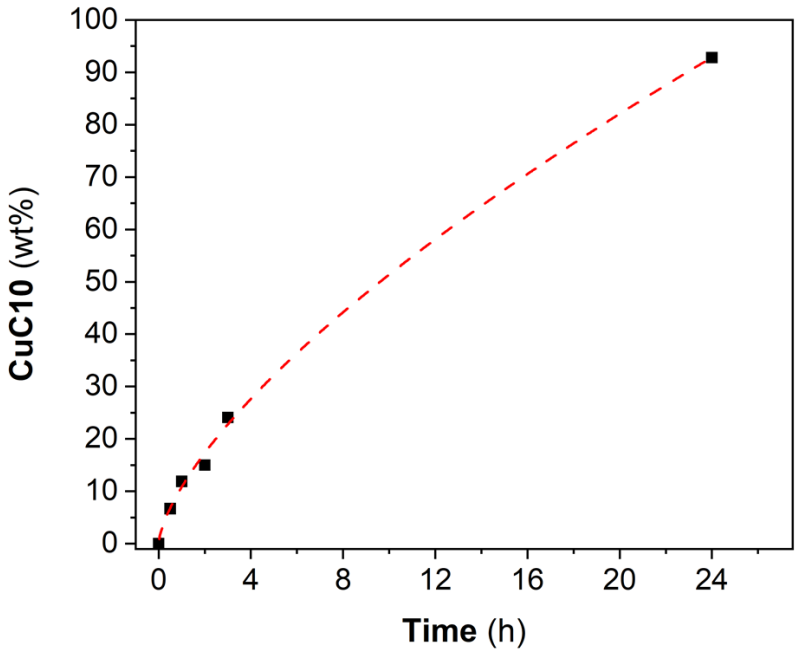

Figure 4. 7: Evolution of copper decanoate formation by reaction with cuprite. Wt% is calculated from diffraction patterns at different reaction times using the reference intensity ratio method. The red line represents the exponential trend of the reaction.

Results of SEM imaging indicate that copper decanoate crystals precipitate as elongated micrometric grains separated from the mineral. Their size increases with increasing reaction time.

The pH evolves in the first stages of the reaction: from the initial acidic value (2.6) of HC10 solution (pKa=4.9) a higher value (3.6) is reached after approximately 10 minutes, remaining stable within the first 2 hours. A pH of 3.9 was measured at 24 hours from the beginning of the reaction. The pH tendency observed here coupled to the analysis of the precipitate suggests that the increase of pH is related to the reduction of oxygen (Equation 14) as a result of the oxidation of Cu(I) in cuprite to Cu(II) (Equation 15) that is consequently involved in the formation of copper decanoate (Equation 16). As the availability of cupric ions is related to the oxidation of cuprite, precipitation of copper decanoate depends on this reaction, which controls and limits the decanoate precipitation rate.

$$\frac{1}{2}O_2 + H_2O + 2e^- \rightarrow 2(OH)^- \quad (14)$$

$$Cu(I) \rightarrow Cu(II) + 2e^- \quad (15)$$

$$Cu(II) + 2RCOOH \rightarrow Cu(RCOO)_2 \downarrow + 2H^+ \quad (16)$$

1.3.2 Reactivity of HC10 with brochantite

From the reaction of HC10 and synthetic brochantite, again a vivid blue compound is separated from the solution at all reaction times. The product of the reaction compound analysed by µRaman and XRD

after 2 and 24 hours corresponds to pure copper decanoate. The morphology of the new phase formed was evaluated at the micrometric scale by SEM: the copper decanoate crystals appear as elongated phases which size considerably increases with increasing immersion time from 11 µm in length after 2 hours to about 500 µm after 24 hours.

The evolution of pH follows an exponential trend (Figure 4.8): within the first 2 hours of the reaction a progressive decrease from pH 3 to pH 1.8 is recorded.

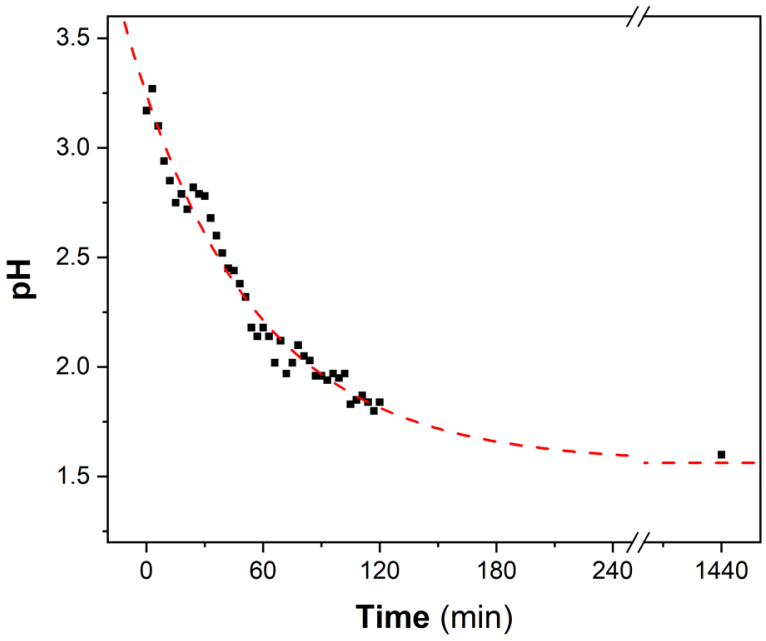

Figure 4. 8: Evolution of pH measured during the reaction between brochantite and decanoic acid. The red line represents the exponential trend followed by pH variation.

The same pH (1.6) is recorded at 2 and 24 hours. The final pH corresponds to the pH calculated for a complete reaction of brochantite with decanoic acid to give copper decanoate (Equation 13).

$$Cu_4SO_4(OH)_6 + 8RCOOH \rightarrow 4Cu(RCOO)_2 \downarrow + H_2SO_4 + 6H_2O \qquad (17)$$

The reaction mechanism proposed consists in a gradual dissolution of brochantite, complete after 2 hours. As soon as cupric ions are available in solution, they bond to the dissociated carboxylic group in HC10. Copper decanoate starts precipitating from the solution and molecules of CuC10 assemble as elongated grains that develop in size as reaction proceeds.

The stability of copper decanoate formed after 2 hours, when no brochantite is detected, is tested in different aggressive solutions. Results show that the compound is stable at pH 7 to 2, while the acidic form is favoured at even lower pH, as measured at pH 1.

1.3.3 Comparing cuprite and brochantite reactivity

Cuprite and brochantite react with a solution containing HC10 to form a blue water-insoluble precipitate identified in both cases as crystalline copper decanoate. The main difference in the reaction with the two minerals is the rate of formation of the decanoate. In the case of cuprite, the reaction proceeds through oxidation of cuprous to cupric ions as evidenced by the increase in pH: the oxidation reaction controls the availability of Cu(II) in solution and therefore the rate of formation of the decanoate. The reaction kinetics can be described by a power function (Figure 4.7) and, according to the trend, complete transformation of cuprite takes place after 27 hours in the conditions chosen. Reactivity with brochantite proceeds in a much faster way; at the pH of the HC10 solution (2.8), the mineral is not stable and solubilizes. As cuprous ions are readily available, without any oxidation step, copper decanoate might form rapidly (Equation 18). The increase in CuC10 grain size testifies a progressive self-assembly of CuC10 molecules as reaction proceeds.

$$Cu(II) + 2RCOOH \rightarrow Cu(RCOO)_2 \downarrow + 2H^+ \qquad (18)$$

Considering the stability of copper decanoate, the compound does not undergo any modification in NaCl solution down to pH 1, when the acidic (HC10) form is detected. The measured pH for the reaction with brochantite does not decrease below 1.6, while a higher pH is reached as the reaction with cuprite proceeds due to oxygen reduction.

As the phases, minerals and CuC10, are differently soluble in solvents, an important role is played in terms of reaction kinetics by solvent composition. In fact, the solvent polar and apolar components can modify the dissolution of the minerals and therefore the availability of cupric ions in solution necessary for complexation.

1.4 Comparison of the three compounds' reactivity

Table 2.1 summarizes the results obtained from the reactions between the three organic compounds and the synthetic mineral phases.

Table 4. 1: Summary of the observations on the three inhibitors.

		BTAH	5CBT	HC10
Cuprite	Composition	Cu(I)-BTA cuprite	Cu(I)/Cu(II)-5CBT cuprite	Cu(II) decanoate
	Morphology	Core-shell (3 nm layer)	Core-shell (11 nm layer)	Acicular crystals
	Mechanism	Adsorption + dissolution/self-assembly	Adsorption + dissolution+oxidation/ self-assembly	Dissolution+oxidation/ precipitation
Brochantite	Composition	Cu(II)-BTA brochantite	Cu(II)-5CBT brochantite	Cu(II) decanoate
	Morphology	Core-shell (29 nm layer)	Core-shell (9 nm layer)	Acicular crystals
	Mechanism	Adsorption/dissolution/self-assembly	Adsorption/dissolution/self-assembly	Dissolution/precipitation

1.4.1 Composition

In all reactions, an organic ligand, constituted by the deprotonated inhibitor, bonds to cuprous or cupric ions to give a water insoluble[16] precipitate. In the case of BTAH and 5CBT, the bond with copper concerns predominantly the N atoms in the azole ring. Decanoic acid bond through the oxygen atoms in the carboxylic group.

For the reactions involving BTAH and 5CBT, the mineral, brochantite or cuprite, is always identified in combination with a new phase, the complex Cu-BTA or Cu-5CBT. The new compound is amorphous as proved by TEM analysis (SAED and HR-TEM images), while the structural analysis indicates that a bond between copper and the inhibitor has formed. Moreover, when the complex is formed from brochantite, its polymeric nature is confirmed by the broad hump detected on the XRD patterns.

In the case of decanoic acid, crystalline copper decanoate precipitates from the solution. The mineral is only identified after short reaction time and exclusively in the case of cuprite.

1.4.2 Morphology

The nanometric scale analysis of the precipitates (TEM) revealed to be particularly useful for the study of the morphology of the reaction products. The reason is that the aforementioned complexes of BTAH and 5CBT are present in the form of nanometric amorphous layers specifically located at the mineral surface. The layer thickness corresponds to few tenths' nanometres. The film formed on cuprite after

[16] And ethanol insoluble in the case of Cu-5CBT and Cu-BTA.

2 hours is thinner for BTAH (3 nm after) and thicker for 5CBT (11 nm), nevertheless, high thickness variability is observed for the latter. The situation is reversed in the case of the layer formed on brochantite after 2 hours: a thicker layer of Cu-BTA (29 nm) and a thinner layer for the Cu-5CBT (9 nm) are observed.

Different observations concern the reactions with decanoic acid. First, the copper decanoate crystals are observed as separate grains from the unreacted mineral when this is not completely reacted. Secondly, the decanoate formed is micrometric in size and the elongated grains can reach up to 500 µm in length. In this case, nanometric analysis was not required. Last, the decanoate formed has a micrometric-size and it is constituted by elongated grains. The size of the crystals increases with reaction time.

1.4.3 Protective role of the complex

The role of the Cu-BTA and Cu-5CBT surface layer is to limit brochantite dissolution as demonstrated by the immersion experiments in different aggressive solutions. Brochantite reacts in concentrated NaCl solution and atacamite is formed at all pH. When the surface azole layer is present, the reactivity of the brochantite still present in the core changes. No transformation into atacamite is detected at near-neutral pH, while atacamite is detected at lower pH (2 and 1). The rate of transformation of brochantite into atacamite at pH 2 is lower for the 5CBT-treated brochantite compared to the BTAH-treated one (Figure 4.9). Transformation of the BTAH-treated brochantite is not complete even at lower pH.

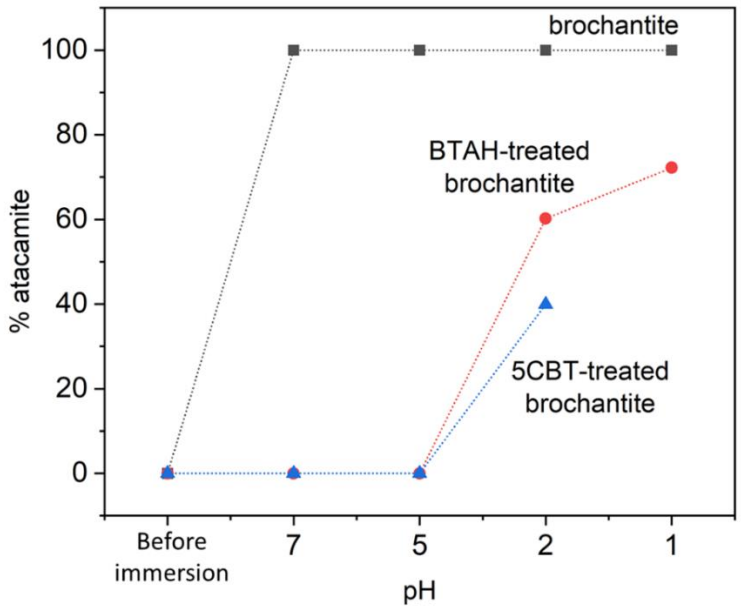

Figure 4. 9: Comparison among the amount of atacamite formed after immersion at different pH of the untreated brochantite (black), BTAH-treated brochantite (red) and 5CBT-treated brochantite (blue). The complex is neglected as it cannot be detected by XRD analysis.

This has been considered as further evidence that an adsorbed layer of molecules and a bond with the outer copper atoms in the surface of the mineral has formed. In the absence of this surface interaction, as ions can diffuse through the layer, a transformation of the brochantite would be expected even at neutral pH. This confirms the effect as stabilizer already reported in the literature especially concerning the protection of archaeological artefacts [145]. Such surface adsorption finally controls the stability of the mineral.

The precipitated decanoate is stable in aggressive NaCl solution at pH≥2, below this value, the acid form is more stable.

1.4.4 Reaction mechanisms

Two main reaction mechanisms are proposed: an adsorption/precipitation mechanism describes the behaviour of the two azoles, while a dissolution/precipitation mechanism better fits the observations on decanoic acid.

The molecules characterized by nitrogen atoms as electron-donor sites, BTAH and 5CBT, interact with copper atoms (the electron deficient site) giving different types of bonding. The first interaction consists in the adsorption of the organic ligand, the deprotonated or protonated molecule, to the copper atoms in the mineral located at the interface with the solution. The adsorption interaction

happens instantaneously as soon as the mineral gets in contact with the solution. The second step consists in the further polymerization of the amorphous complex that grows on the first layer of adsorbed molecules: cupric ions act as bonding sites between organic molecules and the reaction can proceed as a polymerization. This step implies the presence of copper ions, capable of bond formation with several organic molecules: the continuous dissolution of the mineral is therefore necessary as well as the diffusion of ions through the forming film. The solubility of the mineral at the pH of the reaction also plays a role during this second step. The thinner film formed on the cuprite might indicate a low dissolution of the mineral or a lower diffusion through a more compact film. The situation in the case of 5CBT and cuprite is slightly different and the oxidation of cuprite is suggested with formation of a thicker film.

During layer growth, the reactivity is different for BTAH and 5CBT. In fact, if for BTAH and brochantite a steady state is reached almost immediately, in the case of 5CBT, an increase of pH after 30 minutes testifies that brochantite dissolution is faster than film formation at this point of the reaction. An equilibrium between the two reactions is reached again between 80 and 120 minutes. The different behaviour can be related to the diffusion properties of the layer formed.

For BTAH and 5CBT, the bond formed at the mineral surface is weaker compared to the one formed between different cupric ions and different organic molecules in the polymer. This allows a constant bond break and formation during the reaction when the inhibitor is present in solution, although, as the inhibitor is not present, the protons present in solution might attack the bond at the interface thus promoting mineral dissolution.

When considering decanoic acid as reactant, the mechanism of complex formation between copper atoms and organic ligand consists in the dissolution of the mineral on one side and precipitation/growth of the decanoate on the other. Oxidation is involved when cuprite is present.

2. Metz corrosion layer

2.1 Metz samples before treatment

2.1.1 Physico-chemical characterization of the untreated system

The naturally corroded copper samples from the roof of Saint Martin church have been investigated before applying a corrosion inhibitor, as the understanding of the corrosion system prior to treatment is fundamental for interpreting the interaction with the organic compound investigated.

Several observations are in agreement with what has been previously observed on naturally corroded copper from urban environment in the literature (see Chapter 1).

It is the case of the Raman mapping results in cross-section, that permit to distinguish within the patina, two layers characterized by different mineralogical composition: an outer layer, composed by brochantite and an inner layer composed by cuprite. The thickness of the two layers was measured: the outer layer average thickness (45.6 µm) is considerably higher than the inner one (3.2 µm). The thickness values are compared to those obtained on selected copper samples from similar in-land and mostly urban environments in both France and Austria (Figure 4.10 and Table 4.2) [19], [26], [146].

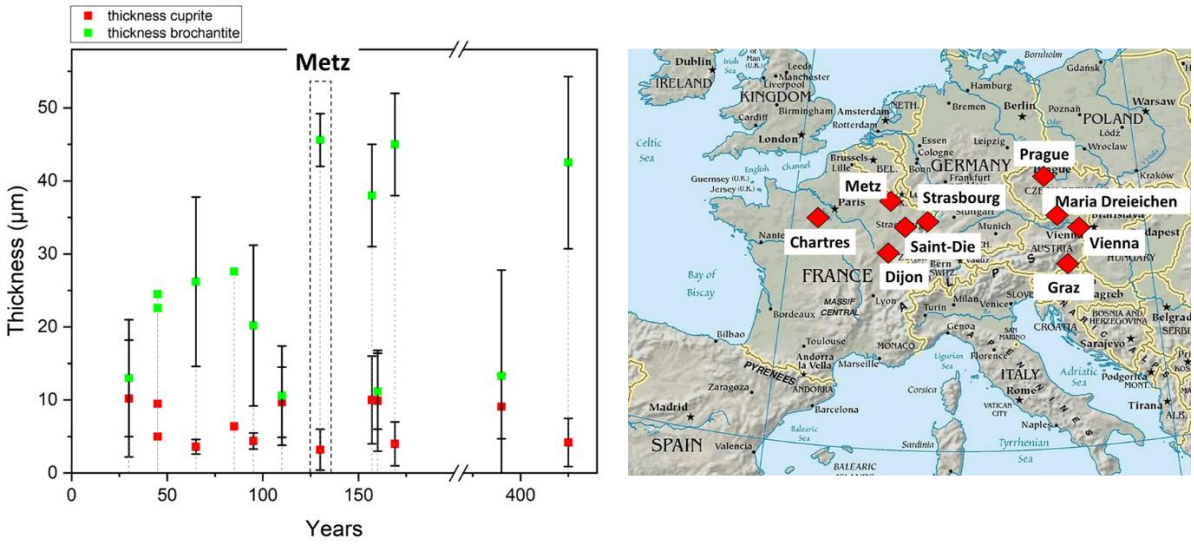

Figure 4. 10: Cuprite (red) and brochantite (green) thickness from different locations and exposures times. The map to the right indicates the locations of exposure of the samples.

Table 4. 2: Reported data on the thickness of cuprite and brochantite from different studies, locations and exposure times.

Ref.	Site	Years of exposure	Cuprite thickness (µm)	Brochantite thickness (µm)
FitzGerald et al. 2006	Saint-Die	30	10.2 ± 8	13 ± 8
	Strasbourg	45	5	24.5
	Saint-Die	45	9.5	22.6
	Vienna	65	3.6 ± 1	26.2 ± 11.6
	Vienna	85	6.4	27.6
	Vienna	95	4.4 ± 1.1	20.2 ± 11
Chang et al. 2017	Vienna	110	9.7 ± 4.8	20.2 ± 11
This study	Metz	130	3.2 ± 2.8	45.6 ± 3.6
Apchain 2018	Chartres	157	10 ± 6	38 ± 7
Chang et al. 2017	Maria Dreieichen	160	9.9 ± 6.9	11.2 ± 5.2
Apchain 2018	Dijon	169	4 ± 3	38 ± 7
Chang et al. 2017	Graz	390	4.4 ± 1.1	13.3 ± 14.5
	Prague	425	4.2 ± 3.3	42.5 ± 11.8

The graph shows that cuprite thickness is fairly stable after 50 years of exposure ranging from 3 to 10 µm in agreement with previous observations by FitzGerald [26]. Differently, brochantite thickness variation with time is less straightforward and, although it seems to follow a linear trend in the first 170 years, this trend is not the same for all the locations especially after long exposure times.

The values obtained for the Metz samples can be inscribed in the general trend for both cuprite and brochantite. based on these measurements and on the nature of the non-metallic inclusions found in similar objects [18], the ancient nature of the samples is confirmed and the year 1887, corresponding to the construction of the bell tower, is compatible with the beginning of the exposure of the copper tiles.

As previously stated, brochantite constitutes the outer interface in direct contact with the atmosphere. The presence of this mineral, a green hydroxy sulphate, is responsible for the light-green coloration that characterizes the plates' surface, conferring the "aesthetically pleasing" appearance already reported in previous studies [17], [26], [30]. When observed in cross-section, another characteristic of the layer is its porosity: a network of connected macro to mesopores and cracks is clearly detected by micrometric secondary electrons imaging, confirming Apchain previous investigation [19]. The high hydrophilicity of the surface with a low contact angle measured (about 20°), has been related by several authors [17], [26] to the porosity of the outer layer, which is confirmed here.

The second main mineral component of the patina, identified by Raman analysis is the cuprous oxide cuprite. The mineral is detected as a continuous layer between the outer brochantite and the metallic substrate. At the micrometric scale (OM, SEM), the cuprite layer appears less porous compared to the outer brochantite.

At the interface between brochantite and cuprite layer, the co-existence of both phases over approximately 10 µm in thickness is highlighted by the µRaman mapping and especially by the peak profile reconstruction (Figure 3.58 pg.145). An additional difference of the interface is pointed out by elemental EDS analysis in cross-section: chlorine, present in very low amount in the rest of the corrosion layer (0.3 to 0.5%wt), is identified in the 20 µm right above the cuprite layer in relatively higher amounts. The relative amount of chlorine in this area is still low (2.1%wt on average can reach locally 6%wt) and the quantification does not allow to associate it to a specific Cl-containing mineral phase. The preferential localization of chlorine in the innermost part of the corrosion layer has been previously observed by Opila [147] in old patinas exposed for long time (44 to 100-years) in urban-marine environment as chlorine was found to be more abundant close to the metallic substrate[17]. The author attributes the finding to a higher mobility of chloride ions compared to sulphate ions due to their different radii of the two ionic species and their charge which suggests a preferential diffusion within the corrosion layer and further precipitation. In addition, the solubility of atacamite in weak acid has also been considered responsible for the absence of the chlorinated mineral in the outermost part of the corrosion layer [151].

In the Metz samples studied here, the absence of atacamite is reasonable as the site of exposure is far from the coats and in most studies atacamite or clinoatacamite are detected on copper exposed to a marine environment [148], leading to suggest a very low amount of the mineral or a different Cl-containing and still unidentified compound.

[17] By Auger electron spectroscopy and Ar^+ sputtering.

The results exposed till here correspond to the morphological, elemental and structural characteristics of copper corroded in urban environment for a considerable amount of time and are similar to those reported in previous studies.

In order to deepen the understanding of the corrosion system, further investigations were undertaken. In-depth characterization of the cuprite layer at the micro and nanoscale was assessed and relevant information came from the study of the corrosion layer after being subjected to a certain external perturbation (D_2O, KBr).

2.1.2 Cuprite layer

A thin section was obtained by FIB milling at the interface copper/cuprite/brochantite. The observation of the section at the micrometric scale evidence the presence of large (micrometric) polygonal crystals located in the outer part of the cuprite layer. A sub-micrometric cuprite is identified underneath: this layer is continuous as it is not fractioned into micrometric grains.

Nanometric scale observations by FIB tomography were used to study this compact cuprite layer. Results of the volume reconstruction reveal that pores of few tenths of nanometre are present within the cuprite, while larger pores are located at the metal/cuprite interface. In both cases, the pores are not connected to each other and 3% total pore volume was estimated. This result confirm that a denser, relatively non-porous and adherent cuprite layer is present in contact with the metal, as proposed in the literature.

The absence of channels allowing direct access of water and dissolved oxygen to the metal confirms the protective character of the cuprite layer, in accordance with the results obtained by electrochemical analysis: a 60% inhibition efficiency was calculated when comparing Metz uncorroded copper samples [130].

2.1.3 Corrosion system after perturbation

The corrosion layer was studied by altering the external environment. The sample immersed in D_2O was studied relative to the deuterium enrichment. As expected, deuterium is detected within the porous brochantite layer. Deuterium is also detected in the cuprite layer implying that deuterated water can diffuse to some extent through the cuprite. It is important to highlight here that by Tof-SIMS

analysis, elemental images resolution corresponds to several tenths micrometres therefore a certain uncertainty must be considered when evaluating the interfaces and it was not possible to separate internal and external cuprite. Nevertheless, the diffusion of D_2O within cuprite is probably favoured in the outer part, characterized by large grains, in opposition with the inner compact layer.

A more severe perturbation of the corrosion system was obtained by relatively long (30 days) immersion in a concentrated KBr solution and several phenomena are observed at the micrometric scale as a result of the immersion:

- Formation of an almost continuous gap (voiding) between the metal and the cuprite.
- Precipitation on the surface and within the outer layer of a new phase (copper bromide hydroxide).
- Presence of bromine enrichment at the cuprite/brochantite interface.

The formation of voiding at the metal/cuprite interface is due to the re-corrosion of the metal due to the loss of passivity of the cuprite layer, as previously observed in the literature [3]. Once the concentrated KBr solution is directly in contact with the metal, the formation of soluble cuprous complexes ($CuBr_2^-$) complexes, similarly to what observed for chlorides-containing solutions, inhibits the formation of a new passivating cuprite layer.

Particularly interesting is the local bromine Tof in the inner part of the brochantite layer. On one side, this confirms the permeability of the brochantite layer due to the high porosity, on the other, such uneven distribution suggests that negatively charged bromide ions are attracted in the specific area due to the presence of positively charged cuprite surface. A competitive adsorption of bromide ions over hydroxide ions is suggested with progressive dissolution/oxidation and therefore destabilization of the cuprite layer with possible re-corrosion of the metal.

The mechanism of reaction with KBr solution and reactions are suggested in Figure 4.11.

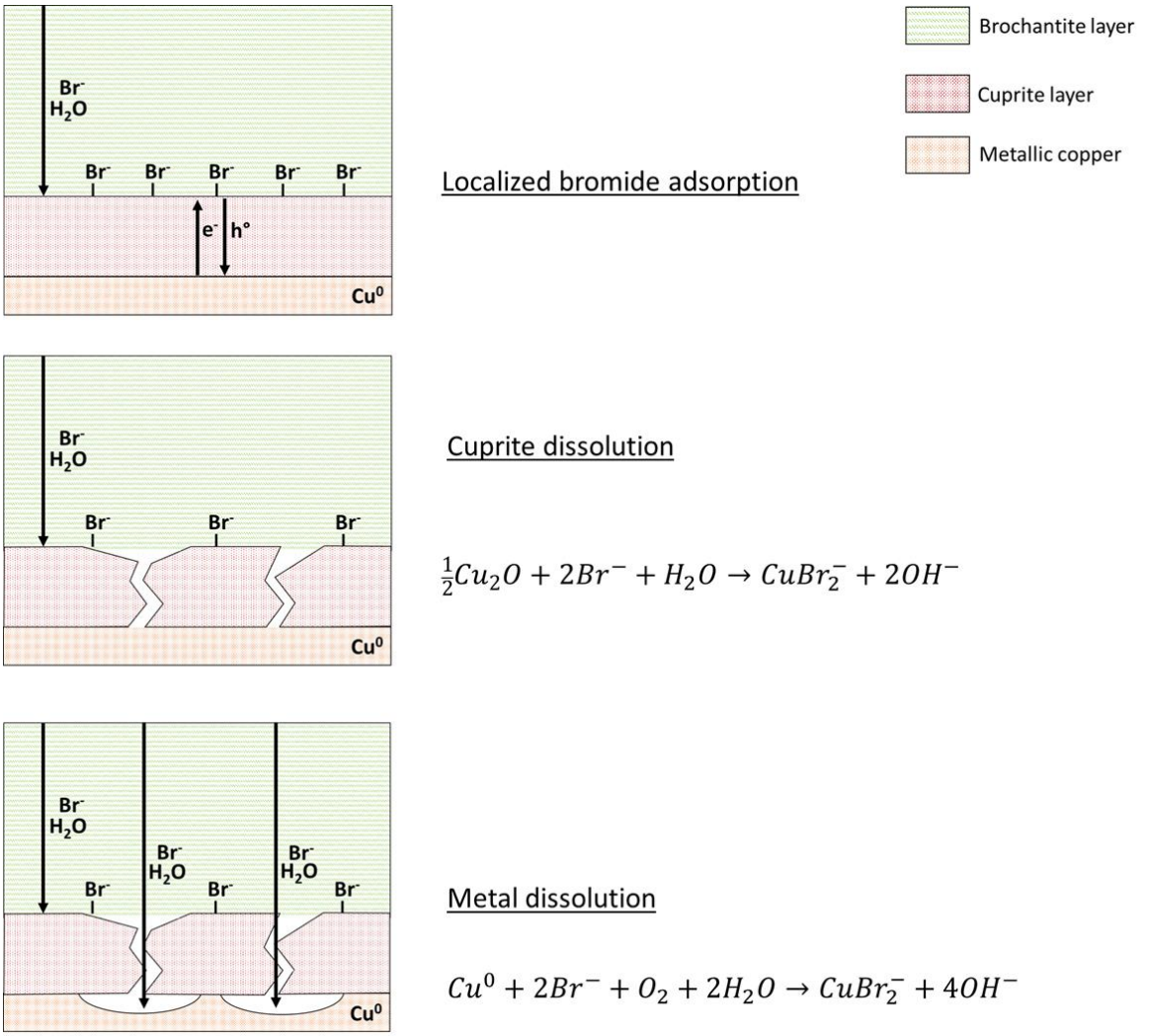

Figure 4. 11: Proposed scheme for the loss of passivity of the untreated sample after immersion in KBr solution.

2.1.4 Modified double-layer structure

The new observations on the Metz samples allow to propose a more detailed model with specific physico-chemical and transport properties for the corrosion system investigated.

First, the results of the analysis at the micrometric scale point out that no sharp interface exists between cuprite and brochantite layer and both phases co-exist in an area of about 10 microns thick.

Secondly, from the micrometric observations in thin section, the cuprite layer morphology can vary. In areas where the layer is several micrometres thick, large polygonal crystals are clearly recognized. Differently, the cuprite closer to the metal and in areas where the layer is thinner (thickness ≤1 µm), compact, characterized by a low and closed porosity and adherent to the metallic substrate with the exception of some microporosity located at the interface.

The presence of large cuprite crystals recalls literature studies [13], [149] referring to the formation of a cuprite layer in aerated moisture environment. In these studies, as the oxide layer grows, microcrystalline cuprite formed on copper develops into micrometric polycrystalline grains assuming typical poly-octahedral shapes. Such growth is accompanied by mechanical stress that causes the layer to fracture, which allows water and oxidants to diffuse easily through the layer compared to a denser cuprite layer. Here, the polygonal cuprite crystals grow on top of a more compact cuprite layer despite the presence of the outer brochantite layer. Pores and cracks resulting from the grain growth favour the progressive dissolution/oxidation of cuprite and can be filled by precipitating cupric species such as brochantite. Tenorite can also be supposed as an intermediate phase but, being unstable, it is readily transformed into another Cu(II) amorphous or mineral phase. The precipitation of brochantite at the surface and in the proximity of cuprite grains can explain Raman results showing the co-existence of both phases mixed at the interface in a micrometric volume as testified by this technique.

The higher porosity of the outer cuprite layer would also justify the water permeability detected after immersion in D_2O, although further analysis at a smaller scale, are needed to confirm this hypothesis.

Another relevant observation at the interface cuprite/brochantite concerns the identification of a higher amount of chlorine in this area. Chlorine is always present in the atmosphere and the high mobility of Cl^- ions permit a migration from the environment to the corrosion layer. Considering that brochantite is extremely porous, chloride can easily diffuse in the outer layer. A reason for the localized accumulation of chlorine could be related to the specific characteristics of the cuprite in the interfacial layer and to the tendency of chloride ions to adsorb on the positively charged cuprite surfaces, similarly to what is observed after KBr immersion. The formation of a metastable phase (copper chloride sulphate) cannot be excluded but no evidence where found in the literature. Such phase would gradually transform into copper hydroxy sulphate, thus losing the chloride ions that, in stagnant conditions, will again be adsorbed on the underlying cuprite.

Some considerations can be drawn concerning the transport mechanism within the intermediate/outer cuprite layer. On one side, the ionic and electronic transfer is hindered compared to the underlying, more compact cuprite layer since the oxidation of the grains' surface determines a change in the conductive properties of the material. Some cuprite grains might be isolated and electrical contact with the metal is lost. On the other hand, grain boundaries with precipitated brochantite (or other copper oxides and hydroxides) constitute preferential channels for water and dissolved species diffusion. Although, the permeability within the interface is lower compared to the brochantite layer itself and it might be influenced by the tortuosity of the diffusion path.

Transport processes that are fast in the outer brochantite (diffusion in solution through a pore network) and in the inner cuprite (diffusion at the solid state in a semiconductor) and are slower in the interfacial layer.

Based on the above considerations, a schematic view of the Metz corrosion layer is proposed in Figure 4.12.

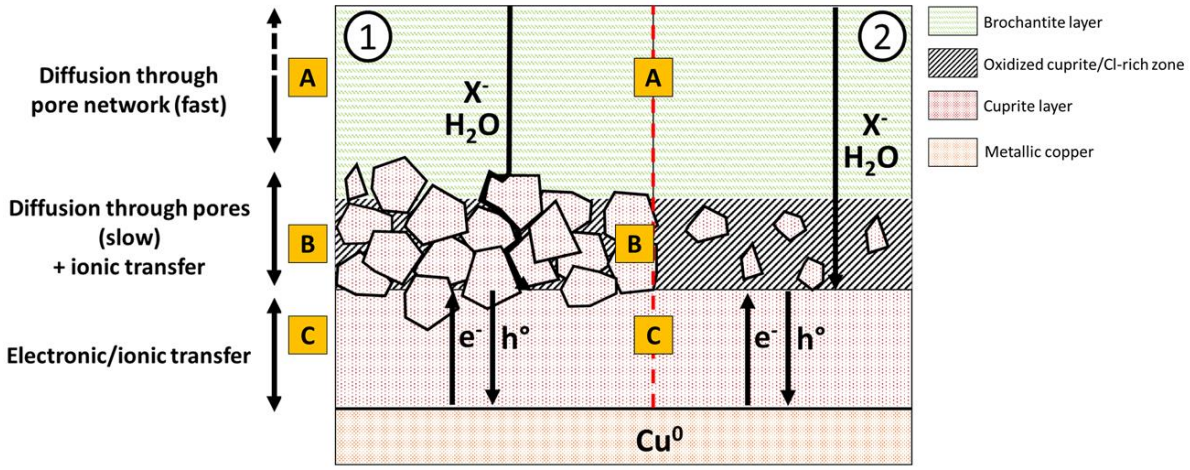

Figure 4. 12: Proposed schematic model for the Metz samples' corrosion layer indicating the main phases and transport properties.

In the left portion of the image (1), the outer green part (A) represents the brochantite layer: here diffusion is permitted thanks to the presence of a connected network of pores. The layer provides only a very limited barrier effect towards water and dissolved oxygen diffusion.

On the contrary, the inner cuprite layer (C) in contact with the metal is characterized by high density and closed porosity. Charged species transfer is favoured compared to diffusion. The porosity observed at the metal/cuprite interface testifies that the anodic dissolution of copper is not immediately followed by cuprite precipitation due to the limited access of oxygen through the cuprite vacancies.

The intermediate layer (B) is composed by large crystals of cuprite partly oxidized to Cu(II) species (brochantite/tenorite). Here chloride ions adsorb on the cuprite grains surface or precipitate as a metastable phase. The transport within the intermediate layer involves electronic and ionic transfer through the cuprite still in electrical contact with the metal and diffusion through the grain boundaries. Both transport processes are limited by the intermediate characteristics of the interfacial layer as previously discussed.

The layer (B) with cuprite grains still connected to the inner cuprite layer is not always present: this scenario is represented in the right part of the scheme (2) where the cuprite layer measures less than 1 µm. In this case, the classical "duplex film" model can be used to represent the corrosion layer with an outer (A) porous layer (brochantite) and an inner (C) compact layer (cuprite). Loose and readily oxidized cuprite can be present.

2.2 Metz samples treated with BTAH

The Metz samples were treated by immersion using a BTAH solution with a concentration commonly employed in conservation (3% w/v) [24], [145]. Electrochemical test after 24 hours in synthetic acid rain at pH=3.1 confirms the efficiency of the treatment in slowing down the corrosion reaction: a current reduction is observed and the calculated inhibition efficiency is equal to 99% [130]. The potential describes a mixed-type behaviour of the inhibitor.

In addition, the experiment using aggressive KBr solution confirms the positive role of the BTAH treatment on the Metz samples since no sign of destabilization are present after 30 days contrary to the untreated sample: no dissolution of the metal with voiding formation at the cuprite/metal interface is observed. No localized bromine enrichment the brochantite/cuprite interface is detected; no newly formed phase ($Cu_2Br(OH)_3$) is found nor in cross-section or on the surface.

2.2.1 Physico-chemical properties after treatment

In order to understand the mechanism of protection, physico-chemical characterization at the global and micrometric scale is undertaken and the results are discussed by comparing information obtained at the nanometric scale on the synthetic mineral phases.

From the structural and morphological point of view, brochantite and cuprite are detected as distinct layers in cross-section, located in the outer and inner part of the corrosion layer, similarly to what was observed on untreated samples. The respective thickness remains unchanged compared to an untreated sample: brochantite layer of the BTAH-treated samples measures 46.7 ± 3.9 µm on average compared to the 45.6 ± 3.6 µm of the untreated samples, while cuprite measures 4.5 ± 3.1 µm on average compared to the 3.2 ± 2.8 µm in the untreated samples. The higher values obtained for BTAH-treated cuprite layer is slight and can be explained by the thickness variability observed on the Metz samples.

Despite these similarities, the BTAH treatment has an impact on the structural components of the outer layer. In fact, in addition to the characteristic frequencies corresponding to brochantite, those assigned to the complex Cu-BTA are detected contemporary by µRaman spectroscopy. Interestingly, the signal corresponding to the Cu-BTA complex is detected together with the one of brochantite along the whole depth of the outer corrosion layer and until the cuprite layer. The detection of both the characteristic Raman shifts on the same spectrum suggests that both compounds are simultaneously present suggesting a similar reaction mechanism as the one observed on the mineral phases of brochantite with a partial transformation of the natural brochantite over 2 hours of reaction in the BTA solution.

The reaction takes place within the whole brochantite layer thanks to the specific morphology of the brochantite layer that, being characterized by high porosity and thus a high specific surface will allow the fast saturation by the inhibitor's containing solution. The reaction will then start on the surface of the brochantite in direct contact with the solution, while the inner part of brochantite grains and compact crystalline domains will not react immediately.

The unchanged surface and cross-section morphology observed by SEM at the micrometric scale can also find an explanation in the specific surface-reaction path of the BTAH solution towards the mineral. The surface modifications produce a visible change in the by global visual appearance of the Metz samples' surface: a colour change is detected (ΔE_{94}=13) with a colour shift towards a dark-green hue and, in particular, a decrease of the parameter relative to brightness. This observation confirms the complexation with the inhibitor that produces a dark-green coloured compound, in agreement with previous studies [24], [144].

Although, complexation does not produce microscopic morphological changes of the brochantite grains, observed only at the nanoscale.

The permeability properties of the treated layer have been studied by surface measurements and micrometric observation. At this last scale, considering morphology, SEM observations of the cross-section point out that, similarly to the untreated sample, a macro to mesopores' network is present. This result is confirmed by the results of the D_2O immersion indicating that deuterium enrichment (δ_n= 1014 ± 97) in the S-rich layer is comparable to the one obtained for the untreated sample (δ_n= 1264 ± 148).

The permeability of the outer corrosion layer is apparently in contrast with the surface tension measurements on the BTAH-treated sample that, with a measured contact angle corresponding to 103°, indicates the formation of a hydrophobic surface. This discrepancy can be related to the different duration of the respective tests: in the first case, the measurement of the contact angle is performed

after only 10 seconds from the drop deposition, while in the second, an immersion of 30-days immersion is employed.

In relation to the different duration, it seems clear that surface tension is more influenced by the immediate ability of the compound present on the surface (the Cu-BTA formed on the brochantite in the case of the treated sample) to interact with the water drop by forming hydrogen bonds. The presence of a pore network has a more important influence on the longer-term permeability of the sample and the two methods are complementary.

Again, a parallel can be drawn with the nanometric-scale observations. In fact, despite the complex Cu-BTA being hydrophobic and not soluble in water, upon prolonged immersion in solution, the layer formed around the brochantite grains is permeable to ionic species.

The permeability experiment highlights that the formation of the Cu-BTA complex by reaction with the brochantite does not produce any water barrier layer.

Unlike brochantite, the structure of the internal cuprite layer seems unaffected by the treatment as only the signal corresponding to cuprite is detected by µRaman spectroscopy. The cuprite layer morphology and thickness do not undergo major changes as an effect of immersion in BTAH solution: as reported earlier in this paragraph, the thickness of the layer is comparable to the one measured on the untreated sample and the layer appears compact and adherent to the metal.

The property that drastically changes after treatment is liquid water permeability with a reduction of deuterium enrichment within the CuO-rich inner layer. Deuterium enrichment passes from 999% ± 471 before treatment to 205% ± 104 after BTAH treatment. This result indicates that water permeability is highly reduced in the cuprite layer of the BTAH-treated sample compared to the cuprite in the untreated one.

2.2.2 Proposed protection mechanism proposition

The decrease in water permeability within the cuprite layer after long immersion time, suggests that a certain hydrophobic and/or barrier effect is present after treatment. Despite the fact that the outer modified brochantite layer is permeable, a decrease in the diffusion rate within this layer due to the presence of the Cu-BTA surface complex cannot be excluded and further investigation at different immersion times are needed to clarify this point.

The difference in water intake between cuprite and brochantite layer, on the other hand, might also indicate the formation of a Cu-BTA complex with cuprite. The penetration of the inhibitor's solution until the interface cuprite/brochantite in the previously described intermediate layer is detected thus

making the interaction with the cuprite possible, although not detectable at the scale of the corrosion layer. Indeed, the lack of evidence at the micrometric scale concerning the presence of such compound can be explained by the fact that, if present, the Cu-BTA film is nanometric and it cannot be detected on the synthetic powder when analysed by µRaman spectroscopy. In accordance with the observations of the Metz untreated samples, the interaction with cuprite at least after a short time of the immersion (2 hours used for the treatment), is reasonably limited to the outer surface or the intermediate layer, where BTAH can react with the cuprite large grains. The penetration of the inhibitor within the compact cuprite layer and until the metal is less probable considering the unconnected porosity of the inner layer.

A dual role might be exerted by the suggested Cu-BTA formed on cuprite: on one side, it might, despite its low thickness, reduce the diffusion of water and dissolved species (barrier effect), on the other side, it might block the copper atoms in the outer cuprite layer, limiting the dissolution/oxidation processes. In fact, indirect evidence on the formation of a surface bond between Cu atoms and BTAH/BTA^- molecules comes from the KBr experiment. The highly mobile bromide ions are able to diffuse in the outer corrosion layer, although, no accumulation and local enrichment of bromine is detected in the intermediate layer, where the outer oxidizing cuprite grains are located. This demonstrates that the copper atoms in the cuprite are bond to the inhibitor and there are no (or not many) available sites for bonding with bromide.

This last observation would confirm that the Cu-BTA is not present as a surface precipitate but as a chemisorbed layer. Bromine adsorption on cuprite, otherwise responsible for the progressive loss of oxide passivity and re-corrosion of the metallic substrate is not observed.

The lack of cupric ions in solution due to absence of available ions from either metal re-corrosion or corrosion minerals dissolution, as they are stabilized by the Cu-BTA surface layer, also explain the fact that no copper bromide hydroxide precipitates after KBr immersion. Moreover, as an effect of the mineral stabilization, a lower dissolution of brochantite might improve protection as a lower amount of Cu^{2+} ions (as $Cu(H_2O)_4^{2+}$ ions) would be in equilibrium with the adsorbed water in atmospheric condition, resulting in a lower acidity of the solution. This is beneficial for the stability of the underlying cuprite and the Cu-BTA adsorbed layer itself that is otherwise sensitive to solution pH.

In conclusion, the complexation of brochantite and cuprite can play a complementary role in the protectiveness of the BTAH-treated Metz samples.

A schematic representation of the corrosion layer after treatment is proposed (Figure 4.13). The image highlights the structural changes detected at the micrometric scale and the proposed mechanisms involved in corrosion inhibition are mentioned.

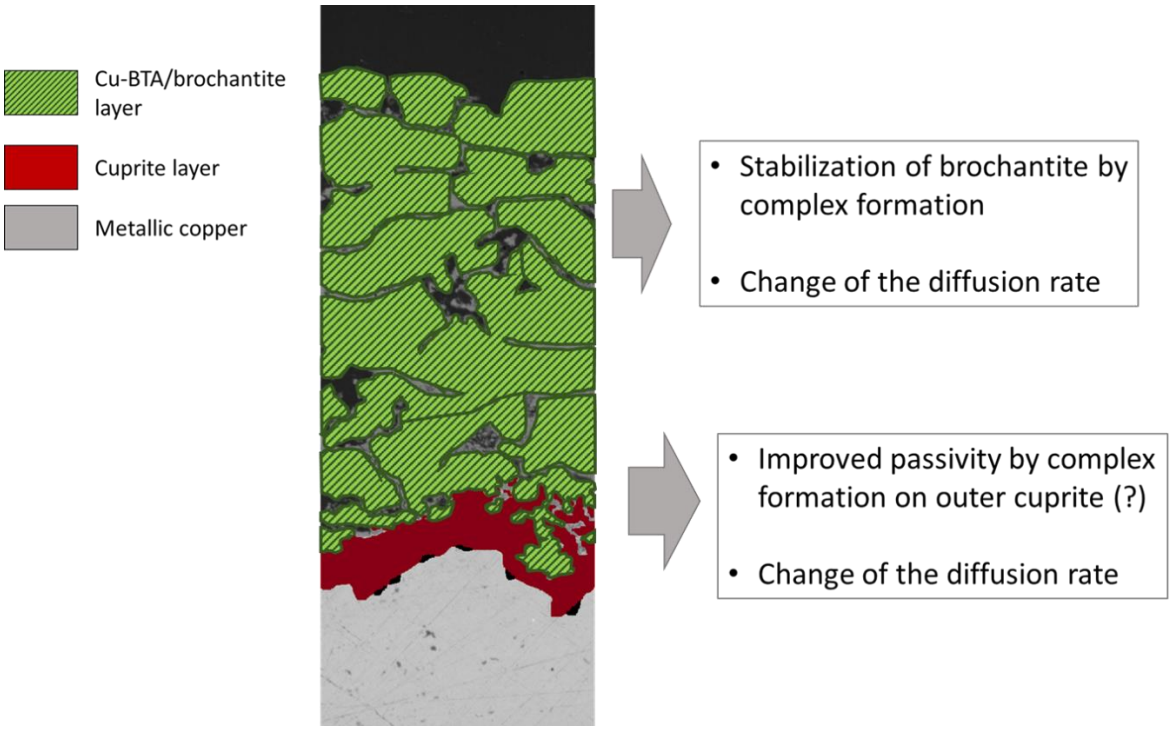

Figure 4. 13: Schematic representation of the Metz samples after 2 hours immersion in 0.25M BTAH solution.

2.2.3 Durability of the treatment outdoors: results after 6 months

The durability of the treatment was evaluated by exposing BTAH-treated samples outdoors for 6 months during the winter period.

The presence of Cu-BTA has been verified by µRaman mapping in cross-section: the frequencies allowing to identify the complex are present in three representative areas along the corrosion layer. Similarly to what has been observed before exposure, a mix between complex and brochantite is identified at any point within the brochantite layer and until the cuprite layer.

After the exposure time, the properties of the corrosion layer were evaluated. Colour change remains the same in terms of ΔE_{94} (13.6), although a shift of the a* parameter towards more positive values is registered indicating a shift towards the red colour. The surface remains hydrophobic with high contact angle (124°) measured after exposure.

The change in colour and the improved impermeability of the outer brochantite layer might suggest a modification at the molecular level (crystallization, depolymerization) that has not yet been clarified. Surprisingly, a reduced permeability is measured in the brochantite layer (667% ± 40) compared to the exposed untreated sample (2302% ± 140). The difference in deuterium enrichment within cuprite is comparable to the one previously detected for the unexposed samples with an enrichment 4 times lower in the treated cuprite (δ_n= 666 ± 220) compared to the untreated one (δ_n= 2778 ± 836).

The results obtained on the treated and exposed samples after immersion in KBr are similar to the unexposed ones. In particular, no metal re-corrosion is observed.

In conclusion, the short duration of exposure did not affect the physico-chemical properties of the corrosion layer compared to the situation before exposure. Despite the absence of a coating, the presence of copper benzotriazolate is confirmed both on the surface and within the brochantite layer until the interface with the cuprite layer. This confirms that the properties (volatility, solubility) of the complex Cu-BTA are different from those of the pure compound. Such properties are considered responsible for the assumed volatilization or dissolution of complex by several authors [37], [50], [62], [76] when a coating is not applied. Longer exposure times are needed to evaluate the effective durability of Cu-BTA on brochantite.

2.3 Metz samples treated with 5CBT

The application protocol employed for the treatment with 5CBT were the same as for the BTAH treatment. The inhibition efficiency of the treatment after 24 hours in synthetic acid rain is lower compared to BTAH but a certain protectiveness is detected (IE=85%). The unchanged potential value compared to the untreated sample indicates a mixed-type inhibition behaviour, again similarly to the BTAH treatment.

The results after immersion in aggressive solution are less clear on the efficiency of this compound in limiting corrosion reaction. In fact, the presence voiding at the interface cuprite/metal and indicating the re-corrosion of the metal is observed but it is localized to some areas and does not interest the whole interface along the corrosion layer. Another aspect that is highlighted is the locale enrichment in bromine at the brochantite/cuprite interface, while no surface crystals of $Cu_2Br(OH)_3$ are observed.

Both electrochemical and KBr immersion test suggest a lower protection towards corrosion of the 5CBT treatment compared to BTAH.

2.3.1 Physico-chemical properties after treatment

The structural components of the corrosion layer after treatment were assessed by µRaman mapping. Again, the double-layer structure is found with cuprite detected on top of the metal as a thin layer (3.9 ± 2.8 µm) and brochantite detected in the outer thicker layer (43.5 ± 3.6 µm). The values obtained for the thickness of the respective layers are comparable to the values obtained on untreated samples.

In addition to the characteristic frequencies of brochantite, in the outer layer, the signal corresponding to a complex Cu-5CBT is detected. The intensity of the characteristic peaks decreases as increasing depth within the brochantite layer and the complex is only detected within approximately 20 µm from the outer surface, where brochantite and Cu-5CBT are both detected. As a consequence, no complex is present at the brochantite/cuprite interface.

Differently from BTAH, the reaction between 5CBT and brochantite present in the corrosion layer is influenced by the distance from the surface, with a higher effectiveness in the part of the layer closer to the solution. One hypothesis could be the immediate formation of the complex in the outer layer which might block the solution thus limiting the access of inhibitors molecules. Another hypothesis could be related to the different initial pH of 5CBT solution (2.6) when compared to BTAH (4.7). This might cause a rapid dissolution of brochantite and copper ions would diffuse by gradient outwards to the solution and reacts in the outer part of the corrosion layer.

The reaction of 5CBT and brochantite in the outer part of the corrosion layer has an influence on the surface properties: a shift toward dark-green colour with a colour variation perceivable by human eye (ΔE_{94} = 12.6) and no surface morphological modification are appreciable at the micrometric scale level compared to an untreated sample. As highlighted in the previous discussion on reaction with synthetic brochantite, the specific mechanism of interaction of 5CBT by surface reaction can be claimed as responsible for the absence of microscopical morphological changes compared to the untreated brochantite. On the other hand, the nanometric layer formed on brochantite does modify the colour of the treated mineral and the same mechanism can be applied to the corrosion layer.

After 5CBT treatment, a higher hydrophobicity compared of the untreated sample is measured (CA=98°) and, as discussed in the previous part, the formation of a water insoluble Cu-5CBT on the outer layer is responsible for the improved surface hydrophobicity.

Despite the surface hydrophobicity, the deuterium enrichment indicating water permeability after 30 days immersion is comparable to the untreated samples obtained values in both the brochantite and the cuprite layer. Therefore, the treatment does not have a marked influence in decreasing water intake.

2.3.2 Proposed protection mechanism

The permeability test is in agreement with the observations after KBr immersion, pointing out a re-corrosion of the metal even if/albeit localized, and with the lower inhibition efficiency value obtained for the 5CBT-treated samples when compared to BTAH-treated samples.

The lower protectiveness exerted by the 5CBT treatment can be related to the reduced volume of brochantite interests by complexation. In fact, as only the outer part of the brochantite layer is the one which is more interested by the reaction with the inhibitor, it seems reasonable to state that the complex only partly or did not reach at all the cuprite layer. Therefore, no complexation took place at the intermediate layer and, in particular, on the surface of cuprite grains. This is confirmed not only by the permeability experiment, but also by the bromine enrichment evidenced by EDS analysis and precisely located at the intermediate layer.

As suggested for the BTAH treatment, a certain protectiveness might be related to the different diffusion rate of water though the modified-brochantite layer, as the surface tension measurement indicates. Being the interaction limited to the outer 20 µm of brochantite, the effect on diffusion in the long term is less evident over 30 days immersion while a higher efficiency can be exerted in the 24 hours immersion prior to Potentiodynamic measurement.

In addition, a complexation of 5CBT with cuprite although probably more localized cannot be completely excluded and nanoscale analysis are again needed to verify and locate eventual interactions of the organic compound and the cuprite grains in the corrosion layer. This type of interaction, in addition to the limitation to diffusion justify the mixed-type behaviour of the inhibitor in the short term, similarly to BTAH.

The treatment might be improved by longer immersion time while the same protocol could be maintained in case of corrosion layer with comparable porosity but lower thickness of the outer brochantite layer.

A schematic representation of the corrosion layer after 5CBT treatment is given in Figure 4.14.

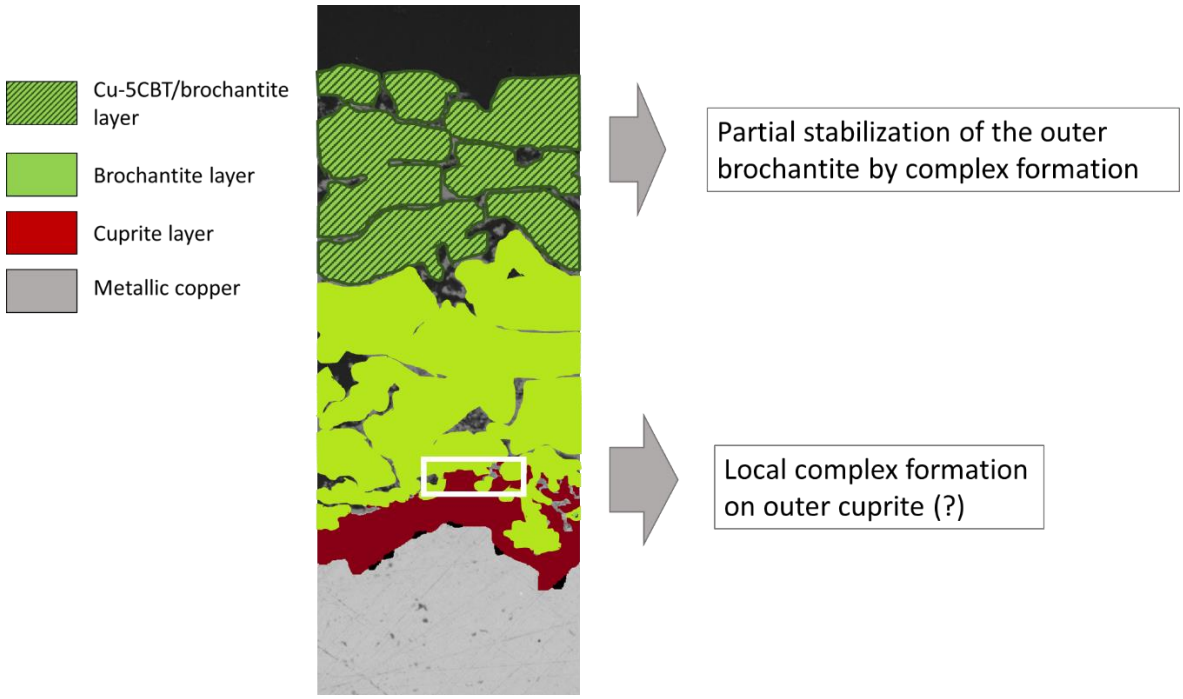

Figure 4. 14: Schematic representation of the Metz samples after 2 hours immersion in 0.25M 5CBT solution. The dark-green colour indicates the complexation zone limited to the outer corrosion layer.

2.3.3Durability of the treatment outdoors: results after 6 months

Results on short-term exposure in outdoor conditions show that the treatment does not undergo any major change. Colour difference (ΔE_{94}=14.7) and colour parameters does not change after exposure. The measured contact angle (CA=78°) slightly below 90° indicates a lower hydrophobicity of the surface compared to the situation before exposure.

Interestingly, the Cu-5CBT complex is detected after 6 months and it is again located in the outermost part of the surface (20 µm approximately).

A surprising result concerns the permeability of the outer brochantite layer: a lower value (784% ± 83) compared to the untreated sample (2302% ± 140) is measured. Within the cuprite layer a certain reduction in permeability is also registered (1496% ± 806) compared to the untreated cuprite (2778% ± 836), although for this last measurement a higher standard deviation indicates a higher variability of in the three different zones considered. These results remain to be verified.

Results of re-corrosion experiment does not vary considerably to those before exposure, nevertheless, a higher crystallization of the new $Cu_2Br(OH)_3$ is detected in the lower part of the corrosion layer, noticeably the area that is not interested by complexation with the inhibitor. This observation indicates that cupric ions are available and precipitate as copper hydroxide with the bromide present in solution. The origin of such cupric ions might be the unprotected brochantite as well as copper ions due to the

metal and cuprite dissolution. In fact, localized voiding formation also indicate partial re-corrosion of the metal substrate as bromide ions cause loss of passivity of the cuprite layer.

2.4 Metz samples treated with HC10

The protocol used for the treatment with decanoic acid corresponds to the one employed by Apchain in a recent work [19], [106]. A concentration of 30 g/L of HC10 in a hydro-alcoholic solution is employed.

After treatment, the inhibition efficiency in synthetic acid rain is considerably high (94.2 %) and the potential is shifted towards more negative values indicating a cathodic behaviour of the HC10-treated Metz samples compared to the untreated ones.

The results of the depassivation experiment with immersion in KBr solution for 30 days confirm the protectiveness of the treatment as no re-corrosion of the metal was found in form of voiding at the metal/cuprite interface. Surface crystallization of the new crystalline phase $Cu_2Br(OH)_3$ was observed.

2.4.1 Physico-chemical properties after treatment

The treatment with HC10 induces different structural and morphological modifications compared to the azoles.

The analysis of surface indicates that copper decanoate is formed on the external surface of the Metz samples and it is clearly observed on the surface as elongated flower-like crystals. As previously reported in the literature [96], copper decanoate crystals provide a hydrophobicity to the treated surface, which is confirmed by contact angle measurements: average high contact angle is detected (CA=140°) and the surface is nearly super-hydrophobic.

The presence of the surface copper decanoate crystals determine the colour change measured (ΔE_{94}=13.2) and specifically the shift towards a blue hue as the copper decanoate forming with reaction of both synthetic minerals is blue. The brightness of the surface is less affected.

When the samples are analysed in cross-section, no copper decanoate was detected inside the corrosion layer. Surprisingly, this result differ from what reported by Apchain, who detected copper decanoate as an independent layer in the external part of the corrosion layer. Such discrepancy can be

due to the preparation protocol employed here that includes the protection of the samples' sides. This specific behaviour reveals that the interaction of the decanoic acid solution with the brochantite layer is highly much influenced by the way solution have access to the internal pore network.

Despite the presence of a high hydrophobic surface, the permeability experiment indicates that after 30 days immersion in D_2O deuterated water is present in the porosity of the outer and inner layer. The enrichment value inside the S-rich layer (δ_n= 1300% ± 131) is close to the one obtained for the untreated sample (δ_n=1264% ± 148), while the value obtained in the CuO-rich layer is on average higher (δ_n=1842 ± 1246) than the untreated sample (δ_n= 999 ± 471). The considerable error obtained might indicate that areas with high and low enrichment are present in the HC10-treated sample.

A scheme of the samples after treatment with HC10 is proposed in Figure 4.15.

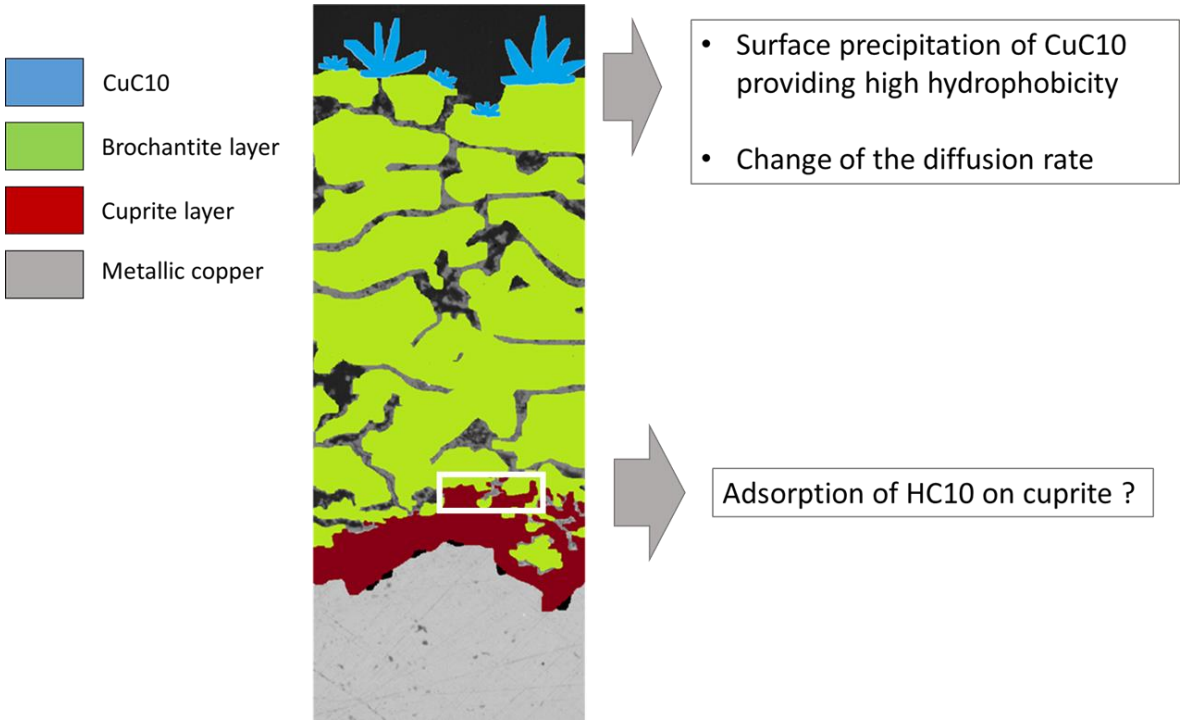

Figure 4. 15: Schematic representation of the Metz samples after 2 hours immersion in 0.17M HC10 solution. Blue surface crystals represent copper decanoate precipitate.

2.4.2 Durability of the treatment outdoors: results after 6 months

After outdoor exposure, the surface decanoate crystals are no more detected. Such results confirm literature studies where the adherence of CuC10 and CuC12 to the surface are questioned [104]. As an effect of the crystals' disappearance, the colour parameters after exposure are comparable to those of an untreated sample and surface hydrophobicity drastically decreases.

In addition, the immersion in KBr aggressive solution of exposed samples treated with HC10 shows that the passivity of cuprite is compromised and metal dissolution can occur. Precipitation of the new phase is also detected both on the surface and within the porosity of the sample.

2.3.3 Proposed protection mechanism

The main detectable interaction of the HC10 solution with the naturally corroded copper corresponds to the formation of a super-hydrophobic layer composed by copper decanoate crystals and located at the samples' outer surface.

As observed for the synthetic mineral phases, the precipitation of copper decanoate is related to the availability of cupric ions in solution from the dissolution or dissolution/oxidation of mineral phases and the precipitation of the phase is not dependent from the minerals' surface morphology ad no adsorption is involved. Therefore, the formation of copper decanoate implies that a partial dissolution of the copper phases took place due to the acidic conditions in decanoic acid solution. The specific precipitation on the surface observed at the macro to micrometric scale might be related to a surface-induced nucleation has been suggested in the literature [150]. Moreover, as minerals dissolve, the concentration gradient of cupric ions diffusing outwards might also induce the precipitation and growth of the copper decanoate specifically at the samples' surface.

The formation of surface copper bromide hydroxides after KBr immersion can be related to the different interaction of HC10 with brochantite compared to BTAH. If in the case of BTAH, the complex formed with brochantite blocks dissolution by modifying surface properties of the brochantite, in the case of HC10, this does not happen and brochantite in the outer layer is free to dissolve in the KBr solution.

The copper decanoate crystals are completely lost after short-term exposure. After exposure, the protectiveness of the treatment is also lost as shown by the KBr experiment where voiding formation and metal re-corrosion are clearly observed ono the exposed and immersed HC10-treated samples.

The formation of a hydrophobic surface layer can explain the cathodic inhibition tendency after treatment, although it is in contrast with the permeability experiment that highlights a high water intake after 30 days immersion.

An important data concerns the enrichment in bromine at the cuprite/brochantite interface. Before exposure, no enrichment is measured in this area (0.4%wt in Br), while an enrichment (2%wt of Br) is detected on the HC10-treated sample after outdoor exposure.

As previously discussed for the two azole inhibitors, these results might indicate a possible interaction of the carboxylic acid group with copper in cuprite though adsorption of single molecules to the cuprite outer layer right after treatment. The adsorption would not be accompanied by complex formation, which would be a reason for the unchanged water permeability of the underlying cuprite layer. The presence of the organic treatment at the nanometric scale was previously observed by L'héronde [107] even at lower immersion times.

Considering that a different reaction mechanism is involved and possibly, no adsorbed multi-molecular layer of copper decanoate is formed on cuprite in the corrosion layer, it can be considered that the interaction is weaker and the carboxylate adsorbed on cuprite is lost after exposure.

Further in-depth investigation at the nanometric scale is needed to confirm this hypothesis.

At the specific conditions of concentration and solvent used here, HC10 treatment represents a short-term protection strategy for outdoor monuments, or, in alternative, it might constitute a conservation treatment in indoor conditions.

2.5 General considerations for the three inhibitors

Results for the different treatments before and after outdoor exposure are summarized in Table 4.3.

After treatment, the inhibition efficiency calculated from the Tafel plots, attests that the three treatments provide a generally good protection compared to the untreated Metz copper plate. Based on the compound employed, the IE% calculated decreases as BTAH>HC10>5CBT. The first observation that marks a considerable difference among the three treatments is the depth of interaction with the corrosion layer, detectable at the micrometric scale. Evidence of reaction among benzotriazole and brochantite consists in the detection of the Cu-BTA complex: the complex was found within the whole brochantite layer until the intermediate brochantite/cuprite inter-layer. Similarly, a Cu-5CBT complex was detected as a solution of benzotriazole-5-carboxylic acid is used as treatment. In this case, the signal corresponding to the complex was found only in the outer 20 µm of the brochantite layer. Finally, a different behaviour was observed when decanoic acid is employed: the interaction with the Metz samples is limited to the external surface and leads to the formation copper decanoate crystals.

Table 4. 3: Summary of the results of the main experiments before and after exposure. The metal dissolution is qualitatively evaluated based on the presence of voiding at the metal/cuprite interface and indicated as (-) not observed, (+) observed locally and (++) diffused.

		After treatment		
	Untreated	**BTAH**	**5CBT**	**HC10**
IE%		99%	85%	95%
Interaction with the CL		until cuprite	20 µm from surface	surface
Permeability D_2O in cuprite		Drastically reduced	No change	No change
Metal Dissolution	++	-	+	-
Br localized enrichment	yes	no	yes	no
		After outdoor exposure		
Interaction with the CL		until cuprite	20 µm from surface	-
Permeability D_2O in cuprite		Drastically reduced	No change	No change
Loss of passivity	+	-	+	++
Br localized enrichment	yes	no	yes	yes

A measurement of the permeability to deuterated water has been used to evaluate the barrier effect of the treatment. After 30 days the values obtained for the freshly treated samples show that no barrier effect is provided to the outer brochantite layer and comparable deuterium enrichment to the untreated samples were found. The situation is similar for the cuprite layer with the exception of the BTAH-treated sample, which experienced a drastic decrease of the enrichment value.

The loss of passivity of the cuprite layer was studied by immersion in KBr solution and by comparing results on the treated samples to those obtained on the untreated sample, described earlier in this chapter. After treatment, local voiding, indicating metal dissolution and local enrichment in bromine were observed in the case of the 5CBT-treatment, despite the voiding being localized to some areas of the corrosion layer. The BTAH and HC10 treatments did not undergo re-corrosion and the new phase observed on the HC10-treated samples can be attributed to a partial dissolution of brochantite.

The durability of the treatments was also evaluated after 6-moths outdoor exposure in unsheltered conditions. The main goal of this experiment was to understand the possible disappearance of the inhibitors as discussed in the literature, especially concerning benzotriazole.

Results show that both complexes Cu-BTAH and Cu-5CBT are still present within the corrosion layer and their distribution inside the brochantite layer did not vary after 6 months outdoors. Possible changes in the polymeric and amorphous structure of the complexes after exposure were not investigated.

The exposure did affect the HC10-treated samples and the surface hydrophobic layer is completely lost probably because the low adherence of the copper decanoate to the underlying brochantite.

From the investigation of the permeability of the treated and exposed samples, comparable results to the unexposed samples were find especially when looking at the cuprite layer. In addition, the KBr immersion after exposure evidenced that only the BTAH-treated sample is immune to re-corrosion (absence of voiding) and to bromine local enrichment. No change compared to results prior to exposure are found for the 5CBT treatment, while the HC10 treatment after exposure does not provide any protection to re-corrosion in the aggressive solution chosen.

The possible protective mechanisms discussed in the previous paragraphs highlight that the efficiency of the two azoles ca be partly related to their access and, possibly, bond formation with the cuprite layer. The presence of adsorbed carboxylate on cuprite has also been suggested for the HC10 treatment; this could explain the lack of bromine enrichment at the interface. On the contrary, the formation of the hydrophobic surface layer after HC10 treatment is probably responsible for a high inhibition efficiency in the short-term.

Finally, it is possible to propose that the durability of the treatments is related to their reaction mechanism with the mineral components of the corrosion layer that was investigated on synthetic mineral phases. For the two azole compounds, reaction takes place at the mineral surface and implies a chemically bond molecular layer between the copper in the mineral and the azote in the molecule. The result in the corrosion layer is a complex that is linked to the underlying mineral phase, which allows the layer not to be mechanically removed during the time and in the exposition conditions chosen.

Differently, the decanoate, being a surface precipitate, is more subjected to the mechanical action of rainfalls and wind, which causes it to be lost even after a short exposure time.

2.5.1 Role of brochantite layer and its passivation

The role of brochantite is described as detrimental for corrosion of copper. The precise mechanism seems unclear although, the reason is generally associated to the high porosity of the layer.

Considering the inhibitor treatment, a high porosity and therefore high surface area are preferred as the inhibitor's containing solution better penetrates the outer layer and will be able to reach cuprite.

An additional consideration can be done on the effect of complex forming between azoles and brochantite. It was shown early that the complex modifies the stability and reactivity of brochantite, which finally gives a lower solubility of the surface-modified mineral until a considerably low pH. This effect is evident when comparing BTAH and HC10 treated samples in KBr solution: in the case of BTAH, no dissolution takes place in neutral conditions since the surface of the brochantite is stabilized. On the contrary, the HC10 treatment does not have an effect on the brochantite and crystallization of the copper bromide hydroxide can take place simply by brochantite dissolution.

The effect of a lower solubility of brochantite leads to a lower copper run-off. This might have an effect on the pH of the water adsorbed by the outer layer with a less acidic pH due to a lower amount of $Cu(H_2O)_4^{2+}$ ions, resulting in a higher stability of the complex and a less aggressive characteristics of the adsorbed water layer.

Another consideration on the brochantite layer concerns its complete transformation by azole-type compounds. Turgoose and Duncan [76] lament that a long immersion time is needed to completely transform the brochantite layer. We could doubt about the effectiveness of a complete transformation, as this would determine a loss of layer morphology followed by complete amorphization due to formation of azolate salt. This is not envisaged as copper benzotriazolate would lose its support and would be more subjected to loss by mechanic action (rain, wind).

2.5.2 KBr depassivation experiment: a preliminary testing method for protectives

Based on the experiment performed using a concentrated solution of KBr in stagnant conditions, a methodology for testing new corrosion inhibitors is proposed.

The immersion in concentrated solution containing aggressive ions causes depassivation of the cuprite layer as observed on the untreated copper samples. Depassivation of cuprite results in the progressive dissolution of the metal that can be easily identified in cross-section by SEM as voiding formation between the cuprite layer and the underlying metal. Other effects of the exposure of the samples to the aggressive solution are the formation of surface crystals of copper bromide hydroxide and the presence of a bromine enrichment within the corrosion layer. The first indicates that copper ions are available in solution: the source is the dissolving metal but also dissolution of brochantite and cuprite. The higher concentration of bromine at the brochantite/cuprite interface is due to the preferential adsorption of bromide ions on the positively charged cuprite.

Depending on the final application of the inhibitor, naturally or artificially corroded samples can be used. Samples having the same dimensions are embedded in resin as described in the methodology in order to protect the cut sides. Samples are then treated according to a specific protocol chosen for the inhibitor that is intended to test. When possible, samples' surface properties are examined after treatment by non-invasive techniques (colour change, surface tension, and surface structure). A series of samples can be exposed outdoors or, in alternative, exposed to specific environmental conditions in a climatic chamber. After treatment and after exposure in a certain environment, the samples are immersed in a concentrated 1.3M KBr solution for 30 days (time can be adapted to the kind of sample). After the time, samples are removed from the solution, washed with deuterated water and oven-dried at 60°C for 24 hours. The surface of the samples can be examined directly under the optical microscope and by µRaman spectroscopy. Further analysis in cross-section is required. Samples are embedded in resin and prepared for SEM observations. The observations under the electron microscope will allow an evaluation of the treatment before and after exposure to aging.

Three observations will be crucial to determine the efficiency of the inhibitor's treatment:

1. Absence of metal re-corrosion
2. Absence of a bromide gradient throughout the CL
3. Absence of surface crystallization: both mineral phases and metal are blocked by the inhibitor.

When all these three requirements are fulfilled the experimentation on the chosen compound can be pursued and the protocol be improved.

The testing methodology is briefly schematized in Figure 4.16.

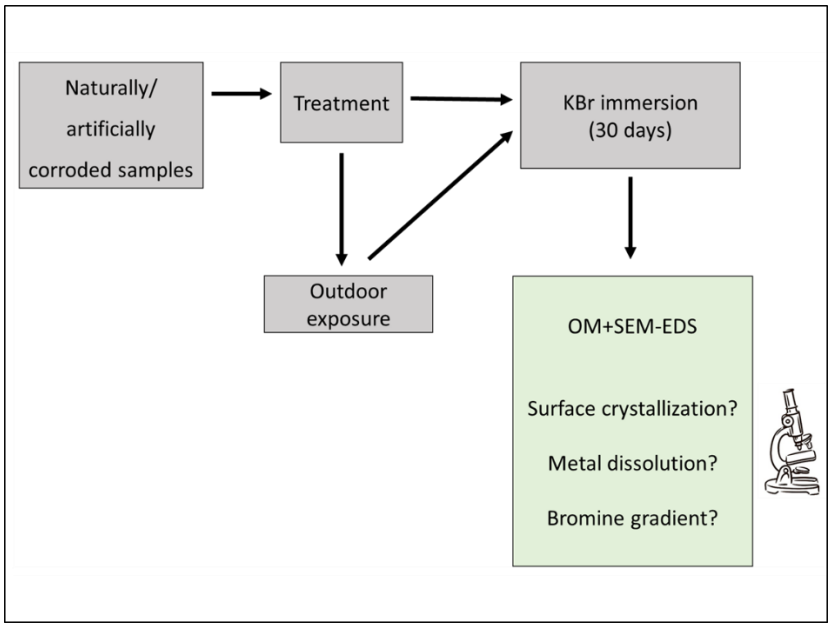

Figure 4. 16: Summary of the KBr testing procedure.

The proposed testing method has the advantage of being inexpensive as it only requires the use of optical and electron microscopy, analytical tools present in most research laboratories. The need of naturally or artificially corroded samples is the major drawback as they are usually not readily available.

Conclusions and perspectives

This research project has been conducted in the framework of the protection of heritage copper-based metals exposed outdoors by corrosion inhibitors. It aims at bringing new insights on the chemical mechanisms behind the use of organic molecules against corrosion in order to promote optimized protocols for the future development of protection strategies based on corrosion inhibitors in the conservation field.

Three inhibitors have been chosen as testing molecules for the protection of a naturally corroded copper samples, considered as a reference substrate for long-term corrosion. Benzotriazole (BTAH), an azole compound, a commonly employed compound in both industrial and conservation field, decanoic acid (HC10), a long-chain fatty acid which has been suggested as possible treatment for copper-based outdoor artefacts and benzotriazole-5-carboxylic acid (5CBT), a testing molecule characterized by both the azole and the carboxylic functions.

The study developed along two main axes that allowed to provide complementary results. The first axis aims at the study and understanding of the interactions and the reaction mechanism between the inhibitors and the two main mineral phases detected on long-term corroded copper in atmosphere. The analysis has been carried out by following the pH during the reaction and by analysing the reaction product according to a multi-analytical protocol that specifically allows nanometric observations (TEM analysis). Specific tests concerning the reactivity of the phases formed have been also explored in this part of the study.

The second axis involves the study of naturally corroded samples. The 100 years-old copper tiles from the Saint Martin's church in Metz constitute a privileged substrate as they are representative for outdoor corrosion layers formed naturally thus presenting specific structural and transport properties that are difficult to reproduce on freshly patinated coupons. In this second part, the physico-chemical properties of the corrosion layer before and after treatment with the inhibitors have been analysed following a specific multi-scale multi-analytical protocol, again following adapted to the complexity of the corrosion layer. Devoted experiments have been improved or designed to highlight specific properties of the layer before and after treatment. These experiments include the determination of permeability to liquid water by deuterium tracing and the determination of the passivity reinforcement or breakdown as an effect of a prolonged immersion in aggressive solution. The durability of the treatments has been also evaluated as result of an outdoor exposure in uncontrolled environment for 6 months.

A first contribution of this study concerns the understanding of the copper corrosion layer. In particular, the cuprite layer, investigated at a sub-micrometric scale by FIB-tomography and STEM analyses in thin section, is complex exhibiting an internal layer with unconnected nanometric porosity and an external layer constituted by larger grains. The analysis of the results coupled to the observations found in the dedicated literature allow to propose, for the Metz corrosion system and together with the classical double-structure, an intermediate layer with specific structural and transport properties.

The results concerning the inhibitors and their ability to interact with the corrosion layer are discussed in the light of the outcomes from the experimental on synthetic phases. The three inhibitors can be mainly distinguished based on their reaction mechanism, which depends on their chemical structure.

On one side, BTAH and 5CBT interact with the copper atoms through the nitrogen present in the azole ring as reported in the literature for BTAH, while no evidence of interaction with the carboxylic group in 5CBT has been detected.

Confirming the film-forming ability previously described in the literature, at the nanometric scale, the two azole compounds give a specific core-shell morphology with the mineral enveloped in an amorphous layer composed by the respective copper organic complex (Cu-BTA or Cu-5CBT). The layer does not constitute a physical barrier and diffusion is permitted, although its presence has a role in modifying the reactivity of the mineral phase to which it is chemically bonded. As comparable results were obtained for the two inhibitors, a common reaction mechanism based on adsorption and progressive layer growth formation is suggested.

Differently, decanoic acid reacts with mineral phases giving copper decanoate, a precipitated phase and the reaction proceeds through a dissolution/precipitation mechanism without surface interaction being detected during reaction.

The study of the corrosion layer after treatment at the global and micrometric scale, shows that the mechanisms evoked for the mineral phases in controlled conditions are useful to explain the effects of the inhibitors when applied to a natural corrosion layer and the two approaches are complementary.

BTAH and 5CBT react with the outer brochantite, which determines the change of surface properties (colour and surface tension). Other properties such as porosity and permeability of the outer brochantite layer are not modified. Structural changes in cross-section are different for the two compounds as the interaction with brochantite occurs at different depths within the corrosion layer. BTAH forms a detectable Cu-BTA complex over the whole thickness of brochantite until the cuprite layer, while Cu-5CBT complex is only detected in the external 20 µm.

This difference in penetration is considered fundamental for explaining the different behaviour towards permeability and improve the passive role of the cuprite layer. The fact that Cu-BTA is detected until the cuprite layer couple with evidence of complex formation from previous literature studies on oxidized copper surfaces, allows to propose that a complex formed on the outer cuprite grains and this complexation is responsible to the improved passivity behaviour of the cuprite. A partial complexation of the corrosion layer and of the cuprite in particular, has been proposed for the 5CBT treatment as localized passivity breakdown and high permeability within the cuprite were observed after treatment.

The stability of the Cu-BTA and Cu-5CBT complexes is confirmed after 6 months exposure. Unlike what suggested in the literature, this result confirms that the properties of the complex are not the same as the pure compound and the treatment based on the inhibitor can withstand outdoor exposure to a certain extent thanks to the strong bonding with the mineral on which it is adsorbed.

Decanoic acid forms a surface superhydrophobic layer that has been detected at the micrometric scale only on the external surface. Previous findings on similar samples treated with decanoic acid showed that the organic molecule is found within the corrosion layer down to the cuprite. The results concerning passivity of the layer after treatment, confirm that the treatment provides a good protection in aggressive conditions despite no change in permeability has been detected (that remains unclear). The proposed mechanism evokes on one side the high hydrophobicity of the surface as responsible for modifying the rate of penetration of aggressive species, on the other, an adsorption between the carboxylic function and the cuprite surface, not detectable at the micrometric scale is suggested and remains to be clarified.

After outdoor exposure, the copper decanoate crystals are lost from the surface and the corrosion experiments prove that neither of the proposed protective effects after treatment are present after exposure, which confirms the prominent role in corrosion protection of the copper decanoate precipitated surface layer. These results justify the recommended use of fatty acids treatments as temporary protection.

In general, this work has demonstrated the necessity of setting up a methodology based on the combination of both with parametric tests on synthetic minerals and with corroded surfaces representative of the physical and chemical properties of corrosion layers formed in the long-term.

Additionally, the research opens to several perspectives. First, direct evidence of bonding between the outer cuprite grains surface within the corrosion layer and the inhibitors' molecules remains to be fully proven with the aid of nanoscale techniques such as Auger spectroscopy directly in cross-section.

Concerning the understanding of the permeability of ionic species through the complexes formed as well as inside the corrosion layer, a study of the kinetics of diffusion is envisaged. Such study would be of great interest to understand the properties of the layer on one side but also to elucidate the possible effect of brochantite complexation on the transport properties of the outer layer.

Longer outdoor exposures coupled with electrochemical tests performed at regular intervals and supported by the physico-chemical analytical protocol followed in this study can provide further complementarity in the results as well as a better idea of the protectiveness of inhibitors not covered by coatings in the long term.

Finally, considering that outdoor statuary is mainly constituted by bronze substrates, it would be relevant to investigate naturally corroded bronze samples to compare reactivity, structural and transport properties.

Bibliography

[1] E. Bardal, *Corrosion and Protection*. Springer-Verlag London, 2004.

[2] E. McCafferty, "Thermodynamics of Corrosion: Pourbaix Diagrams. In: Introduction to Corrosion Science.," *Springer, New York, NY*, p. 328, 2010, [Online]. Available: http://link.springer.com/10.1007/b97510.

[3] P. Marcus, V. Maurice, and H. H. Strehblow, "Localized corrosion (pitting): A model of passivity breakdown including the role of the oxide layer nanostructure," *Corros. Sci.*, vol. 50, no. 9, pp. 2698–2704, 2008, doi: 10.1016/j.corsci.2008.06.047.

[4] V. Maurice and P. Marcus, "Progress in corrosion science at atomic and nanometric scales," *Prog. Mater. Sci.*, vol. 95, pp. 132–171, 2018, doi: 10.1016/j.pmatsci.2018.03.001.

[5] C. Leygraf, I. O. Wallinder, J. Tidblad, and T. Graedel, *Atmospheric corrosion*. John Wiley & Sons, 2016.

[6] R. Francis, *The Corrosion of Copper and its Alloys: a Practical Guide for Engineers*, vol. 46, no. 3. 2011.

[7] Y. S. Hedberg, J. F. Hedberg, G. Herting, S. Goidanich, and I. Odnevall Wallinder, "Critical review: Copper runoff from outdoor copper surfaces at atmospheric conditions," *Environ. Sci. Technol.*, vol. 48, no. 3, pp. 1372–1381, 2014, doi: 10.1021/es404410s.

[8] C. Gattinoni and A. Michaelides, "Atomistic details of oxide surfaces and surface oxidation: the example of copper and its oxides," *Surf. Sci. Rep.*, vol. 70, no. 3, pp. 424–447, 2015, doi: 10.1016/j.surfrep.2015.07.001.

[9] D. J. G. Ives and A. E. Rawson, "Copper Corrosion: III . Electrochemical Theory of General Corrosion," *J. Electrochem. Soc.*, vol. 109, no. 6, p. 458, 1962, doi: 10.1149/1.2425447.

[10] D. de la Fuente, J. Simancas, and M. Morcillo, "Morphological study of 16-year patinas formed on copper in a wide range of atmospheric exposures," *Corros. Sci.*, vol. 50, no. 1, pp. 268–285, 2008, doi: 10.1016/j.corsci.2007.05.030.

[11] F. Noli, P. Misaelides, A. Hatzidimitriou, E. Pavlidou, and M. Kokkoris, "Investigation of artificially produced and natural copper patina layers," *J. Mater. Chem.*, vol. 13, no. 1, pp. 114–120, 2003, doi: 10.1039/b206773k.

[12] I. T. Vargas, D. A. Fischer, M. A. Alsina, J. P. Pavissich, P. A. Pastén, and G. E. Pizarro, “Copper Corrosion and Biocorrosion Events in Premise Plumbing,” *Materials (Basel).*, vol. 10, no. 9, p. 1036, 2017.

[13] T. H. Merkel and S. O. Pehkonen, “General corrosion of copper in domestic drinking water installations: Scientific background and mechanistic understanding,” *Corros. Eng. Sci. Technol.*, vol. 41, no. 1, pp. 21–27, 2006, doi: 10.1179/174327806X94009.

[14] P. A. Korzhavyi and B. Johansson, “Literature review on the properties of cuprous oxide Cu2O and the process of copper oxidation,” Swedish Nuclear Fuel and Waste Management Company, 2011.

[15] Y. Feng, W. K. Teo, K. S. Siow, K. L. Tan, and A. K. Hsieh, “The corrosion behaviour of copper in neutral tap water. Part I: Corrosion mechanisms,” *Corros. Sci.*, vol. 38, no. 3, pp. 369–385, 1996, doi: 10.1016/0010-938X(96)00110-2.

[16] J. H. Payer, G. Ball, B. I. Rickett, and H. S. Kim, “Role of transport properties in corrosion product growth,” *Mater. Sci. Eng. A*, vol. 198, no. 1–2, pp. 91–102, 1995, doi: 10.1016/0921-5093(95)80063-Z.

[17] T. Graedel, K. Nassau, and J. P. Franey, “Copper patinas formed in the atmosphere—I. Introduction,” *Corros. Sci.*, vol. 27, no. 7, pp. 639–657, 1987, doi: http://dx.doi.org/10.1016/0010-938X(87)90047-3.

[18] M. Morcillo *et al.*, “Characterisation of a centuries-old patinated copper roof tile from Queen Anne’s Summer Palace in Prague,” *Mater. Charact.*, vol. 133, no. July, pp. 146–155, 2017, doi: 10.1016/j.matchar.2017.09.034.

[19] E. Apchain, “Apport des traitements carboxylates à la protection des alliages cuivreux,” Cergy-Pontoise, 2018.

[20] V. Vestreng, G. Myhre, H. Fagerli, S. Reis, and L. Tarrasón, “Twenty-five years of continuous sulphur dioxide emission reduction in Europe,” *Atmos. Chem. Phys.*, vol. 7, no. 13, pp. 3663–3681, 2007, doi: 10.5194/acp-7-3663-2007.

[21] W. Aas *et al.*, “Global and regional trends of atmospheric sulphur,” *Sci. Rep.*, vol. 9, no. 1, pp. 1–11, 2019, doi: 10.1038/s41598-018-37304-0.

[22] H. Strandberg, “Reactions of copper patina compounds—II. influence of sodium chloride in the presence of some air pollutants,” *Atmos. Environ.*, vol. 32, no. 20, pp. 3521–3526, 1998, doi: http://dx.doi.org/10.1016/S1352-2310(98)00058-2.

[23] A. Krätschmer, I. Odnevall Wallinder, and C. Leygraf, “The evolution of outdoor copper patina,” *Corros. Sci.*, vol. 44, no. 3, pp. 425–450, 2002, doi: 10.1016/S0010-938X(01)00081-6.

[24] D. A. Scott, *Copper and bronze in art: corrosion, colorants, conservation*. Getty publications, 2002.

[25] A. H. Zittlau, Q. Shi, J. Boerio-goates, B. F. Woodfield, and J. Majzlan, “Thermodynamics of the basic copper sulfates antlerite , posnjakite , and brochantite,” *Chemie der Erde - Geochemistry*, vol. 73, no. 1, pp. 39–50, 2013, doi: 10.1016/j.chemer.2012.12.002.

[26] K. P. FitzGerald, J. Nairn, G. Skennerton, and A. Atrens, “Atmospheric corrosion of copper and the colour, structure and composition of natural patinas on copper,” *Corros. Sci.*, vol. 48, no. 9, pp. 2480–2509, 2006, doi: 10.1016/j.corsci.2005.09.011.

[27] J. M. Muller and C. McCrory-Joy, “Chromatographis analysis of copper patinas formed in atmosphere,” vol. 27, no. 7, pp. 695–701, 1987.

[28] A. Lins and T. Power, “The corrosion of bronze monuments in polluted urban sites : a report on the stability of copper mineral species at different PH levels,” in *Ancient and historic metals : conservation and scientific research*, D. A. Scott, Ed. Santa Monica, CA, United States: Getty Conservation Institute, 1994, pp. 119–151.

[29] W. He, I. O. Wallinder, and C. Leygraf, “A laboratory study of copper and zinc runoff during first flush and steady-state conditions,” *Corros. Sci.*, vol. 43, no. 1, pp. 127–146, 2001.

[30] C. Leygraf, T. Chang, G. Herting, and I. Odnevall Wallinder, “The origin and evolution of copper patina colour,” *Corros. Sci.*, vol. 157, no. March, pp. 337–346, 2019, doi: 10.1016/j.corsci.2019.05.025.

[31] G. Trabanelli and V. Carassiti, “Mechanism and Phenomenology of Organic Inhibitors,” *Advances in Corrosion Science and Technology*. pp. 147–228, 1970, doi: 10.1007/978-1-4615-8252-6_3.

[32] C. Monticelli, “Corrosion Inhibitors,” in *Encyclopedia of Interfacial Chemistry*, K. Wandelt, Ed. Elsevier, 2018, pp. 164–171.

[33] G. Trabanelli, “1991 Whitney Award Lecture: Inhibitors—An Old Remedy for a New Challenge,” *Corrosion*, vol. 47, no. 6, pp. 410–419, Jun. 1991, doi: 10.5006/1.3585271.

[34] I. Lukovits, T. Kosztolányi, E. Kálmán, and G. Pálinkás, “Corrosion inhibitors: Correlation between chemical structure and efficiency,” *NACE - Int. Corros. Conf. Ser.*, vol. 1999-April, no.

1, pp. 3–8, 1999.

[35] A. Fateh, M. Aliofkhazraei, and A. R. Rezvanian, “Review of corrosive environments for copper and its corrosion inhibitors,” *Arab. J. Chem.*, vol. 13, no. 1, pp. 481–544, 2020, doi: 10.1016/j.arabjc.2017.05.021.

[36] S. Marzorati, L. Verotta, and S. P. Trasatti, “Green Corrosion Inhibitors from Natural Sources and Biomass Wastes,” *Molecules* , vol. 24, no. 1. 2019, doi: 10.3390/molecules24010048.

[37] B. H. Madsen, “A preliminary note on the use of benzotriazole for stabilizing bronze objects,” *Stud. Conserv.*, vol. 12, no. 4, pp. 163–167, 1967.

[38] P. Letardi, “Testing new coatings for outdoor bronze monuments: A methodological overview,” *Coatings*, vol. 11, no. 2, pp. 1–16, 2021, doi: 10.3390/coatings11020131.

[39] A. Escande, J. L. Galigné, and J. Lapasset, “Structure crystalline et moléculaire du Benzotriazole,” *Acta Crystallogr. Sect. B*, vol. 30, no. 0, pp. 1490–1495, 1974.

[40] F. Grillo *et al.*, “Two-dimensional self-assembly of benzotriazole on an inert substrate,” *Nanoscale*, vol. 8, no. 17, pp. 9167–9177, 2016, doi: 10.1039/c6nr00821f.

[41] D. Tromans and R. Sun, “Anodic Polarization Behavior of Copper in Aqueous Chloride/Benzotriazole Solutions,” *J. Electrochem. Soc.*, vol. 138, no. 11, pp. 3235–3244, 1991, doi: 10.1149/1.2085397.

[42] M. Finšgar and I. Milošev, “Inhibition of copper corrosion by 1, 2, 3-benzotriazole: a review,” *Corros. Sci.*, vol. 52, no. 9, pp. 2737–2749, 2010.

[43] E. Loukopoulos and G. E. Kostakis, “Recent advances in the coordination chemistry of benzotriazole-based ligands,” *Coord. Chem. Rev.*, vol. 395, pp. 193–229, 2019, doi: 10.1016/j.ccr.2019.06.003.

[44] R. F. Roberts, “X-Ray Photoelectron spectroscopic characterization of copper oxide surfaces treated with benzotriazole,” *Corros. Sci.*, vol. 4, pp. 273–291, 1974.

[45] D. Chadwick and T. Hashemi, “Adsorbed corrosion inhibitors studied by electron spectroscopy: Benzotriazole on copper and copper alloys,” *Corros. Sci.*, vol. 18, no. 1, pp. 39–51, 1978, doi: 10.1016/S0010-938X(78)80074-2.

[46] P. G. Fox, G. Lewis, and P. J. Boden, “Some chemical aspects of the corrosion inhibition of copper by benzotriazole,” *Corros. Sci.*, vol. 19, no. 7, pp. 457–467, 1979, doi: 10.1016/S0010-938X(79)80052-9.

[47] B. S. Fang, C. G. Olson, and D. W. Lynch, “A photoemission study of benzotriazole on clean copper and cuprous oxide,” *Surf. Sci.*, vol. 176, no. 3, pp. 476–490, 1986, doi: 10.1016/0039-6028(86)90050-6.

[48] Y. Jiang, J. B. Adams, and D. Sun, “Benzotriazole adsorption on Cu 2O(111) surfaces: A first-principles study,” *J. Phys. Chem. B*, vol. 108, no. 34, pp. 12851–12857, 2004, doi: 10.1021/jp049457b.

[49] A. Kokalj and S. Peljhan, “Density functional theory study of adsorption of benzotriazole on Cu2O surfaces,” *J. Phys. Chem. C*, vol. 119, no. 21, pp. 11625–11635, 2015, doi: 10.1021/acs.jpcc.5b01677.

[50] D. Watkinson, “Preservation of metallic cultural heritage,” *Shreir’s Corros.*, pp. 3307–3340, 2010, doi: 10.1016/B978-044452787-5.00172-4.

[51] M. Albini, “Fungal biogenic patina: optimization of an innovative conservation treatment for copper-based arterfacts,” Université de Neuchatel, 2017.

[52] P. Letardi, “Laboratory and field tests on patinas and protective coating systems for outdoor bronze monuments,” in *Proceedings of Metal2004*, 2004, vol. 48, p. 379387, [Online]. Available: http://www.nma.gov.au/__data/assets/pdf_file/0005/346064/NMA_metals_s3_p12_patinas_protective_coating.pdf.

[53] B. Salvadori *et al.*, “Traditional and innovative protective coatings for outdoor bronze : Application and performance comparison,” vol. 46011, pp. 1–12, 2018, doi: 10.1002/app.46011.

[54] T. Kosec, D. K. Merl, and I. Milošev, “Impedance and XPS study of benzotriazole films formed on copper, copper-zinc alloys and zinc in chloride solution,” *Corros. Sci.*, vol. 50, no. 7, pp. 1987–1997, 2008, doi: 10.1016/j.corsci.2008.04.016.

[55] G. Žerjav and I. Milošev, “Protection of copper against corrosion in simulated urban rain by the combined action of benzotriazole, 2-mercaptobenzimidazole and stearic acid,” *Corros. Sci.*, vol. 98, pp. 180–191, 2015, doi: 10.1016/j.corsci.2015.05.023.

[56] I. Dugdale and J. B. Cotton, “An electrochemical investigation on the prevention of staining of copper by Benzotriazole,” *Corros. Sci.*, vol. 3, no. January, pp. 69–74, 1963.

[57] L. B. Brostoff, “Coating strategies for the protection of outdoor bronze art and ornamentation,” 2003.

[58] G. Bierwagen, T. J. Shedlosky, and K. Stanek, “Developing and testing a new generation of protective coatings for outdoor bronze sculpture,” *Prog. Org. Coatings*, vol. 48, no. 2–4, pp. 289–296, 2003, doi: 10.1016/j.porgcoat.2003.07.004.

[59] A. Balbo, C. Chiavari, C. Martini, and C. Monticelli, “Effectiveness of corrosion inhibitor films for the conservation of bronzes and gilded bronzes,” *Corros. Sci.*, vol. 59, pp. 204–212, 2012, doi: 10.1016/j.corsci.2012.03.003.

[60] T. Kosec, A. Legat, and I. Milošev, “The comparison of organic protective layers on bronze and copper,” *Prog. Org. Coatings*, vol. 69, no. 2, pp. 199–206, 2010.

[61] T. Kosec, A. Legat, and P. Ropret, “Raman investigation of artificial patinas on recent bronze protected by different azole type inhibitors in an outdoor environment,” *J. Raman Spectrosc.*, vol. 45, no. 11–12, pp. 1085–1092, 2014, doi: 10.1002/jrs.4532.

[62] M. Albini *et al.*, “Comparison of a bio-based corrosion inhibitor versus benzotriazole on corroded copper surfaces,” *Corros. Sci.*, vol. 143, no. July, pp. 84–92, 2018, doi: 10.1016/j.corsci.2018.08.020.

[63] A. Frignani, L. Tommesani, G. Brunoro, C. Monticelli, and M. Fogagnolo, “Influence of the alkyl chain on the protective effects of 1,2,3-benzotriazole towards copper corrosion. Part I: Inhibition of the anodic and cathodic reactions,” *Corros. Sci.*, vol. 41, no. 6, pp. 1205–1215, 1999.

[64] F. MANSFELD, T. SMITH, and E. P. Parry, “Benzotriazole as corrosion inhibitor for copper,” *corrosion*, vol. 27, no. 7, pp. 289–294, 1971.

[65] H. B. Madsen, “Further remarks on the use of benzotriazole for stabilizing bronze objects,” *Stud. Conserv.*, vol. 16, no. 3, pp. 114–122, 1971, doi: 10.1179/sic.1971.014.

[66] V. Brusic *et al.*, “Copper corrosion with and without inhibitors,” *J. Electrochem. Soc.*, vol. 138, no. 8, pp. 2253–2259, 1991, doi: 10.1149/1.2085957.

[67] A. Kokalj, “Ab initio modeling of the bonding of benzotriazole corrosion inhibitor to reduced and oxidized copper surfaces,” *Faraday Discuss.*, vol. 180, no. October, pp. 415–438, 2015, doi: 10.1039/c4fd00257a.

[68] J. Rubim, I. G. R Gutz, and W. J. Orville-thomas, “Surface Enhanced Raman Spectra of Benzotriazole Adsorbed on a Copper Electrode,” *J. Mol. Struct. Elsevier Sci. Publ. B.V*, vol. 100, pp. 571–583, 1983.

[69] G. Xue, J. Ding, P. Lu, and J. Dong, “SERS, XPS, and electroanalytlcal studies of the chemisorption of benzotriazole on a freshly etched surface and an oxidized surface of copper,” *J. Phys. Chem.*, vol. 95, no. 19, pp. 7380–7384, 1991, doi: 10.1021/j100172a050.

[70] J. B. Cotton and I. R. Scholes, “Benzotriazole and related compounds as corrosion inhibitors for copper,” *Br. Corros. J.*, vol. 2, no. 1, pp. 1–5, 1967.

[71] G. W. Poling, “Reflection infra-red studies of films formed by benzotriazole on Cu,” *Corros. Sci.*, vol. 10, no. 5, pp. 359–370, 1970, doi: 10.1016/S0010-938X(70)80026-9.

[72] L. B. Brostoff, T. J. Shedlosky, and E. R. de la Rie, “External reflection study of copper-benzotriazole films on bronze in relation to pretreatments of coated outdoor bronzes,” *Stud. Conserv.*, vol. 45, no. sup1, pp. 29–33, 2000, doi: 10.1179/sic.2000.45.Supplement-1.29.

[73] A. Mezzi *et al.*, “Investigation of the benzotriazole inhibition mechanism of bronze disease,” *Surf. Interface Anal.*, vol. 44, no. 8, pp. 968–971, 2012, doi: 10.1002/sia.4841.

[74] L. B. Brostoff, “Investigation into the interaction of benzotriazole with copper corrosion minerals and surfaces,” in *Conférence internationale sur la conservation des métaux*, 1997, pp. 99–108.

[75] Brostoff L.B., “lnvestigation into the Interaction of Benzotriazole with Copper corrosion minerals and surfaces,” in *METAL 95 : Proceedings of the international conference on metals conservation*, 1995, pp. 99–108.

[76] T. Drayman-Weisser (Ed.), *Dialogue/89 The conservation of bronze sculpture in outdoor environment: a dialogue among conservators, curators, environmental scientists and corroison engineers*. NACE International, Houston, TX (United States), 1992.

[77] Y. Li, M. Gong, K. Ramji, and Y. Li, “Role of Cu-benzotriazole nanoparticles in passivation film formation,” *J. Phys. Chem. C*, vol. 113, no. 42, pp. 18003–18013, 2009, doi: 10.1021/jp904782t.

[78] E. Cano and D. Lafuente, “Corrosion inhibitors for the preservation of metallic heritage artefacts,” in *European Federation of Corrosion (EFC) Series*, P. Dillmann, D. Watkinson, E. Angelini, and A. B. T.-C. and C. of C. H. M. A. Adriaens, Eds. Woodhead Publishing, 2013, pp. 570–594.

[79] F. Ammeloot, C. Fiaud, and E. M. M. Sutter, “Characterization of the oxide layer on a Cu-13Sn alloy in a NaCl aqueous solution without and with 0.1 M benzotriazole. Electrochemical and photoelectrochemical contributions,” *Electrochem. Acta*, vol. 44, pp. 2549–2558, 1999.

[80] G. Brunoro, A. Frignani, A. Colledan, and C. Chiavari, “Organic films for protection of copper and bronze against acid rain corrosion,” *Corros. Sci.*, vol. 45, no. 10, pp. 2219–2231, 2003, doi: 10.1016/S0010-938X(03)00065-9.

[81] A. Galtayries, A. Mongiatti, P. Marcus, and C. Chiavari, “Surface characterisation of corrosion inhibitors on bronzes for artistic casting,” in *Corrosion of Metallic Heritage Artefacts*, P. Dillmann, G. Béranger, P. Piccardo, and H. Matthiesen, Eds. EFC, 2007, pp. 335–351.

[82] A. N. Abu-Baker, I. D. MacLeod, R. Sloggett, and R. Taylor, “A comparative study of salicylaldoxime, cysteine and benzotriazole as inhibitors for the active chloride-based corrosion of copper and bronze artifacts,” *Eur. Sci. Journal, ESJ*, vol. 9, no. 33, 2013.

[83] J. van der Stok-Nienhuis, “Artefact bibiography 2.0,” TU Delft, 2017.

[84] V. C. Sharma, U. S. Lal, and T. Singh, “Method for Stabilization of Leaded Bronzes Affected by Corrosion of Lead,” *Stud. Conserv.*, vol. 48, no. 3, pp. 203–209, Jan. 2003, doi: 10.1179/sic.2003.48.3.203.

[85] W. A. Oddy, “On the toxicity of benzotriazole,” *Stud. Conserv.*, vol. 17, no. 3, p. 135, 1972.

[86] W. A. Oddy, “Toxicity of benzotriazole,” *Stud. Conserv.*, vol. 19, no. 3, pp. 188–189, 1974, doi: https://doi.org/10.1179/sic.1974.016.

[87] V. Beltoft, E. Nielsen, and O. Ladefoged, “Benzotriazole and Tolyltriazole. Evaluation of health hazards and proposal of health based quality criteria for soil and drinking water,” *Environ. Proj. No. 1526*, no. Environ. Proj. No. 1526, p. 1, 2013, [Online]. Available: https://www2.mst.dk/Udgiv/publications/2013/12/978-87-93026-81-0.pdf.

[88] H. C. of the Netherlands, “Health Council of the Netherlands. Dutch Expert Committee on Occupational Standards 430 (DECOS). 1,2,3-Benzotriazole,” The Hague, 2000.

[89] X. Chen *et al.*, “Prenatal exposure to benzotriazoles and benzothiazoles and cord blood mitochondrial DNA copy number: A prospective investigation,” *Environ. Int.*, vol. 143, no. June, p. 105920, 2020, doi: 10.1016/j.envint.2020.105920.

[90] F. Zucchi, G. Brunoro, C. Monticelli, and G. Trabanelli, “Corrosion resistance of copper and copper alloys surface treated with benzotriazole derivative in sodium chloride salt,” 1993.

[91] L. Tommesani, G. Brunoro, A. Frignani, C. Monticelli, and M. Dal Colle, “On the protective action of 1, 2, 3-benzotriazole derivative films against copper corrosion,” *Corros. Sci.*, vol. 39, no. 7, pp. 1221–1237, 1997.

[92] V. Otieno-Alego, N. Huynh, T. Notoya, S. E. Bottle, and D. P. Schweinsberg, “Inhibitive effect of 4- and 5- carboxybenzotriazole on copper corrosion in acidic sulphate and hydrogen sulphide solutions,” *Corros. Sci.*, vol. 41, no. 4, pp. 685–697, 1999, doi: 10.1016/S0010-938X(98)00138-3.

[93] E. Rocca and F. Mirambet, “18 - Corrosion inhibitors for metallic artefacts: temporary protection,” in *European Federation of Corrosion (EFC) Series*, P. Dillmann, G. Béranger, P. Piccardo, and H. B. T.-C. of M. H. A. Matthiesen, Eds. Woodhead Publishing, 2007, pp. 308–334.

[94] M. Ormellese, L. Lazzari, S. Goidanich, G. Fumagalli, and A. Brenna, “A study of organic substances as inhibitors for chloride-induced corrosion in concrete,” *Corros. Sci.*, vol. 51, no. 12, pp. 2959–2968, 2009, doi: 10.1016/j.corsci.2009.08.018.

[95] M. A. Malik, M. A. Hashim, F. Nabi, S. A. AL-Thabaiti, and Z. Khan, “Anti-corrosion ability of surfactants: A review,” *Int. J. Electrochem. Sci.*, vol. 6, no. 6, pp. 1927–1948, 2011.

[96] W. Xu *et al.*, “Superhydrophobic copper surfaces fabricated by fatty acid soaps in aqueous solution for excellent corrosion resistance,” *Appl. Surf. Sci.*, vol. 399, pp. 491–498, 2017, doi: 10.1016/j.apsusc.2016.12.099.

[97] A. D. Mercer, “The properties of carboxylates as corrosion inhibitors for steel and other metals in neutral aqueous solutions,” *Corros. Inhib. Fifth.*, vol. 2, pp. 563–581, 1980.

[98] C. Rapin, “Etude de l’inhibition de la corrosion aqueuse du cuivre.” 1994.

[99] E. Rocca and J. Steinmetz, “Inhibition of lead corrosion with saturated linear aliphatic chain monocarboxylates of sodium,” *Corros. Sci.*, vol. 43, no. 5, pp. 891–902, 2001.

[100] E. Rocca, C. Rapin, and F. Mirambet, “Inhibition treatment of the corrosion of lead artefacts in atmospheric conditions and by acetic acid vapour: Use of sodium decanoate,” *Corros. Sci.*, vol. 46, no. 3, pp. 653–665, 2004.

[101] J. Peultier, E. Rocca, and J. Steinmetz, “Zinc carboxylating: a new conversion treatment of zinc,” *Corros. Sci.*, vol. 45, no. 8, pp. 1703–1716, 2003.

[102] S. Hollner *et al.*, “Development of new non-toxic corrosion inhibitors for cultural property made of iron and copper alloys,” *Proc. Int. Conf. Conserv. Strateg. Sav. Indoor Met. Collect. Cairo 25 Febr. – 1 March 2007*, pp. 156–161, 2007.

[103] A. Elia, M. Dowsett, and A. Adriaens, “On the use of alcoholic carboxylic acid solutions for the

deposition of protective coatings on copper," in *Metal 10 Proceedings of the interim meeting of the ICOM-CC metal working group, Charleston, South Carolina, USA*, P. Mardikian, C. Chemello, C. Watters, and P. Hull, Eds. 2011, pp. 193–200.

[104] A. Elia, "Application of electrochemical methods for the study and protection of heritage copper alloys," p. 198, 2013.

[105] I. Milošev, T. Kosec, and M. Bele, "The formation of hydrophobic and corrosion resistant surfaces on copper and bronze by treatment in myristic acid," *J. Appl. Electrochem.*, vol. 40, no. 7, pp. 1317–1323, 2010.

[106] E. Apchain *et al.*, "Efficiency and durability of protective treatments on cultural heritage copper corrosion layers," *Corros. Sci.*, vol. 183, p. 109319, 2021, doi: https://doi.org/10.1016/j.corsci.2021.109319.

[107] M. L'héronde *et al.*, "Multiscale Study of Interactions Between Corrosion Products Layer Formed on Heritage Cu Objects and Organic Protection Treatments," *Heritage*, vol. 2, no. 3. 2019, doi: 10.3390/heritage2030162.

[108] C. Degrigny, "Examination and conservation of historical and archaeological metal artefacts: a Europe overview," in *Corrosion of Metallic Heritage Artefacts*, P. Dillmann, G. Beranger, P. Piccardo, and H. Matthiesen, Eds. EFC, 2017, pp. 1–17.

[109] S. Hollner, "Developpement De Nouveaux Traitements De Protection a Base D'Acide Carboxylique Pour La Conservation D'Objets En Fer Du Patrimoine Culturel," *These*, vol. UHP Nancy, 2009.

[110] G. Masi, "Atmospheric corrosion of outdoor bronze: mechanism of decay and conservation strategies," Alma Mater Studiorum – Università di Bologna, 2018.

[111] E. Cano and D. Lafuente, "Corrosion inhibitors for preservation of metallic heritage artefacts," in *Corrosion and conservation of cultural heritage metallic artefacts*, P. Dillmann, D. Watkinson, E. Angelini, and A. Adriaens, Eds. EFC, 2013, pp. 570–594.

[112] S. Varvara, M. Popa, G. Rustoiu, R. Bostan, and L. Mureşan, "Evaluation of some amino acids as bronze corrosion inhibitors in aqueous solution," *Stud. Univ. Babes-Bolyai Chem.*, vol. 2, pp. 73–85, 2009.

[113] R. Ben Channouf, N. Souissi, and N. Bellakhal, "Juniperus communis Extract Effect on Bronze Corrosion in Natural 0.5 M Chloride Medium," *J. Mater. Sci. Chem. Eng.*, vol. 03, no. 11, pp. 21–29, 2015, doi: 10.4236/msce.2015.311004.

[114] M. B. Petrović Mihaijlović and M. M. Antonijević, “Copper corrosion inhibitors. Period 2008-2014. A review,” *Int. J. Electrochem. Sci.*, vol. 10, no. 1, pp. 1027–1053, 2015.

[115] M. M. Mennucci *et al.*, “Local electrochemical investigation of copper patina,” *J. Solid State Electrochem.*, vol. 16, no. 1, pp. 109–116, 2012, doi: 10.1007/s10008-010-1290-7.

[116] C. Chiavari *et al.*, “Predicting the corrosion behaviour of outdoor bronzes: assessment of artificially exposed and real outdoor samples,” in *Metal 10 Proceedings of the interim meeting of the ICOM-CC metal working group, Charleston, South Carolina, USA*, P. Mardikian, C. Chemello, C. Watters, and P. Hull, Eds. 2011, pp. 218–226.

[117] C. Chiavari *et al.*, “Protective silane treatment for patinated bronze exposed to simulated natural environments,” *Mater. Chem. Phys.*, vol. 141, no. 1, pp. 502–511, 2013, doi: 10.1016/j.matchemphys.2013.05.050.

[118] G. Masi *et al.*, “Characterization of typical patinas simulating bronze corrosion in outdoor conditions,” *Mater. Chem. Phys.*, vol. 200, pp. 308–321, 2017, doi: 10.1016/j.matchemphys.2017.07.091.

[119] E. Joseph, P. Letardi, R. Mazzeo, S. Prati, and M. Vandini, “Innovative treatments for the protection of the outdoor monuments,” *Met. 07*, vol. 5, pp. 71–77, 2007.

[120] E. Cano, D. Lafuente, and D. M. Bastidas, “Use of EIS for the evaluation of the protective properties of coatings for metallic cultural heritage: a review,” *J. Solid State Electrochem.*, vol. 14, no. 3, pp. 381–391, 2010, doi: 10.1007/s10008-009-0902-6.

[121] P. Letardi and R. Spiniello, “Characterisation of bronze corrosion and protection by contact-probe electrochemical impedance measurements,” in *Metal 2001: proceedings of the international conference on metals conservation, Santiago, Chile, 2-6 April 2001*, 2004, pp. 316–319.

[122] F. Wieduwilt, C. Lenth, G. Ctistis, U. Plachetka, M. Möller, and H. Wackerbarth, “Evaluation of an on-site surface enhanced Raman scattering sensor for benzotriazole,” *Sci. Rep.*, vol. 10, no. 1, pp. 1–8, 2020, doi: 10.1038/s41598-020-65181-z.

[123] P. K. Nampoothiri, M. N. Gandhi, and A. R. Kulkarni, “Effect of surface grafting coefficient and chain length of fatty acids on the luminescence of neodymium3+-doped LaF3 nanoparticles,” *J. Mater. Chem. C*, vol. 3, no. 8, pp. 1817–1822, 2015, doi: 10.1039/c4tc02646b.

[124] Y. Gong, X. H. Huang, Z. N. Xia, M. X. Gao, and H. L. Zheng, “Catena-Poly[copper(II)-μ-aqua-di-μ-benzotriazole],” *Acta Crystallogr. Sect. E Struct. Reports Online*, vol. 63, no. 1, 2007, doi:

10.1107/S1600536806052822.

[125] L. Robinet and M. C. Corbeil, “The characterization of metal soaps,” *Stud. Conserv.*, vol. 48, no. 1, pp. 23–40, 2003.

[126] A. Kratschmer, I. Wallinder, and C. Leygraf, “The evolution of out copper patina,” *Corros. Sci.*, vol. 44, no. 44, pp. 425–450, 2002.

[127] I. Milošev, “The effect of various halide ions on the passivity of Cu, Zn and Cu-xZn alloys in borate buffer,” *Corros. Sci.*, vol. 49, no. 2, pp. 637–653, 2007, doi: 10.1016/j.corsci.2006.06.009.

[128] T. Aben and D. Tromans, “Anodic Polarization Behavior of Copper in Aqueous Bromide and Bromide/Benzotriazole Solutions,” *J. Electrochem. Soc.*, vol. 142, no. 2, pp. 398–404, 1995, doi: 10.1149/1.2044031.

[129] F. H. Assaf, S. S. Abd El-Rehiem, and A. M. Zaky, “Pitting corrosion of zinc in neutral halide solutions,” *Mater. Chem. Phys.*, vol. 58, no. 1, pp. 58–63, 1999, doi: 10.1016/S0254-0584(98)00253-3.

[130] M. Donnici, E. Ferrari, D. Neff, and S. Daniele, “Green protectives on corroded copper artworks: Surface characterization and electrochemical behaviour in simulated acid rain,” *J. Cult. Herit.*, vol. 51, pp. 97–106, 2021, doi: https://doi.org/10.1016/j.culher.2021.08.004.

[131] UNI EN 15886 (2010), “Conservation of cultural property - Test methods - Colour measurement of surfaces. Official Italian version of EN 15886:2010,” vol. 15886, 2010.

[132] UNI EN 15802 (2010), “Conservation of cultural property - Test methods - Determination of static contact angle,” vol. 15802, 2010.

[133] A. P. Hammersley, S. O. Svensson, M. Hanfland, A. N. Fitch, and D. Häusermann, “Two-dimensional detector software : from real detector to idealised image or two-theta scan,” *High Press. Res.*, vol. 14, pp. 235–248, 1996.

[134] J. Kieffer and D. Karkoulis, “PyFAI, a versatile library for azimuthal regrouping,” *J. Phys. Conf. Ser.*, vol. 425, no. PART 20, 2013, doi: 10.1088/1742-6596/425/20/202012.

[135] A. Vaitkus, A. Merkys, and S. Gražulis, “Validation of the Crystallography Open Database using the Crystallographic Information Framework,” *J. Appl. Crystallogr.*, vol. 54, no. 2, pp. 661–672, 2021.

[136] E. Gardés, M. Laumonier, M. Massuyeau, and F. Gaillard, “Unravelling partial melt distribution

in the oceanic low velocity zone," *Earth Planet. Sci. Lett.*, vol. 540, p. 116242, 2020, doi: 10.1016/j.epsl.2020.116242.

[137] M. Bouchard and D. C. Smith, "Catalogue of 45 reference Raman spectra of minerals concerning research in art history or archaeology, especially on corroded metals and coloured glass," *Spectrochim. Acta - Part A Mol. Biomol. Spectrosc.*, vol. 59, no. 10, pp. 2247–2266, 2003, doi: 10.1016/S1386-1425(03)00069-6.

[138] V. Hayez, J. Guillaume, A. Hubin, and H. Terryn, "Micro-Raman spectroscopy for the study of corrosion products on copper alloys: setting up of a reference database and studying works of art," *J. Raman Spectrosc.*, vol. 35, no. 89, pp. 732–738, 2004, doi: 10.1002/jrs.1194.

[139] H. Y. H. Chan and M. J. Weaver, "Vibrational structural analysis of benzotriazole adsorption and phase film formation on copper using surface-enhanced Raman spectroscopy," *Langmuir*, vol. 15, no. 9, pp. 3348–3355, 1999, doi: 10.1021/la981724f.

[140] S. Thomas, S. Venkateswaran, S. Kapoor, R. D'Cunha, and T. Mukherjee, "Surface enhanced Raman scattering of benzotriazole: A molecular orientational study," *Spectrochim. Acta - Part A Mol. Biomol. Spectrosc.*, vol. 60, no. 1–2, pp. 25–29, 2004, doi: 10.1016/S1386-1425(03)00213-0.

[141] M. Saggu, J. Liu, and A. Patel, "Identification of Subvisible Particles in Biopharmaceutical Formulations Using Raman Spectroscopy Provides Insight into Polysorbate 20 Degradation Pathway," *Pharm. Res.*, vol. 32, no. 9, pp. 2877–2888, 2015, doi: 10.1007/s11095-015-1670-x.

[142] R. L. Frost, W. Martens, J. T. Kloprogge, and P. A. Williams, "Raman Spectroscopy of the basic copper chloride minerals atacamite and paratacamite : implications for the study of copper, brass and bronze objects of archeological significance," *J. Raman Spectrosc.*, vol. 33, pp. 801–806, 2002, [Online]. Available: file://drec-ca-001071/commun archeo/bibliographie/Articles pdf/JRS_Frost-et-al_2002-JRS-Cu-Cl.pdf.

[143] J. C. Rubim, "Surface enhanced Raman scattering (SERS) from benzotriazole adsorbed on brass electrodes," *Chem. Phys. Lett.*, vol. 167, no. 3, pp. 209–214, 1990, doi: 10.1016/0009-2614(90)85007-Y.

[144] S. Turgoose and S. J. Duncan, "Techniques for Metal Sculpture Inhibitions," in *Dialogue/89 The conservation of bronze sculpture in outdoor environment: a dialogue among conservators, curators, environmental scientists and corroison engineers*, NACE International, Houston, TX (United States), 1992, pp. 275–287.

[145] C. Sease, “Benzotriazole: a Review for Conservators,” *Stud. Conserv.*, vol. 23, no. 2, pp. 76–85, 1978, doi: 10.1179/sic.1978.011.

[146] T. Chang *et al.*, “Analysis of Historic Copper Patinas. Influence of Inclusions on Patina Uniformity,” *Materials (Basel).*, vol. 10, no. 3, p. 298, 2017, doi: 10.3390/ma10030298.

[147] R. L. Opila, “Copper patinas: an investigation by Auger electron spectroscopy,” *Corros. Sci.*, vol. 27, no. 7, pp. 685–694, 1987, doi: 10.1016/0010-938X(87)90050-3.

[148] P. Lopesino, J. Alcántara, D. de la Fuente, B. Chico, J. A. Jiménez, and M. Morcillo, “Corrosion of copper in unpolluted chloride-rich atmospheres,” *Metals (Basel).*, vol. 8, no. 11, 2018, doi: 10.3390/met8110866.

[149] D. J. G. Ives and A. E. Rawson, “Copper Corrosion I. Thermodynamic Aspects,” *J. Electrochem. Soc.*, vol. 109, no. 6, p. 447, 1962, doi: 10.1149/1.2425445.

[150] S. Khodaparast, J. Marcos, W. N. Sharratt, G. Tyagi, and J. T. Cabral, “Surface-Induced Crystallization of Sodium Dodecyl Sulfate (SDS) Micellar Solutions in Confinement,” *Langmuir*, vol. 37, no. 1, pp. 230–239, 2021, doi: 10.1021/acs.langmuir.0c02821.

[151] T. E. Graedel, “Copper patinas formed in the atmosphere-II. A qualitative assessment of mechanisms,” *Corros. Sci.*, vol. 27, no. 7, pp. 721–740, 1987.

Annexes

ANNEX 1 – Environmental parameters during outdoor exposure

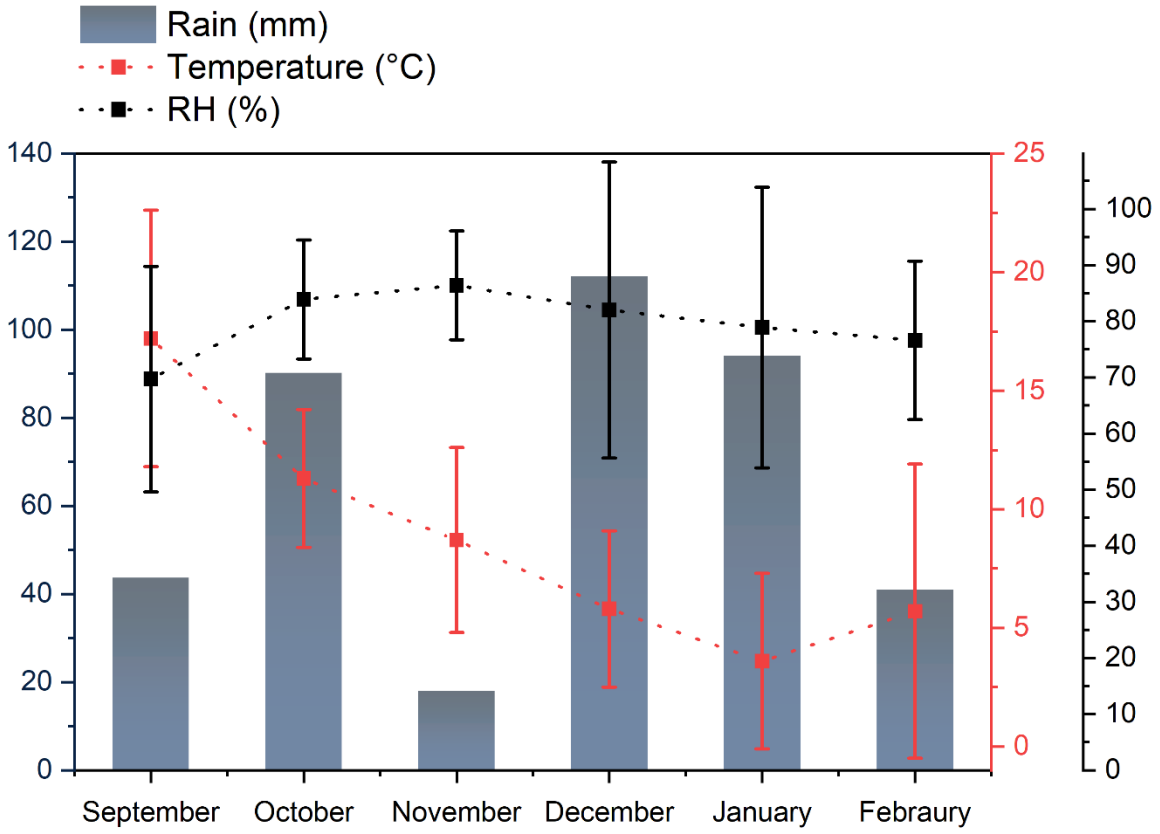

Figure A 1: Variation of Temperature and Relative Humidity during the 6-months exposure. Measurements were recorded at the exposure site (CEA Saclay) using a KIMO® KILOG KH200 instrument. Pluviometry data are also reported. In this case, data were collected at the environmental station of Toussus-le-Noble on the Saclay plateau, about 5 km away from the exposure site.

ANNEX- 2 – EDS mapping of the treated samples before exposure

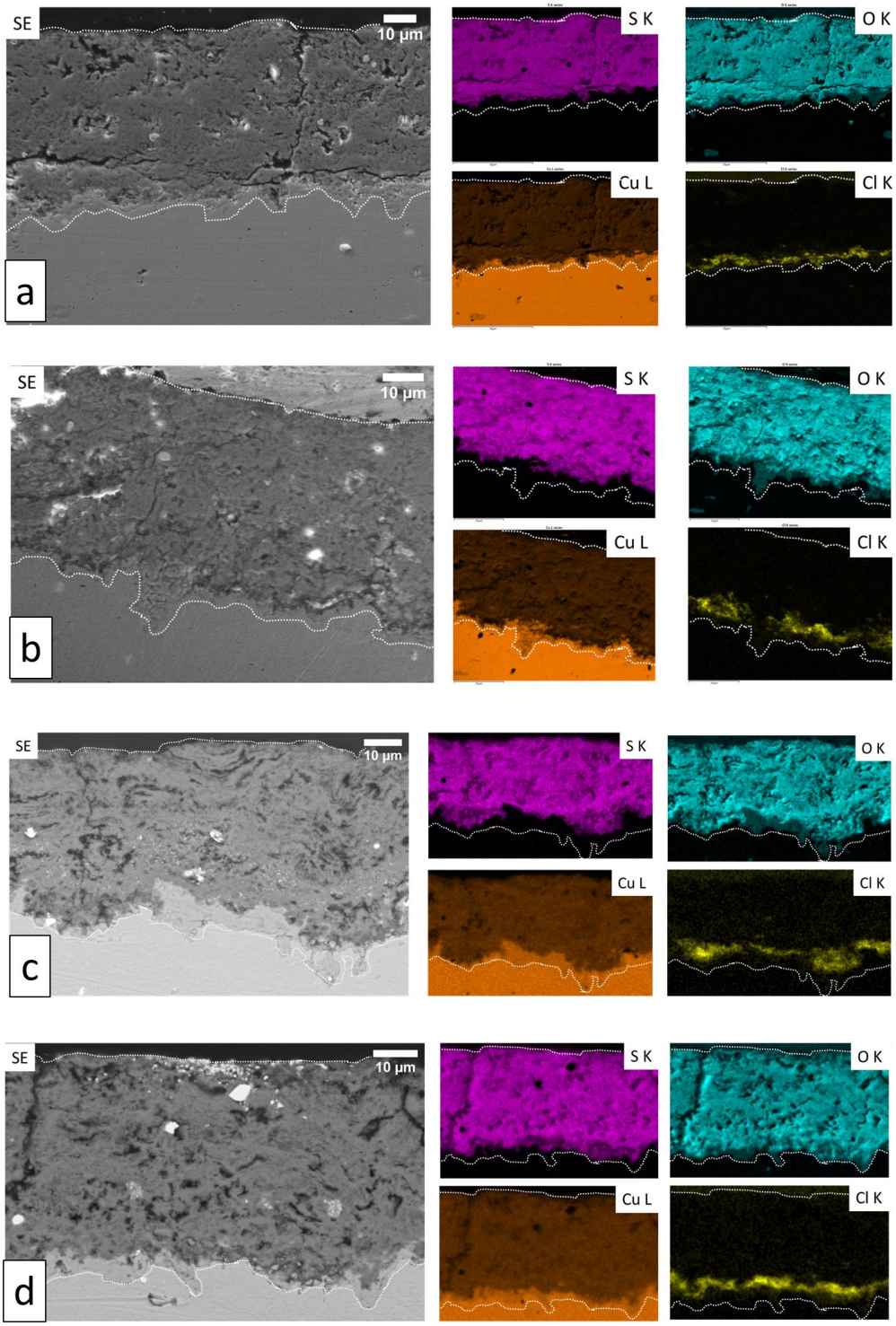

Figure A 2: EDS elemental maps corresponding to the samples (a) untreated, (b) BTAH-treated, (c) 5CBT-treated and (d) HC10-treated. Analysis was performed after treatment.

ANNEX- 3 – EDS mapping of the treated samples after exposure

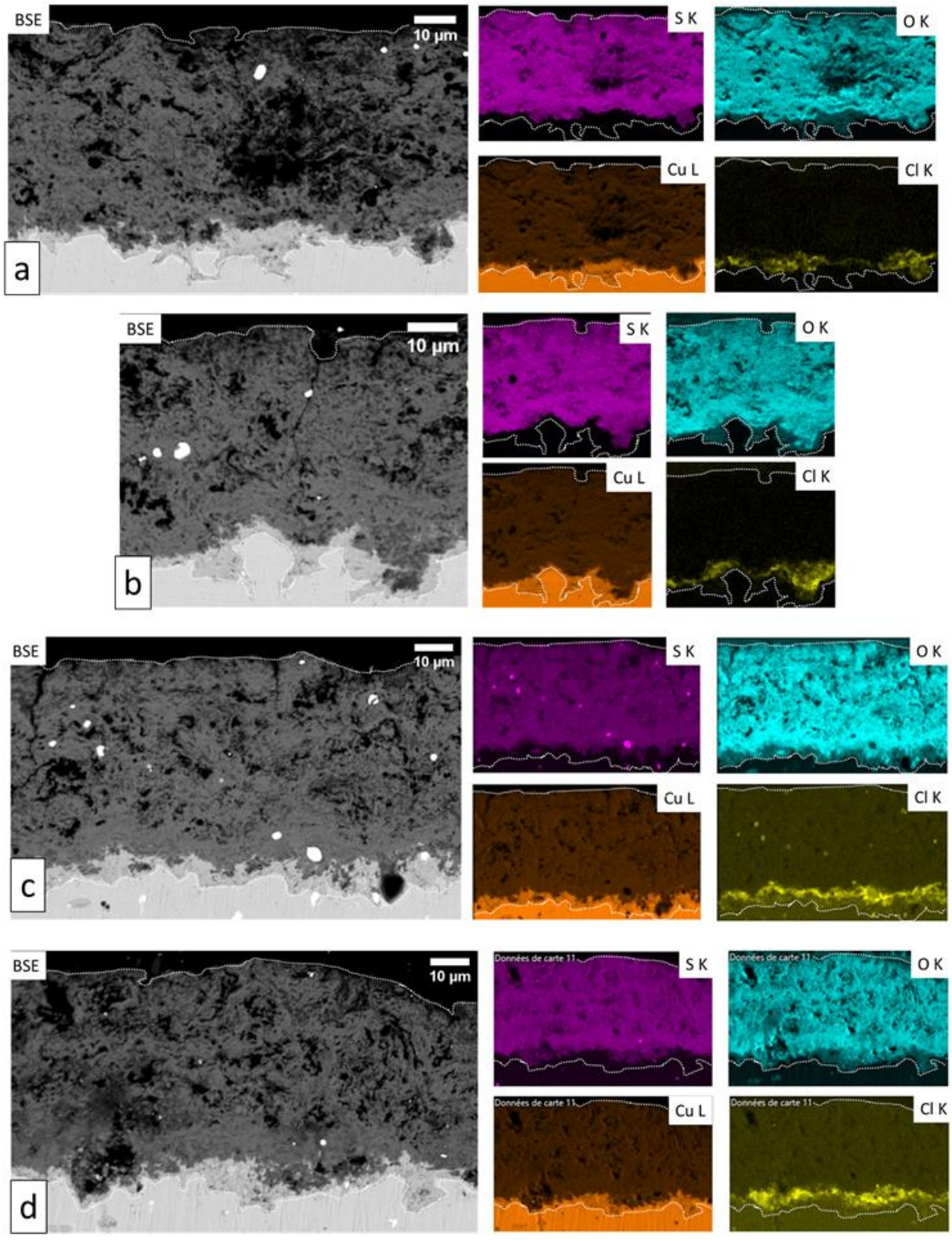

Figure A 3: EDS elemental maps corresponding to the samples (a) untreated, (b) BTAH-treated, (c) 5CBT-treated and (d) HC10-treated. Analysis were performed after 6-months outdoor exposure.

Résumé de la thèse en français

Compréhension des mécanismes d'inhibition de la corrosion du patrimoine métallique cuivreux par une approche physicochimique multi-échelle

La protection du patrimoine métallique exposé en extérieur en tant que témoin culturel de notre passé représente un défi pour les scientifiques compte tenu des particularités de ce domaine d'application. En effet, contrairement aux applications industrielles courantes, les objets métalliques exposés à l'extérieur sont des matériaux complexes dans lesquels la partie en contact avec l'environnement est constituée de couches de produits de corrosion dont la nature et les propriétés physico-chimiques dépendent des propriétés internes de la matrice métallique (composition du métal/alliage, présence de scories) et externes (composition et variations atmosphériques, inclinaison, temps d'exposition). L'évolution des couches de produit de corrosion des cuivreux a été étudiée par plusieurs auteurs [1]–[3]. En particulier, la corrosion atmosphériques du cuivre en milieu urbain conduit à la formation d'une couche d'oxyde de cuivre, cuprite (Cu_2O), en contact du métal à laquelle s'ajoute progressivement une couche de sulfate hydrate de cuivre, dont la phase stable en milieu pauvre en chlorures est la brochantite ($Cu_4SO_4(OH)_6$) [4]. Cette dernière donne à l'objet exposé sa couleur caractéristique vert clair. En conservation du patrimoine, lorsque les produits de corrosion n'affectent pas la stabilité de l'objet, il est généralement préférable de ne pas les éliminer selon le principe d'intervention minimale [5]. La couche de produit de corrosion témoigne aussi de la valeur historique de l'objet et est esthétiquement acceptée.

Pour retarder et prévenir la perte du matériel dû aux phénomènes de corrosion, les conservateurs utilisent généralement des stratégies [6] basées sur la formation d'une barrière entre l'environnement et la surface externe de l'objet avec l'utilisation de revêtements organiques (cire microcristalline, résines acryliques). Une autre méthode repose sur l'application d'inhibiteurs de corrosion suivie par l'application d'un revêtement Le rôle lié à l'application d'inhibiteurs organiques sur des surfaces corrodées n'est pas clair et l'efficacité d'inhibiteurs comme le benzotriazole, largement utilisé en conservation, reste controversée étant donné que la plupart des études ont été réalisées sur du métal nu ou à travers l'étude du système inhibiteur associé à un revêtement.

Cette thèse pose comme objectif d'étudier spécifiquement les inhibiteurs de corrosion pour la conservation des artefacts cuivreux exposés et pour cela une approche physico-chimique innovante a été développée. En vue d'étudier les processus physico-chimiques en jeu, des échantillons

représentatifs de la corrosion à long terme ont été étudiés : il s'agit de plaques en cuivre corrodée en milieu urbain pendant plus de 100 ans qui constituaient l'ancienne toiture de l'église de Saint Martin à Metz.

Trois composées organiques ont été sélectionnées pour leurs fonctions chimiques différentes. Le benzotriazole (BTAH) est un composé caractérisé par une fonctionne azole ou les atomes d'azote fonctionne comme donateurs d'électrons à la base de la liaison avec les atomes de cuivre [7]. Le BTAH est couramment employé en conservation même si son efficacité est débattue et son utilisation déconseillée en raison de sa possible toxicité.

Un deuxième composé est l'acide décanoïque (HC10), un acide gras qui porte une fonction carboxylique qui forme une liaison avec les atomes de cuivre et une chaine aliphatique qui confère des propriétés hydrophobiques intéressantes. Le HC10 a été étudié comme traitement pour les objets patrimoniaux et du cuivre en particulier [8], [9] aussi en raison de l'absence de risques pour l'opérateur et l'environnement.

Enfin, un composé qui est caractérisé par les deux fonctionnes, azole et carboxylique a été choisi. Il s'agit de l'acide benzotriazole-5-carboxylique (5CBT). Ce composé n'a jamais été étudié pour des applications pour la protection du patrimoine.

L'approche analytique choisie se base sur des expériences menées en parallèle sur deux types de système : les minéraux synthétiques comme systèmes simplifiés et le système complexe du cuivre corrodé.

La réactivité des inhibiteurs avec des phases minérales synthétiques représentatives des produits de corrosion (brochantite et cuprite) a été étudiée en faisant réagir les solutions contenants les inhibiteurs avec les minéraux de synthèse et en étudiant les produits insolubles obtenus pour chaque réaction. Différentes techniques complémentaires ont été utilisées à l'échelle globale (diffraction des rayons X, DRX), microscopique (µ-spectroscopie Raman) et nanométrique (Microscopie Electronique à Transmission, MET).

Les propriétés physico-chimiques du système complexe de cuivre corrodés historiques ont été évaluées sur les échantillons non traité, après traitement et après 6 mois d'exposition en milieu extérieur en vue d'évaluer leurs modifications dues à la fois au traitement et à l'exposition. Une combinaison de différents technique analytiques a été employée avec une approche multi-échelle : aux observations globales (couleur, tension de surface, polarisation potentiodynamique) se sont ajoutées des analyses à l'échelle microscopique en surface et en coupe transverse (µ-spectroscopie Raman, Microscopie Electronique à Balayage associée à la microanalyse par Energie Dispersive de

rayons X, MEB-EDS) et des observations à l'échelle nanométrique (tomographie par faisceau d'ions focalisé et MET). De plus, des expériences complémentaires en milieux marqués ont été effectuées. L'immersion en eau deuterée des échantillons traité et non traité avant et après exposition six mois en extérieur et suivi par détection des ions par spectrométrie de masse à ions secondaires à temps de vol (ToF-SIMS) a permis de déterminer l'enrichissement en deutérium dans la couche de produits corrosion, afin d'étudier l'évolution de perméabilité à l'eau par approche comparative avec l'échantillon non traité.

Le comportement passif des échantillons et en particulier de la couche de cuprite a été étudiée par immersion dans une solution concentrée de KBr suivie par observations MEB-EDS des coupes transverses.

Sur la base de l'interprétation des différentes expériences, deux mécanismes réactionnels pour les trois inhibiteurs choisis sont mis en évidence.

D'un côté, les molécules caractérisées par la fonction azole (BTAH et 5CBT) réagissent avec les phases minérales selon un mécanisme d'adsorption-précipitation formant un complexe amorphe adsorbé (film nanométrique) qui entoure la phase minérale qui n'a pas réagi. Cette couche amorphe est moins épaisse dans le cas de la cuprite traité avec le BTAH comparé à la brochantite et l'épaisseur reste dans l'ordre de grandeur des quelques nanomètres pour le traitement avec le 5CBT. La détection d'un complexe organométallique toujours avec la brochantite dans la couche externe des produits corrosion confirme ce comportement. Les traitements à base des deux composée BTAH et 5CBT diffèrent par leur profondeur de pénétration, et donc de réaction : la formation du complexe BTAH a été détectée jusqu'à la couche interne de cuprite, tandis que la complexation avec du 5CBT n'est observée que dans la partie externe de la brochantite, à environ 20 µm de la surface extérieure. La différence de pénétration a un impact sur les propriétés de la couche et par conséquence sur l'efficacité du traitement. En particulier, l'étude de l'enrichissement en deutérium montre que si dans la couche externe de brochantite le traitement BTAH et le complexe Cu-BTA précipité ne joue aucun effet sur la diminution de la pénétration de l'eau, en revanche une drastique diminution de la valeur relative de l'enrichissement a été mesurée au niveau de la couche de cuprite. A contrario aucune réduction de cette valeur n'a pas été observée pour le traitement à base de 5CBT dans l'ensemble de la couche de brochantite et de cuprite.

L'immersion en solution de KBr montre une perte de passivation avec des différences majeures sur les échantillons non traités : la formation d'un nouveau composée cristallin ($Cu_2Br(OH)_3$) par réaction des ions cuivre en solution avec les ions bromure, la présence de cavités entre la couche de cuprite et le métal qui témoigne d'une reprise de la corrosion et une distribution inhomogène du brome à

l'intérieur de la couche. En particulier, la reprise de la corrosion et la formation des complexes solubles avec le bromure a été utilisée pour déterminer l'efficacité du traitement en augmentant l'effet passivant de la cuprite.

Le traitement à base de BTAH montre les meilleurs résultats puisqu'aucun des phénomènes décrits pour l'échantillon précédent n'ont été observés. Cela suggère que la formation du complexe Cu-BTA n'est pas limitée à la couche de brochantite mais a lieu également sur la partie externe de la couche de cuprite et a comme effet d'augmenter le caractère passivant de la couche. En revanche le 5CBT est moins efficace même si les phénomènes de re-corrosion sont plus limités comparé à l'échantillon non traité. Cette observation est liée au fait que l'inhibiteur réagit majoritairement avec la partie externe de la couche qui se traduit par une interaction moins importante avec la cuprite.

Après une exposition de six mois en extérieur, les résultats des analyses montrent que les propriétés observées pour les deux traitements ne varient pas et, en particulier, le complexe azole-cuivre est toujours détecté.

Un mécanisme différent a été identifié dans le cas du HC10. La présence de la fonctionne carboxylique dans cette molécule conduit à la formation du decanoate de cuivre par un mécanisme de dissolution-précipitation qui est mis en évidence par les réactions avec les deux phases synthétiques pour lesquelles le decanoate de cuivre (II) est détecté. Des cristaux de decanoate de taille microscopique sont identifiés en surface externe de la couche de brochantite. Cette précipitation confère la couleur tendant vers le bleu caractéristique à ces échantillons traités mais aussi une quasi-superhydrophobicité après traitement. Dans cette étude, à la différence des précédentes expériences, le decanoate n'a pas été identifié à l'intérieur de la couche probablement du fait d'un protocole de traitement légèrement différent.

Après traitement, la protection attendue pour le traitement HC10 est confirmée par une haute efficacité inhibitrice et par l'absence de re-corrosion du métal après immersion en solution KBr. Etonnamment, la mesure de l'enrichissement du deutérium ne semble pas être affectée par le traitement. Malgré ces résultats prometteurs juste après traitement, une exposition en extérieur de six mois provoque la perte de la couche hydrophobe de decanoate de cuivre déposé en surface par lixiviation dû au manque de liaison chimique fortes entre le précipité et la surface. Cela confirme le caractère provisoire d'un traitement à base de decanoate de cuivre pour la protection des cuivreux.

En plus de ces résultats phénoménologiques, une nouvelle méthodologie basée sur l'expérience KBr pour tester les inhibiteurs des artefacts en cuivre corrodés est proposée. La procédure de test mise en place pendant l'étude a révélé une facilité de mise en œuvre, avec l'utilisation des méthodes et matériaux classiquement disponibles dans les laboratoires (solution aqueuse de KBr et MEB-EDS pour

les analyses). Les résultats sont obtenus dans des temps raisonnables (30 jours d'immersion) et sont d'interprétation facile. Cette méthode pourrait constituer une première étape dans l'identification de nouveaux inhibiteurs de corrosion alternatifs et non toxiques pour la protection du patrimoine métallique.

[1] C. Leygraf, I. O. Wallinder, J. Tidblad, and T. Graedel, *Atmospheric corrosion*. John Wiley & Sons, 2016.

[2] C. Leygraf, T. Chang, G. Herting, and I. Odnevall Wallinder, "The origin and evolution of copper patina colour," *Corros. Sci.*, vol. 157, no. March, pp. 337–346, 2019, doi: 10.1016/j.corsci.2019.05.025.

[3] L. Robbiola and L.-P. Hurtel, "Nouvelle contribution à l'étude des mécanismes de corrosion des bronzes de plein air: caractérisation de l'altération de bronzes de Rodin," *Mém. Et. Scien. Revue Mét.*, vol. 12. pp. 809–823, 1991.

[4] A. Kratschmer, I. Wallinder, and C. Leygraf, "The evolution of out copper patina," *Corros. Sci.*, vol. 44, no. 44, pp. 425–450, 2002.

[5] C. Brandi, *Teoria del restauro*. Einaudi, 2000.

[6] D. A. Scott, *Copper and bronze in art: corrosion, colorants, conservation*. Getty publications, 2002.

[7] M. Finšgar and I. Milošev, "Inhibition of copper corrosion by 1, 2, 3-benzotriazole: a review," *Corros. Sci.*, vol. 52, no. 9, pp. 2737–2749, 2010.

[8] A. Elia, M. Dowsett, and A. Adriaens, "On the use of alcoholic carboxylic acid solutions for the deposition of protective coatings on copper," in *Metal 10 Proceedings of the interim meeting of the ICOM-CC metal working group, Charleston, South Carolina, USA*, P. Mardikian, C. Chemello, C. Watters, and P. Hull, Eds. 2011, pp. 193–200.

[9] E. Apchain *et al.*, "Efficiency and durability of protective treatments on cultural heritage copper corrosion layers," *Corros. Sci.*, vol. 183, p. 109319, 2021, doi: https://doi.org/10.1016/j.corsci.2021.109319.

Title : Understanding the inhibition corrosion mechanism for copper based alloys by a physico-chemical multi-scale analytical approach

Keywords : copper-based alloys, atmospheric corrosion, inhibitors, cultural heritage

Metallic heritage artefacts represent cultural traces of our past, and for this reason, their preservation and transmission to future generations is important. To protect copper-based artworks exposed outdoors, several conservation strategies are followed, including the use of organic corrosion inhibitors. Inhibitors are usually borrowed from the industrial field. However, the surface state of the metal with the presence of complex corrosion layers, and the protocol of inhibitors' application differ considerably from the industrial ones. The present study specifically addresses corrosion inhibitors for conservation of copper-based exposed artifacts by an innovative physico-chemical approach. The approach takes into account the complexity of the corrosion layer under investigation: a naturally corroded copper plate, representative for outdoor long-term corrosion have been chosen. For the study, three organic molecules, characterized by different chemical functions have been selected as test inhibitors: benzotriazole (BTAH), an azole compound, employed in conservation, which efficiency is debated and its use discouraged due to toxicity; decanoic acid (HC10) a long-chain fatty acid that has been proposed as treatment for heritage objects; benzotriazole-5-carboxylic acid (5CBT), a compound with mixed azole-carboxylic functions. The reactivity of the inhibitors with synthetic mineral phases representative of corrosion products as well as ancient corroded samples (100 years) before and after 6-months outdoor exposure have been investigated by combining observations at the nanoscale (TEM, FIB-tomography) to those obtained at the microscale (Raman, SEM-EDS) and global/bulk observations (colour, surface tension, XRD). Additional experiments in marked environment allowed to investigate changes in permeability (D_2O immersion) and the evolution of passive behavior (KBr immersion). Two reaction mechanisms have been observed and a relationship with the efficiency and durability of the inhibition is proposed. The molecules BTAH and 5CBT interaction with copper atoms occurs via the azole function and both molecules react according to an adsorption-precipitation mechanism forming an adsorbed amorphous complex (nanometric film) on the substrate mineral phase (cuprite and brochantite). The two treatments on the ancient corrosion layers differ for their depth of penetration, with Cu-BTAH complex formation being detected until the cuprite inner layer, while 5CBT complexation is observed only in the outer part of the brochantite. This has an impact on the water permeability and passivity, with the BTAH treatments showing the best results, and suggests a complex formation with the outer cuprite layer in this last treatment. The carboxylic function in HC10 leads to the precipitation of copper decanoate by a dissolution-precipitation mechanism. Crystals of decanoate are formed on the outer surface of brochantite: this confers near super-hydrophobicity to the sample after treatment. However, the lack of bond between the precipitate and the surface determines the loss of the surface-deposited hydrophobic layer after 6 months of outdoor exposure. In addition to these phenomenological results, a new methodology based on the KBr experiment for testing inhibitors for copper corroded artefacts is also proposed.

Titre: Compréhension des mécanismes d'inhibition de la corrosion du patrimoine métallique cuivreux par une approche physicochimique multi-échelle

Mots clés : cuivreux, corrosion atmosphérique, inhibiteurs, patrimoine

Le patrimoine métallique est un témoin culturel de notre passé et, pour cette raison, sa préservation et sa transmission aux générations futures sont importantes. Plusieurs stratégies sont utilisées pour la protection du patrimoine cuivreux exposée en extérieur, dont l'utilisation des inhibiteurs de corrosion organiques. Les inhibiteurs utilisés pour le patrimoine sont généralement empruntés au domaine de l'industrie. Cependant, l'état de surface du métal, couvert par des couches de produits de corrosion complexes, et le protocole d'application des inhibiteurs diffèrent considérablement de l'application industrielle.

La présente étude porte spécifiquement sur les inhibiteurs de corrosion pour la conservation des artefacts exposés à base de cuivre par une approche physico-chimique innovante. L'approche prend en compte la complexité de la couche de corrosion étudiée : une plaque de cuivre naturellement corrodée, représentative de la corrosion extérieure à long terme a été choisie. Pour l'étude, trois molécules organiques, caractérisées par des fonctions chimiques différentes ont été sélectionnées comme inhibiteurs de test : le benzotriazole (BTAH), un composé azolé, employé en conservation, dont l'efficacité est débattue et l'utilisation déconseillée en raison de sa toxicité ; l'acide décanoïque (HC10) un acide gras à longue chaîne qui a été proposé comme traitement pour les objets patrimoniaux ; l'acide benzotriazole-5-carboxylique (5CBT), un composé à fonctions mixtes azole-carboxyliques. La réactivité des inhibiteurs avec des phases minérales synthétiques représentatives des produits de corrosion ainsi que des échantillons corrodés anciens (100 ans) avant et après 6 mois d'exposition extérieure ont été étudiées en combinant des observations à l'échelle nanométrique (MET, FIB-tomographie) à celles obtenues à l'échelle microscopique (Raman, MEB-EDS) et des observations globales/globales (couleur, tension de surface, XRD). Des expériences complémentaires en milieux marqués ont permis d'étudier les évolutions de perméabilité (immersion en D_2O) et de comportement passif (immersion KBr). Deux mécanismes réactionnels ont été observés et une relation avec l'efficacité et la durabilité de l'inhibition est proposée. Les molécules caractérisées par la fonction azole (BTAH et 5CBT) réagissent selon un mécanisme d'adsorption-précipitation formant un complexe amorphe adsorbé (film nanométrique) sur la phase minérale substrat (cuprite et brochantite). Les deux traitements sur les couches anciennes de corrosion diffèrent par leur profondeur de pénétration, la formation du complexe BTAH étant détectée jusqu'à la couche interne de cuprite, tandis que la complexation 5CBT n'est observée que dans la partie externe de la brochantite. Ceci a un impact sur la perméabilité de l'eau et la passivité pour les traitements au BTAH qui montrent les meilleurs résultats, et suggère une formation de complexe Cu-BTA sur la partie externe de la couche de cuprite dans ce dernier traitement. La fonction carboxylique dans HC10 conduit à la précipitation du décanoate de cuivre par un mécanisme de dissolution-précipitation. Des cristaux de décanoate se forment sur la surface externe de brochantite : cela confère une quasi-superhydrophobie à l'échantillon après traitement. Cependant, le manque de liaison chimique forte entre le précipité et la surface induit la perte de la couche hydrophobe déposée en surface après 6 mois d'exposition à l'extérieur.

En plus de ces résultats phénoménologiques, une nouvelle méthodologie basée sur l'expérience KBr pour tester les inhibiteurs des artefacts corrodés par le cuivre est également proposée.